

# **Biofunctionalization of upconversion nanoparticles for intracellular labeling and imaging**

by Tesfaye Eshete Asrat

Thesis submitted in fulfilment of the requirements for  
the degree of

**PhD thesis: Science**

under the supervision of

Distinguished Professor Dayong Jin

A/Professor Jiajia Zhou; Dr. Qiang Fu; Dr. Peter Su; and  
Dr. Jiayan Liao

University of Technology Sydney

Faculty of Science

25 September 2022

## **Certificate of original authorship**

I, Tesfaye Eshete Asrat, declare that this thesis is submitted in fulfillment of the requirements for the award of Ph.D. in Science in the school of mathematical and physical sciences at the University of Technology Sydney.

This thesis is wholly my own work unless otherwise referenced or acknowledged. In addition, I certify that all information sources and literature used are indicated in the thesis.

This research is supported by the Australian Government Research Training Program.

Signature:

Production Note:  
Signature removed prior to publication.

25 September 2022

## **Acknowledgment**

I am pleased to use this opportunity to thank my supervisors, family, and friends for their unlimited help during the study period. I thank distinguished Professor Dayong Jin, for the Ph.D. opportunity and his inspiration, advice, and support throughout the study period. The end-user and industry-oriented research projects at IBMD are great learning opportunities, and I gained vast experience in how scientific research could be used to address real-life challenges. Besides the comprehensive academic and research experience I acquired during my stay, I have gained many personal and professional development lessons from him.

I want to express my deep gratitude to A/Professor Olga Shimoni, my former principal supervisor, for her support and advice at the start of the Ph.D. project. Her guidance and support helped me a lot, especially in my first year of study. I am very thankful to all my co-supervisors A/Professor Jiajia Zhou, Dr. Qiang Fu, Dr. Peter Su, and Dr. Jiayan Liao. I am grateful for A/Professor Jiajia Zhou's continued advice and support during the experimental works and thesis writing. I am thankful for Dr. Qiang Fu's advice on polymer synthesis and characterization. I greatly appreciate Dr. Peter Su's valuable advice and guidance in cell labeling experiments and microscopy techniques. I thank Dr. Jiayan Liao because she provided me with extensive advice during experimental works and the thesis write-up. I thank all members of IBMD for their help and support during my study period. I am grateful to the chemical technology, MAU, and biological science laboratory technical officers, for the lab inductions and training and their immediate helps whenever I need their support.

To my father, Eshete Asrat, and my mother, Menbere Gebryie, for their sacrifices to raise and educate my siblings and me in challenging situations. All that I have achieved so far is due to their unlimited help. Tizta B. Woldekidan, who is not only my life partner but also secures my family, helped me a lot in managing the home and our children. I thank my daughter Emnet and my sons Natan and Dagim for their patience in staying alone in my home country during the study, including the COVID-19 lockdown period. To all my siblings, especially Zelalem E., Bahru M., Zewge A., and Dejene B., for helping my parents and family; and to my friends A/Professor Yedilfana S., Dr. Amanuel B., Dr. Tessema F., and Dr. Wassie T. for sharing their experiences, and Mr. Anthony Sarabi. for proofreading. I thank the Ethiopian community at Sydney Debre Tsion St Mary church for their encouragement and support. I am grateful to Addis Ababa Science

and Technology University for the study leave, Alcolizer technology, and the APRIntern for the internship. I thank MaPS and GRS-UTS for the IRS and UTSP's scholarships. In a nutshell, I am very grateful to all involved in my Ph.D. study journey, and lastly, I acknowledge my everyday aspiring UTS's motto, 'THINK.CHANGE.DO'.



## Table of Contents

Certificate of original authorship .....	ii
Acknowledgment .....	iii
Table of Contents .....	v
List of Figures .....	ix
List of tables.....	xvi
List of schematic illustrations .....	xvii
Acronym .....	xviii
Abstract .....	xx
1  Introduction.....	1
1.1 Preamble.....	1
1.2 Motivations of the project .....	1
1.3 Molecular imaging .....	4
1.4 Contrast agents in fluorescent imaging .....	6
1.5 Nanoparticles as a contrast agent .....	8
1.6 Objectives of the study.....	17
2  Nanotechnology in Healthcare Applications .....	19
2.1 Preamble.....	19
2.2 Introduction .....	19
2.3 The lanthanides (III) doped UCNPs.....	23
2.3.1 The potential advantages of UCNPs surfaces.....	30
2.3.2 Modification of the UCNPs surfaces .....	33
2.3 Polymers in surface modification of UCNPs .....	39

2.4.1	RDRP in the synthesis of copolymers .....	40
2.4.2	Functionality and architecture of copolymers for UCNPs surface grafting .....	47
2.4	UCNPs-based biomedical applications .....	63
2.5	Conclusion.....	70
3	Synthesis and Characterization of Upconversion Nanoparticles .....	73
3.1	Preamble.....	73
3.2	Introduction .....	73
3.3	Experimental section .....	74
3.3.1	Synthesis of $\beta$ -NaYF <sub>4</sub> :Yb <sup>3+</sup> /Er <sup>3+</sup> nanoparticles .....	75
3.4	Result and discussion .....	78
3.5	Conclusion.....	80
4	Development of RAFT Block Copolymers for UCNPs Surface Functionalization .....	81
4.1	Preamble.....	81
4.2	Introduction .....	81
4.2.1	RAFT polymerization for the synthesis of block copolymers .....	82
4.3	Experimental section .....	84
4.3.1	OESPX-based copolymer synthesis.....	86
4.3.2	CTCPA-based photo-induced triblock polymerization .....	88
4.3.3	CPADB-based thermally initiated triblock polymerization.....	90
4.3.4	CDCPA-based photo-induced triblock polymerization .....	91
4.3.5	CTCPA-based photo-induced diblock polymerization.....	92
4.4	Result and discussion .....	93
4.4.1	OESPX-based triblock copolymer.....	93
4.4.2	CTCPA-based triblock copolymer.....	98

4.4.3	CPADB-based triblock copolymer .....	101
4.4.4	CDCPA-based triblock copolymer .....	104
4.4.5	CTCPA-based diblock copolymer .....	108
4.5	Conclusion.....	111
5	Design and Functionalization of Upconversion Nanoparticles Surfaces .....	113
5.1	Preamble.....	113
5.2	Introduction .....	113
5.2.1	UCNPs surface functionalization.....	114
5.2.2	Coupling of biomolecules .....	116
5.3	Experimental section .....	117
5.3.1	UCNPs copolymer surface grafting .....	117
5.4	Result and discussion .....	120
5.4.1	Hydrodynamic size and zeta potential of surface grafted UCNPs.....	120
5.4.2	Stability of copolymers grafted UCNPs surfaces .....	127
5.4.3	Determination of surface graft density of modified nanoparticles .....	133
5.4.4	Coupling of biomolecules and organic dyes.....	141
5.5	Conclusions .....	146
6	Upconversion Nanoparticles in Intracellular Labeling and Imaging .....	149
6.1	Preamble.....	149
6.2	Introduction .....	149
6.3	Experimental section .....	154
6.3.1	Materials and methods .....	154
6.3.2	The HeLa cell line UCNPs labeling .....	155
6.4	Result and discussion .....	157

6.4.1	UCNPs nanoprobe for intracellular labeling .....	157
6.4.2	UCNPs-dye hybrid probes for intracellular labeling and imaging .....	165
6.5	Conclusion.....	170
7	Summary of the Overall Ph.D. Project results .....	173
7.1	Preamble.....	173
7.2	The UCNPs synthesis and characterization .....	173
7.3	The synthesis of RAFT copolymers.....	175
7.4	Surface grafting and functionalization of the UCNPs.....	180
7.5	UCNPs in intracellular labeling and imaging .....	183
7.6	Conclusion.....	185
8	Conclusion and Perspectives.....	187
	Appendix.....	189
	Internship Project work:.....	189
	Materials Chemistry and scaling-up of nanoparticles fabrication .....	189
1.	Introduction.....	189
2.	Activities performed and experiences.....	190
3.	Conclusion .....	190
	Bibliography .....	191

## List of Figures

Figure 1 Schematic representation of the multidisciplinary nature of nanomedicine and different disciplines involved in its implementation. Adapted with permission <sup>14</sup> © 2009 Wiley-VCH. ....	2
Figure 2 Pictorial representation of roles of nanotechnology in the convergence of different disciplines in the development of nanomaterials for diagnostic and therapeutic applications .....	3
Figure 3 Classification of molecular imaging techniques with a focus on fluorescent-based optical imaging approaches. ....	5
Figure 4 Pictorial representation of contrast creation in fluorescence imaging of tumor, where (A) and (B) stand for labeling of the specific tumor site, and (C) stands for signal generation, and detection. Adapted with permission <sup>42</sup> © 2006 Elsevier B.V. ....	6
Figure 5 The optical EMR regions and the fluorescence modalities used in fluorescence imaging. Reproduced with permission <sup>43</sup> © 2019 Elsevier B.V. ....	7
Figure 6 Timeline on the progressive development of nanoprobes and their use in different fluorescence microscopy. Reproduced with permission <sup>52</sup> © 2018 Wiley-VCH. ....	9
Figure 7 Characteristic emissions from lanthanide (III) doped nanoparticles (A) downshifting and (B) up converting modes. Reproduced with permission <sup>59, 60</sup> © 2018 (A) and © 2019 (B) Elsevier B.V. ....	10
Figure 8 The different UCNP synthesis techniques (A) thermal (B) hydro(solvo)thermal (C) coprecipitation, and (D) sol-gel methods. Adapted with permission <sup>40</sup> © 2020 Elsevier B.V. ....	11
Figure 9 A comprehensive research plan and timeline on the synthesis and developments of UCNPs, products, and envision for their clinical translation. Adapted with permission <sup>73</sup> © 2017 American Chemical Society. ....	12
Figure 10 The 'graft from' (A) and 'graft to' (B) approach surface modification. Reprinted with permission <sup>80</sup> © 2017 American Chemical Society. ....	14
Figure 11 Schematic representation of surface tethering of bifunctional polymer and conjugation of biomolecules to nanoparticle surfaces. ....	15

Figure 12 Schematic illustration of the flow scheme of the Ph.D. research project, which encompasses synthesis of UCNPs, RAFT copolymers design and development, surface grafting and functionalization, and cell labeling and imaging. ....	17
Figure 13 The relationships between nanotechnology with nanobiotechnology and nanomedicine. Reproduced with permission <sup>11</sup> © 2017 Springer. ....	20
Figure 14 Representation of multifunctional nanoparticles developed through surface modification and biofunctionalization of UCNP. Reproduced with permission <sup>107</sup> © 2009 Wiley-VCH. ....	21
Figure 15 List of commonly used labeling agents in fluorescence microscopy that includes both organic and inorganic fluorophores, their sub-classes (A), and organic fluorophores with their respective visible emission (B). Adapted with permission <sup>114, 115</sup> © 2016, and © 2021 Wiley-VCH, respectively. ....	22
Figure 16 The comparative size (A) and luminescence emission wavelength ranges of optical nanoprobos (B). Reproduced with permission <sup>115</sup> © 2016 Wiley-VCH. ....	23
Figure 17 Pictorial representation of the synthesis of UCNPs (A) representation of reaction mixture at the initial stage, (B) formation of cubic phase, and (C) favoring the hexagonal structure formation. ....	25
Figure 18 The UCNPs synthesis reaction setup (A), course of reactions, including the stages in hexagonal phase formation at (B) and (C) Reproduced with permission <sup>10</sup> © 2016 American Chemical Society. ....	26
Figure 19 The energy level diagrams of 4fn electron transitions of lanthanide elements. Reproduced with permission <sup>80</sup> © 2021 Royal Chemical Society. ....	29
Figure 20 Schematic representation of the five kinds of upconversion mechanisms. Adapted with permission <sup>156</sup> © 2020 Elsevier B.V. ....	30
Figure 21 Pictorial representation of the structure of electrical double layer during zeta potential determination using capillary cuvette. Adapted with permission <sup>160, 161</sup> © 2020 Canadian Society for Chemical Engineering and © 2016 Wiley-VCH, respectively. ....	32

Figure 22 Schematic illustration of surface polymer architectures (A), different surface attachment techniques (B), and types of polymers suitable for surface modification (C). Reproduced with permission <sup>174</sup> © 2021 Elsevier B.V. ....	35
Figure 23 Schematic representation of UCNPs surfaces optimization opportunities performance through polymer grafting. ....	36
Figure 24 The progressive development in nanomaterials design and challenges faced in their biological applications. Reproduced with permission <sup>177</sup> © 2012 by Annual Reviews.....	37
Figure 25 Pictorial representation of the potential advantages of RAFT polymers in nanoparticle hybrids development. Reproduced with permission <sup>187</sup> © 2021 The Royal Society of Chemistry. ....	40
Figure 26 Schematic illustration of RDRP in controlled polymerization. Reproduced from Moad et al. <sup>82</sup> .....	41
Figure 27 Representative RAFT agent types for the synthesis of block copolymers. ....	44
Figure 28 Effect and compatibility of the Z- and R- groups of RAFT agents with different monomer types. Reproduced with permission <sup>220</sup> © 2006 CSIRO. ....	46
Figure 29 Pictorial representation of responsive surface. Reproduced with permission <sup>224</sup> © 2020 Wiley-VCH. ....	48
Figure 30 Schematic illustration of surface hydration layer produced by amphiphilic coated surfaces in defending the nanoparticle from protein fouling. ....	50
Figure 31 Representation of dipole moment orientation in the polymer chains (A) and hydration layer formation in zwitterionic surfaces (B). Reproduced with permission <sup>250</sup> © 2020 American Chemical Society. ....	51
Figure 32 Representation of corona effect on nanoparticles targetability (A) without polymer surface graft and (B) with polymer grafting. Reproduced with permission <sup>260</sup> © 2017 The Royal Society of Chemistry.....	52
Figure 33 Schematic illustration of nanoparticle surfaces capped with oleate ligand (A), and grafted from multifunctional copolymer (B). ....	54

Figure 34 Pictorial representation of intracellular delivery of nanoparticles and possible nano-bio interactions during cellular uptake. Reproduced with permission <sup>269</sup> © 2009 Macmillan Publishers Limited.....	55
Figure 35 Pictorial illustration of mechanisms of cellular uptake and endosomal escape for antibody. Reproduced with permission <sup>293</sup> © 2011 The Royal Society of Chemistry.....	57
Figure 36 Schematic representation of surface grafted copolymers (A) and antibody-coupled surfaces (B). .....	60
Figure 37 Schematic representation of coupling of the whole antibody to nanoparticle surfaces having different functionalities. Reproduced with permission <sup>343</sup> © 2020 Elsevier B.V. ....	62
Figure 38 Pictorial representation of EDC activation in coupling and surface biofunctionalization. Reproduced from Conde et al. <sup>116</sup> © 2014 Frontier Chemistry.....	63
Figure 39 A compressive representation of diverse therapeutic and diagnostic roles hold by the UCNPs. ....	64
Figure 40 Schematic illustrations of different optical imaging, widefield (A), confocal (B), TIRF (C), and light sheet (D) techniques in the visualization of intracellular structures. Reproduced from with permission <sup>358</sup> © 2021 Wiley-VCH.....	66
Figure 41 Comparative images of the tubulin structures taken using SIM, STED, and STORM techniques. Reproduced with permission <sup>366</sup> © 2013 American Chemical Society. ....	68
Figure 42 The progressive developments in UCNPs-based super-resolution imaging. ....	70
Figure 43 Schematic representation of the measurement of reagents (A) the steps 1 to 3 and the thermal decomposition synthesis of core-UCNPs (B) in steps 4 to 6.....	76
Figure 44 TEM micrograph of synthesized UCNPs (A) 20 nm, (B), 25 nm, and (C) 35 nm.....	78
Figure 45 The spectroscopic property of $\beta$ -NaYF <sub>4</sub> : 20% Yb <sup>3+</sup> /2% Er <sup>3+</sup> . ....	79
Figure 46 The XRD powder diffraction of the synthesized 25 nm $\beta$ -NaYF <sub>4</sub> : Yb <sup>3+</sup> (20%)/ Er <sup>3+</sup> (2 %) (Red plot) and standard (black plot). ....	80
Figure 47 The <sup>1</sup> H NMR (A) and <sup>13</sup> C NMR (B) spectra of OESPX. ....	94



Figure 48 The $^1\text{H}$ NMR spectra of Polymer 1: synthesis of MAA macro-RAFT agent at 0 hours (A) and 7 hours (B); synthesis of diblock at 0 hours (C) and 8 hours (D) hours; triblock synthesis at 0 hours (E) and 11 hours (F) ( $^1\text{H}$ NMR solvent: DMSO- $d_6$ ). .....	95
Figure 49 The $^1\text{H}$ NMR spectrum (A), ATR-FTIR spectrum (B), and TGA (C) of Polymer 1. ..	97
Figure 50 $^1\text{H}$ NMR spectra of Polymer 2: MAA macro-RAFT agent formation at 0-hour (A) and 12 hours (B) diblock synthesis at 0 hours (C) and 10 hours (D) hours; triblock synthesis at 0 hours (E) and 11 hours (F) (NMR solvent: DMSO- $d_6$ ). .....	99
Figure 51 The $^1\text{H}$ NMR spectrum (A), ATR-FTIR spectrum (B), and TGA (C) of Polymer 2.	100
Figure 52 $^1\text{H}$ NMR spectra of Polymer 3: MAA macro-RAFT agent synthesis at 0 hours (A), and 12 hours (B); diblock synthesis at 0 hours (C) and 8 hours (D) hours; triblock synthesis at 0 hours (E) and 11 hours (F) (NMR solvent: DMSO- $d_6$ ). .....	102
Figure 53 The $^1\text{H}$ NMR spectrum (A), ATR-FTIR spectrum (B), and TGA thermograph (C) of Polymer 3. ....	103
Figure 54 The $^1\text{H}$ NMR spectrum (A), ATR-FTIR spectrum (B), and its TGA thermograph (C) of Polymer 4. ....	105
Figure 55 The $^1\text{H}$ NMR spectra of Polymer 5: MAA macro RAFT agent formation at 0 hours (A) and 8 hours (B) diblock synthesis at 0 hours (C) and 10 hours (D) hours; triblock synthesis at 0 hours (E) and 11 hours (F) (NMR solvent: A-E DMSO- $d_6$ ; and F - in deuterated water. ....	106
Figure 56 The $^1\text{H}$ NMR spectrum (A), ATR-FTIR spectrum (B), and TGA thermograph (C) of Polymer 5. ....	108
Figure 57 The $^1\text{H}$ NMR (A) FTIR (B) and TGA (C) of Polymer 6. ....	109
Figure 58 Schematic representation of UCNPs surfaces oleate capped as-synthesized nanoparticles(A) and copolymer grafted particles through ligand exchange (B). ....	115
Figure 59 Flow Scheme for polymer surface grafting of the UCNPs. ....	117
Figure 60 Pictorial representation of UCNPs surfaces (A) oleate capped, (B) first copolymer grafted, and (C) second copolymer grafted. ....	118

Figure 61 Number weighted DLS particle size distribution of the oleate capped and copolymers grafted UCNPs. ....	121
Figure 62 Zeta potential of Polymer 3 modified heterogeneous nanoparticle surfaces at pH 8.5. ....	124
Figure 63 Number weighted DLS hydrodynamic size of the oleate capped, separate Polymer 6 grafted and double copolymer grafted UCNPs. ....	125
Figure 64 shows the stability of the different copolymers grafted nanoparticles stability in deionized water. ....	128
Figure 65 ATR-FTIR spectra of the oleate capped, and copolymers modified nanoparticles. ..	130
Figure 66 ATR-FTIR spectrum of combined copolymers grafted UCNPs. ....	131
Figure 67 TGA thermograph of the as-synthesized oleate capped and copolymers grafted UCNPs. ....	134
Figure 68 Thermograph of the combined copolymers grafted UCNPs. ....	138
Figure 69 Schematic illustration of an end-group modification of the OEPSX copolymers, where (A) before and (B) after end-group modification. ....	139
Figure 70 Schematic illustration of the coupling of FITC-NCS at the amine (A) and sulfhydryl of the modified end groups and (B) FITC-coupled surfaces. ....	140
Figure 71 FTIR spectra of post-surface graft end group modified surfaces (black spectrum); with hydrazine treatment (red spectrum) and FITC coupled surfaces (blue spectrum). ....	141
Figure 72 DLS hydrodynamic size of different antibody concentration coupled UCNPs. ....	143
Figure 73 The hydrodynamic size of poly arginine and TAT-HIV peptide coupled UCNPs. ...	145
Figure 74 FTIR spectra of Antibody, Polyarginine, and TAT-HIV peptide-functionalized UCNPs. ....	146
Figure 75 Representation of the integration of antibody to polymer grafted UCNPs. ....	151

Figure 76 Schematic visualization of different fluorescence imaging techniques in intracellular imaging (a) and nanoparticles in use by those instruments (b). Reprinted with permission <sup>479</sup> © 2022 American Chemical Society. ....	153
Figure 77 Functionalized UCNPs, and hybrid nanoprobes, for intracellular labeling and imaging. ....	154
Figure 78 Overall procedure on cell culture and nanoparticles labeling of the intracellular structures. ....	155
Figure 79 Schematic visualization of layout of the wide-field microscope.....	156
Figure 80 The TIRF confocal images from UCNPs-polyarginine labeled nucleolus at particle dose 100 µg/mL @980 nm excitation. ....	158
Figure 81 Widefield microscope images of nucleolus labeled with UCNPs-TAT HIV at particle dose of 60 µg/mL (A), (B), and (C), and at 100 µg/mL (D) @980 nm excitation. ....	159
Figure 82 Widefield microscope images of NPC labeled with UCNPs-NUP98 at a concentration of 60 µg/mL (A) – (C), and 75 µg/mL (D) @980 nm excitation. ....	161
Figure 83 Wide-field images of microtubules labeled with UCNP-anti-tubulin antibody at particle doses of 100 µg/mL (A) & (B), 200 µg/mL (C) & (D) @980 nm excitation.....	163
Figure 84 Widefield images of Polymer 2 grafted UCNPs-anti actin antibody labeling with particle concentration of 60 µg/mL (A) & (B), and 75 µg/mL (C) & (D), @980 nm excitation. ....	164
Figure 85 Images captured from UCNPs-FITC-TAT labeled nucleolus (A) and (B), and UCNPs-FITC anti-tubulin antibody labeled microtubules (C) and (D) @488 nm excitation.....	165
Figure 86 Images of NPC labeled from UCNPs-FITC-NUP98 antibody @980 nm excitation (A) and (B) using a homemade widefield microscope; @488 nm excitation using Lecia Stellaris Confocal microscopy. ....	167
Figure 87 Imaging of microtubules from UCNP-Alexa Fluor 488-Antibody labeled cell (A) using a home-made widefield microscope @980 nm UCNPs excitation and (B) using Lecia Stellaris confocal microscopy @488 nm Alexa-Fluor excitation (B).....	168

Figure 88 Labeling of F-actin using UCNPs-alpha antibody (A) labeling of NPC using UCNPs-FITC-NUP98 (B) @488 nm using Lecia Stellaris confocal microscopy. ....	169
Figure 89 The TEM micrographs (A-C), electronic emission properties (D), and the XRD pattern of the synthesized UCNPs (E). ....	174
Figure 90 List of copolymers developed using the RAFT copolymerization technique. ....	176
Figure 91 The <sup>1</sup> H NMR of the different purified final copolymers (NMR solvent: Polymer 5 run using deuterated water; and the rest run in DMSO-d6). ....	179
Figure 92 Thermograph of combined copolymers grafted UCNPs. ....	182
Figure 93 Images captured from UCNP probes labeling of F-actin (A), NPC (B), nucleolus (C), and microtubules (D). ....	184

## List of tables

Table 1 Common monomers used in RAFT polymerization and their reactivity <sup>199</sup> .....	43
Table 2 Summary of RAFT agents and monomers used in the polymerization.....	85
Table 3 Summary of the DLS particle size and zeta-potential of copolymers grafted nanoparticles .....	122
Table 4 Comparative hydrodynamic sizes of the separate and double copolymer grafted 25 nm substrate UCNPs. ....	126
Table 5 The stability of different copolymers obtained from separated and double-grafted nanoparticles in different buffer solutions .....	133
Table 6 TGA data on weight loss and graft density of a 25 nm oleate capped and polymer grafted nanoparticles .....	136

## List of schematic illustrations

Scheme 1 Schematic representation of AIBN during radical generation and monomer insertion (A) and reversible addition-fragmentation chain transfer and propagation (B): where M stands for monomer and R stands for radical .....	45
Scheme 2 The mechanisms of RAFT polymerization that include the initiation, re-initiation, and polymerization equilibrations (Adapted from Keddie et al.) .....	47
Scheme 3 The representation of the synthesis of OESPX .....	86
Scheme 4 Schematic illustration of the sequential synthesis of Polymer 1 .....	88
Scheme 5 Schematic representation of the synthesis of Polymer 2 .....	89
Scheme 6 Schematic representation of the synthesis of Polymer 3 .....	90
Scheme 7 Schematic representation of the step-wise synthesis reactions for Polymer 4 .....	91
Scheme 8 Schematic illustration of the sequential synthesis of Polymer 5 .....	92
Scheme 9 Schematic representation of the synthesis of Polymer 6 .....	93
Scheme 10 Representation of the hydrazinolysis of Polymer 1 to introduce amine and sulfhydryl functionalities .....	98
Scheme 11 Mechanisms of EDC/NHS activation and stabilization, and antibody coupling .....	142
Scheme 12 Schematic illustration of the synthesis of the xanthate RAFT agent and subsequent development of Polymer 1 .....	177

## Acronym

UCNPs	Up conversion nanoparticles
UC	Up conversion
DS	Down shifting
OA	Oleic acid
ODE	1-Octadecene
DLS	Dynamic light scattering
RESOLFT	Reversible Saturable optical fluorescence transitions
VIS	Visible
CT	Computed tomography
IVM	Intravital microscopy
NIR	Near infrared
XRD	X-ray Powder Diffraction
FDA	Food and drug administration
SNR	Signal to Noise Ratio
SR	Super-resolution
LED	Light emitting diode
STED	Stimulated emission depletion
STORM	Stochastic optical reconstruction microscopy
SMLM	Single-molecule super-resolution imaging
TIRF	Total internal reflection fluorescence
ATR-FTIR	Total internal reflectance
NIR	Near-infrared radiation (light)
DMEM	Dulbecco's modified eagle medium
MAMs	More activated monomers
LAMs	Less activated monomers
RDRP	Reverse deactivation radical polymerization
RAFT	Reversible addition-fragmentation chain transfer polymerization
MADIX	Macromolecular design via the interchange of xanthates
NMP	Nitroxide-mediated polymerization
DP	Degree of polymerization
DMF	dimethylformamide
PEG	Poly (ethylene glycol)
CRP	Controlled radical polymerization
OEGMA	Oligo (ethylene glycol) methyl methacrylate)
OEGMA-500:	Oligo (ethylene glycol) methyl methacrylate) (MW 500 g/mol)
OEGMA-480	Oligo (ethylene glycol) methyl methacrylate) (MW 480 g/mol)
OEGMA-300	Oligo (ethylene glycol) methyl methacrylate) (MW 300 g/mol)
TGA	Thermogravimetric analysis
MW	Molecular weight
HSAB	Hard-soft acid-base
MOEP	2-(methacryloyloxy)ethyl phosphate

AMPS	2-acrylamide-2-methylpropane sulphonic acid
MAA	Methyl methacrylic acid
CTCPA	4-(((2-carboxyethyl) thio) carbonothioyl) thio)-4-cyanopentanoic acid
CDTPA	Cyano-4-(((dodecylthio)carbonothioyl) thio) pentanoic acid
OESPX	O-Ethyl S-Phthalimidyl methyl xanthate
CPADB	4-Cyano-4-(phenyl carbonothioylthio) pentanoic acid
PAA	Poly (acrylic acid)
ATRP	Atom transfer reversible polymerization
GPC	Gel permeation chromatography
SEC	Size exclusion chromatography
NMR	Nuclear magnetic resonance
DLS:	Dynamic light scattering
CTA	Chain Transfer Agent
MPC	2-(Methacryloyloxy) ethyl Phosphorylcholine
GNP	Grafted nanoparticles
FRET	Fluorescence Resonance Energy Transfer
NP	Nanoparticles
SIM	Structured illumination microscope
CLSM	Confocal laser scanning microscope
MRI	Magnetic resonance imaging
SPECT	Single-photon emission computerized tomography
PDI	Polydispersity index
PET	Positron emission tomography
NP	Nanoparticle (s)
GNP(s)	Grafted Nano Particle (s)
NA	Numerical aperture
NPC	Nuclear pore complex
F-actin	Actin filament
DMEM	Dulbecco's Modified Eagle Medium
PBS	Phosphate Buffered Saline
MTT	3-(4,5-Dimethyl-2-thiazolyl)-2,5-diphenyl-2H-tetrazolium bromide
PFA	Paraformaldehyde
TAT	Trans-activator of transcription
HIV	Human immunodeficiency virus
FITC	Fluorescein isothiocyanate
CPPs	Cell penetrating peptide
EDC	1-ethyl-3-(3-dimethylaminopropyl) carbodiimide
NHS	N-hydroxysuccinimide
LFA	Lateral flow immunoassay
NA	Avodadro number
TEM:	Transmission electron microscopy

## **Abstract**

Lanthanide-doped upconversion nanoparticles (UCNPs) are emerging as the next-generation agent for intracellular fluorescent labeling and imaging. To label the subcellular structures using UCNPs, vast opportunities and immense potential lay in their surface functionalization and subsequent bioconjugations. The surface stability and reactivity of UCNPs determine their specific interactions with target molecules, and it enables control of the degree of non-specific bindings to the surroundings. The targetability of UCNPs could be optimized by molecule-specific moiety via conjugating to the grafted polymers on the surface of nanoparticles. As the surface of UCNPs is highly positively charged, due to the exposed lanthanide ions at the lattice termination sites, the nanocrystal surfaces allow the tethering of polymers with negative charges. Therefore, the design and tethering polymers is the key factor in producing functional inorganic nanoparticles with a desirable surface property.

Throughout the Ph.D. study, a new understanding of the roles of polymers in functionalizing UCNPs has been achieved by systematic investigations of multiple RAFT copolymers. RAFT copolymers play a crucial role in controlling surface features and reactivities of UCNPs by manipulating physicochemical properties. The UCNP's surface coupling efficiency could be enhanced using highly reactive triblock RAFT copolymers containing methacrylic acid (MAA). Through increasing surface carboxylic acids density and by enabling an extended surface reactive site, advances in reactivity and dispersibility of UCNPs could be achieved. The surface graft copolymer composition determines the amphiphilicity, dispersibility, and stability of UCNPs. The concept of double copolymer surface grafting using stepwise co-grafting has been implemented to attain high control of surface composition. Efficient immobilization of antibodies and peptides to UCNPs enables the targeting and imaging of single biomolecules and intracellular structures. The performed intracellular labeling and imaging experiments prove that the functionalized UCNPs are suitable for detailed intracellular labeling and investigations. This thesis, therefore, contributes to developing the next-generation super-resolution probes for single-molecule tracking and live cell imaging applications. Moreover, besides visualization of structural features and dynamics of molecular-level phenomena, the functionalized nanoparticles could be implemented as a nanotheranostic tool for personalized nanomedicine.

Key words: Nanomedicine, Nano(bio)technology, RAFT polymers, Nanoprobes, Optical imaging



# 1 | Introduction

## 1.1 Preamble

In this chapter, preliminary information about the overall Ph.D. project has been presented. The motivations behind the Ph.D. research project are stated. The main topics covered in the experimental sections of the project have been briefed. The relationships between the multiple disciplines that are covered in the project are elaborated. The roles of the various fluorescent probes in molecular imaging and the existing bottlenecks are stated. The advantages of a multidisciplinary research approach to realize molecular imaging is indicated. The progressive developments and relationships of optical microscopy, nanoparticle-based probes, and medical sciences have been discussed. The promising future applications of UCNPs in developing nanoprobe are pointed out, and lastly, the objectives of the Ph.D. project are clearly stated.

## 1.2 Motivations of the project

As the noble laureate Richard Feynman envisioned, nanotechnology has enabled atomic and molecular-level scientific investigations.<sup>1, 2</sup> The advanced nanotechnology tools, like super-resolution imaging techniques, and the electron microscopes, provide vast opportunities to fabricate new classes of nanosized particles in a controlled manner.<sup>3</sup> Nanotechnology solutions are vital in developing biomedical materials and devices to address the unmet and future critical health challenges.<sup>4</sup> Many human health challenges demand for an up to date scientific solutions. The untimed loss of precious human life, the psychological impacts, and the economic burden at individual and governmental levels remain critical concerns.<sup>5</sup> A recent report shows 233 million, 111 million, and 422 million people are affected by cancer, neurological disorder, and diabetes, respectively.<sup>6, 7</sup> The data indicates that immediate and reliable scientific solutions are required to tackle the current and future health challenges.

Nanomedicine, the new era of disease diagnosis and treatment, has emerged with innovative solutions by implementing nanotechnology in medicine, medical technology, and pharmacology.<sup>8, 9</sup> Nanotechnology is widely implemented in preparing therapeutics and diagnostic materials.<sup>10</sup> It has enormous potential advantages in developing nanomaterials for molecular diagnostics applications.<sup>11</sup> Nanomedicine aims to establish novel goals in the medical and clinical sectors.<sup>5,</sup>

<sup>10,12</sup> Personalized nanomedicine deals with understanding differences between individual patients suffering from complex diseases.<sup>12</sup> The progressive advancements in biology, materials science, chemistry, and medicine and integrated research efforts between those disciplines have empowered nanomedicine.<sup>13</sup> The current multidisciplinary researches have significant potentials to realize personalized medicine as schematically presented in Figure 1.

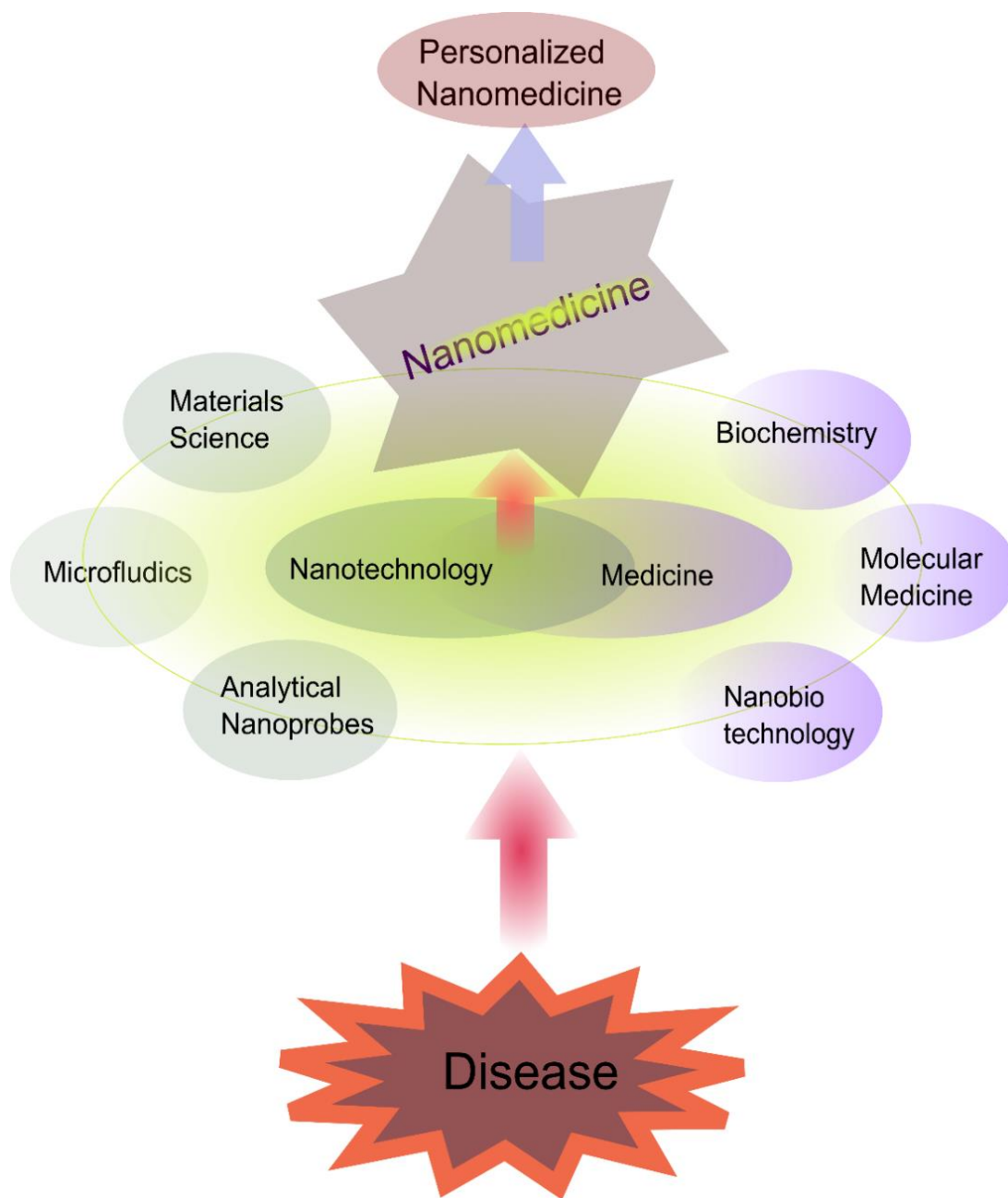


Figure 1 Schematic representation of the multidisciplinary nature of nanomedicine and different disciplines involved in its implementation. Adapted with permission<sup>14</sup> © 2009 Wiley-VCH.

Nanotechnology has played tremendous roles in diverse technological advancements, including the medical and pharmaceutical sectors. An integrated research efforts that encompass the vast physical and biological science disciplines could be devised to attain a cumulative impact. The multidisciplinary nature of nanotechnology allows integration of varies natural science fields that could enables to address specific health challenges. The amalgamation of biochemistry with nanotechnology has enabled a cutting-edge interdisciplinary research field, nanobiotechnology. The combination of nanoparticles and biomolecules produces nanohybrids with improved and tailored performances. Figure 2 shows how nanotechnology allows to converge numerous scientific disciplines to realize nanomedicine such as in bioimaging, targeted delivery, and biosensing.

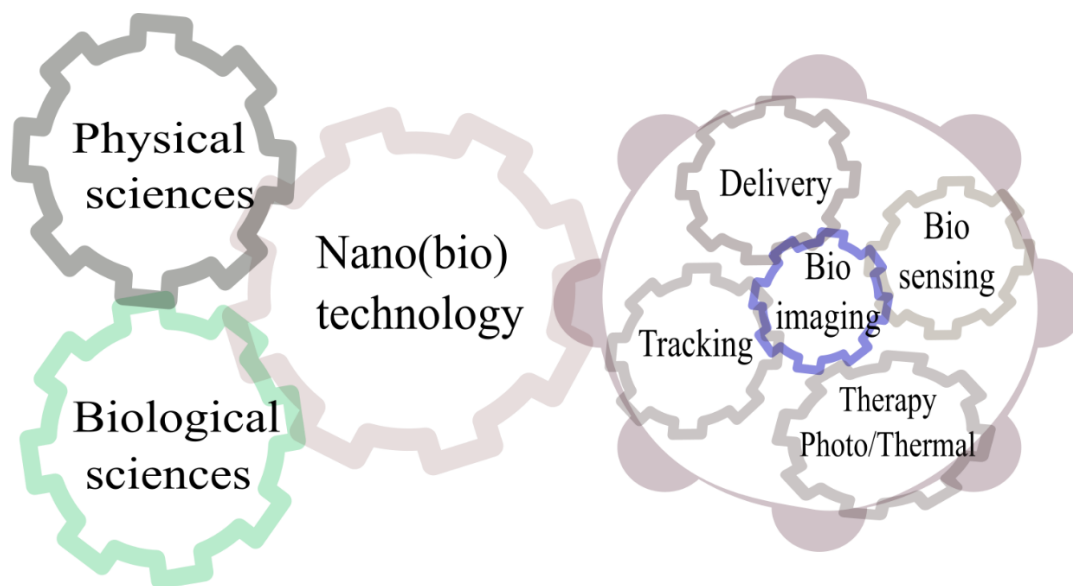


Figure 2 Pictorial representation of roles of nanotechnology in the convergence of different disciplines in the development of nanomaterials for diagnostic and therapeutic applications

Personalized treatment is one of the most ambitious goals of nanomedicine.<sup>12</sup> The persuasion to realize personalized nanomedicine relies on setting new disease diagnostic and therapeutic approaches.<sup>12, 14, 15</sup> Molecular imaging is essential for health practitioners to evaluate anatomical or physiological structures and functions.<sup>16,17</sup> The precision in patient outcomes strongly relies on the accuracy of implemented diagnostic devices. Here, in this project, effective implementation of upconversion nanoparticles (UCNPs) probes in intracellular labeling and imaging is aimed. The primary purpose of this Ph.D. project is to develop UCNP probes for intracellular labeling and

visualize the 'never seen' physiological world of life. As 'seeing is believing,' achieving molecular-level direct observation of cellular structures and functions using UCNP probes opens vast future opportunities in the academia and clinical sectors.

### 1.3 Molecular imaging

Microscopy is an essential device for the exploration of intracellular structures and components. Molecular-level imaging of living subjects is vital in analyzing and understanding life activities at cellular and subcellular levels. It enables visualization, characterization, and measurement of biological processes at a molecular level.<sup>18</sup> Non-invasive bioimaging techniques, such as X-ray, CT, and MRI, are widely implemented for morphological investigations. The nuclear imaging technologies such as PET and SPECT are susceptible techniques; however, they require nanomolar blood tracers to produce images.<sup>19</sup> Although the current anatomical imaging techniques have a good resolution capability, they are insufficient to attain a high spatial resolution. An efficient biomedical device is required to obtain a clear image and to detect structural and molecular alterations during lesion formation.<sup>20 21</sup> The traditional molecular imaging techniques, however, give poor multiplicity, low spatial resolution, low sensitivity, and poor tissue signal penetration.

The history of optical microscopes began in the 18<sup>th</sup> century when Antonie van Leeuwenhoek made the first light microscope.<sup>22</sup> In previous times, seeing things below 0.1 mm was impossible. The capability to observe single-cell animals using the light microscope was an incredible achievement in advancing biological sciences.<sup>23</sup> Nowadays, multiple and high-notch microscopes have flourished. Particularly, the breakthrough in overcoming the Abbe diffraction limit has led microscopy technology to current super-resolution techniques.

Molecular imaging is an integrated approach in academia and medical centers that encompass extensive research efforts.<sup>24, 25</sup> Molecular imaging is an efficient technique for gathering cellular and intracellular information. It provides incredible potential advantages to monitor, diagnose and measure biological processes.<sup>19</sup> Molecular imaging allows the investigation of molecular-level interactions, including disease pathology.<sup>12</sup> The molecular imaging techniques help improve diagnostics accuracy and sensitivity; however, they are not to replace traditional imaging techniques.<sup>25</sup>

Currently, numerous molecular imaging techniques are flourishing for clinical and research purposes. However, earlier-stage detection and diagnosis of critical health challenges like cancer provide many economic and psychological benefits in controlling diseases before it causes severe harm.<sup>20</sup> The creation of capabilities in disease diagnosis before the manifestation of the symptoms is made possible through molecular imaging. Fluorescence imaging is one of the most promising optical techniques for in-vivo diagnostics and therapeutics. It allows the replacement of the classical in-vitro bioassay-based diagnosis.<sup>24</sup> Figure 3 depicts different molecular imaging techniques, including the optical imaging approaches which is the main focus of the Ph.D. project work.

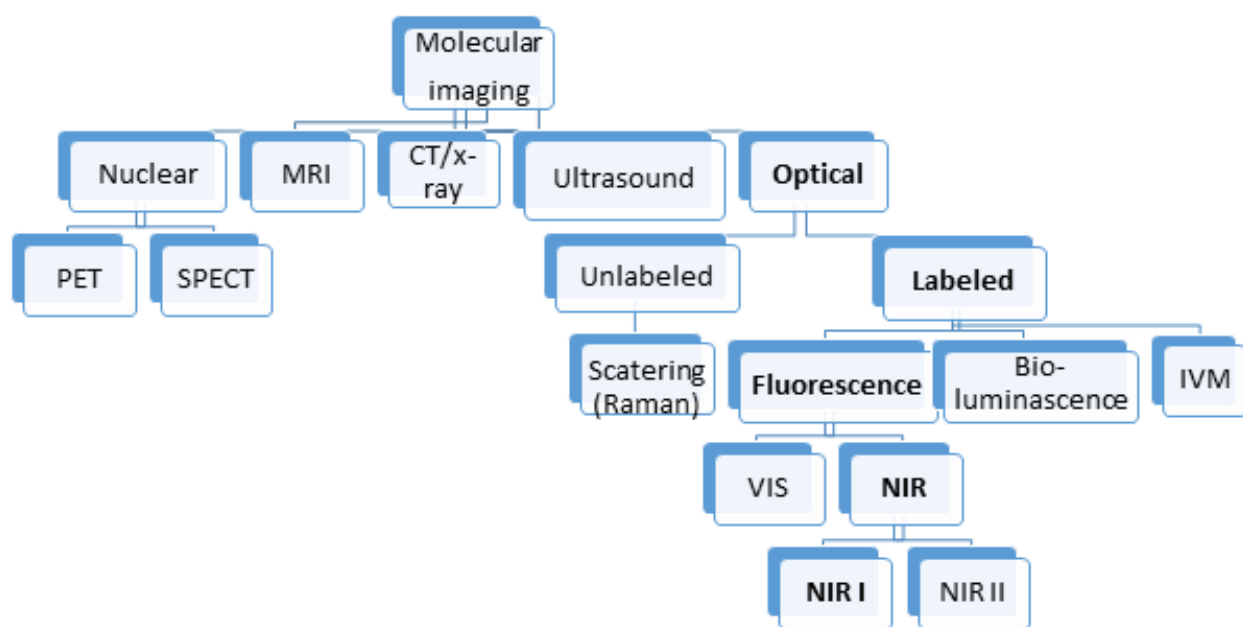


Figure 3 Classification of molecular imaging techniques with a focus on fluorescent-based optical imaging approaches.

Optical imaging is the most powerful technique in biology and nanomedicine.<sup>26-28</sup> It has many attractive features.<sup>7</sup> For instance, it enables high-speed data acquisition and accurate time visualization of physiological events. Optical imaging could be complemented with X-rays and MRI imaging. Label-based optical imaging requires contrast agents to generate light from the luminescence of the labeled agents. Spontaneous emission of visible radiation, photoluminescence, happens through excitation of a molecule or chemical species using appropriate radiation.<sup>29</sup> Luminescence occurs when an electronically or vibrationally excited chemical species releases radiation upon relaxation as fluorescence or phosphorescence.

## 1.4 Contrast agents in fluorescent imaging

The term fluorescence was coined in 1852, associated with investigating the blue emission of quinine solution.<sup>30</sup> Contrast agents, fluorophores, are a crucial component of optical imaging. Fluorophores from organic and inorganic origins are widely used for contrast formation in fluorescence imaging. The typical contrast agents are organic dyes, fluorescent proteins, quantum dots, and lanthanide (III) doped upconversion nanoparticles.<sup>31</sup> The creation of high contrasts in optical imaging enables observation of tiny objects that are impossible to see with the naked eye. Currently, different fluorophores are being used in fluorescence imaging.<sup>32</sup> The current fluorescence imaging approaches mainly rely on fluorescence proteins and organic dyes.<sup>33</sup> Conventional labeling agents like organic dyes require short-wavelength excitation and are prone to significant drawbacks.<sup>34-40</sup> Although organic dyes exhibit numerous intrinsic qualities like high brightness and smaller size advantages, they suffer from photobleaching and toxicity. It is associated with their exposure to a reactive imaging environment and the requirement of high excitation wavelength.<sup>3, 41</sup>

The advent of fluorescence imaging has transformed the transmitted light-based optical imaging into contrast-based visualization. Currently, the most widely used fluorophores are as follows: fluorescence proteins (48%), small molecules fluorophores (36%), and quantum dots (14%). Figure 4 is a pictorial representation of how fluorescence labeling and imaging of tumors are performed.<sup>42</sup>

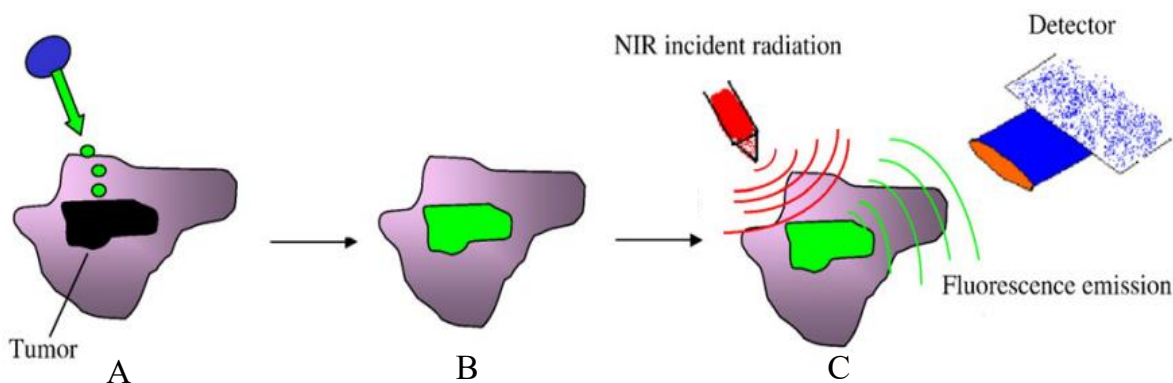


Figure 4 Pictorial representation of contrast creation in fluorescence imaging of tumor, where (A) and (B) stand for labeling of the specific tumor site, and (C) stands for signal generation, and detection. Adapted with permission<sup>42</sup> © 2006 Elsevier B.V.

Optical microscopy is based on optical light, which covers from 400 to 1700 nm and covers the visible light, ultraviolet, and near-infrared regions, as represented in Figure 5.<sup>43,44</sup> In fluorescence imaging, fluorophores have fundamental roles in contrast formation. When fluorophore molecules absorb photons of a particular wavelength, their electrons transit to an excited energy state and light is released upon their return to the ground state. The interaction of fluorophore molecules with visible, ultraviolet, or near-infrared light produces a visible emission that the human naked eye or instrument can detect. Traditional fluorescence imaging techniques suffer from autofluorescence and light scattering, especially during deep tissue imaging.<sup>45</sup>

Fluorescence imaging is performed through the interaction of the specimen with UV/Vis/NIR light. NIR light is among the most relevant electromagnetic radiation in various modern applications, like display technologies.<sup>46</sup> Near-infrared (NIR) light-based fluorophores are preferable in fluorescence imaging because they exhibit reduced light scattering and background autofluorescence.<sup>45</sup> The NIR could be categorized into two main groups: NIR-I (700 - 950 nm) and NIR-II (1000 - 1700 nm).

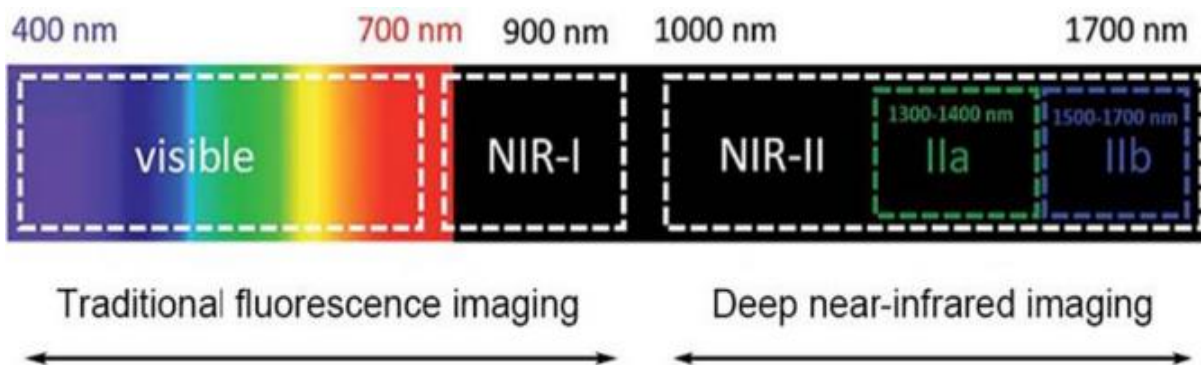


Figure 5 The optical EMR regions and the fluorescence modalities used in fluorescence imaging. Reproduced with permission<sup>43</sup> © 2019 Elsevier B.V.

NIR is the most abundant light compared to visible and ultraviolet; moreover, it is non-destructive and preferable in biological applications. Although the NIR could be accessible as a laser, its photon energy is too low. A higher energy infrared light could be generated through photon frequency upconverters like second-harmonic generation (SHG) and two-photon absorption (TPA). The lanthanide ions are ideal for photon upconversion because they do not need an intense NIR source compared to the SHG and TPA.<sup>46</sup> UCNPs becomes one of the suitable agent for NIR-based emerging applications.<sup>47</sup> The UCNPs-based NIR light has received significant interest

because of its soft tissue penetrating efficiency and due to the high in vivo structure's resolution capability. The NIR-I window, 800 nm, is optically transparent because the radiation absorption due to water is low.<sup>48</sup> The heating effect, due to tissue water, is relatively lower at 800 nm compared to the high-water absorption wavelength regions: 1150, 1450, and 1900 nm. The NIR-II windows lay at 1000 to 1400 nm and exhibits a relatively negligible water absorption compared to 1400 to 1700 nm. NIR-II-based imaging reduces light scattering and enables a more profound tissue penetration than NIR-I.<sup>48</sup>

## 1.5 Nanoparticles as a contrast agent

Nanoparticles are emerging as transformative contrast agents in intracellular labeling and imaging.<sup>49</sup> Nanoparticles based probes have several advantages over conventional fluorophores. Nanoprobes have a strong capability to resist photobleaching and cytotoxicity that arise from high-energy excitation in the case of organic dye labeling. Due to their longer engineered circulation period and well-designed clearance mechanisms, nanoprobes have received strong attention to attain improved in-vivo performances. Rational design of their photophysical properties, nanoparticles gain distinct structures and provide excellent photostability and brightness. Since their composition controls nanoprobes' fluorescence, environmental conditions cannot affect it.<sup>3</sup> Although nanoprobes have numerous attractive features, size compatibility, surface suitability, and batch-to-batch reproducibility challenges are major drawbacks.<sup>3, 49</sup>

An intense interest in acquiring suitable biomarking agents for different molecule imaging techniques like MRI, CT, SPECT, PET, and the optical microscope has been shown.<sup>50</sup> Fluorescent imaging could be categorized into labeled and non-labeled techniques, as diagrammatically classified in Figure 3. As the name indicates, efficient labeling agents are necessary for the labeled fluorescent technique to produce a good contrast. Although organic dyes and fluorescent proteins are extensively implemented labeling agents, fluorescent nanoparticle-based probes are emerging as an alternative to address the limitations of conventional contrast agents.

In recent decades, nanoparticles have been extensively investigated in bioimaging, biosensing, and delivery applications. Nanoparticle-based fluorescence imaging has wide applications, such as gene detection, protein analysis, enzyme activity evaluation, element tracing, cell tracking, early-stage disease diagnosis, tumor-related research, and real-time therapeutic effects monitoring.<sup>20</sup>



Recently, several nanoparticles received FDA approval and were implemented in clinical applications. Inorganic fluorescent nanoparticles, such as QDs, have contributed significantly to cell labeling and imaging. The QDs provide an improved quantum yield and photo-stability over the organic dyes.<sup>51</sup>

In recent years, novel nanoprobe like carbon-based nanoparticles, polymeric nanoparticles, and UCNPs have been investigated to meet the fast-growing probe demands<sup>51</sup> Among the multiple nanoparticles under investigation, and the UCNPs have received strong attention for their nanoprobe application. Figure 6 is an adopted figure on the implementation of nanoparticles in different fluorescence imaging techniques and a timeline for their progressive developments.

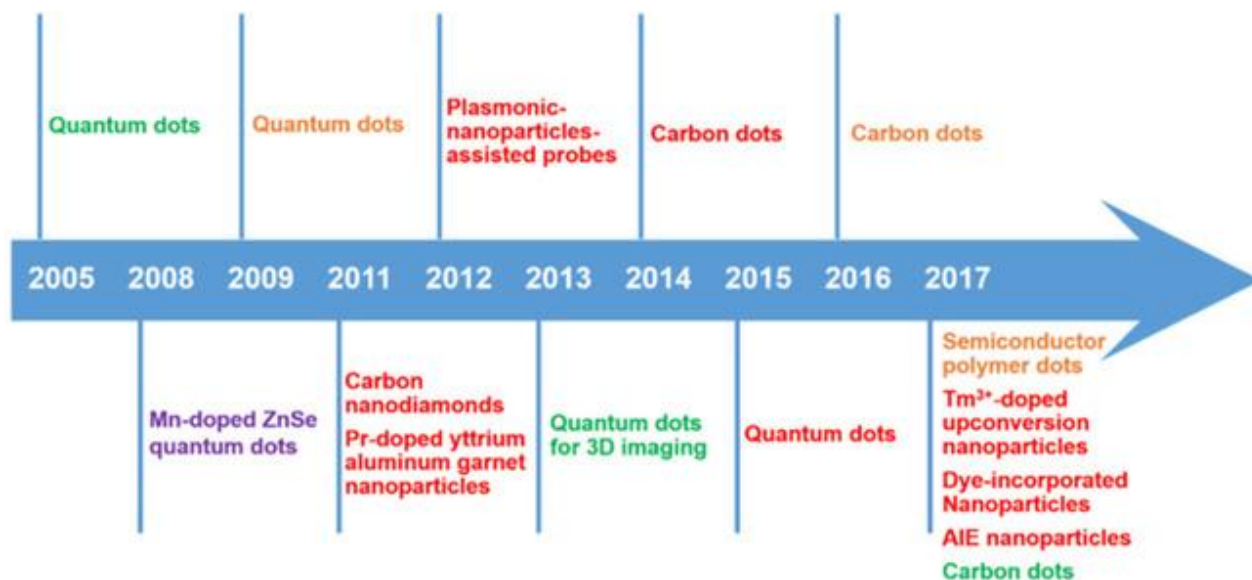


Figure 6 Timeline on the progressive development of nanoprobe and their use in different fluorescence microscopy. Reproduced with permission<sup>52</sup> © 2018 Wiley-VCH.

The timeline shows that different nanoprobe have been used in various fluorescence microscopy as coded in color fonts. The nanoparticles with the green flag represent their implementation in super-resolution localization microscopy. The red-flagged ones are to indicate their STED applications, the orange-flagged ones are used in SOFI, and the purple-flagged nanoparticles are implemented in RESOLFT.<sup>53</sup>

➤ UCNPs as a novel contrast agent

Lanthanide (III) (Ln<sup>3+</sup>) doped nanomaterials are extensively employed in multiple biomedical technologies.<sup>54</sup> UCNPs are composites usually consisting of a host material, sensitizer, and

activator metal ions.<sup>55, 56</sup> The unique electronic configuration of UCNPs, and their nano chemistry enables them to transform lower-energy photons into higher energy. As the 4f-4f orbital is well shielded by the outer 5s and 5p orbitals, the Ln<sup>3+</sup> doped UCNPs can produce stable and sharp luminescence emission peaks.<sup>10, 57</sup> However, most lanthanides do not emit light unless they are found in a chelated form or a doped crystal structure.<sup>58</sup> In Figure 7, the adopted figures show the lanthanide series elements, their intrinsic luminescence emissions (A), and upconversion luminescence emissions from their doped nanocrystals (B) are presented.<sup>59, 60</sup>

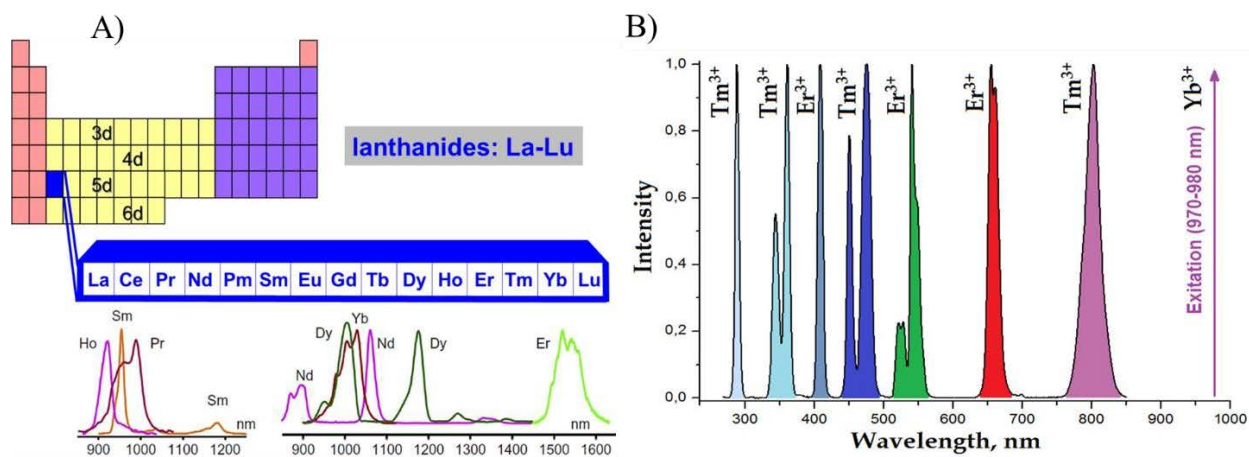


Figure 7 Characteristic emissions from lanthanide (III) doped nanoparticles (A) downshifting and (B) up converting modes. Reproduced with permission<sup>59, 60</sup> © 2018 (A) and © 2019 (B) Elsevier B.V.

These days, UCNPs have become one of the best alternative nanoprobe in intracellular labeling.<sup>61, 62</sup> UCNPs are new fluorescent probes for bioimaging, biosensing, and delivery applications.<sup>63</sup> Although the upconversion phenomena were explored in 1959<sup>64, 65</sup>, the luminescence emission of Ln (III) upconversion nanoparticles was identified in the 2000s.<sup>46</sup> The first upconversion phenomena were observed in 1966 by Auzel, Ovsyankin, and Feofilov, and NaYF<sub>4</sub>/Er phosphor was investigated in 1972.<sup>66</sup> UCNPs play extensive roles in molecular imaging, such as optical, magnetic, radioactive, and x-ray techniques. The UCNPs has promising potential to perform as fluorescent labeling agents in different advanced fluorescent imaging applications.<sup>67</sup> Thus, UCNP probes are promising to transform the bio-imaging approach into a new realm.<sup>68</sup>

With the current technological advancements, ample opportunity to synthesize and develop sensitive nanoprobe for molecular imaging has been gained.<sup>50</sup> Since the first bottom-up UCNP

synthesis was achieved in 1999, various synthesis approaches, including co-precipitation, thermal decomposition, sol-gel, and hydrothermal methods, have been employed to synthesize high-quality UCNPs. Figure 8 provides a comprehensive diagrammatical representation of the standard UCNP synthesis techniques.<sup>40</sup>

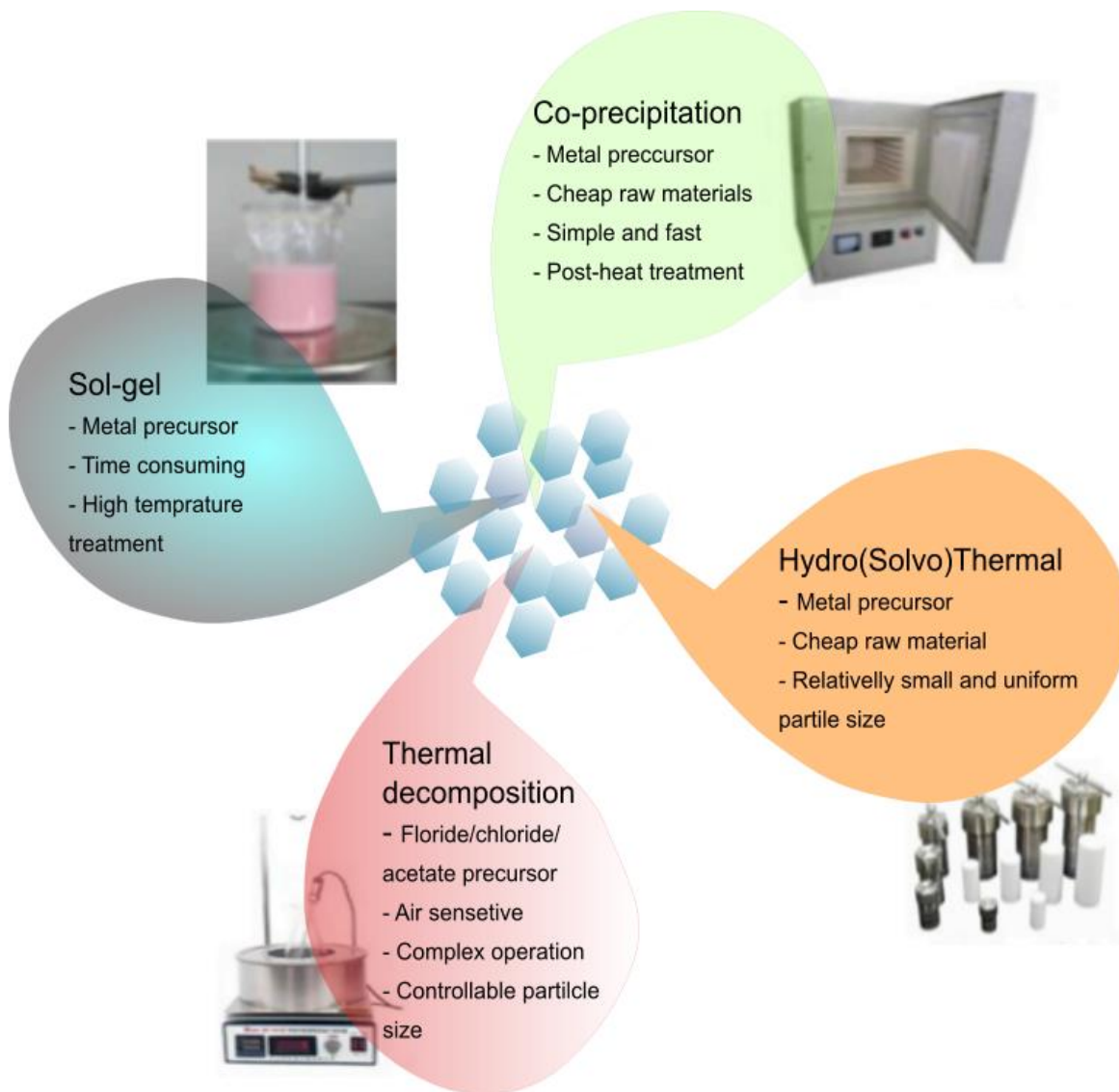


Figure 8 The different UCNP synthesis techniques (A) thermal (B) hydro(solvo)thermal (C) co-precipitation, and (D) sol-gel methods. Adapted with permission<sup>40</sup> © 2020 Elsevier B.V.

Currently, the UCNPs have received high popularity in diverse technological applications, and extensive research has been performed to develop the nanoparticle's performance further.<sup>69, 70</sup> The advancement in materials science and nanotechnology have played prominent roles in developing

fluorescent nanomaterials in a highly controlled manner.<sup>14-16</sup> UCNPs, for instance, could be developed in a controlled manner for molecular-level diagnostic and therapeutic applications. Thermal synthesis is the most popular technique to produce high-quality UCNPs.<sup>71 72</sup> Figure 9, provides perspectives on the UCNPs development plan and timeline for the accomplishment of significant milestones in the realization of technology transfer.<sup>73</sup>

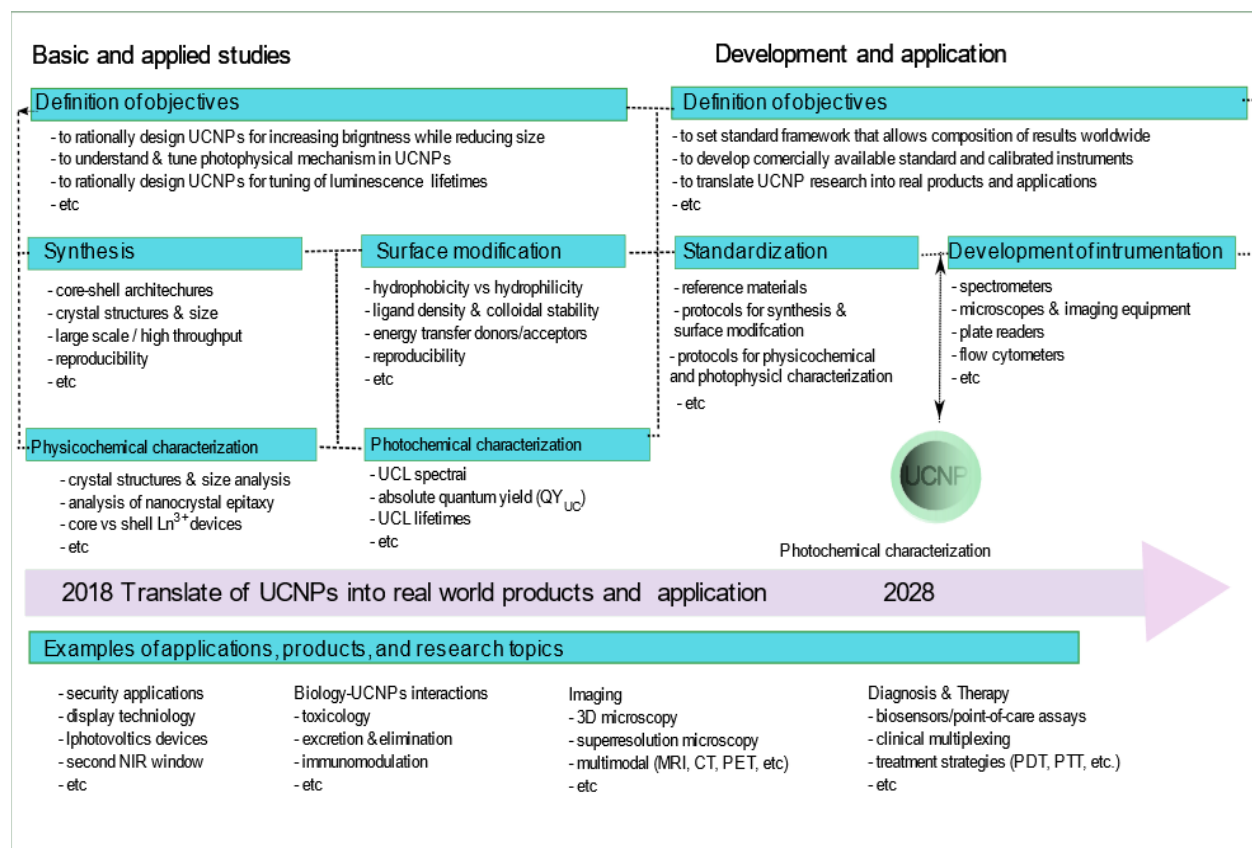


Figure 9 A comprehensive research plan and timeline on the synthesis and developments of UCNPs, products, and envision for their clinical translation. Adapted with permission<sup>73</sup> © 2017 American Chemical Society.

Figure 9 gives a timeline for the development of UCNPs and the numerous current and future research activities to realize UCNPs-based advanced technologies. The experimental plan covers several activities to be accomplished by 2028. This Ph.D. project has multiple overlapped interests with the proposed plan. The functionalized UCNPs helps develop efficient nanoprobes for diagnostic and therapeutic applications, which is the most shared interest in the proposed plan. In this current project, new surface functionalizing copolymers are employed to enable efficient bio-

coupling. The copolymer functionalized UCNPs are promising for various nanomedicine and analytical applications.

➤ The surface chemistry of UCNPs

The surface chemistry of UCNPs determines how they interact with their surrounding environments. Surface optimization is an untapped opportunity to advance the UCNPs intracellular performances. Post-synthesis surface optimization is mandatory to implement UCNPs in nanomedicine.<sup>14, 74</sup> The surface tailoring could be performed using different materials and techniques. Polymer-based nanoparticle surface grafting, for instance, is a potential method to produce multifunctional surfaces. Since its birth in 1920<sup>75</sup>, polymer chemistry has continually evolved to enable the development of polymers with sophisticated architectures. Polymers like Poly (ethylene glycol) (PEG) have been widely known for their diverse pharmaceutical and biomedical applications.<sup>7, 76</sup>

Surface functionalization of nanoparticles enables the introduction of a specific receptor affinity to define nanoparticle function. UCNP surfaces allow the production of nanocomposites consisting of inorganic nanoparticles and polymers. Surface reactivity, chemical stability, hydrophilic/hydrophobic stability, and biocompatibility are critical parameters that could be controlled through surface optimization.<sup>77</sup> Replacement of the synthesis capping ligands with a new polymer is one powerful strategy for surface modification of the nanoparticles.<sup>78</sup> The polymer-based functionalization of nanoparticles helps to produce well-tailored surfaces.<sup>79</sup> Nanocomposites from integrating nanoparticles with polymer produce attractive physicochemical properties to develop efficient nanoproboscopes.

The polymers-nanoparticle surface attachment could be done through the 'graft from' or 'graft to' approach. In the case of the 'graft from' approach, the polymer chains are grown from the nanoparticle's surface, which enables more surface coverage. The 'graft to' technique uses ready-made polymer ligands, which enables low surface graft coverage.<sup>80</sup> A schematic representation of the "graft from" and "graft to" techniques is presented in Figure 10.

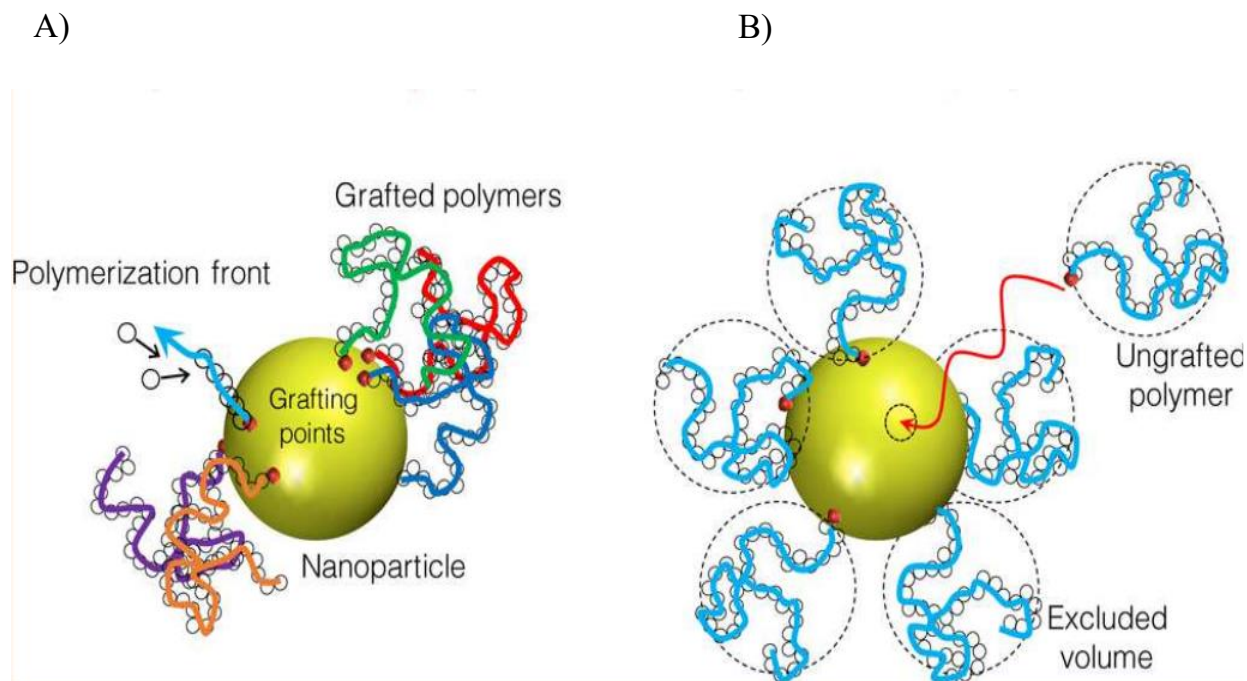


Figure 10 The 'graft from' (A) and 'graft to' (B) approach surface modification. Reprinted with permission<sup>80</sup> © 2017 American Chemical Society.

Copolymers' design and development approach is essential in producing functional and stable UCNP surfaces. Reverse deactivation radical polymerization (RDRP) is prominent in developing suitable surface-modifying polymers.<sup>81</sup> RDRP is the most efficient technique for developing complex architectures with well-defined end groups.<sup>82, 83</sup> The latest RDRP techniques like the ATRP, RAFT and MADIX, and NMP, for instance, are potential techniques in the controlled synthesis of surface ligands.<sup>84</sup> RAFT polymerization is very useful for the synthesis of surface functionalizing polymers. The history of RAFT polymerization began in 1995 when the name "macromonomer chain transfer agents" was coined by Kristina et al.<sup>82</sup> The term RAFT polymerization, however, was officially disclosed in 1998 by CSIRO, and Rhodia Chimie reported MADIX technique.<sup>81</sup>

#### ➤ Coupling of bioactive molecules to nanoparticles surfaces

The connection of nanoparticles with biomolecules helps to combine the potentials of biochemistry with nanotechnology. Bio-conjugated particles gain improved biorecognition because of the attached biomolecule. The surface-attached polymer helps to bridge nanoparticles with suitable biomolecules. The bioconjugation of nanoparticles could be done either through physical or



chemical methods.<sup>85</sup> The biomolecules could be integrated into the nanoparticle's surface through physical forces like hydrophobic interactions, electrostatic adsorption, and hydrogen bonding. Covalent bioconjugation helps to attain stable surface attachment. EDC/NHS chemistry helps to immobilize biomolecules on nanoparticle surfaces through covalent bonding. The maleimide-thiol coupling and click chemistry are the other well-known techniques in immobilizing biomolecules to nanoparticle surfaces, as schematically represented in Figure 11.

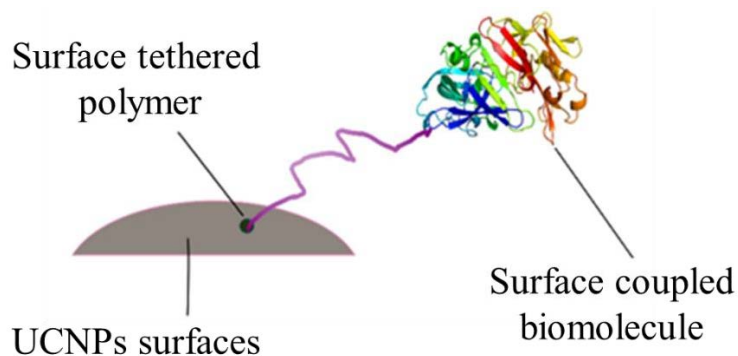


Figure 11 Schematic representation of surface tethering of bifunctional polymer and conjugation of biomolecules to nanoparticle surfaces.

➤ The microscopic techniques in intracellular imaging

Achievement of high spatial resolution remains a significant bottleneck in obtaining well-resolved images.<sup>3</sup> The diffraction of light, Abbe's diffraction limit, was a sustained change to reveal tiny details of intracellular structures and biological functions. Since nanoscale-level cellular functions are core life activities, adequate visualization of those detailed structures and dynamics helps determine the cell conditions and take interventions if necessary. Abbe's diffraction limit obscures the visualization of subcellular structures smaller than the diffraction limit.<sup>86</sup> PET has a better resolution capacity than SPECT, but the low spatial resolution is still the main drawback.<sup>87, 88</sup>

The CT, PET, and SPECT techniques rely on deep radiation using electromagnetic waves and subatomic particles. The low spatial resolution capability and hazardousness of conventional molecular techniques are the main driving forces to inspire new imaging modalities.<sup>89</sup> In the last decade, Abbe's diffraction limit could be surpassed by the incredible developments in optical microscopy associated with the recently emerged advanced super-resolution techniques.<sup>90</sup> These

days, multiple new optical modalities such as STED/RESOLFT, STORM, and PALM are widely implemented in exploring molecular-level biological events.<sup>91</sup>

The intense interest in UCNP probes is mainly associated with the high demand for nanoprobe in optical imaging.<sup>61, 92</sup> The progressive advancement in human lifestyle requires sensitive and accurate diagnosis and therapeutic facilities. Moreover, the rapidly rising health challenges, including life-threatening diseases like cancer, diabetes mellitus, Alzheimer, and COVID-19, are seriously impacting precious human health and life. To cope with those health challenges, developing efficient nanoprobe to cope with the rapid advancements in fluorescent imaging techniques is necessary.

The UCNP-based biomedical technologies are potential options for developing next-generation diagnostic and therapeutic tools. The integration of UCNP with biomolecules through specifically designed surface functionalizing polymers enables the production of nanoprobe. The primary purpose of this Ph.D. project is to functionalize the UCNP surfaces and develop probe for detailed intracellular labeling and imaging. Functionalized UCNP probe are fabricated to enable precise intracellular delivery and specific targeting. Then, successful intracellular imaging allows the monitoring of cellular activities. In parallel, the realization of intracellular imaging helps to perform other intracellular investigations, like biosensing and intracellular delivery. In Figure 12, the overall experimental design of the Ph.D. project is schematically represented.



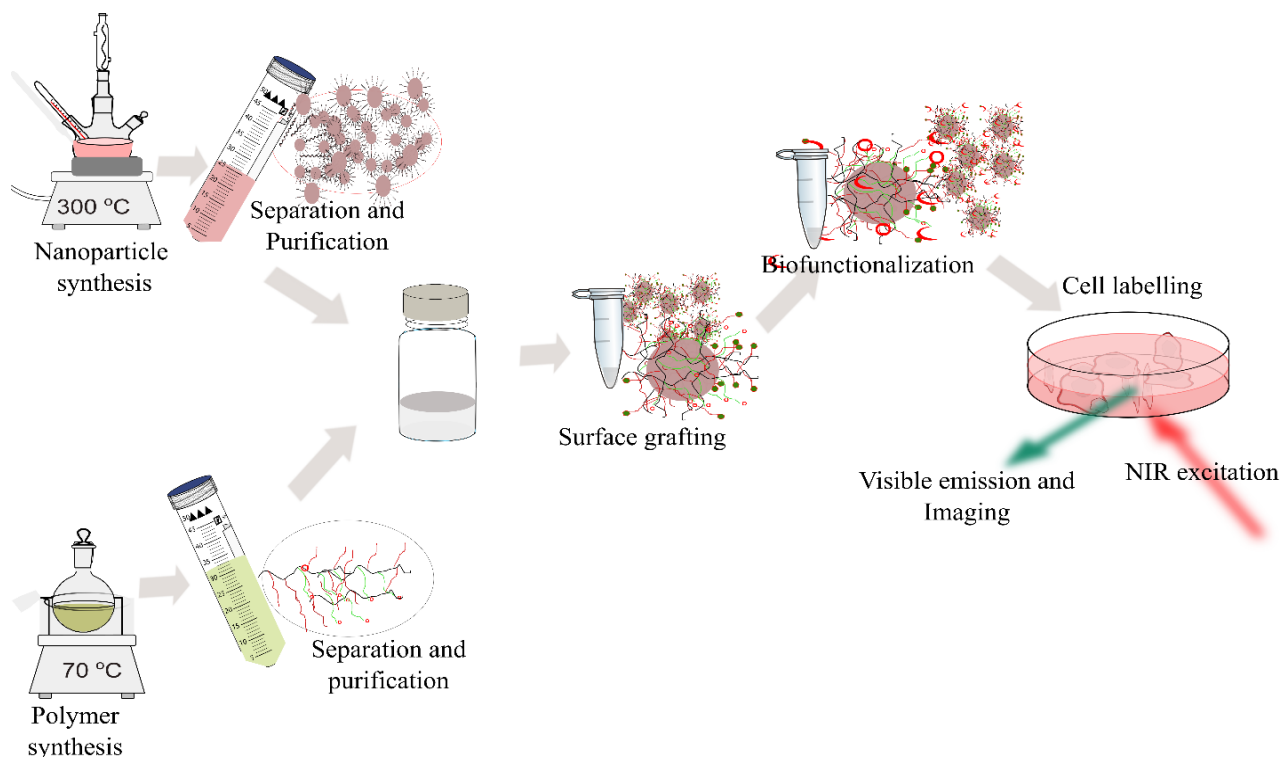


Figure 12 Schematic illustration of the flow scheme of the Ph.D. research project, which encompasses synthesis of UCNPs, RAFT copolymers design and development, surface grafting and functionalization, and cell labeling and imaging.

## 1.6 Objectives of the study

### ➤ General objective

The project aims to functionalize UCNPs surface for intracellular labeling and imaging applications. The experimental work comprises the synthesis of nanoparticles, design and synthesis of RAFT copolymers, surface grafting of UCNPs, biofunctionalization, and intracellular cell labeling and imaging.

### ➤ Specific objectives

- To synthesize  $\text{Ln}^{3+}$  UCNPs using the thermal decomposition technique
- To synthesize different RAFT-based copolymers
- To modify surfaces of UCNPs using synthesized block copolymers
- To functionalize the polymer modified UCNPs using biomolecules, such as antibodies and peptides

- To investigate the targetability of UCNPs using a homemade widefield microscope and TIRF and Leica Stellaris confocal microscope, and
- To prepare efficient UCNP nanoprobe for future uses in single-molecule and live-cell imaging

➤ Organization of the thesis

The thesis consists of a total of eight chapters which are outlined as follows.

- ❖ **Chapter one** introduces the motivation, background, and aims of the project
- ❖ **Chapter two** is a literature review on the fundamentals of the study
- ❖ **Chapter three** contains the synthesis and characterization of UCNPs
- ❖ **Chapter four** explains the synthesis of block copolymers and the characterization techniques
- ❖ **Chapter five** is about the surface modification and functionalization of UCNPs.
- ❖ **Chapter six** covers cell labeling and imaging experiments
- ❖ **Chapter seven** is a summary of the overall project outcomes, and
- ❖ **Chapter eight** gives a conclusion and perspective

# 2 | Nanotechnology in Healthcare Applications

## 2.1 Preamble

This chapter provides a detailed literature review of the topics addressed in the overall Ph.D. project which includes the roles of nanotechnology in healthcare. It discusses the current upconversion nanoparticle development techniques, including synthesis and functionalization methods. The potential advantages of controlling UCNPs crystal structure and surface properties are briefed. The multiple opportunities gained through UCNPs surface to address functionality and colloidal stability challenges are well stated. The possible UCNPs surface modification techniques and the advanced polymer synthesis approach in developing surface grafting polymers are stated explicitly. The advantages of copolymers' functionality in the surface immobilization of biomolecules are reviewed. The use of UCNP probes in cell labeling and imaging and the current advanced microscopic techniques for efficient intracellular imaging are elaborated.

## 2.2 Introduction

Nanotechnology revolutionized the broad spectacular of sciences resulted in numerous innovative applications.<sup>63, 93, 94, 95</sup> Nanotechnology has enormously contributed to the improvement of healthcare approaches and human life quality. The implementation of nano-sized materials and devices for disease diagnosis prevention, treatment, and diagnosis is termed nanomedicine.<sup>96</sup> Nanomedicine is a new era of medical approach with novel concepts and applications to support the healthcare sectors.<sup>10, 96, 97</sup> Currently, nanotechnology-assisted diagnostics and therapeutics are the most vibrant biomedical research topics.<sup>98</sup> Nanotechnology-based solutions have prominent roles in the advancements of biomedical devices, including diagnostic tools and drug-delivery systems.<sup>99, 100</sup> Nanobiotechnology is a cutting-edge approach operates with a rational combination of nanotechnology with biotechnology.<sup>101 102</sup> Nanobiotechnology is an interdisciplinary field of research allows to combine nanoparticles with biomolecules to produce functionalized nanomaterials.<sup>12, 103</sup>

Nanobiotechnology creates new opportunities to prepare novel nanomaterials and devices for various nanomedicine applications.<sup>11, 103</sup> The attachment of synthetic nanomaterials with nano-

sized biomolecules produces combined bio-mimicked properties.<sup>98</sup> The nano-hybrids made from nanoparticles and biomolecules have multiple advantages, such as optimization of nanoparticles' biocompatibility and targetability. Nano-systems from the combination of various nanomaterials allow diagnostics and therapeutic actions to be performed simultaneously.<sup>102</sup> Multimodality is a unique feature of nanomedicine that enables numerous diagnostics and therapeutics.<sup>10</sup> The relationships between biotechnology, nanotechnology, nanobiotechnology, and nanomedicine are diagrammatically sketched as presented in Figure 13.

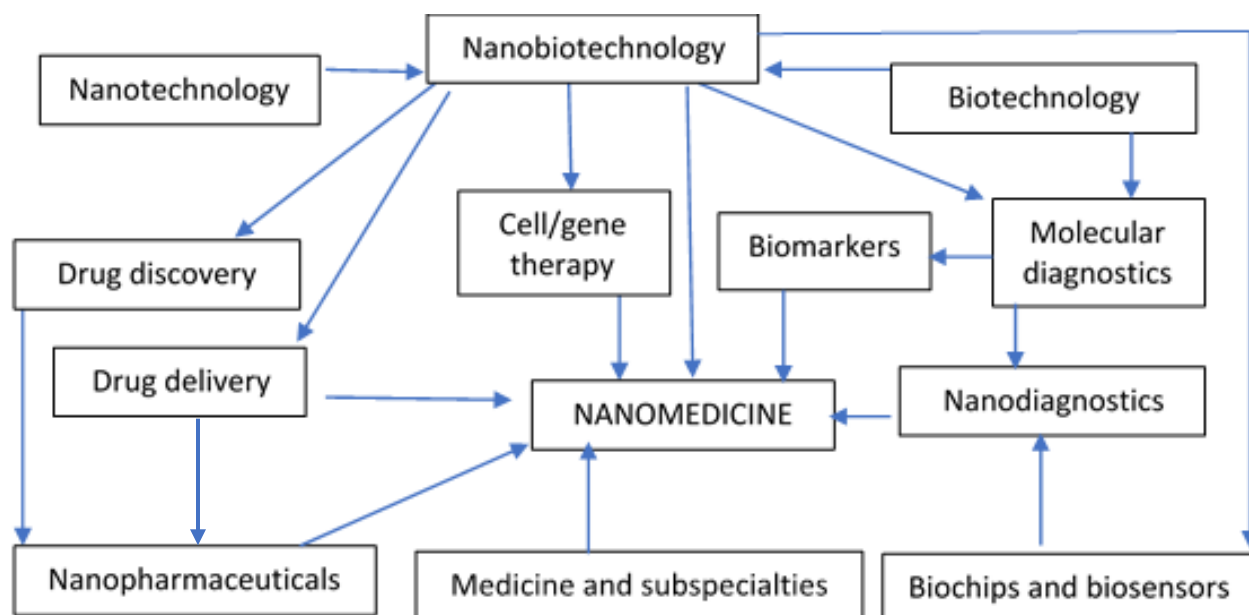


Figure 13 The relationships between nanotechnology with nanobiotechnology and nanomedicine. Reproduced with permission<sup>11</sup> © 2017 Springer.

The biomedical applications of nanoparticles demand specific surface design and development to attain desired physicochemical properties. It comprises designing and developing nano-systems for nano imaging, delivery, and therapeutics.<sup>96</sup> The versatility and tunability of nanomaterials, such as polymers, help suit their physicochemical properties for the intended application.<sup>4, 104</sup> The advances in materials science and molecular biology have significant roles in producing tailored functional nanomaterials.<sup>105,106, 15</sup> To produce nanomaterials with the desired physicochemical properties for biomedical applications, the materials development approach has significant contributions. Figure 14 illustrates a multifunctional upconversion nanoparticle produced by integrating the UCNPs with linker polymer and bio-recognition elements.<sup>107</sup>

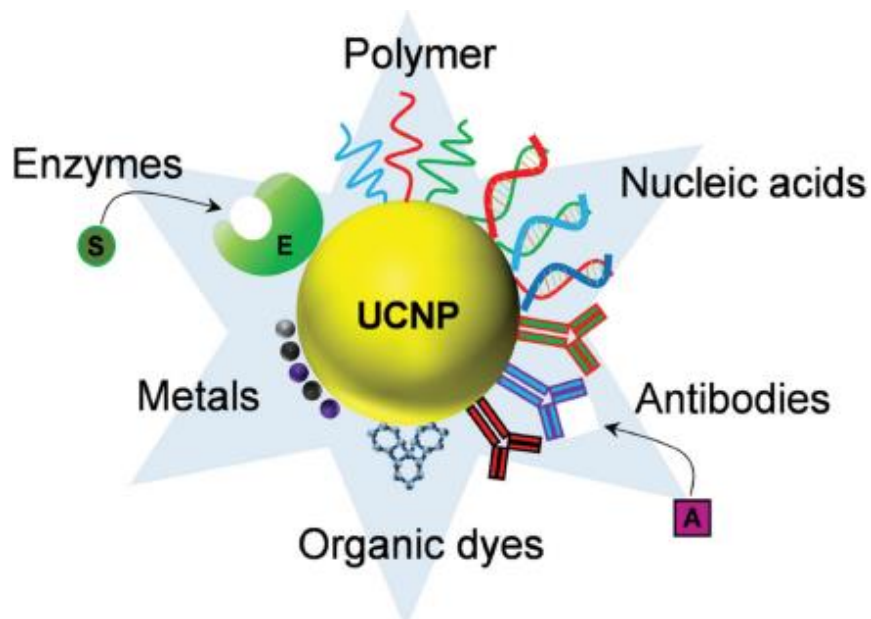


Figure 14 Representation of multifunctional nanoparticles developed through surface modification and biofunctionalization of UCNP. Reproduced with permission<sup>107</sup> © 2009 Wiley-VCH.

Molecular imaging is an essential technique in measurement and valuation of biological processes. Optical imaging is one of the potent tools for in vitro and in vivo molecular-level biological investigations.<sup>108</sup> Optical imaging exhibits many exciting features compared to conventional molecular imaging techniques.<sup>109-111</sup> Optical imaging is a non-invasive and non-ionizing technique for cellular and intracellular molecular investigation.<sup>52, 112</sup> Optical imaging enables deep tissue penetration with reasonably high sensitivity and spatial resolution.<sup>40, 59</sup> Real-time intracellular imaging, for instance, is the most prioritized pre-clinical and clinical diagnosis.<sup>113</sup> Fluorescence imaging is widely implemented in examinations of cells and intraoperative purposes and remains a gold standard. Although advanced electron microscopic techniques like cryo-TEM are known for their high-resolution capability, fluorescence imaging enables us to capture high-contrast images non-invasively. The common fluorophores in cell labeling agents are small-molecule organic dyes, fluorescent proteins, carbon nanomaterials, and metal nanoparticles. Figure 15 is an adapted figure to show the different classes and sub-classes of fluorophores.<sup>114, 115</sup>

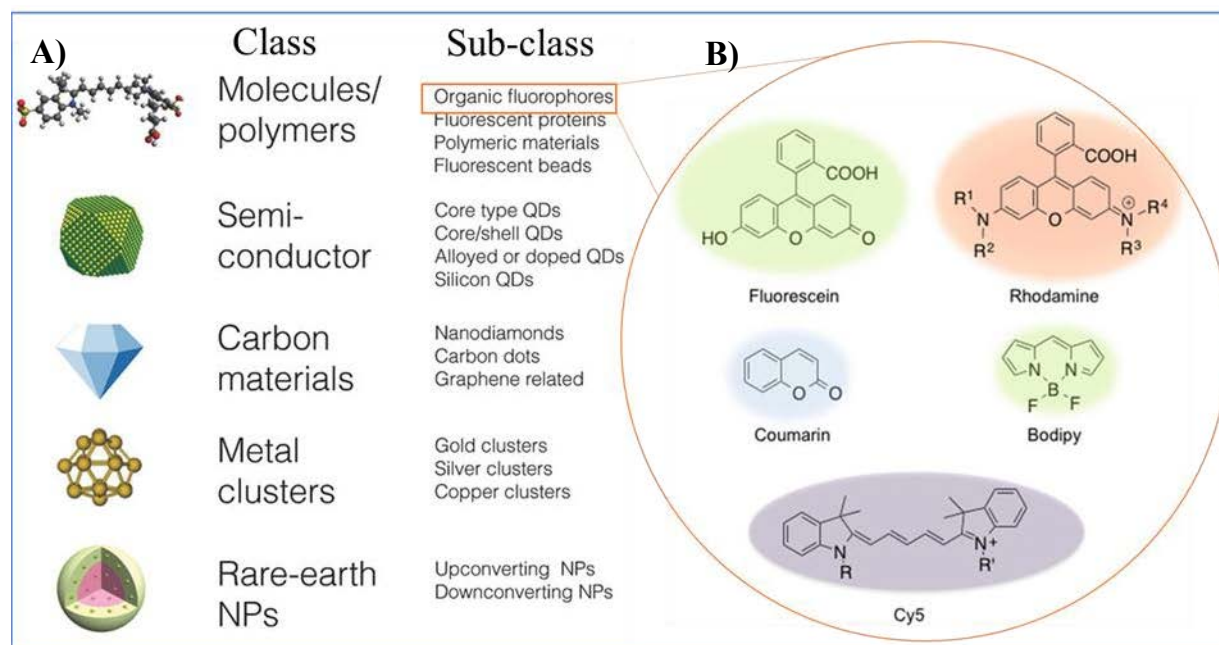


Figure 15 List of commonly used labeling agents in fluorescence microscopy that includes both organic and inorganic fluorophores, their sub-classes (A), and organic fluorophores with their respective visible emission (B). Adapted with permission<sup>114, 115</sup> © 2016, and © 2021 Wiley-VCH, respectively.

In Figure 15, fluorophores, such as small molecules, polymers, semiconductors, carbon nanomaterials, metal clusters, and rare-earth elements are classified. Moreover, some selected organic dyes, such as fluorescein, rhodamine, coumarin, BODIPY, and Cy5, are presented with corresponding visible emissions. Conventional labeling agents like organic dyes require short-wavelength excitation and are prone to significant drawbacks like photobleaching.<sup>34-40</sup> A recent survey on the use of fluorophores in cell labeling indicates the employment of nanoparticles, as the probe is not yet explored well.<sup>32</sup> For example, the current use of nanoparticles in cell labeling, like the UCNPs, gold, carbon, and graphene dots, in cell labeling is less than 2%.<sup>32</sup> The anticipation for stable, specific, sensitive, and targetable probes remains unrealizable.<sup>3, 25</sup> Figure 16 displays the different classes of organic and inorganic optical probes. The two adopted images show the comparative advantages of fluorophores size Figure 16A and the working wavelength range Figure 16B.<sup>115, 116</sup>

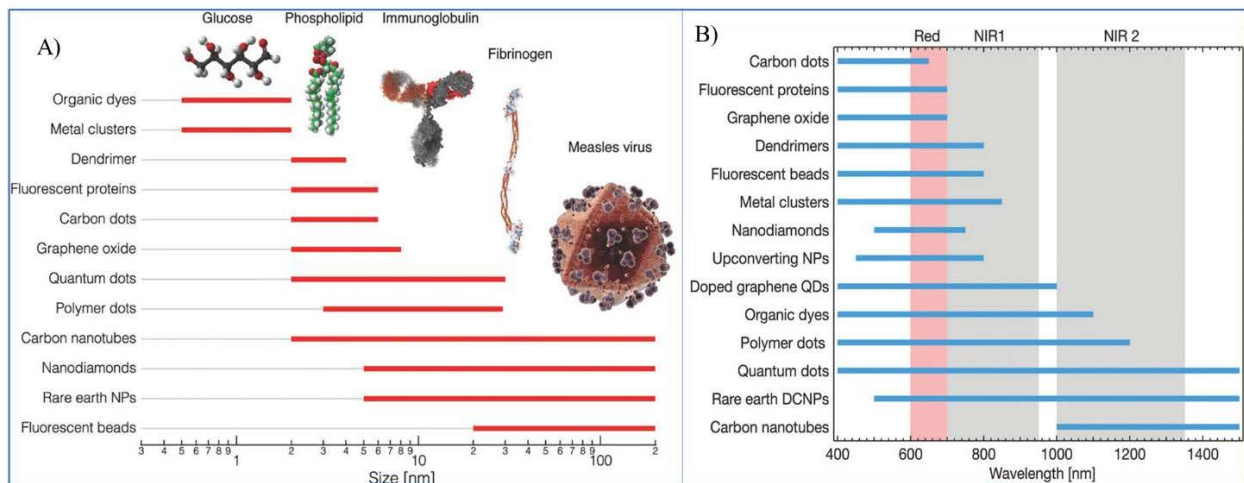


Figure 16 The comparative size (A) and luminescence emission wavelength ranges of optical nanoprobe (B). Reproduced with permission<sup>115</sup> © 2016 Wiley-VCH.

To perform a precise medical diagnosis and therapy, the employment of a sensitive and accurate probe is important.<sup>31, 117</sup> The specificity and speed of data acquisition of nanoprobe determine the instrument's performance and image quality.<sup>118, 119</sup> Ideally, contrast agents are expected to attain reasonable specificity, integrity, improved signal intensity, and clearance mechanism.<sup>28, 120</sup> Biological and chemical stability and localizability are the main parameters in the design of nanoprobe.<sup>113</sup> The optical probes need to be consistent with signaling and targeting components.<sup>121</sup> The signaling part of nanoprobe is responsible for generating valuable information. Various inorganic probes, including the UCNPs, have been extensively investigated in fluorescent imaging. The current high demand for UCNP probes in optical imaging is due to their unique potential advantages in molecular imaging.<sup>61, 92, 122</sup>

### 2.3 The lanthanides (III) doped UCNPs

The upconversion process of lanthanide (III) doped crystals generates visible and UV emissions. The lanthanide (III) elements can produce both downshifted and upconverted emissions.<sup>57, 123 124</sup> Recently, downshifting emissions from lanthanide-doped particles have attracted great attention in fluorescence imaging.<sup>124</sup> Simultaneous Nd<sup>3+</sup> and Yb<sup>3+</sup> co-doped nanoparticles, for instance, exhibit both up-converted and down-shifted emissions.<sup>123</sup> The excited state of Nd<sup>3+</sup> doped structures demonstrates unique energy transfer capacity to the neighboring lanthanides and generates a tunable downshift emission.<sup>123</sup> The NIR-II gets more attraction than NIR-I because it

exhibits a reduced tissue heating effect.<sup>10, 124</sup> The merits and potential advantages of the NIR in optical imaging have been discussed in detail in chapter 1, section 1.3.

➤ The  $\beta$ -NaYF<sub>4</sub> UCNPs

The hexagonal ( $\beta$ ) UCNPs are the most exploited phosphors.<sup>125</sup> Synthesis of  $\beta$ -UCNPs requires a suitable matrix or host material. The host material in UCNPs serves to isolate dopant ions and helps to facilitate energy transfers between the activator and sensitizer.<sup>126</sup> The UCNP crystal formation is achieved by replacing the host ions with the activator and sensitizer.<sup>78</sup> Nanocrystals with high dopant concentration are confirmed for their enhanced emissions.<sup>127</sup> The emission efficiency of the nanocrystals depends on the solid-state structure of the nanoparticles. The hexagonal lattice structure generates bright emissions compared to cubic crystals.

Different host materials and dopant ions are widely investigated in synthesizing UCNPs. The commonly used host materials for synthesizing UCNP are fluorides like LaF<sub>3</sub>, LiYF<sub>4</sub>, NaYbF<sub>4</sub>, NaGdF<sub>4</sub>, or oxides such as YVO<sub>4</sub>. Due to their high stability and low phonon energy, NaYF<sub>4</sub>-based nanoparticles are popular.<sup>62, 78, 128</sup> The NaYF<sub>4</sub>-based UCNPs occur in two polymorphs, cubic ( $\alpha$ -NaYF<sub>4</sub>) and hexagonal ( $\beta$ -NaYF<sub>4</sub>) phases.<sup>129</sup> The  $\beta$ -NaYF<sub>4</sub> doped with Yb<sup>3+</sup> sensitizers and Er<sup>3+</sup> or Tm<sup>3+</sup> activators are well-known efficient green and blue emitters.<sup>130</sup> The doped lanthanide ions serve as center of the energy conversion process. The Er<sup>3+</sup>, Ho<sup>3+</sup>, and Tm<sup>3+</sup> are well-known activators because they have equally spaced ladder-like energy levels and exhibit long-lived metastable excited states.<sup>131</sup> Yb<sup>3+</sup> is the standard type of sensitizer in presence of Er<sup>3+</sup>, Ho<sup>3+</sup>, and Tm<sup>3+</sup> activators. Yb<sup>3+</sup> has a high absorption cross-section and produces a single excited state through an electronic transition of <sup>2</sup>F<sub>7/2</sub> - <sup>2</sup>F<sub>5/2</sub> when excited at 980 nm.<sup>55</sup> Nd<sup>3+</sup> is known for production of intense emissions in solid-state devices.<sup>132</sup> In Figure 17, the solid-state structural representations are adapted to represent the transformation of lanthanide (III) precursor salts to cubic and hexagonal phases.<sup>133</sup>



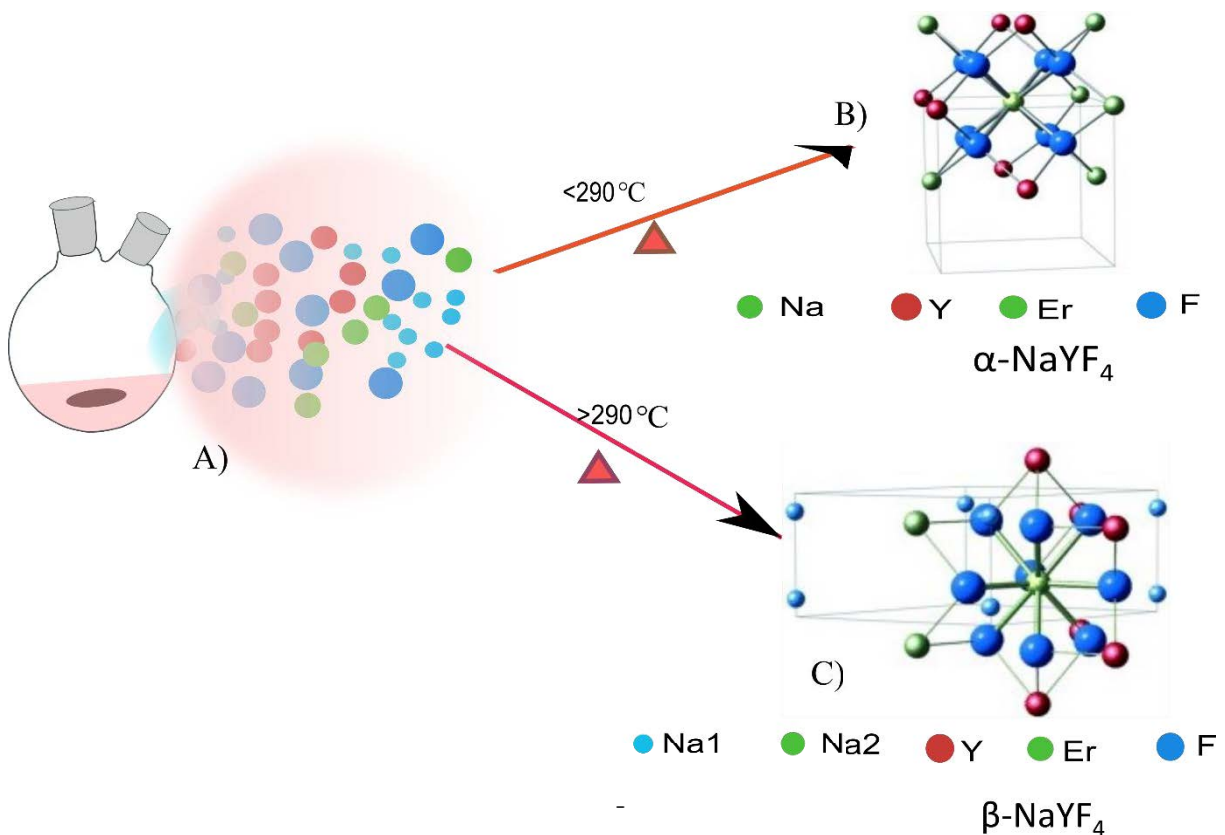


Figure 17 Pictorial representation of the synthesis of UCNPs (A) representation of reaction mixture at the initial stage, (B) formation of cubic phase, and (C) favoring the hexagonal structure formation.

The thermal decomposition technique is an efficient method to produce a crystalline hexagonal structure.<sup>65</sup> The gradual transformation of precursors through a progressive nucleation and crystal growth enables to produce particles with a hexagonal phase. In the heat up UCNP synthesis, the cubic structure is favored at lower temperatures. A well-crystallized hexagonal phase could be produced by a rapid increase of temperature closer to 300 °C and by maintaining for an hour.<sup>125</sup> In the first stage of the synthesis, the formation of the cubic phase is favored, which ends up at 300 °C. The second stage favors formation of hexagonal structures by transforming the preformed cubic phase.<sup>125</sup> In stages three and four, a complete cubic phase transformation to the hexagonal phase and crystal growth takes place.<sup>134, 135</sup> <sup>125</sup> Nanoparticles with a hexagonal structure are preferable to produce bright emissions.<sup>40, 136</sup> Figure 18 depicts the different phases transformation in the synthesis of upconverting nanoparticles including the nucleation stage during controlled temperature treatment.<sup>10</sup>

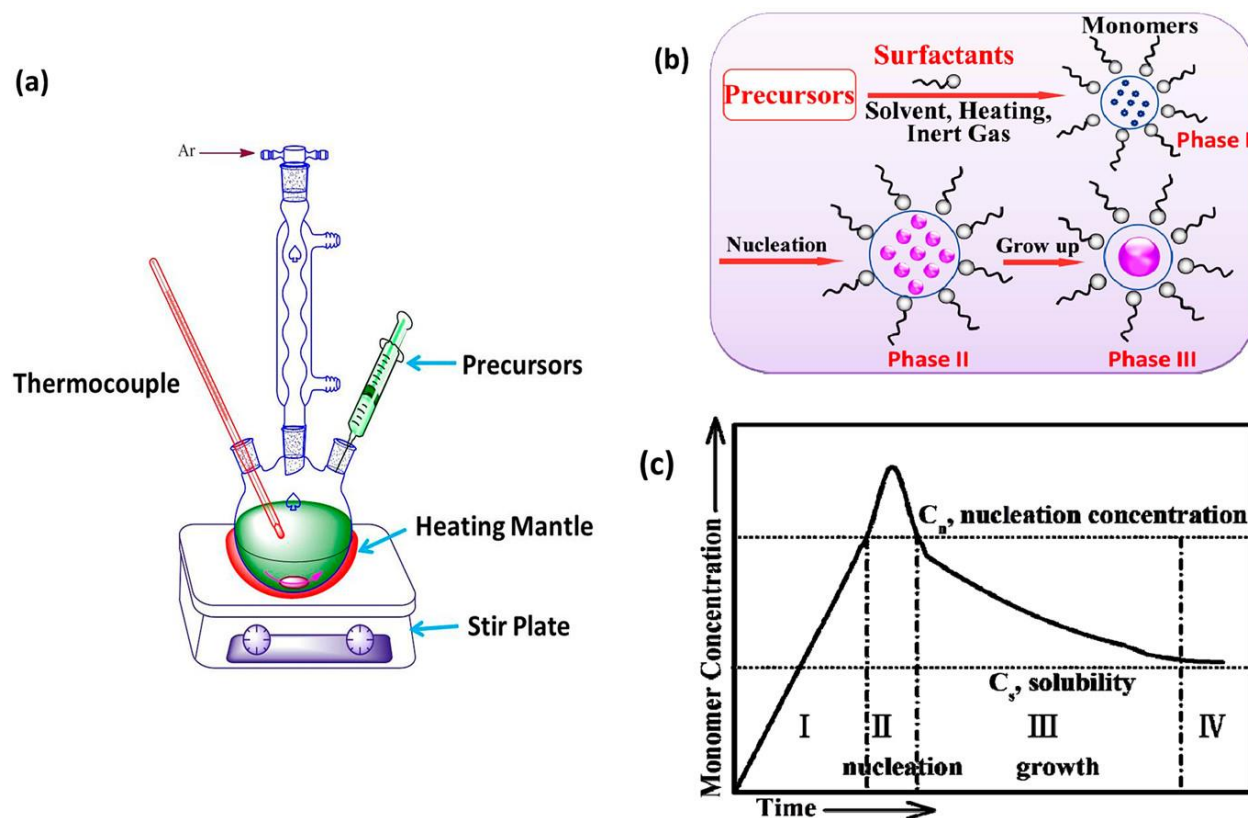


Figure 18 The UCNPs synthesis reaction setup (A), course of reactions, including the stages in hexagonal phase formation at (B) and (C) Reproduced with permission<sup>10</sup> © 2016 American Chemical Society.

### ➤ Characterization of UCNPs

UCNPs characterization helps to monitor reaction progress and to confirm the fulfillment of essential physicochemical properties for the intended specific application.<sup>134, 137</sup> An appropriate nanoparticle characterization technique is necessary to get reliable data and clear understanding of essential properties, such as optical properties.<sup>137</sup> Characterization of UCNP physicochemical properties enables to translate their inherent performance to real-world applications.<sup>138</sup> An investigation of UCNPs' surface charge, composition, size, shape, and crystallinity helps to understand their behavior.<sup>139</sup>

The standard UCNPs characterization techniques include fluorescence spectrometry, TEM, DLS, ATR-FTIR, XRD, TGA, and zeta sizer. Zeta sizer is helpful for the assessment of particle size and surface electrical potential.<sup>137</sup> The surface potential determination is beneficial in assessing the stability and dispersity of polymer-modified nanoparticles. The ATR-FTIR technique helps to

check the change in surface functionality nanoparticles with the surface-integration of polymers.<sup>140</sup> TGA is the most commonly used technique in determining the type of surface-grafted polymer and the density of ligands on nanoparticle surfaces.<sup>141, 140</sup> XRD analysis is implemented to determine the crystal structure and degree of crystallinity.<sup>142</sup>

The solid-state structure of the UCNP phosphors is a crucial factor in their luminescence performance. The arrangement of atoms in the crystal structure of the nanoparticles and the force of interaction between them determines their physical properties.<sup>143 144</sup> The hexagonal crystal structure are well known for their strong luminescence emission compared to the cubic structure.<sup>143</sup> The real-time NIR monitoring allows for in-situ monitoring of the crystal growth progress.<sup>134</sup> The purity of the hexagonal structure could be evaluated by comparing the sample XRD spectrum with a reference spectrum. The XRD analysis helps to assess the effectiveness of UCNP synthesis and its purity.

#### ➤ Determination of UCNPs size and morphology

Since the particle size fundamentally defines nanotechnology, and an accurate nanoparticle size estimation is a primary concept.<sup>137, 145</sup> The determination of particle size is related to the spatial extent of the particle. The current particle size determination techniques follow a one-dimension measurement, and inaccurate estimation could occur for non-spherical particles.<sup>138</sup> The transmission electron microscopy (TEM) and dynamic light scattering (DLS) are the most common techniques in determining UCNP size. Generally, particle size, size distribution, and shape are essential in evaluating nanoparticles' suitability for specific applications.

Dynamic light scattering (DLS) is a standard technique for determining the hydrodynamic diameter of nanoparticles.<sup>146</sup> It is frequently used in colloids size determination.<sup>137, 147</sup> The small sample requirement, short acquisition, and analysis time are some of the merits of the DLS technique. DLS allows for a wide range of size measurements covering from nanometers to 10  $\mu\text{m}$ . The recommended sample concentration for DLS analysis ranges from 50 -100  $\mu\text{g/mL}$ .<sup>137</sup>

The nanoparticle's hydrodynamic size determination is dependent on its Brownian motion. Due to their fast and random mobility, in concentrated solutions the interaction between the colloids is high.<sup>137</sup> Hydrodynamic size determination is unsuitable for non-spherical particles and heterogeneous size distributions.<sup>148</sup> The particles' surface nature determines their mobility and

light-scattering properties. The random motion of suspended nanoparticles induces a time-dependent scattered light intensity fluctuation. During hydrodynamic particle size analysis, measurement of the diffusion coefficient of freely suspended particles is performed from the fluctuation of scattered light using the Stocks-Einstein equation, as given in equation 1.<sup>137</sup>

$$D = \frac{k_B T}{6\eta \pi R_h} \dots\dots\dots(1)$$

Where: D stands for diffusion coefficient;  $k_B$  represents the Boltzmann constant; T stands for working temperature;  $\eta$  is for the solvent's viscosity; and  $R_h$  stands for the hydrodynamic radius of the particle.

TEM is a powerful and most frequently used technique in nanoparticle characterization. It is a sensitive technique for characterizing particle size and morphology.<sup>149</sup> The current advanced TEM can perform an atomic level resolution of 0.05 - 0.1 nm<sup>138</sup>, which helps investigate particle size, shape, and crystallographic structures at a single particle level. TEM is beneficial for the direct capturing of UCNP images and for chemical analysis.<sup>148</sup> However, TEM characterization of UCNPs provides a 2D projection of nanoparticle shape, and the quality of the captured image relies on the particle's orientation.<sup>138</sup>

➤ The spectroscopic properties of UCNPs

The UCNPs' luminescence results from a non-linear optical process. It involves a sequential absorption of multiple lower energy photons by the sensitizer, which is followed by energy transfer to the activator. It leads to the release of high-energy photons as luminescence emissions.<sup>40, 65, 150,151</sup> The intensity and type of light emitted from the UCNPs depends on the composition and solid-state structure of the nanocrystal. The sharp recognizable emission of UCNPs arises from the shielding effect of the filled 5s<sup>2</sup>5p<sup>6</sup> subshells. Due to the high shielding effect from the outer 5s<sup>2</sup>5p<sup>6</sup>, the inner 4f electrons are protected from the external fields and produce stable and sharp emissions.<sup>152</sup> It is also associated with spin-orbit coupling and crystal field interaction during electron transitions in the 4f<sup>n</sup> orbitals. A multiple photon emission could be obtained from lanthanide (III) doped nanoparticles by controlling the excitation wavelength, as shown in Figure 19.<sup>153</sup>

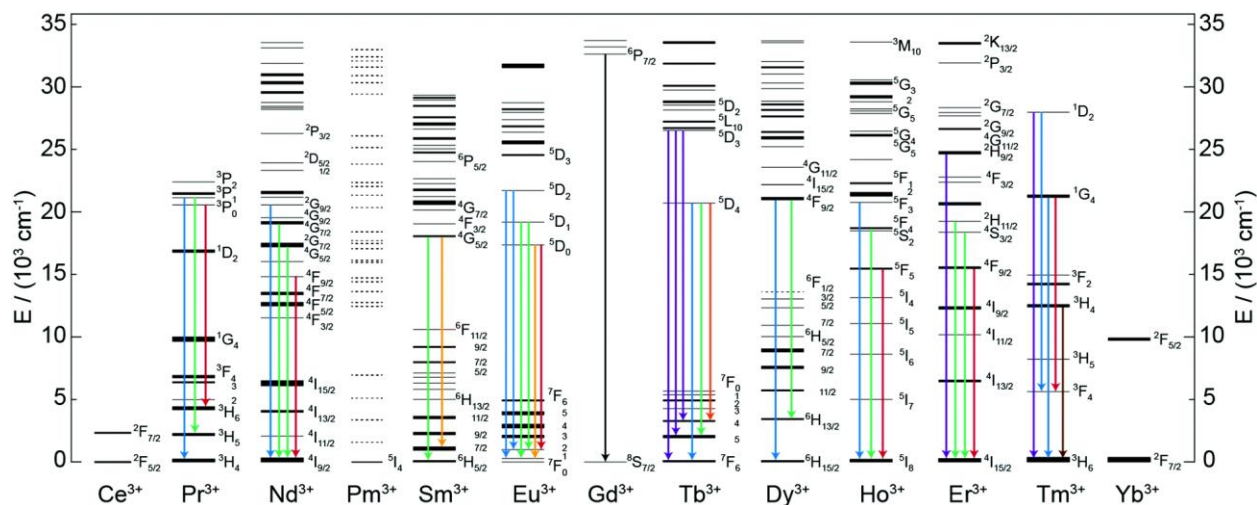


Figure 19 The energy level diagrams of 4fn electron transitions of lanthanide elements. Reproduced with permission<sup>80</sup> © 2021 Royal Chemical Society.

UCNPs are capable to produce multiple emissions compared to conventional fluorophores such as organic dyes and quantum dots.<sup>154</sup> The availability of multiple electronic states of the 4f electrons helps to generate numerous electronic levels from lanthanide-doped nanocrystals. The main up-conversion mechanisms can be classified as excited-state absorption (ESA), energy transfer up-conversion (ETU), cooperative sensitization up-conversion (CSU), cross-relaxation (CR), and photon avalanche (PA). The ETU is the most efficient energy-converting mechanism. ETU involves two co-doped lanthanide elements as sensitizers and activators to facilitate the emission.<sup>155</sup> In ETU, the two neighboring ions are involved in the energy transfer process, in which ion 1 is a sensitizer, and ion 2 is an activator. Figure 20 shows for the five broad classifications of upconversion mechanisms.<sup>156</sup>

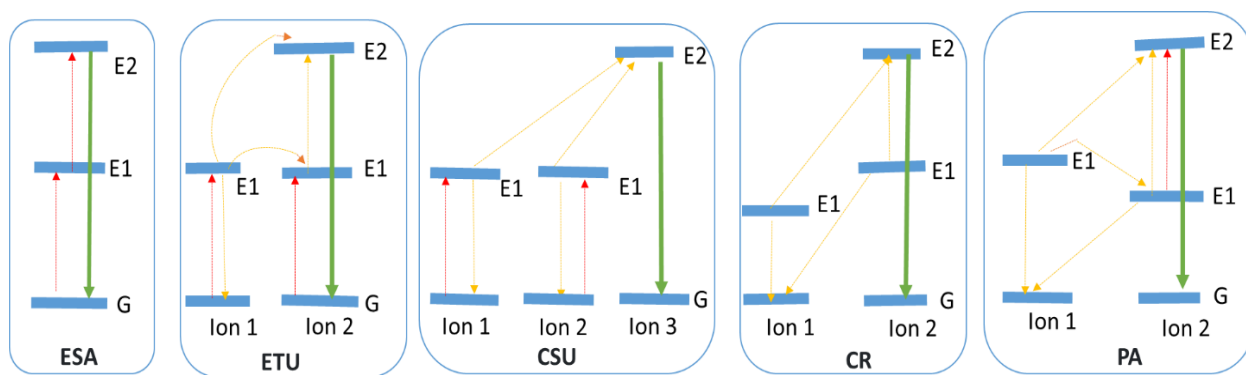


Figure 20 Schematic representation of the five kinds of upconversion mechanisms. Adapted with permission<sup>156</sup> © 2020 Elsevier B.V.

So far, profound experience has been documented in the synthesis and characterizations of UCNPs. Multiple standard UCNP synthesis techniques, such as thermal decomposition, hydro(solo)thermal, co-precipitation, and sol-gel are well established.<sup>40, 56, 157</sup> Thermal decomposition, thermolysis, is the efficient technique in controlling particle size and morphology. The traditional thermal technique was based on a high-temperature decomposition of trifluoroacetic acid and halide salts.<sup>157</sup> Currently, thermal synthesis is implemented using precursor salts like chloride, fluoride, or acetate in high-boiling organic solvents, 1-octadecene, and oleic acid as capping agent.<sup>143, 150, 157</sup>

### 2.3.1 The potential advantages of UCNPs surfaces

The UCNPs surface is a vital component of the particle because it holds vast opportunities to govern the essential parameters like interface interactions with the surroundings that determines their ultimate performances.<sup>39</sup> The intracellular application of UCNP demands a bright luminescence from a well-performing crystalline structure. However, besides their improved bulk luminescence performance, the UCNPs' surface chemistry significantly determines their biological interactions and routes. Surfaces of UCNPs include the crystallographic texture and surface-attached polymers.<sup>158</sup> The native UCNP crystal surfaces are positively charged, which arise from crystal terminating surface cations. Due to the partial coordination of surface-residing lanthanide ions, the surface gains a high affinity toward negatively charged ligands. The partially coordinated positively charged surfaces efficiently coordinate with a wide range of negatively charged ligands.

The surface charge and zeta potential of nanoparticles are independent properties.<sup>159</sup> The surface charge could originate from the surface termination ions or due to functionality of the surface capping ligand. The nanoparticles could be stabilized through electrostatically or sterically repulsion among surface polymer groups. The surface charge helps colloids to maintain their stability for a longer period. Unless the pre-established equilibrium of the dispersed particles is disturbed, colloids tend to remain stable.<sup>160</sup> In the case of positively charged surfaces, like in UCNPs, a negative inner electrical layer has been developed as a counter layer known as the 'stern layer.' The surface charge of nanoparticles has significant roles in cellular uptake and inflammation effects during their bio-applications. Zeta potential ( $\zeta$ ) is an interfacial property between the nanoparticle and the surrounding solution. It helps to determine the long-term stability of colloidal suspensions. The zeta potential is also considered as a measure of toxicological effect and biocompatibility.<sup>161</sup> Particles with zeta potentials  $< \pm 30$  mV are considered moderately stable. Nanoparticles with higher zeta potential  $> \pm 30$  mV are known as electrostatically stabilized.<sup>162</sup>

Charged colloids tend to develop a surface counter layer called an electrically charged layer.<sup>10</sup> The ions present in the surrounding solution rearrange themselves on the particle surface to form a counter layer. The initially formed electrical layer induces a second counter layer and then propagates infinitesimally. Consequently, an electrical double layer has been developed at the solid-liquid interface regions.<sup>160, 161</sup> The electrical double-layer strength gradually decreases at the furthest distance, forming a diffused layer. The diffused layer is dynamic and constantly changes with a slight temperature, pH, concentration, and ionic strength variations. When applying an external electric field, the charged nanoparticles migrate toward the oppositely charged electrode. Due to the induced particle mobility, a hypothetical shear plane has been developed between the diffused layer and the surrounding dispersant, as represented in Figure 21. The nanoparticle surface potential is also called Nernst potential. It cannot be determined from direct measurement of nanoparticle surface potential. However, it could be assessed from electrophoretic mobility ( $\mu_e$ ) of dispersed nanoparticles. Equation 2 represents surface potential at some distance from the stern layer.

$$\psi = \Psi_d e^{-\kappa x} \dots\dots\dots(2)$$

Where  $\kappa$  = Debye-Hückel parameter,  $\psi$  = surface potential at a distance x from the stern layer, and  $\Psi_d$  = surface potential at the stern layer, x = distance

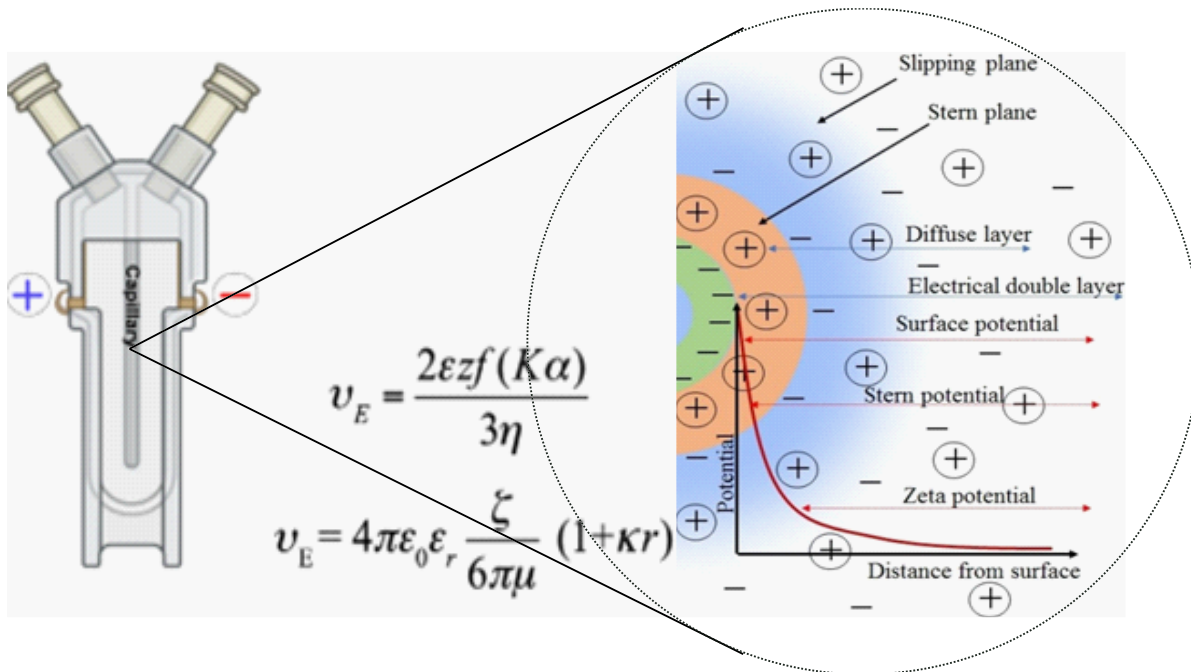


Figure 21 Pictorial representation of the structure of electrical double layer during zeta potential determination using capillary cuvette. Adapted with permission<sup>160, 161</sup> © 2020 Canadian Society for Chemical Engineering and © 2016 Wiley-VCH, respectively.

Where  $\epsilon_r$  is relative permittivity,  $\epsilon_0$  is the electric permittivity of vacuum,  $\eta$  is the dynamic viscosity of the solution,  $f(Ka)$  Henry's function,  $r$  stands for distance, and  $\zeta$  represents zeta potential.<sup>162</sup> The electrophoretic mobility of a given system could be defined by equation 3.

$$\mu_e = V/E \dots \dots \dots (3)$$

$V$  stands for particle velocity, and  $E$  represents the applied external field. Based on Henry's equation, the relationship between electrophoretic mobility and zeta potential is given in equation 4.<sup>137</sup>

$$\mu_e = \frac{2\epsilon_r\epsilon_0 f(KA)}{3\eta} \zeta \dots \dots \dots (4)$$

Where  $\eta$  is dynamic viscosity,  $\epsilon_r$  is relative permittivity,  $\epsilon_0$  is the electric permittivity of vacuum,  $f(KA)$  represents Henry's function, and  $\zeta$  stands for zeta potential<sup>162</sup>

The zeta-potential measurement allows for the evaluation of particle stability.<sup>160</sup> According to DLVO theory, which is an acronym for the theory developers Verjaguin, Landau, Verwey, and Overbeek, stability of colloids could be determined from the total potential energy exerted by



nanoparticles and solvent. The balance between attraction and repulsion forces among dispersed particles, the van der Waals force of attraction, and the electrical double-layer repulsive forces determine the colloidal stability of nanoparticles. The presence of strong repulsive between particles enables extended period stability. Zeta potential is dependent on the pH of the solution. In an acidic medium, the particle surfaces gain higher positive zeta potential, and in a basic medium, the surfaces could develop negative zeta potential. In a recent review by Kamble et al., the relationship between the DLVO and the colloidal stability of particles has been discussed in detail.<sup>160</sup>

Surface polymer characterization is vital in understanding particle surfaces' functionality. It also helps assess the surface graft density of the particles. ATR-FTIR allows the determination of surface polymer functionality. TGA has been used widely in quantitatively determining surface-grafted polymers by measuring weight losses associated with the decomposition of organic ligands attached to the metal nanoparticles. The ratio between grafted polymer and metal particles is helpful in quantifying graft density.<sup>163</sup> The TGA thermograph; however, does not allow to identify the individual polymer components.

### 2.3.2 Modification of the UCNPs surfaces

Surface tailoring provides many potential advantages in optimizing the particles' performances. One primary goal of nanoparticle surface modification is to control stability and aggregation of particles.<sup>164</sup> Well-designed surfaces help to maintain particle stability and to obtain prolonged in vivo performances. For instance, the UCNPs' crystal of chemical stability is essential to maintain their luminescence performances in intracellular labeling and imaging. Surface polymer grafting enables strong polymer-nanoparticles attachments. The strong coordination bond formation between the particles' surfaces and the polymer stabilizes the crystal by reducing surface energy. In addition, the surface-attached polymer protects the nanoparticles from water attack. Hydrophilic polymers like zwitterionic functionalities have strong hydration which results in antifouling capacity.

The UCNPs' colloidal stability could be evaluated regarding their resistance to coagulation and/or from the detachment of surface-grafted polymers. At high nanoparticles concentrations, the distance between the surfaces of particles decreases, and the presence of high particles trapping

tendency by Vander walls forces results in aggregation.<sup>164</sup> The presence of strong luminescence intensity and a reduced change in hydrodynamic size indicates the extended particles' stability in certain conditions. The extent of surface grafting determines the stability of UCNPs in the presence of competitive ions.<sup>146</sup> Tong et al. investigated multidentate tetraphosphate derivatized ligands, and an improved stability PBS buffer has been achieved.<sup>146</sup> Surface functionalization of UCNPs is a crucial approach to improve nanoparticle biostability, biocompatibility, and responsiveness.

Surface integration of biological molecules to nanoparticles improves biocompatibility and targetability. Biocompatibility is essential for implementing nanoparticles in biomedical applications. Nanoparticle surface modification helps mediate the particles' interactions with the surrounding environments. The physiological system responses would be determined from the surface feature of the nanoparticle. Undesired nano-bio interface interactions are significant challenges that need careful consideration during surface modification. The complex intracellular pathway taken by nanoparticles has made the nano-bio interface challenges more sophisticated to understand.<sup>165-167</sup> Surface functionalization allows suiting the nanoparticles for intended purposes.<sup>78</sup>

The currently available multiple surface modification techniques, such as polymer grafting through ligand exchange and surface coating, are widely implemented to manipulate UCNPs' surface. Hydrophilic polymer-based surface tailoring of inorganic nanoparticles is suitable for obtaining good dispersibility of particles. The surface coating of UCNPs could be done with inorganic materials like silica coating or using organic ligands, for instance, small molecules and polymers.<sup>33, 35, 37, 168, 169</sup> The polymer-modified UCNPs gains improved dispersibility and stability due to steric effects and electrostatic repulsions from surface-grafted polymers. Polymer-based surface grafting is the most promising one. Amphiphilicity, electrical charge, and chemical functionality of surface-grafted copolymers help improve particle stability and dispersibility.<sup>170, 171, 172</sup>

The polymers-nanoparticle attachment could be achieved either through chemical or physical forces. In physical UCNPs surface modification, the surfaces of the particles are encapsulated with amphiphilic polymers.<sup>143</sup> Affinity-based nanoparticles-ligand interaction stabilizes the particles by surface chelating with suitable anchoring groups. The chemical integration of polymers to nanoparticle surfaces is either through 'graft to' or 'graft from' attachment. Among these grafting techniques, the 'graft to' method is a straightforward approach; however, it is affected by steric

hindrance. However, compared to the ‘graft from’ technique, ‘graft to’ enables introducing a lower number of polymers to the nanoparticle surfaces.<sup>173</sup> Figure 22 depicts the possible structure of polymers on the nanoparticle surface, their architecture, and functionalities.<sup>174</sup>

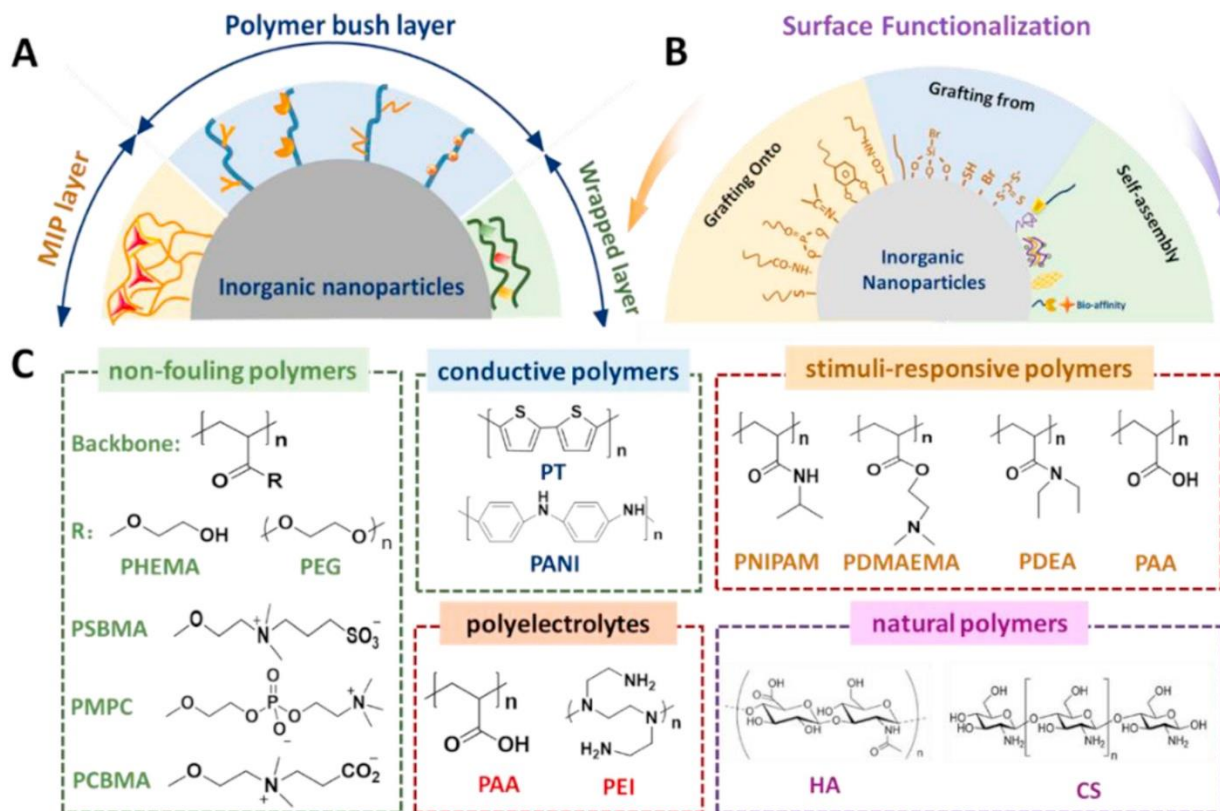


Figure 22 Schematic illustration of surface polymer architectures (A), different surface attachment techniques (B), and types of polymers suitable for surface modification (C). Reproduced with permission<sup>174</sup> © 2021 Elsevier B.V.

The surface design and development approach determine the functionalities of the final surfaces. Multifunctional surfaces could be produced by introducing polymers with unique advantages. The production of controlled surface functionalities enables for effective implementation of UCNPs in bioimaging, biosensing, and intracellular delivery applications. Nanoparticle surfaces with optimized surface features could overcome nano-bio interface challenges. The nano-bio interface challenges include endosomal trap, surface fouling, and loss of targetability. As pictorially visualized in Figure 23, the UCNPs surface could be designed to introduce different functionalities through polymer grafting.

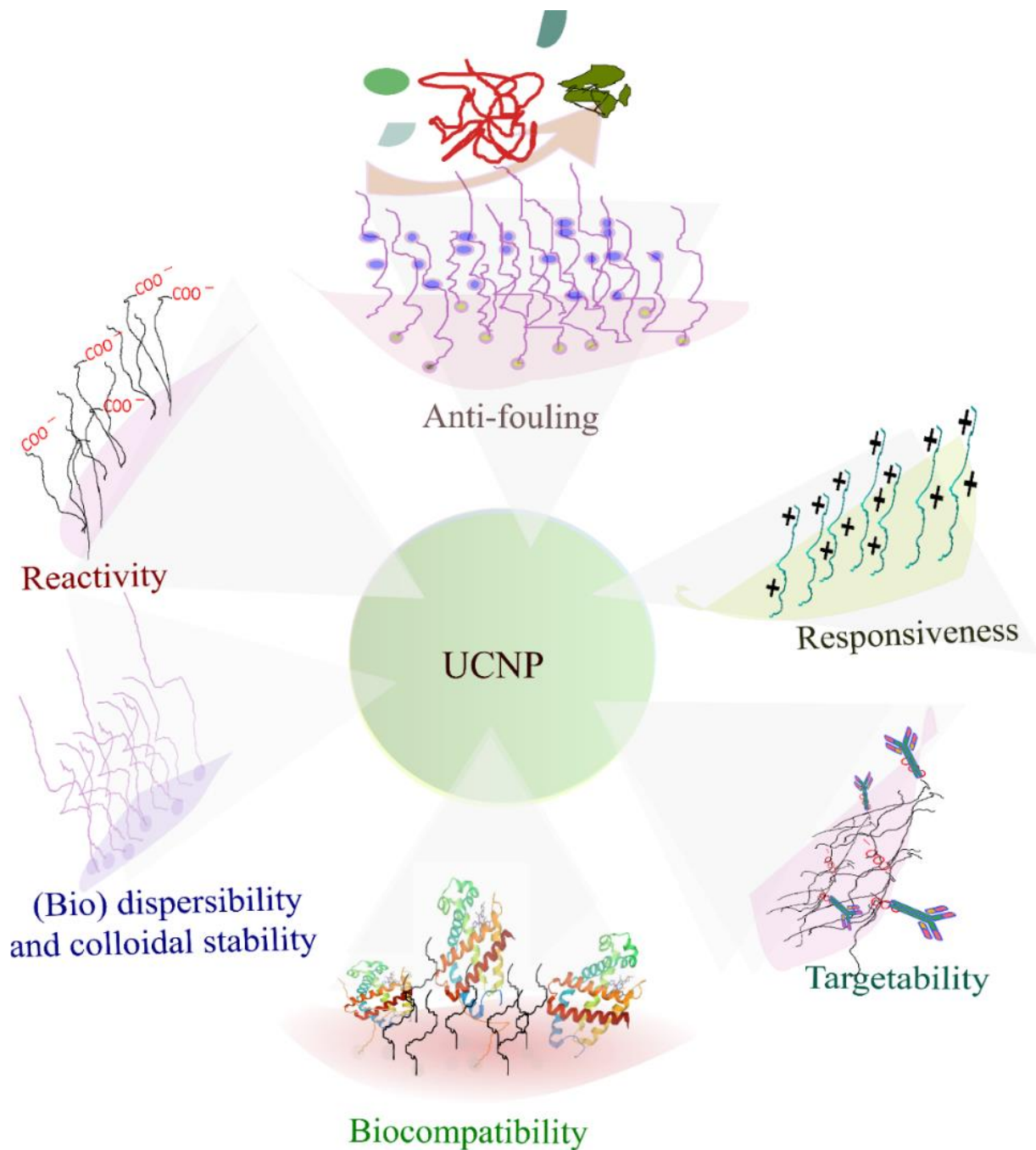


Figure 23 Schematic representation of UCNPs surfaces optimization opportunities performance through polymer grafting.

The as-synthesized oleate-capped UCNP surfaces must be transformed into hydrophilic ones for nanomedicine uses. Since hydrophobic surfaces are not dispersible in aqueous media, and are highly susceptible to non-specific adsorption, UCNPs hydrophilic surface transformation is a mandatory task.<sup>4</sup> The post-synthesis UCNPs surface modification is the typical approach to

transform the inherent hydrophobic surfaces into a hydrophilic phase. Surface modification of UCNPs surface modification using pre-designed copolymers allows for introducing desired surface physicochemical properties. Consequently, the surface-grafted polymer improves the nanoparticles' targeting ability, cellular internalization, bio-distribution, and colloidal stability.<sup>175</sup>  
<sup>176</sup> Albanese et al. describe how the nanoparticle development progressively evolved, as represented in Figure 24.

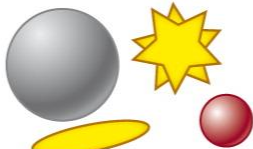
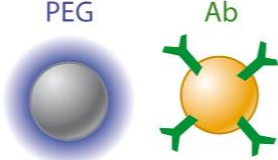
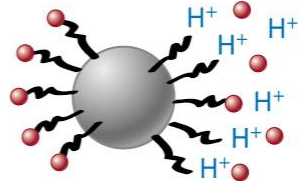
	<b>1<sup>st</sup> generation</b>	<b>2<sup>nd</sup> generation</b>	<b>3<sup>rd</sup> generation</b>
			
<b>Nano-materials</b>	<ul style="list-style-type: none"> <li>• Material design</li> <li>• Water solubility</li> <li>• Biocompatibility</li> </ul>	<ul style="list-style-type: none"> <li>• Maximize delivery</li> <li>• Stealth (passive)</li> <li>• Active targeting</li> </ul>	<ul style="list-style-type: none"> <li>• Environment-responsive</li> <li>• Dynamic properties</li> <li>• Biological or external cues</li> <li>• Theranostic abilities</li> </ul>
<b>Biological challenges</b>	<ul style="list-style-type: none"> <li>• Unstable</li> <li>• Removal by MPS</li> <li>• Poor tumor targeting</li> </ul>	<ul style="list-style-type: none"> <li>• Overreliance on EPR effect</li> <li>• No “universal” antigen</li> <li>• Active targeting is disappointing</li> <li>• &lt;10% dose in tumor</li> </ul>	<ul style="list-style-type: none"> <li>• To be determined</li> </ul>

Figure 24 The progressive development in nanomaterials design and challenges faced in their biological applications. Reproduced with permission<sup>177</sup> © 2012 by Annual Reviews.

In Figure 24, according to Albanese et al., the nonmaterial development stages are categorized into three generations. The first-generation nanoparticle development was intended to achieve improved water dispersibility and biocompatibility. However, the particles efficiency in tumor maintaining colloidal stability and targetability remain sign challenging. In the design of the second-generation nanoparticles, hydrophilic surface coatings using amphiphilic polymers like PEG were implemented to assure stability and enhance delivery. The active targetability of nanoparticles was planned to be addressed using an antibody to target specific receptor antigens. An efficient accumulation of nanoparticles in the tumor is necessary to deliver therapeutics and imaging agents. The observed biological challenge with the second-generation nanoparticles was the overreliance on enhanced permeation and retention.

The third-generation nanoparticle design is intended to develop responsive properties. Responsive surfaces are ideal for overcoming entrapments of particulates inside the tumor. Responsive nanoparticle surfaces produced using a well-designed surface polymer are promising to overcome sustained challenges in nanoparticle-based nanomedicine. Responsive surfaces developed by attaching zwitterionic polymers have a strong capacity to overcome nano-bio interactions. The third-generation nanoparticles design still requires further improvements. The post-synthesis nanoparticles surface chemistry optimization enables multiple advantages in developing functional nanoparticles.<sup>177</sup> The functionality of surface-attached polymer has determinant roles in maintaining stability, biocompatibility, and reactivity.<sup>178, 179</sup>

The surface ligand exchange technique is a common approach in the surface modification of UCNPs.<sup>10, 180, 181</sup> In direct ligand exchange, the oleate is replaced with suitable (co)polymers derivatized with a strong anchoring ligand. The newly introduced surface groups produce particles with improved colloidal stability, hydrophilicity, reactivity, and functionality. The preferential interaction of the charged particle surface between a strong nucleophilic ligand and the positively charged nanoparticle surface with electron-rich groups allows for adequate ligand exchange. Polymers connected with multivalent inorganic ligands with  $\text{COO}^-$ ,  $\text{N}$ ,  $\text{PO}_4^{3-}$ , or  $\text{SO}_3^{2-}$  tend to coordinate with positively charged nanocrystal surfaces.<sup>130</sup> The major drawback of the ligand exchange technique is the absence of complete replacement due to steric hindrance and the gradual release of residual oleate ligands.<sup>182</sup>

The nanoparticle's inherent surface charge determines the type of interactions and ligand anchoring efficiency.<sup>78</sup> The effectiveness and strength of the ligand exchange process depend on the electron donation capacity of new ligand moieties to the positively charged nanoparticle surface.<sup>168</sup> The size and architecture of the polymer in use determine the extent of ligand exchange. Polymers with phosphate anchoring moiety have recently been widely investigated to replace the oleic acid from UCNPs surfaces.<sup>204</sup> The oxygen in phosphate ligand forms a dative covalent bonding with UCNPs surface residing lanthanide cations.<sup>37, 183</sup> The carboxylate ligand leaves the UCNPs surfaces due to the nucleophilic dominancy of phosphate ions. Duong et al. investigated different copolymers made with carboxylate, sulphonate, and phosphonate anchoring ligands in UCNPs surface modification.<sup>146</sup> The study shows phosphate ligand anchored UCNPs gained better stability than carboxylate and sulphonate-stabilized ones.<sup>178, 179</sup> According to the Hlavec et al., the effect of

the number of phosphate groups per ligand has been studied. In that study, the effect of mono, di-, and tetra-phosphate functionality containing copolymers were investigated to stabilize the UCNPs. UCNPs coordinated with strong anchoring tetra phosphonate functionalized PEG exhibit high stability.<sup>146</sup> The tetraphosphate-anchored UCNPs prevent aggregation in buffer and high pH conditions.<sup>146</sup> The efficient replacement of the oleate ligand minimizes the gradual release of residual oleate ligand upon exposure to different media.<sup>184</sup>

The attachment of ligands to nanoparticle surfaces is governed by the hard-soft acid-base (HSAB) theory.<sup>122, 185</sup> According to Pearson, R. G.<sup>185</sup>, hard acids are cations that strongly interact with strong bases like  $R-CO_2^-$ ,  $R-PO(OH)O^-$ , and  $R-NH_2$ . The stability of polymer-grafted nanoparticles arises from electrostatic repulsion between surface-grafted chains and the steric effect of surface-attached polymer brushes. Anchoring moieties of the polymer could be phosphate and carboxylate functionalities. The high affinity of the electron-rich ligands towards the positively charged nanoparticles' surfaces helps to tether them strongly.

### 2.3 Polymers in surface modification of UCNPs

These days, polymers are playing vital roles in humans' day-to-day life, including advanced biomaterials applications.<sup>186</sup> Since Hermann Staudinger reported it in 1920 for the first time, these days, multiple advanced polymer synthesis techniques have flourished.<sup>186</sup> Among the numerous advanced polymerization techniques, living polymerization, including controlled radical polymerization (CRP), is very convenient for developing polymers with innovative functionalities.<sup>186</sup> A high-precision polymer could be developed at a level where single monomer unit insertion is made possible. Thus, polymers with sophisticated architectures and physicochemical properties could be effectively developed to meet current and future materials demands. The adaptability of polymers has many potential advantages in integrating them into nanoparticle surfaces. In Figure 25, comprehensive information on the merits of RAFT polymers and their suitability for developing nanomaterials is pictorially organized.



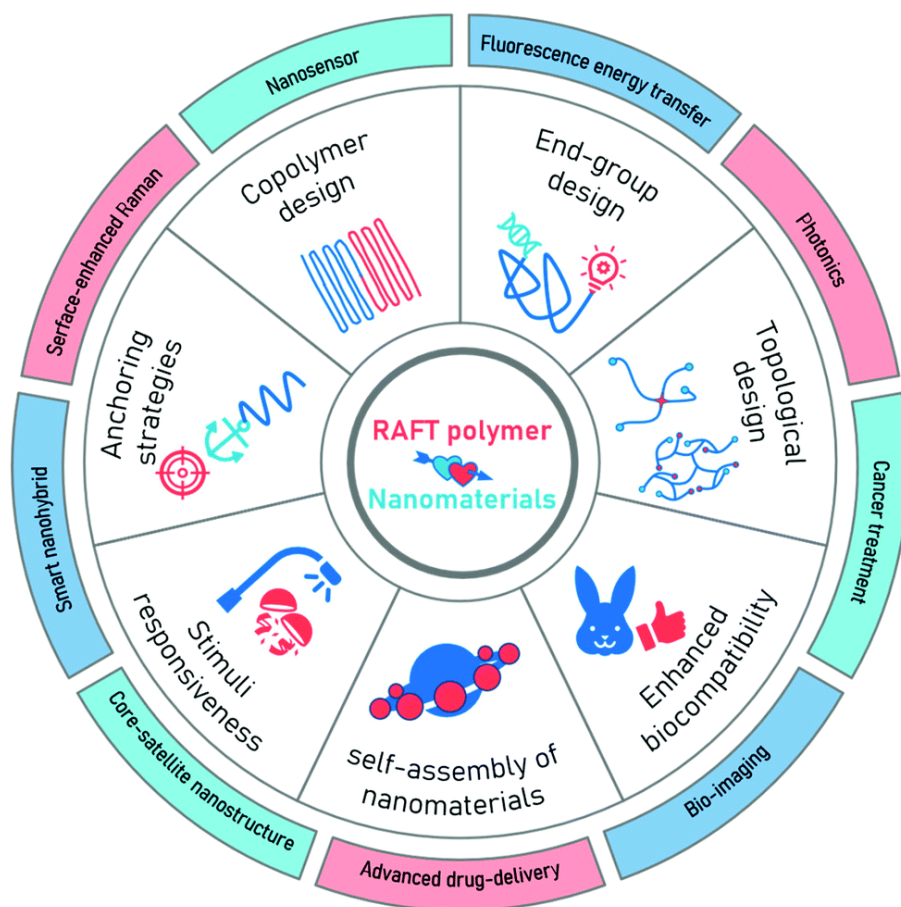


Figure 25 Pictorial representation of the potential advantages of RAFT polymers in nanoparticle hybrids development. Reproduced with permission<sup>187</sup> © 2021 The Royal Society of Chemistry.

#### 2.4.1 RDRP in the synthesis of copolymers

The advent of controlled living radical polymerization significantly reshaped polymer chemistry and materials science.<sup>188</sup> It empowered polymer chemists with the ability to design and develop application-oriented polymers. Controlled radical polymerization has an immense contribution to developing surface-modifying polymers.<sup>189</sup> A precise development of polymers is a crucial prerequisite in fabricating complex polymer-nanoparticle hybrids. RDRP is an efficient living polymerization technique to prepare polymers with high molecular weight control. Living polymer-based nanoparticle surface modification generates an optimized physicochemical property. The chain interrupting possibilities like termination and chain transfers should be negligible to obtain a living polymer.<sup>190</sup> The tailor-made polymers allow for the incorporation of numerous surface functionalities simultaneously. Figure 26 is a schematic illustration of living



polymerization in RDRP which is adopted from Moad et al. that depicts the monomer addition and subsequent activation and deactivation process.

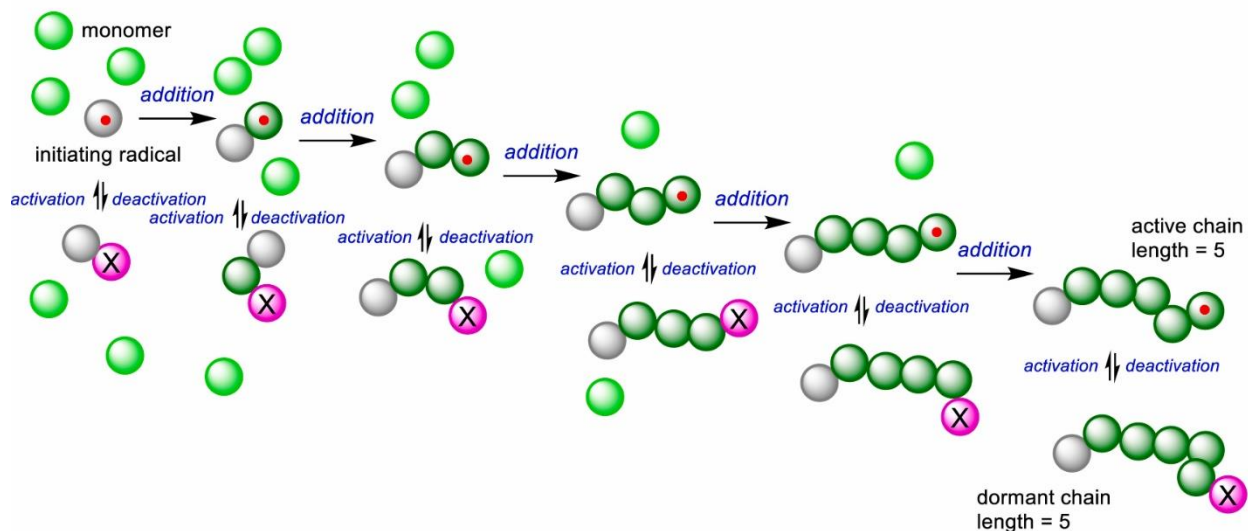


Figure 26 Schematic illustration of RDRP in controlled polymerization. Reproduced from Moad et al.<sup>82</sup>

RDRP is the most widely implemented technique in developing diverse modifying polymers.<sup>187</sup> Polymers with high precision in molecular weight and complex macromolecular architecture using the RDRP.<sup>187, 189, 191</sup> The RDRP techniques, like RAFT/MADIX, ATRP, and NMP, greatly revolutionized the current polymerization approaches.<sup>192-194</sup> RDRP allows the incorporation of desired functionalities like biocompatibility, dispersibility, and bio-stability from a single polymer chain.<sup>195, 196</sup> The sequential insertion of monomers in RDRP reduces chain termination and helps to maintain their livingness.<sup>82</sup>

➤ RAFT polymers for UCNPs surface modification

RAFT polymerization is a well-established method for developing polymers with living characteristics.<sup>197-199</sup> It operates in various reaction conditions to polymerize desired monomers.<sup>200</sup> The RAFT technique enables reasonable control of molecular weight and dispersity.<sup>198</sup> The high tolerance of different monomer functionality and sequential incorporation of precisely known end-groups are advantages of RAFT polymerization.<sup>82</sup> RAFT polymers are ideal for modulating the biocompatibility, specificity, and bio-stability of nanoparticles from their surface modification.<sup>187, 195, 201</sup> RAFT technique is efficient in developing copolymers with controlled block size and

functionalities in a single chain.<sup>202, 203</sup> RAFT copolymers could be made from immiscible blocks of polymers that are covalently connected end-to-end.<sup>204</sup> A high degree of monomer insertion and sequence control with narrow dispersity in the presence of oxygen and at room temperature conditions is made possible with the recent RAFT synthesis techniques.<sup>205, 206</sup>

These days, multiple specific and tailorable RAFT polymerization techniques have emerged.<sup>194, 207</sup> RAFT polymerization is continually evolving, and novel techniques like photo energy transfer (PET)-, enzyme facilitated- and electro-RAFT polymerization techniques are widely used in developing polymers with desired functionality and molecular weight.<sup>193</sup> The novel RAFT techniques do not require an exogenous thermal initiator to start polymerization. Selective photo-activation through modifying R-group of RAFT agents is widely investigated in the novel RAFT techniques. The tricarbonylthio RAFT agent has unique advantages in mediating degenerate chain transfer with the novel RAFT techniques. Mitchell et al. describe in-depth the novel RAFT techniques.<sup>208</sup> The novel RAFT techniques have emerged with new opportunities, like mild conditions-based polymer synthesis and spatiotemporal control of polymer architecture.<sup>209</sup> PET, for example, is an oxygen-tolerant visible light-catalyzed polymerization.<sup>209, 210</sup> A high degree of monomer insertion sequence control with narrow dispersity in the aqueous system, and in the presence of oxygen and room temperature conditions, is made possible.<sup>205, 206</sup>

#### ➤ Elements of RAFT polymerization

Conventional RAFT polymerization has three main elements: a monomer, a chain transfer agent, and a radical initiator.<sup>173</sup> Monomers with pendant vinyl functionality are suitable for RAFT polymerization. According to their activities towards RAFT agents, monomers could be grouped into two main categories: more activated monomers (MAMs) and less activated monomers (LAMs)<sup>211</sup>. MAMs are monomers with a double bond in conjugation with the vinyl group. In LAMs, the vinyl group is adjacent to heteroatoms, such as oxygen, nitrogen, halogen, or saturated carbons, like in vinyl acetate, N-vinylpyrrolidone, vinyl chloride, and 1-alkenes.<sup>212</sup>

RAFT technique has broader monomer scope. RAFT-based polymerization exhibits a high tolerance for impurities, except for monomers containing highly reactive groups like primary and secondary amines.<sup>213</sup> Monomers containing reactive groups, such as carboxylic or amine functionality, could be designed specifically for biological applications.<sup>199</sup> Monomers with ionic

functionalities, like carboxylic groups, and charged groups, such as zwitterionic functionalities, have received broad interest for nanoparticle surface modification. Monomers can be classified based on their functionalities as (meth) acrylates, (meth) acrylamides, vinyl, and styrene monomers, as seen in table 1.

Table 1 Common monomers used in RAFT polymerization and their reactivity<sup>199</sup>

Monomer and derivatives	MAMs	LAMs
(Meth) Acrylates	X	
(Meth) Acrylamides	X	
Vinyl acetate		X
Styrene	X	

Chain transfer agents (RAFT agents or Xanthate) are essential for RAFT polymerization. The RAFT agent is a molecule consisting of three major chemical groups: radical sensitive or reactive sites called thiocarbonyl, or xanthate, connected with two peripheral groups called the Z- and R-groups. The C=S bond is reactive towards electrophilic, nucleophilic, and radicals.<sup>211</sup> The thiocarbonyl group is a versatile reagent in controlling polymerization. The RAFT agent interacts with the exogenous radical initiator or undergoes self-initiation through the C=S radical susceptible site.<sup>214</sup> The compatibility of the RAFT agent to the specific monomer in use is an essential factor for the effectiveness of polymerization. An appropriate RAFT agent choice helps to achieve good monomer conversion and a low degree of dispersity.<sup>197, 215, 197</sup> The R- and Z-groups control the RAFT polymerization.<sup>81, 194, 211</sup> The reactivity of the C=S depends on the Z-group.<sup>200</sup> The Z-group helps facilitate the radical addition by maintaining and stabilizing the intermediate radical. RAFT agents having a Z-group made from S-alkyl and phenyl groups are suitable for stabilizing MAMs. Tri-thiocarbonates and di-thiobenzoates, for instance, are convenient for controlling MAMs. The xanthate RAFT agents containing O-alkyl or N-alkyl Z-group are good enough to prevent LAMs polymerization. The R- group is a good leaving group, facilitating the polymerization initiation through radical cleavage. The R-group is responsible for controlling the sequential addition of monomers during polymerization.

Several RAFT agents are commercially available to choose the compatible one for the interest monomer.<sup>211</sup> The common chain transfer agents are the thiocarbonyl, di-thiocarbamates, and

xanthate RAFT agents. The thiocarbonyl RAFT agents could be either di-thioesters or tri-thiocarbonates. The di-thioester RAFT agents are known for their capacity to control MAMs. However, the possible conditions like unwanted side reactions, retardation in monosubstituted MAMs, and complete suppression of LAMs are significant challenges in using di-thioester RAFT agents.<sup>212</sup> The tri-thiocarbonates are the most versatile RAFT agents with reasonable polymerization control, especially for MAMs with a tertiary R-group. The di-thiocarbamates and Xanthate RAFT agents show reasonable control over LAMs; however, they are good with MAMs.<sup>212</sup> In Figure 27, selected representative RAFT agents are presented.<sup>215, 216</sup>

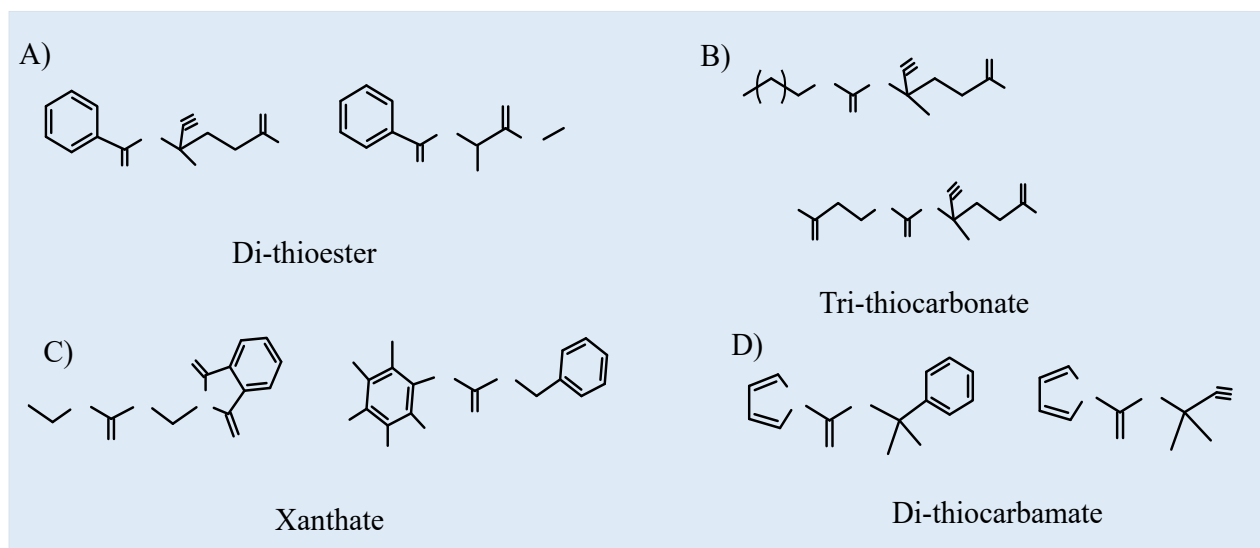
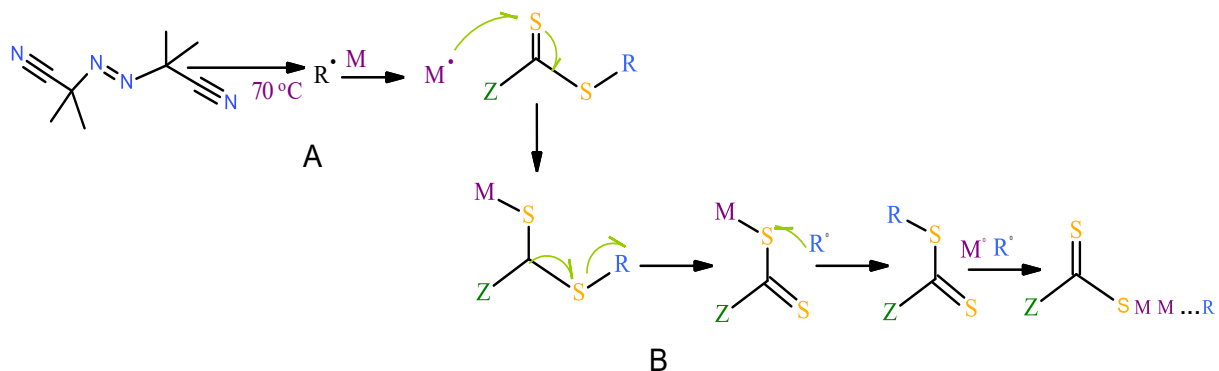


Figure 27 Representative RAFT agent types for the synthesis of block copolymers.

The radical generation approach in RAFT polymerization has its effects. The polymerization rate is dependent on the number of radicals generated. The initiator-derived radicals trigger polymerization through a subsequent monomer radical attack. In RAFT polymerization, the radical initiation could be done through thermal, chemical, or photochemical processes. The thermal technique requires exogenous reagents as a radical source, whereas the photopolymerization is done by initiating radicals from the RAFT agent. A thermally activated exogenous reagent is required in the conventional RAFT polymerization. The typical exogenous thermal initiators are diazo compounds like AIBN, and peroxides, for instance, benzoyl peroxide. The first stage of RAFT polymerization involves two radical initiation steps: initiator radical homolytic splitting and then followed by the formation of monomer radical.<sup>190</sup> The reversible addition-fragmentation

capability of the chain transfer agent facilitates the monomers' addition in the subsequent polymerizations and dispersity control. The radical initiation and polymerization processes are represented in Scheme 1.<sup>211</sup>



Scheme 1 Schematic representation of AIBN during radical generation and monomer insertion (A) and reversible addition-fragmentation chain transfer and propagation (B): where M stands for monomer and R stands for radical.

The photopolymerization could be initiated using visible light as a triggering agent. Endogenous photo initiation is the best alternative to conventional thermal initiation because it helps to avoid impurities associated with the use of an exogenous radical initiator.<sup>217</sup> Photopolymerization could be done using direct or indirect activations. Direct photo-activation requires a tricarbonylthio RAFT agent to initiate the polymerization. The endogenous radical initiation avoids contamination arising from using exogenous initiators. The tricarbonylthio-based chain transfer, RAFT polymerization, could be performed through direct and indirect photoactivation. The tricarbonylthio functionality also serves in the indirect redox catalyst-based photoinduced electron/energy transfer PET-RAFT polymerization.<sup>218</sup> Direct photoactivated polymerization is also known as a photo-inverter. The R-group substituents of the RAFT agent define the light wavelength used for polymerization. Direct photoactivation could be performed through blue light excitation of the 'C=S' double-bond electrons. The rate of polymerization could be regulated by controlling the intensity of light. An increase in the intensity of the blue light results in an increased polymerization rate. The selectivity of the catalyst in PET-RAFT was also investigated for polymerization using dithiobenzoate RAFT agents.<sup>208</sup>

In RAFT block copolymer synthesis, the sequence in monomer addition significantly affects the polymerization process and physicochemical properties. A change in connectivity and sequence

of monomer addition leads to polymer structural change and final properties of the polymer.<sup>219</sup> The change in molecular weight of the R-group, due to the newly inserted polymer chains, strongly affects the polymerization process. The monomer reactivity has a significant effect on the controllability of the polymerization. In the synthesis of copolymers of MAMs with LAMs, the MAMs should be polymerized at first. The macro-RAFT polymers of LAMs have a poor leaving tendency, and retardation of polymerization occurs. Figure 28 shows the compatibility of different monomers with the RAFT agent's Z- and R- groups.

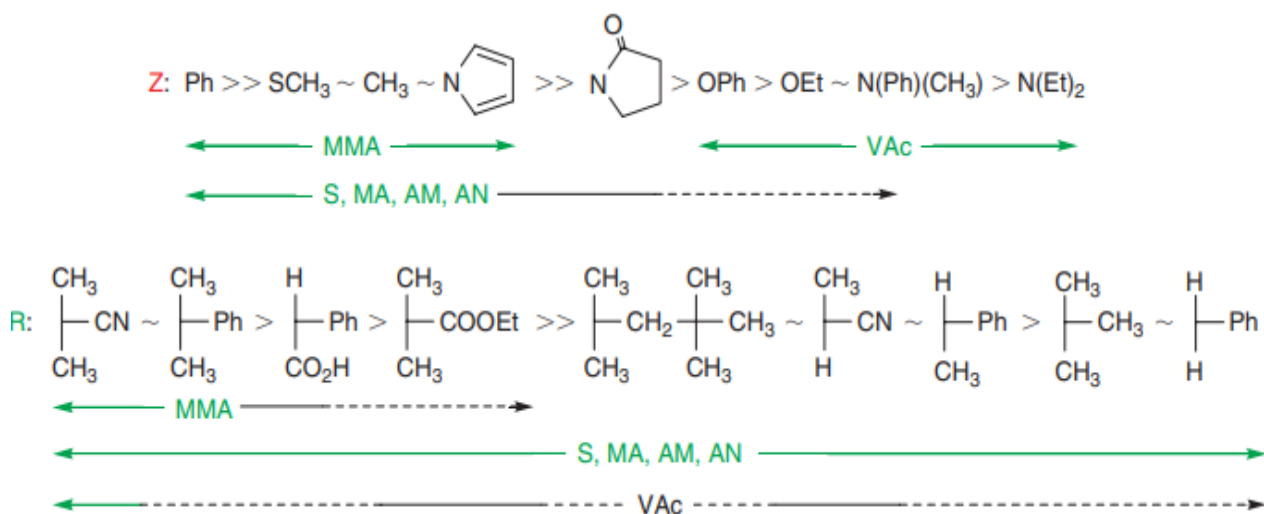


Figure 28 Effect and compatibility of the Z- and R- groups of RAFT agents with different monomer types. Reproduced with permission<sup>220</sup> © 2006 CSIRO.

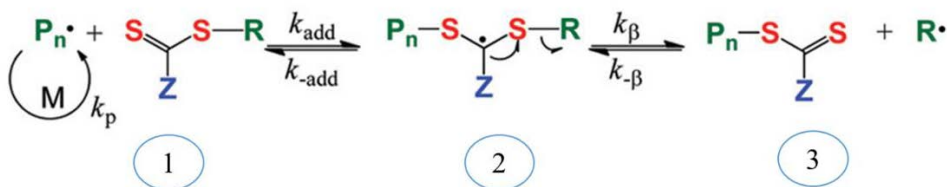
➤ The mechanisms of RAFT polymerization

The progression of RAFT polymerization relies on the equilibration rate between active and dormant chains. The reversible deactivation and degenerative chain transfer have two possible equilibrium mechanisms. At the start of RAFT polymerization, a macro-RAFT polymer is formed by inserting monomers. As shown in Scheme 2, a pre-equilibration occurs between the macro-RAFT and the RAFT agent, as sketched in **1**. The second equilibration occurs at **2**, associated with fragmentation of the macro-RAFT to adducts, and the rate constants are designated by  $k_{\beta}$  and  $k_{-\beta}$ . The overall equilibrium of radical initiation is defined in equation 5.

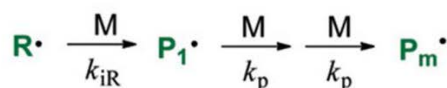
$$K_{eq} = k_{ad} / k_{\beta} \dots \dots \dots (5)$$

At **3**, the R-group could take different reaction pathways in further steps. For instance, it undergoes the monomer, macro-RAFT, or it reacts further with the chain transfer agents.<sup>221</sup> Upon insertion of an additional monomer, the system equilibrates as a new, as represented at **4**.<sup>197</sup>

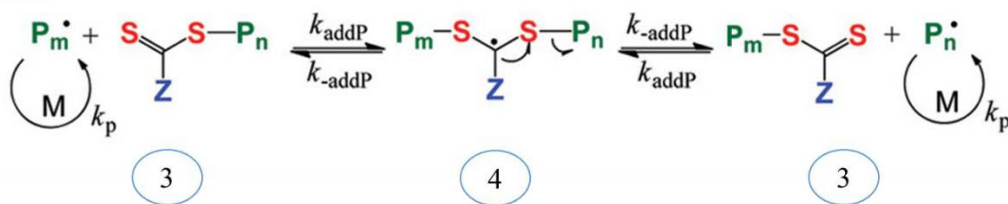
Initialization:



Reinitiation:



Main equilibrium:



Scheme 2 The mechanisms of RAFT polymerization that include the initiation, re-initiation, and polymerization equilibrations. Reproduced with permission<sup>197</sup> © 2012 American Chemical Society.

RAFT polymerization ( $R_p$ ) obeys first-order kinetics for monomers. The concentration of monomers remains constant throughout the reaction.  $R_p$  is dependent on the efficiency of polymerization initiation ( $f$ ), rate constants of initiation ( $k_{ad}$ ), propagation ( $k_p$ ), and termination ( $k_t$ ). At high reaction temperature or high initiator concentration, the polymerization progress faster; as a result, rapid, radical formation and chain termination occur, and lower molecular weight polymer is favoured.<sup>190</sup>

#### 2.4.2 Functionality and architecture of copolymers for UCNPs surface grafting

The RAFT technique offers multiple monomer options to develop functional polymers with desired composition and architecture.<sup>190, 214</sup> The functionalities of surface-modifying copolymers could be controlled from the monomer's functionality and the RAFT agent end groups. Post-

modification of RAFT polymer end groups gives additional options to introduce desired functionalities. The surface-attached polymer could produce different surface appearances, like a bush-like surface. Polymers tethered to nanoparticle surfaces at their one end produce brush-like surface architecture.<sup>188, 222</sup> Surface brush-like architecture has enormous potential in defending the particles from nonspecific binding.<sup>223</sup> The surface polymer structure dictates how proteins and other biological components interact with nanoparticle surfaces. A brush-like surface architecture of polymers helps nanoparticles to overcome the complex and dynamic interactions with the physiological microenvironment.<sup>222</sup> As represented in Figure 29, stimuli-responsive surfaces could be developed using polymers to develop nanoparticle surfaces for intracellular delivery and biosensor application.

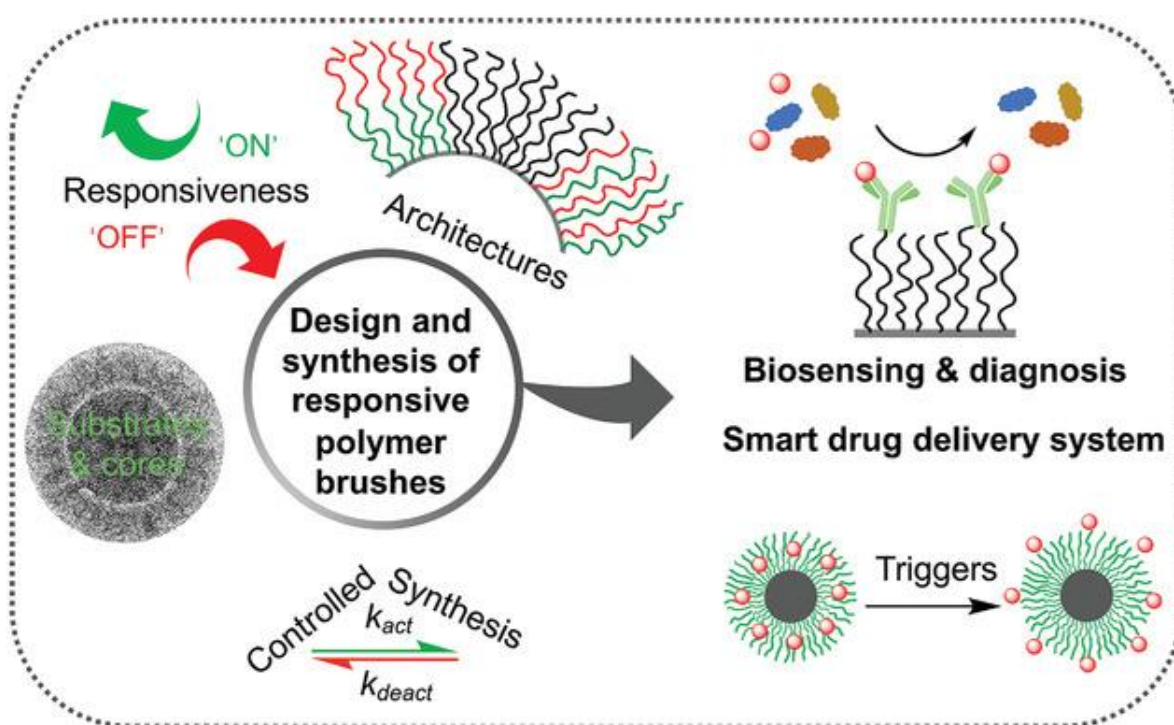


Figure 29 Pictorial representation of responsive surface. Reproduced with permission<sup>224</sup> © 2020 Wiley-VCH.

Stimuli-responsive or smart surfaces have drawn considerable interest in wide biomedical applications, such as biosensing.<sup>189</sup> Surface responsiveness is the most desired property for intracellular applications of nanoparticles.<sup>224</sup> The responsiveness of surface polymers arises from their sensitivity to changes in the physical and chemical environment like light, thermal, and pH.<sup>225</sup> Responsive surfaces help mitigate the nano-bio interface challenges of UCNPs during their



intracellular applications.<sup>224</sup> Incorporating synthetic or natural responsive ligands into polymer chains during synthesis or post-modification techniques helps develop responsiveness.<sup>226</sup> Nanoparticles with responsive surfaces act as nanorobots and can circulate in the biological environment effectively.<sup>227</sup>

Amphiphilic polymers are good mediators to get a homogeneous mixture in immiscible liquids.<sup>228</sup> <sup>229</sup> PEG is a well-known amphiphilic polymer in diverse applications like cosmetics, pharmaceuticals, and nanomedicine.<sup>37, 76, 224</sup> The copolymers of PEG and derivatives are well-known in different biomedical applications.<sup>7</sup> PEG has been known since the 1970s<sup>116, 230-232</sup>, and it has played a prominent role in the surface modification of nanoparticles.<sup>233</sup> To enhance amphiphilicity and stability of nanoparticles, copolymers of PEG are widely investigated in UCNPs surface modification.<sup>116, 230-232</sup> <sup>204</sup> PEG-modified nanoparticles get prolonged stability because surface-induced steric repulsion and hydration layer formation from ether groups, respectively.<sup>234, 235</sup> The PEG-modified surfaces are also proven to have the potential to develop anti-fouling properties.<sup>231, 236, 237</sup>

The stimuli-responsive ligands introduce additional advantages to nanoparticle surfaces.<sup>190, 238</sup> A slight change in a chemical or physical conditions induces surface polymer's structural conformation or chemical alteration.<sup>239</sup> The implementation of pH-responsive polymers in surface modification of UCNPs, for instance, helps to overcome endosomal traps during intracellular delivery of UCNPs.<sup>224, 240</sup> The antifouling surfaces produced from PEG and MPC-based polymers have a strong capacity to resist protein fouling challenges through hydration layer formation. Figure 30 illustrates how the PEG-based copolymers grafted surfaces defend the nanoparticles from undesired protein adsorption through a hydration layer formation.

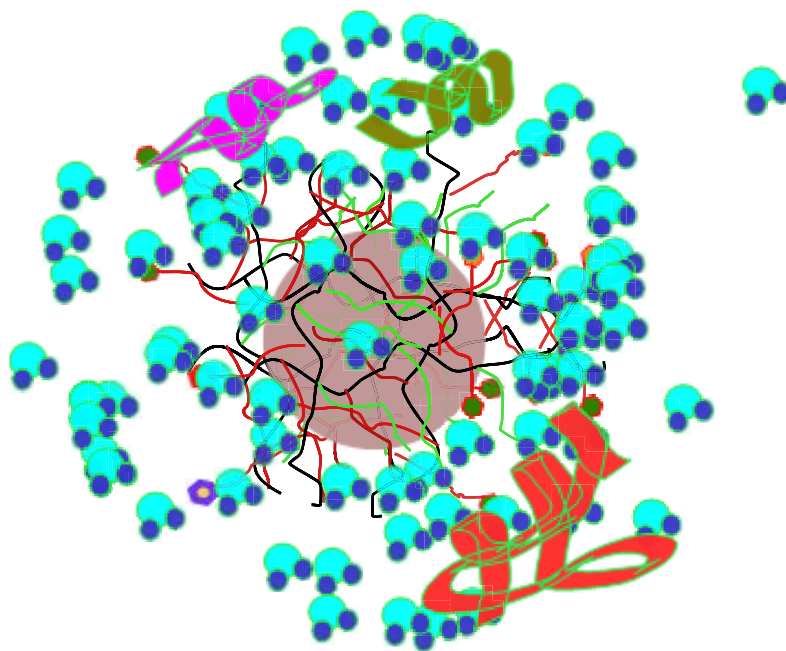


Figure 30 Schematic illustration of surface hydration layer produced by amphiphilic coated surfaces in defending the nanoparticle from protein fouling.

The antifouling property of PEG is due to the development of a short-range surface hydration layer at its partially charged ether functionality.<sup>241, 242</sup> Figure 32 shows how the PEG-based copolymer defends the surfaces of the nanoparticles from undesired protein adsorption by developing a hydration layer. The covalent attachment of PEG to proteins and peptides, PEGylation, has significantly enhanced the biomedical roles of PEG.<sup>229, 243, 244</sup> The hydrophobic parts of PEG, such as the ether methylene (-O-CH<sub>2</sub>CH<sub>2</sub>-) and methoxy (-O-CH<sub>3</sub>) terminals induces nonspecific interactions and immune responses.<sup>242</sup> Previous reports indicate PEG exhibits some drawbacks like improper metabolism, cytotoxicity, low bioactivity, and instability in an ionic environment.<sup>229, 231, 245, 246</sup> Alternative polymers such as zwitterionic ligands are investigated to substitute PEG in nanoparticle surface modification.<sup>39, 232, 245, 247, 248</sup>

#### ➤ Polyzwitterionic ligands for antifouling surfaces

Zwitterionic polymers are ionic amphiphiles with an equal number of anions and cations, leading to an overall neutral net charge. The oppositely charged groups in zwitterionic polymers induce a high dipole moment change. Zwitterionic ligands behave differently due to their high dipole moments than other ionic polymers.<sup>246, 249</sup> As shown in Figure 31, surfaces modified with zwitterionic ligand polymer like 2-(methacryloyloxy)ethyl phosphorylcholine (MPC) strongly

binds water away from the polymer backbone.<sup>250</sup> The surface hydration layer protects adsorption proteins and other biological particles like microbes on nanoparticle surfaces.<sup>246, 251, 252, 235</sup>

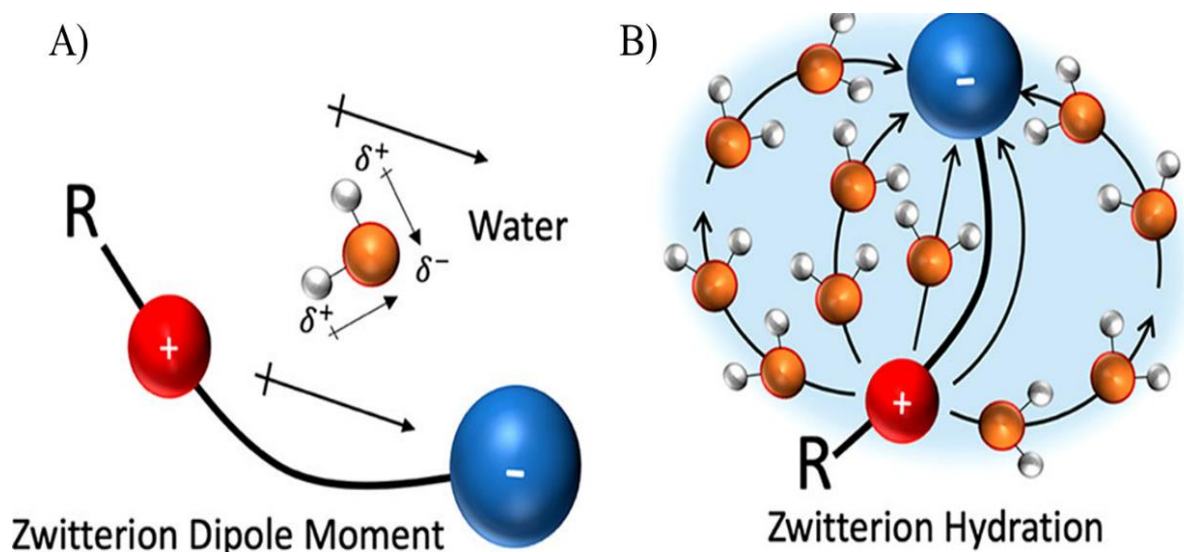


Figure 31 Representation of dipole moment orientation in the polymer chains (A) and hydration layer formation in zwitterionic surfaces (B). Reproduced with permission<sup>250</sup> © 2020 American Chemical Society.

The ionic solvation layer produced by zwitterionic ligands induces a relatively high surface energy compared to hydrogen bonding forces demonstrated by hydrophilic polymers.<sup>248</sup> The balanced surface charges in zwitterionic polymers help to generate a desirable physicochemical property. Surface hydration forces induced by interactions of water molecules help produce good colloidal dispersion.<sup>253</sup> The zwitterionic modified nanoparticles, as a result, gain improved stability in extended pH range and salt solution and exhibit low nonspecific interaction.<sup>254</sup>

Biofouling remains a significant challenge in implementing colloidal nanoparticles in nanomedicine. The deposition of biological components to the surface of nanoparticles significantly alters their biological identity. The surface fouling phenomenon happens due to Van der Waals, electrostatic and hydrophobic interaction between the nanoparticle's surface and biological components in the physiological system.<sup>227</sup> Mammalian cells are known for their inherent capability in defending protein corona.<sup>4</sup> The cell membrane is efficient in protecting the cell surface from fouling. The mammalian cell membrane comprises lipids like phosphatidylcholine and phosphatidylserine containing zwitterionic polymers. Protein corona is one of the significant critical challenges in the intracellular application of nanoparticles. Non-

specific protein adsorptions remain a bottleneck in translating academic research to clinical application.<sup>255</sup> The undesired protein adsorption significantly affects the performance of synthetic biomaterials by altering nanoparticle size, shape, and surface charge.<sup>256, 257</sup>

The undesired adsorption of protein could be reduced by optimizing the nanoparticle's surfaces. For instance, mimicking nanoparticle surfaces using zwitterionic ligands is an ideal approach for developing antifouling surface properties. Human cells are protected from nonspecific protein adsorption with hair-like amphiphilic surface ligands.<sup>258</sup> Mimicking nanoparticles' surfaces' with a zwitterionic-based polymer like methyl acrylate phosphorylcholine (PC) enhances cellular uptake. The charged brush-like surface structure forms a layer of water that defends the nanoparticles from non-specific adsorption.<sup>233</sup> The presence of high osmotic pressure exerted among the opposite surface charges of the polymer chains induces strong nanoparticle stability. The brush-like zwitterionic moieties effectively prevent surface protein fouling and improve dispersibility in the hydrophobic environment.<sup>259,249</sup> Figure 32 depicts how protein corona affects the ligand-receptor interactions during intracellular delivery of nanoparticles.<sup>260</sup>

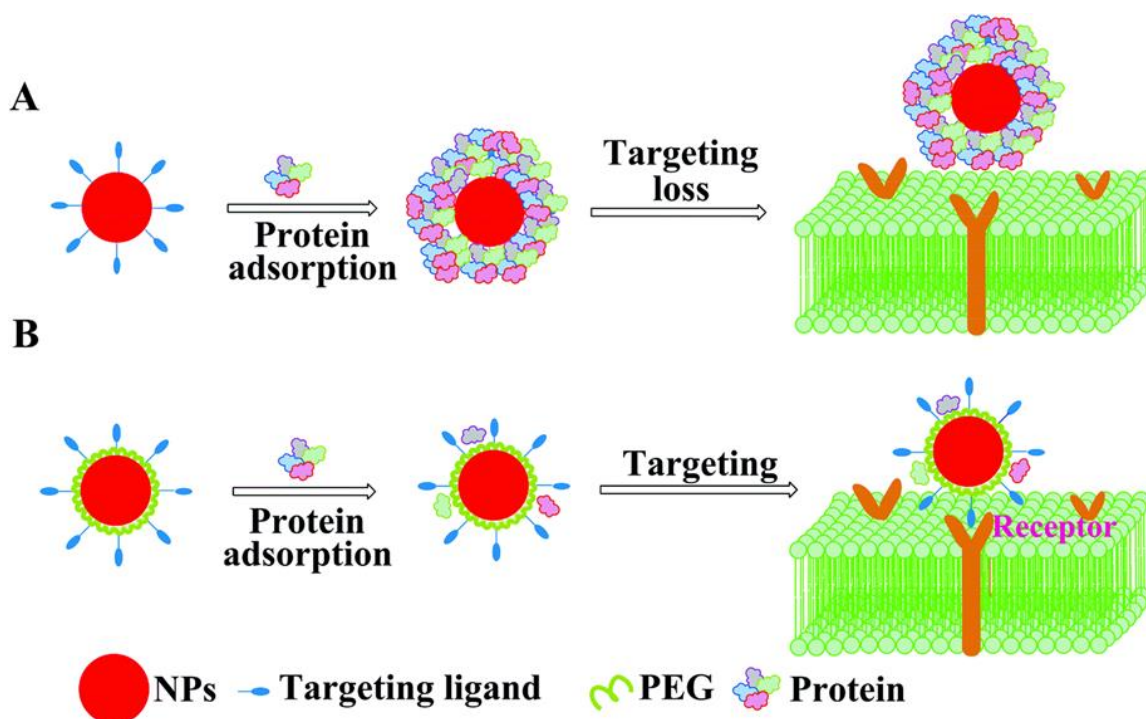


Figure 32 Representation of corona effect on nanoparticles targetability (A) without polymer surface graft and (B) with polymer grafting. Reproduced with permission<sup>260</sup> © 2017 The Royal Society of Chemistry.

### ➤ Nanohybrids from polymer-UCNPs combination

Polymers are sustained materials to alter the surfaces' of nanoparticles.<sup>180</sup> Polymers have gained strong attention in tailoring nanoparticles' surfaces because they provide unique adaptability.<sup>261</sup> The nanoparticle polymer-based surface modification helps the nanoparticles to fulfill sophisticated biomedical requirements.<sup>262</sup> The combination of the best properties from nanoparticles and polymers through surface integration is one of the potential approaches in advanced materials development.<sup>84</sup> A nanoparticle-polymer nanocomposite material could be developed from their physical interaction and the formation of primary or secondary bonds.<sup>84</sup> The polymer-based surface grafting of nanoparticles gives vast opportunities to impart desired functionality and improve colloidal stability.<sup>122, 263, 264</sup> The functionality of the polymers could be introduced during polymerization or through post-modification modification techniques.

Surface grafting nanoparticles using functional polymers is a fascinating approach to developing versatile biomedical characters.<sup>157, 222</sup> The polymer-grafted nanoparticle surfaces gain improved hydrophilicity and minimize protein corona.<sup>265</sup> Polymer-coated nanoparticles are known for improved colloidal stability, diminished self-aggregation, and surface oxidation.<sup>237</sup> Besides introducing multiple reactive and responsive sites, the surface tethered polymers protect the crystal surface from disintegration.<sup>169</sup> The achievement of coordination bonding between the surface-attached polymer moieties, such as phosphate groups and the nanoparticle surface cations, produces a stable composite. Polymers containing multiple end groups functionalities are preferable to attain improved chelation and to produce desired functionality, simultaneously. The stability of polymer-coated nanoparticles arises either from surface-induced electrostatic repulsion or due to steric interactions occurring at peripheral end groups.<sup>4</sup> Steric stabilization arising from extended polymer chains is also advantageous to induce colloidal stability.<sup>231</sup>

Polymer-based surface modification could be achieved by attaching small-molecule ligands and macromolecular polymers to nanoparticles. The small molecule ligands are known for their nanoparticle stabilization capability by forming a thin hydrodynamic layer.<sup>266</sup> However, the small molecule-modified surfaces gain minimal surface functionality since they were made from a single unit. Copolymer-based nanoparticle surface modification gives better advantages than small molecule surface modification.<sup>141, 180</sup> A well-designed copolymer helps to introduce multiple functionalities to the particle surfaces from a single polymer chain.<sup>122, 267</sup> Polymers consisting of

various units and functionalities are ideal for the surface modification of nanoparticles. The replacement of oleate ligands with polymers produces multifunctional surfaces, as schematically illustrated in Figure 33.

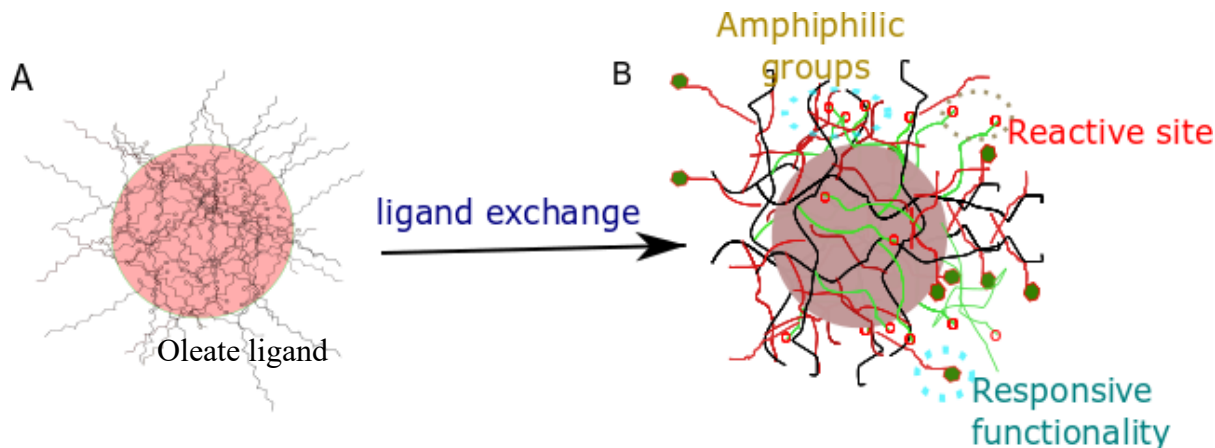


Figure 33 Schematic illustration of nanoparticle surfaces capped with oleate ligand (A), and grafted from multifunctional copolymer (B).

➤ The nano-bio interface interactions

The intracellular delivery of nanoparticles encounters positive and negative interactions in the physiological microenvironment. The surface functionalities of the nanoparticles determine the possible interactions with the biological system.<sup>268</sup> Normally, the surface chemistry of nanoparticles determines how the physiological system responds.<sup>269</sup> Surface chemical composition of the nanoparticles dictates the cellular uptake and endocytic release mechanisms.<sup>172, 270</sup> The amphiphilicity and biocompatibility of nanoparticles are some factors in defining nanoparticle-cell interactions. Since plasma proteins are negatively charged at pH 7.4, positively charged nanoparticles suffer from opposite charge interaction.<sup>255</sup> The affinity of proteins to the surface of nanoparticles is associated with surface physical forces like Van Der Waal interactions, hydrogen bonding, and hydrophilic interactions.<sup>236</sup>

An optimized UCNP surface development using polymers is a typical approach to address the nano-bio interface challenges.<sup>271</sup> Multifunctional surfaces help to mediate the interface interactions and strongly determine the performance of nanoparticles.<sup>20, 272-276</sup> The capability of the surface in defending protein adsorption depends on surface graft density. The surface graft density also determines the nanoparticles' in vivo performance. An optimal surface coverage helps to control

nanoparticles' cellular uptake, biodistribution, and targetability.<sup>277</sup> A report from a previous study shows how surface ligand density significantly affects the nanoparticles' performance.<sup>277, 278</sup> Figure 34 depicts how nanoparticles interact with cell membrane during cellular uptake.

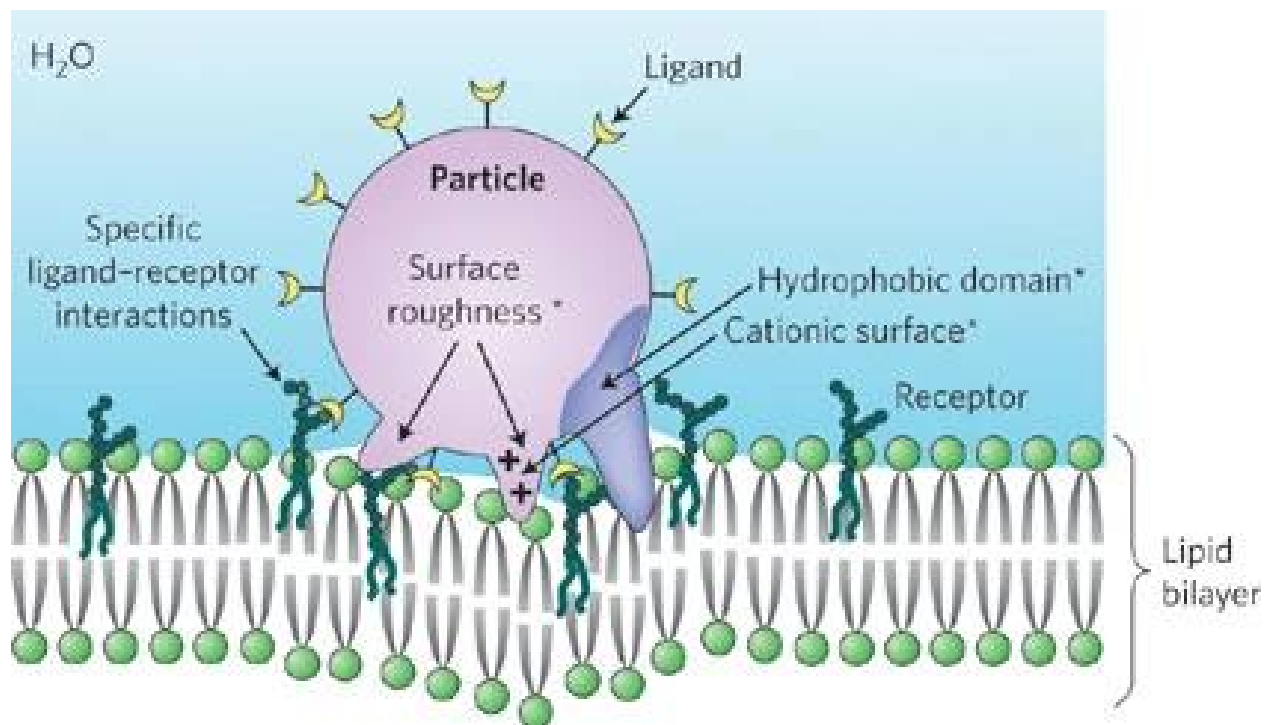


Figure 34 Pictorial representation of intracellular delivery of nanoparticles and possible nano-bio interactions during cellular uptake. Reproduced with permission<sup>269</sup> © 2009 Macmillan Publishers Limited.

Protein-mediated endocytosis during virus-cell invasion is an aspiring phenomenon in developing nanohybrids with mimicked surfaces.<sup>279</sup> The biofunctionalized nanoparticles have significant roles in the advancement of therapeutics and diagnostics.<sup>280</sup> The nanohybrids from combinations of upconversion nanoparticles, synthetic copolymers, and biomolecules are a potential approach to developing a high-performing biomaterial. Those nano-hybrid materials enable the production of desired combined physicochemical properties. Biologically tailored nanoparticles have vital roles in addressing complex health challenges like cancer.<sup>281, 282</sup>

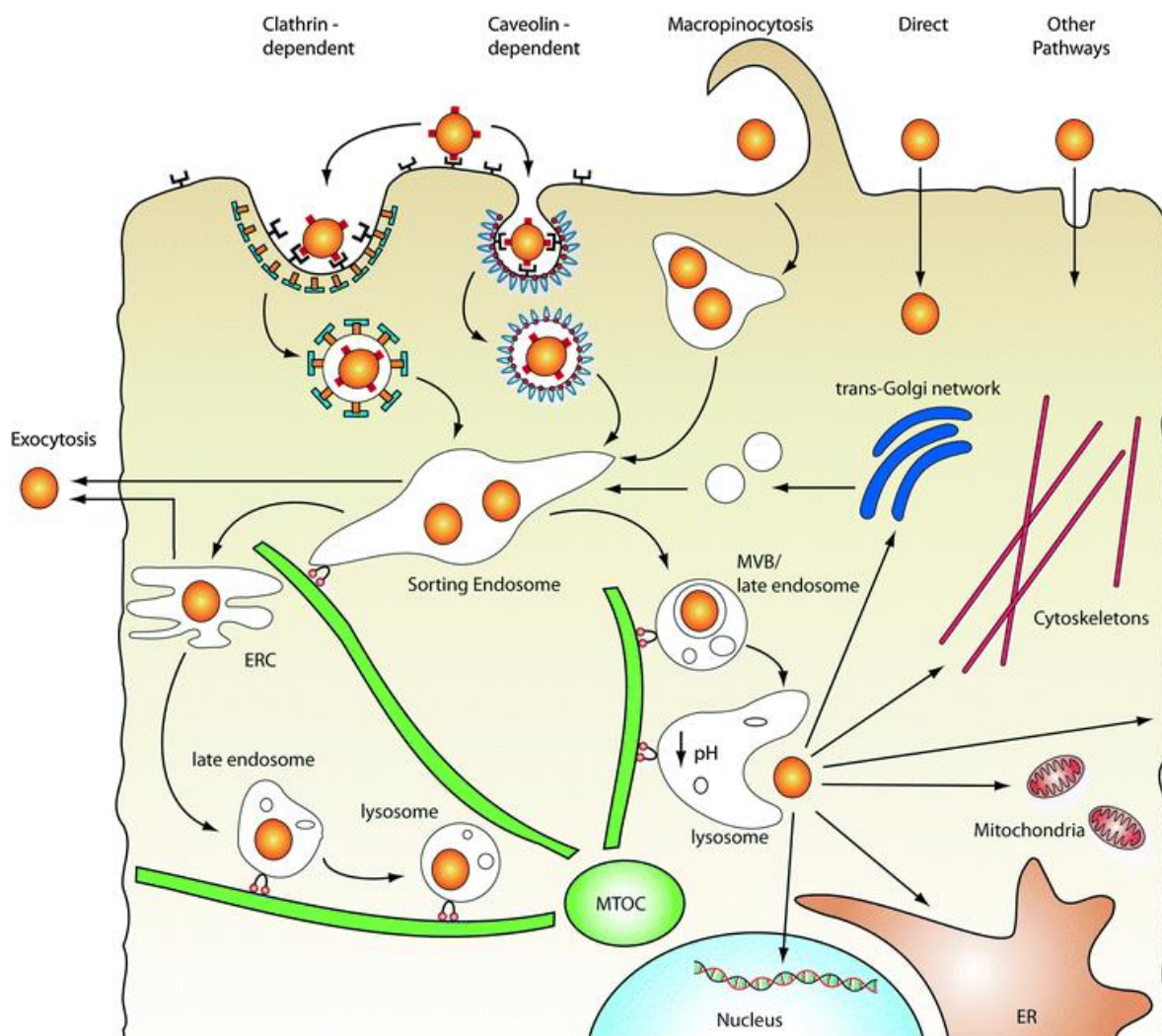
➤ Intracellular delivery and targeting of nanoparticles

The subcellular level structures and dynamics are a good source of information about the cell's condition. Since many diseases originate from the molecular level of the physiological systems<sup>283,</sup>

<sup>284</sup>, delivery of therapeutics and imaging agents enables to monitor and treat them effectively. Integrating biomolecules into nanoparticle surfaces is a powerful approach in various therapeutic and diagnostic agents.<sup>285-287</sup> The bio-integrated nanoparticles are helpful in the achievement of specific labeling. Biofunctionalized particles are widely used in developing responsive sensors, nanoscale carriers, and stimuli-reactive triggered deliveries.<sup>288, 289</sup> Nanoparticles integrated with proteins, cell-penetrating peptides, and antibodies have brought a paradigm shift in tumor diagnosis and targeted therapy.<sup>290</sup> Peptide-based organelle targeting has many advantages, such as single-molecule imaging and cell tracking.<sup>284</sup> Combining nano-sized biomolecules with their analogous synthetic metal nanoparticles provides good compatibility and minimizes interference.<sup>98</sup> However, achieving targeted delivery of nanoparticles to a specific intracellular location and the clinical transition of nanomedicine remains a significant challenge.<sup>171, 291, 292</sup>

Prediction of nanoparticles' behavior in the biological environment is essential to understand their bio-interactions.<sup>231</sup> The trajectory followed by the nanoparticle upon cellular uptake is sophisticated to control. Quantitative information on the endosomal release and the kinetics of delivered nanoparticles would benefit their clinical translation.<sup>293 294</sup> Biofunctionalization permits nanoparticles to overcome the nano-bio challenges.<sup>295, 296</sup> Nano-hybrids developed from synthetic nanoparticles and coupled with biomolecules help address gaps arising during separate uses of the individual materials. Surface integration of biorecognition molecules helps to introduce biocompatibility and target ability to the synthetic particles.<sup>297</sup> The mechanisms of intracellular delivery of nanoparticles has been given in Figure 35, which is adopted from Chou et al.





Abbreviations: ERC, endocytic recycling compartment; ER, endoplasmic reticulum; MTOC, microtubule-organizing centre; MVB, multivesicular bodies;

Figure 35 Pictorial illustration of mechanisms of cellular uptake and endosomal escape for antibody. Reproduced with permission<sup>293</sup> © 2011 The Royal Society of Chemistry.

Cell membrane access is required to successfully deliver and target therapeutic and imaging agents inside the cell.<sup>298</sup> Nanoparticles' cellular uptake and endosomal release could be altered by optimizing nanoparticle surfaces.<sup>268</sup> Surface functionalization helps to tune the nanoparticles' surface properties and cellular interaction.<sup>299</sup> The hydrophobic nature of the cell membrane hinders the entry of exogenous molecules into the cell.<sup>300</sup> The current nanotechnology approaches provide numerous potential solutions to target specific organelles such as mitochondria, nuclei, endoplasmic reticulum, and lysosome.<sup>283, 301</sup> The nanoparticles' endosomal escape mechanism is the other important aspect of intracellular delivery, which is not yet fully understood.<sup>302</sup> Endosomal

escape mechanism is speculated to occur in two possible ways. The first approach to the nanoparticle's cellular uptake is the interaction of Cell-penetrating peptides (CPPs) with the cell membrane, which induces a pH gradient. The second mechanism is expected from the interactions of positive charges of CPPs with the negatively charged cell membrane.<sup>294, 303, 304</sup>

➤ Introduction of biorecognition elements to UCNPs surfaces

Active targeting of nanoparticles to desired cellular or subcellular sites is a hot research topic in nanomedicine. Nanoparticles with specifically tailored surface features enable the targeted delivery of nanoparticles to the intended site.<sup>171</sup> Fine-tuning of nanoparticle-cell interactions helps optimization of cell membrane passage, possible subcellular interactions, and targetability.<sup>305, 306</sup> The advancements in polymer synthetic chemistry and subsequent bio-conjugation techniques give numerous advantages to modulate the physicochemical properties of synthetic materials.<sup>264</sup> Protein-polymer conjugation is widely practiced in therapeutic applications.<sup>307</sup> The challenges associated with the complex nanotechnology-biology interaction demand a clear understanding of possible responses from the physiological world.<sup>171</sup> Nanoparticle surface design for a specific targeting application requires proper identification of interest target antigen.<sup>308</sup>

Most current bio-analytical applications of nanoparticles require integrating them with bioactive molecules.<sup>309 330</sup> Nanoparticles off-target delivery and toxicity are primary concerns in their intracellular applications.<sup>285, 310</sup> Biofunctionalization has multiple advantages, such as binding and delivery of drug molecules, tumor targeting, labeling and tracking of cells, and bioanalysis.<sup>311</sup> The conventional therapeutic and diagnostic agents cannot penetrate cell membranes and require delivery assistance vectors, for instance, peptides.<sup>294</sup> Peptides are well-known for maintaining physiological processes such as signaling agents, activation of immune defense as antigens, and carrier or lytic agents across cellular and organelle membranes.<sup>312</sup>

Peptide-based nanomedicine formulations are emerging as potential diagnostic and therapeutic approaches.<sup>284 306</sup> Peptide-modified surfaces effectively facilitate cellular uptake and endosomal escape of nanoparticles during intracellular delivery.<sup>313</sup> The intrinsic cellular, subcellular, and intracellular roles of peptides make them ideal for guiding and targeting nanoparticles in intracellular specific sites.<sup>306, 314, 298</sup> The smaller size and suitable structural features of peptides make them preferable in nanoparticle functionalization compared to antibodies and proteins.<sup>315, 316</sup>

Cell-penetrating peptides (CPPs); for instance, have been known for their inherent cell membrane passage and intracellular delivery capability since the 1990s.<sup>317</sup> The discovery of the trans-activator of transcription (TAT) gave a better understanding of the transport mechanisms of peptides across the cell membrane.<sup>284, 318</sup>

The CPPs help to overcome the bio-interface challenges of most synthetic intracellular delivery agents.<sup>314</sup> The arginine-rich and other cationic CPPs improve cellular uptake processes.<sup>274, 317</sup> CPPs are versatile tools for intracellular cargo delivery of cell membrane-impermeable therapeutic and diagnostic agents.<sup>300, 314</sup> CPPs such as TAT peptides, penetration, and oligoarginine are short cationic peptides with vast potential in intracellular delivery applications.<sup>319, 320</sup> It is due to their specific interactions with the cell membrane.<sup>321</sup> Besides their surface charge nature, the availability of functional groups such as guanidinium and hydrophobic residues helps improve the ionic interaction of CPPs with cell membrane lipids.<sup>274, 322</sup> The improved intracellular delivery of CPP functionalized nanoparticles, for example, is due to interactions of positive charges of CPPs with the negatively charged lipid membrane.<sup>117, 319, 323</sup>

Peptide-based UCNPs functionalization helps to develop an efficient theranostic agent.<sup>312</sup> CPPs are well-known for surface modification of nanoparticles. The positive charges of the CPPs facilitate cellular internalization.<sup>324</sup> The inherent capability of CPPs could be used for translocating therapeutics and diagnostic agents across cell membranes.<sup>325, 274, 294</sup> Surface-immobilized CPPs accelerate the translocation of the nanoparticles by following the natural pathway to overcoming the membrane permeability barrier.<sup>326</sup> Functionalization of UCNPs using NGR, SP94, and YIGSR is recommended for its effective delivery and targeting.<sup>291</sup> Peptide-based ligand exchange of native UCNPs has been investigated to improve sensitivity and targetability.<sup>327</sup> A pH-sensitive peptides such as lysine and arginine are well-known for facilitating the endosomal escape of nanoparticles.<sup>274</sup>

The immunoglobulins (Ig) (antibody) decorated nanoparticles have several advantages for diverse bioanalytical applications. Antibodies have indispensable roles in the biomedical sector as scientific tools, as therapeutic and targeting agents.<sup>308, 328, 329</sup> Antibodies are classified into alpha (IgA), delta (IgD), epsilon (IgE), and gamma (IgG).<sup>330</sup> The alpha (IgA) is the most abundant IgG family categorized as IgG1, IgG2, IgG3, and IgG4. The head region of the antibody is known for its antigen-binding (Fab) capability, and the end region is known as fragment-crystallizable (Fc)<sup>330</sup>

Recently, conjugates of antibodies-nanoparticle have gained tremendous attention in targeted delivery.<sup>85</sup> The surface-immobilized antibody introduces bioactivity and targetability to locate the nanoparticle precisely. The antigen-binding domain, complementary determining region (CDR), is responsible for specific ligand-receptor interactions.<sup>331,332</sup> The binding affinity of antibodies to epitopes of the antigen could be achieved either due to hydrogen bonding, van der Waals forces or hydrophobic interactions.<sup>333</sup>

Antibodies are the most potent tools for targeted therapeutic and diagnostic applications.<sup>334, 109, 315</sup> Monoclonal antibodies have revolutionized cancer therapy.<sup>335</sup> The integration of antibodies' unique molecular recognition capability to surfaces of nanoparticles could be done through chemical conjugation. Immobilization of antibodies to nanoparticle surfaces helps to introduce their unique specificity and affinity.<sup>336</sup> Antibodies-cargo conjugates, such as small molecules and nanoparticles, are attractive approaches in the pharmaceutical and diagnostics sectors. Random or site-specific orientation of antibodies could happen during their conjugation.<sup>337</sup> Site-specific antibody immobilization helps to orient the complementarity-determining region (CDR) functionality.<sup>337</sup> The surface-oriented antibody receives a closer appearance to the analyte epitope.<sup>295,338</sup> These days, nanobodies, fragmented antibodies, are investigated as targeting agents to overcome the impact of their large size during whole antibody-based targeting.<sup>339</sup> The surface-coupled antibody could take a random or oriented surface appearance, as schematically represented in Figure 36.<sup>340</sup>

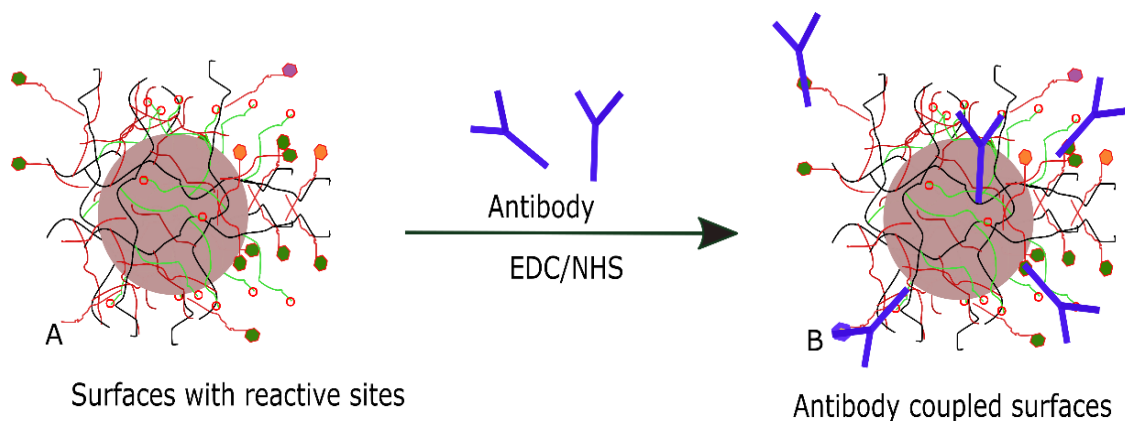


Figure 36 Schematic representation of surface grafted copolymers (A) and antibody-coupled surfaces (B).

The net charge of the antibody determines its initial interactions with the nanoparticle surfaces.<sup>341</sup> The commencement of antibodies to the nanoparticle surfaces is primarily driven by electrostatic interactions.<sup>341</sup> The electron-rich site of the antibody interacts with the surface of the nanoparticles preferentially, which is the Fc region. The initial interaction of the antibody is a physical association and gradually forms a covalent bond through its amine groups through EDC/NHS activation. The heavy chain parts tend to align themselves toward the nanoparticle surface. The negatively charged regions of the antibody have a strong affinity to bind themselves with the positively charged surfaces. Covalent immobilization antibody commences after it resides on the nanoparticles particle's surfaces, and some antibodies may remain attached physically.

The effectiveness of antibody functionalized surfaces depends on the antibodies' density and orientation. The amine and carboxylate groups distributions of antibodies define their surface coupling efficiency and orientation. Amine is the most abundant antibody functional group to be reacted with the nanoparticle surface reactive site.<sup>342</sup> Specific coupling of antibodies at the  $\alpha$ -amine group of lysine, for instance, could be accomplished through selective activation of the Fc region. The immobilization must be performed in a mild condition to avoid losing biological functions for the antibody-antigen interactions.<sup>308</sup> The working pH has a crucial role in bio coupling, and it should be one value lower than the PI of the interest amine group to attain.<sup>341</sup>

#### ➤ Mechanisms of bio-conjugation

The substrate surface functionality and the biomolecule type determine the conjugation mechanism.<sup>343</sup> The bioconjugation mechanism determines the performance of functionalized UCNPs. The modes of bioconjugation are usually categorized into physical and chemical conjugation.<sup>85</sup> Physical attachment of biomolecules to nanoparticle surfaces occurs through different forces of interactions such as hydrophobic interactions, electrostatic adsorption, and hydrogen bonding. The biotin-avidin conjugation, for example, relies on site-specific non-covalent interactions. Conjugation through chemical bonding is more preferable in attaining a stable surface attachment of biomolecules. The typical chemical conjugation techniques are classified as EDC/NHS chemistry, maleimide-thiol coupling, and click chemistry.<sup>343, 344</sup> Figure 37 depicts how different bio-coupling approaches could be selected based on the substrate surface functionalities.

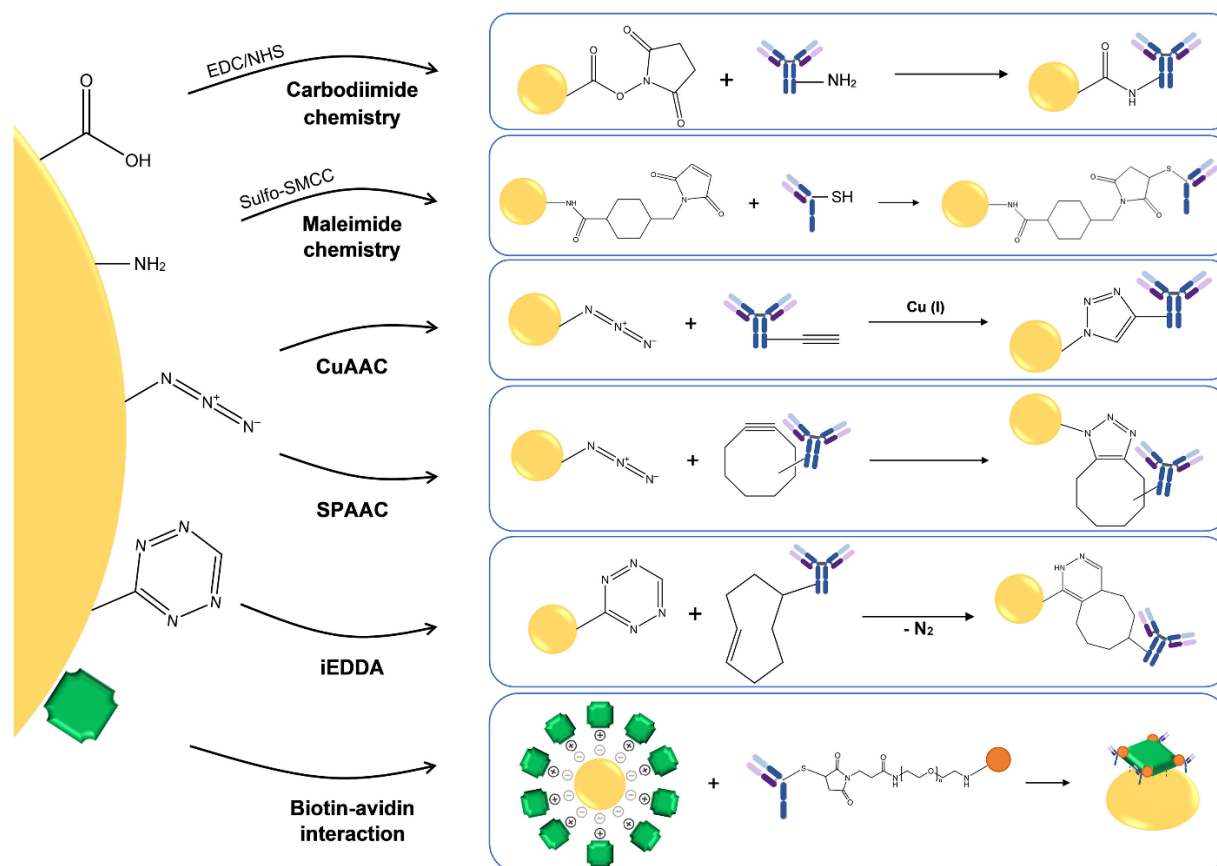


Figure 37 Schematic representation of coupling of the whole antibody to nanoparticle surfaces having different functionalities. Reproduced with permission<sup>343</sup> © 2020 Elsevier B.V.

➤ The EDC-NHS coupling

The EDC-based bio-coupling chemistry is the most popular technique to couple biomolecules to nanoparticle surfaces.<sup>51</sup> The EDC coupling approach requires the presence of accessible surface carboxylic or amine functionalities.<sup>337</sup> Nanoparticle surfaces with sufficient carboxylic groups provide good accessibility to perform covalent attachment of biomolecules. EDC-NHS enables biomolecule coupling through zero linkage length. The EDC-based coupling is pH sensitive and requires pre-activation o/f carboxylate groups at a low pH range of 4.5 to 6, whereas the amine coupling is favorable at pH 8 to 9.<sup>345</sup> The EDC surface activation induces an amine-reactive site, the O-acyl urea adduct, susceptible to nucleophilic attack. The O-acyl urea intermediate has a slow reaction rate and hydrolyzes fast or undergoes a re-arrangement to an N-acyl urea adduct, which is unreactive towards carboxylic groups.<sup>346</sup> Although a single-step EDC activation could enable bio coupling, a two-step EDC/NHS-based reaction is more reliable in attaining stable and efficient

conjugation. Figure 38 is a schematic illustration depicts the overall EDC/NHS surface activation and stabilization mechanisms.

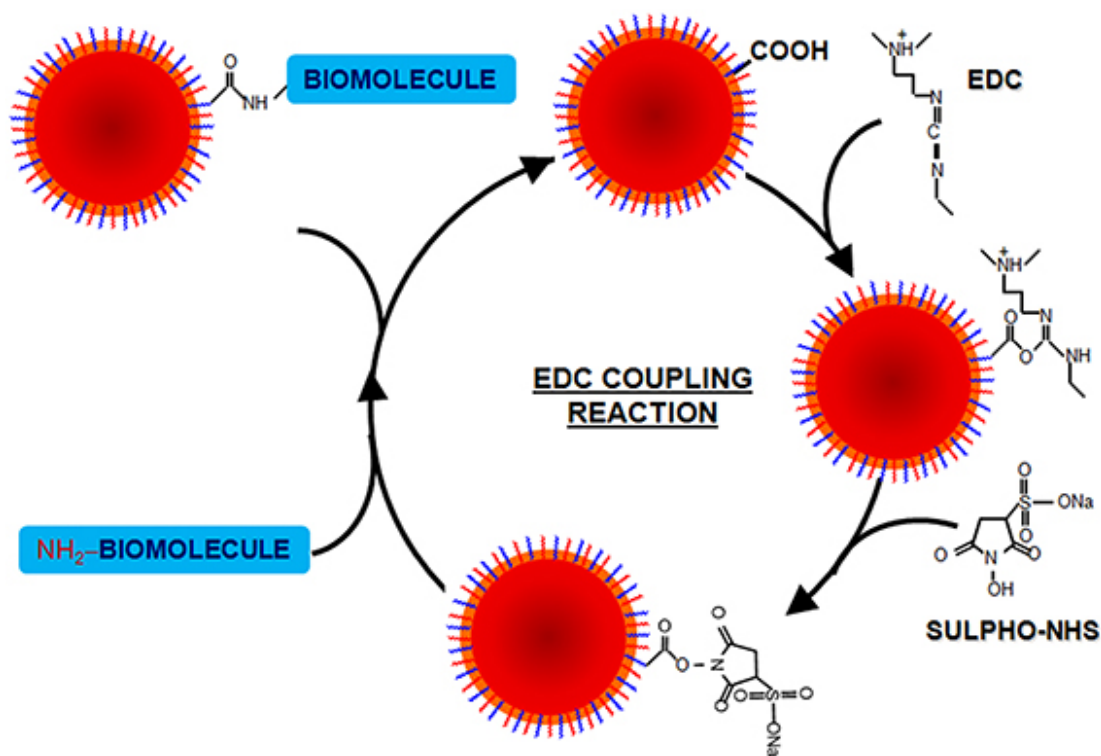


Figure 38 Pictorial representation of EDC activation in coupling and surface biofunctionalization. Reproduced from Conde et al.<sup>116</sup> © 2014 Frontier Chemistry.

## 2.4 UCNPs-based biomedical applications

The UCNPs are widely researched for their photonic and bioanalytical applications. The UCNPs have broad roles in developing advanced biomedical materials and devices. The current UCNP synthesis and development has vast potential opportunities in manipulating the nanoparticle size and morphology, providing immense advantages in tuning the optical performances. The potentials of UCNPs in developing advanced biomedical applications such as optical imaging, multiplexing, sensing, tracking, therapeutic, and delivery could be utilized effectively managed through surface optimization.<sup>35, 59, 347</sup> Figure 39 presents the multiple existence forms, like core-only and core-shell; and the various applications of UCNPs, such as core-only and core-shell, single particle-based such as single particle imaging and tracking, and theranostic applications.



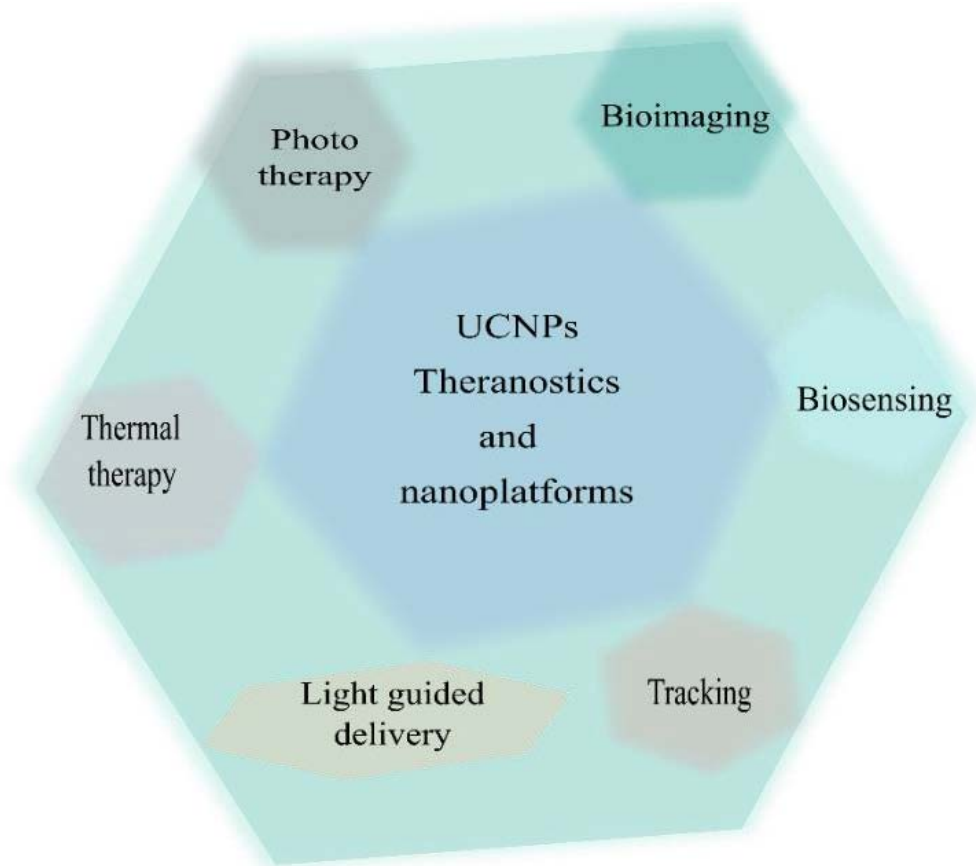


Figure 39 A compressive representation of diverse therapeutic and diagnostic roles hold by the UCNPs.

UCNP holds tremendous potential to serve as a future theranostic tool. UCNPs could simultaneously serve as contrast agents, nanocarriers, and therapeutic agents.<sup>348</sup> The simultaneous diagnosis and therapeutic approach, theranostic, has vast promises to achieve personalized nanomedicine.<sup>135</sup> Theranostic provides a single platform for diagnostics and treating diseases.<sup>135</sup> They could provide a wide range of photon emissions, including the UV and Visible regions, making them suitable as theranostic nanoplatforms.<sup>59, 349, 350</sup> Theranostic is highly promising to transform conventional therapeutic approaches into personalized treatments.<sup>15, 171, 349, 351-353</sup>

The UCNPs have been widely implemented in intracellular labeling, therapeutic and delivery applications.<sup>354</sup> Adequate intracellular visualization gives numerous advantages to monitoring intracellular activities. The high interest in intracellular labeling arises from the prominent roles of organelles in governing the fundamental activities of life. The subcellular structures, including the organelles, perform specific activities to maintain and regulate cellular functions.<sup>118</sup> The gene



expression of a cell is controlled by the nucleus. The nucleus is known as a container for the majority of DNA.<sup>355</sup> The endoplasmic reticulum is the leading protein synthesis, folding, and transportation site.<sup>355</sup> The nuclear pore complex controls the transport of materials into and out of the nucleus.<sup>356</sup> UCNPs-NPC labeling allows monitoring of diseases like leukemia, HIV, HCV infection, and congenital heart diseases.<sup>357</sup>

Currently, UCNP probes are widely implemented in different fluorescence imaging techniques, such as confocal, widefield, and total internal reflectance fluorescence microscopy (TIRFM) and super-resolution techniques. The widefield and confocal fluorescence imaging techniques, Figures 40A and 40B, are convenient for entire cellular and intracellular imaging.<sup>358</sup> The confocal techniques eliminate out-of-focus lights and generate a sharp, high-resolution image through specimen sectioning up to 1 μm thick.<sup>359</sup> The widefield technique suffers from the diffraction of light. Abbes' criterion has set for the smallest resolvable distance between two objects. The axial resolution ( $\Delta$ ) is mathematically represented from the emission wavelength,  $\lambda$ , and numerical aperture (NA) as represented in equation 6.<sup>360</sup>

$$\Delta = \frac{\lambda}{2 NA} \dots\dots\dots(6)$$

Where NA is represented as 'n sin  $\theta$ ': n is the refractive index, and  $\theta$  is the half-angle of the maximum cone of light collected by the objective.

Although biologists are interested in investigating intracellular dynamics and nanoscale protein structures, the far field optical microscope couldn't allow observing life activities below 200 nm.<sup>32, 157</sup> The Abbe's criterion limits the resolution level to 200 to 300 nm.<sup>157</sup> The two options to increase resolution are either through wavelength reduction or by increasing the numerical aperture of the objective lens, NA ~2. However, live cell imaging requires oil or water immersion objectives limited to NA ~1.45. Thus, both approach cannot enable high-resolution imaging using conventional optical techniques.<sup>360</sup> The diffraction limit challenge was initially overcome by achieving a sub-diffraction limit using near-field optical scanning microscopy in 1972.<sup>32</sup> The different intracellular structures and the multiple imaging techniques used to visualize them are schematically represented in Figure 40.<sup>358</sup>

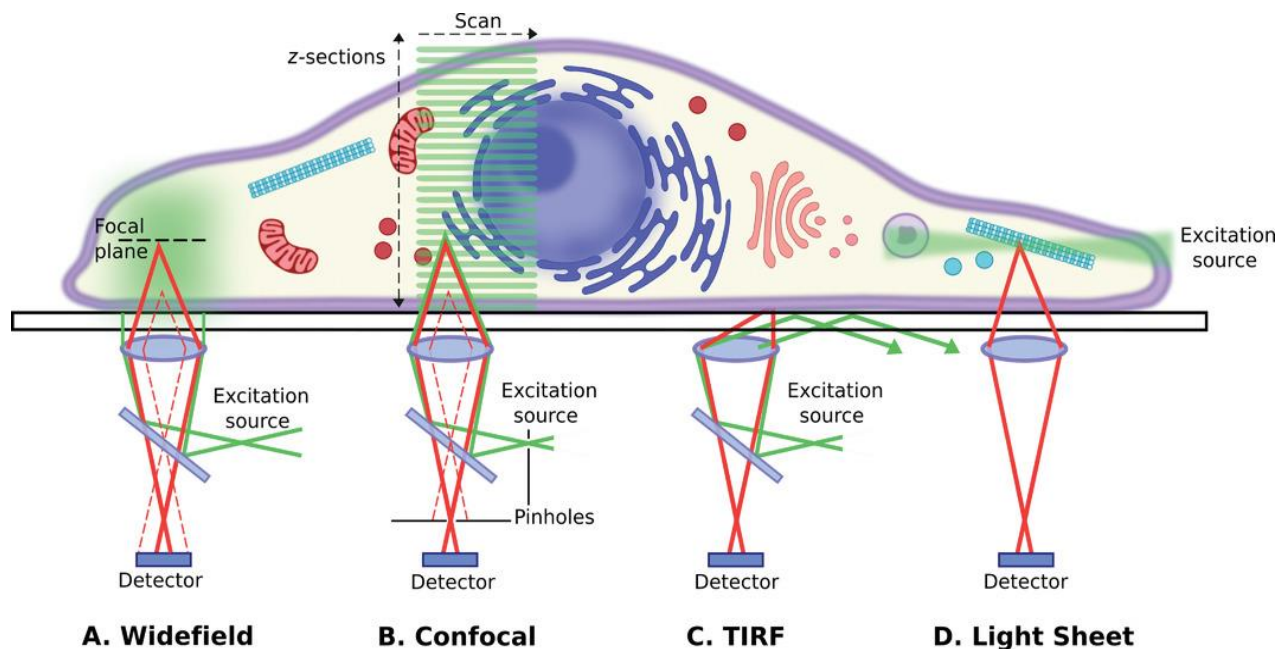


Figure 40 Schematic illustrations of different optical imaging, widefield (A), confocal (B), TIRF (C), and light sheet (D) techniques in the visualization of intracellular structures. Reproduced from with permission<sup>358</sup> © 2021 Wiley-VCH.

The widefield technique, Figure 40A, is an epi-illumination technique. It is like the bright field microscope, except using specific wavelength excitation. A widefield microscope generates images from different plane lights resulting from epi-illumination. The out-of-focus lights in a widefield microscope generate blurry images. In Figure 40B, the pin-hole-based illumination in a confocal laser scanning microscope (CLSM) helps to eliminate non-focused lights. Total internal reflectance fluorescence microscopy (TIRFM) and lights-sheet microscopy (LSM) are based on optical sectioning. Compared to STED and TIRFM, the light sheet method is preferable for thicker sectioning, as shown in Figure 40D. LSM is highly recommended for 3D live cell imaging. Since live cells are susceptible to perturbation, LSM helps monitor cell dynamics in their native environment.<sup>361</sup> The TIRFM is a powerful technique to selectively capture images in an aqueous environment at a depth of 100 to 200 nm, with a sectioning capacity of 60 to 80 nm and an axial resolution of 100 nm.<sup>362 361</sup>

The emergence of advanced super-resolution techniques has drastically revolutionized the history of bioimaging.<sup>119, 123, 157, 360</sup> The super-resolution imaging techniques significantly affect how we perceive the world.<sup>363</sup> Advancements in super-resolution techniques allow physicians and

researchers to visualize and monitor nanoscale-level biological events.<sup>364, 365</sup> The multiple super-resolution imaging techniques are categorized based on how the non-linear responses are investigated.<sup>3</sup> The nanoscopic methods such as stochastic optical reconstruction microscopy (STORM) or photo-activated localization microscopy (PALM), stimulated emission depletion (STED) microscopy, and structured illumination microscopy (SIM) have enabled us to overcome the sustained Abbe's diffraction limit effectively.<sup>365</sup> Although theoretically, the spatial resolution of most super-resolution techniques is unlimited, a sub-10 nm level molecular resolution is unpractical so far.<sup>3</sup>

The current super-resolution techniques devised their unique approach to overcoming Abbe's light diffraction barrier. STED, for instance, uses two laser beam illuminations for the sample excitation and depletion. The STED imaging is done by fluorescence excitation, followed by depletion to the ground state. A 'focal spot' is generated when the two beams are superimposed and scanned to produce an image. STORM uses photo-switchable fluorescent probes to create 'on' (bright) and 'off' (dark) contrasts. The SIM works by applying patterned barcodes like illumination and generates Moiré interference, and the image requires further processing using a computer algorithm.<sup>32</sup> The compressed images, Figure 41 adopted from Stender et al., are taken using different super-resolution techniques such as SIM, STED, and STORM/PALM/FPALM through fluorescent protein-based labeling.

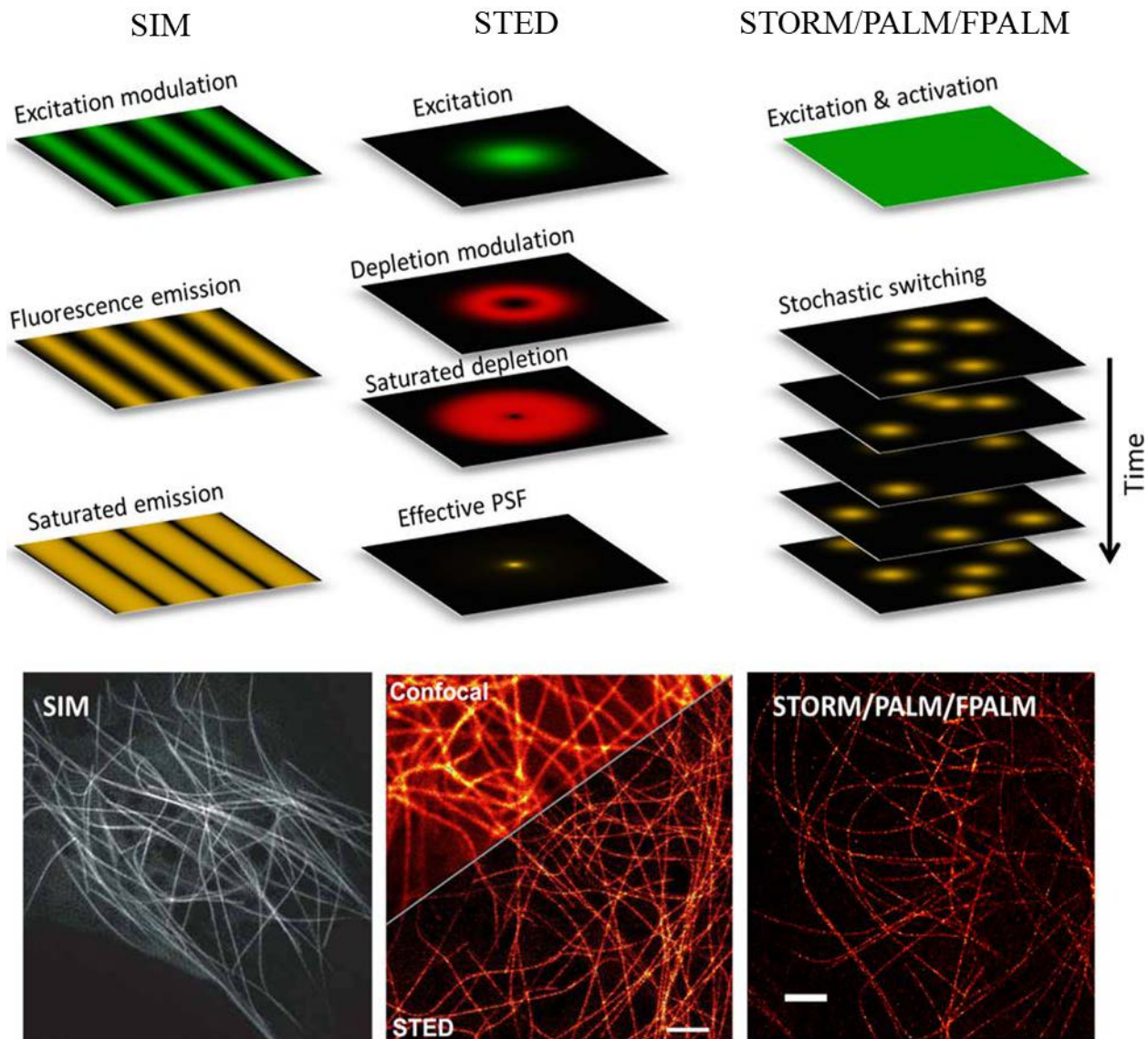


Figure 41 Comparative images of the tubulin structures taken using SIM, STED, and STORM techniques. Reproduced with permission<sup>366</sup> © 2013 American Chemical Society.

In Figure 41, the images from the different super resolution techniques clearly show the resolution capacity of the individual techniques. The SIM and confocal images produce relatively low-resolution; however, the STORM and STED techniques generate highly resolved images.

➤ Super-resolution techniques and UCNPs

The UCNPs are recently evolving probes compared to conventional labeling agents.<sup>152</sup> The alarming advancements in the development of optical microscopes strongly demand compatible

fluorescent probes. As pointed out by Jin et al., the UCNP has attractive features for nanoscopic applications.<sup>39</sup> The nonlinear excitation saturation emission and the photon avalanche-like process of UCNP make them suitable in diverse super-resolution imaging modalities.<sup>135, 367</sup> Currently, UCNP probes are implemented in different super-resolution techniques such as beam excitation, STED microscopy, and SIM, has been practiced well.<sup>152</sup> The UCNP probes could be ideal for intracellular labeling and super-resolution imaging.<sup>152, 157</sup>

The current super-resolution techniques can control fluorescence emitters at the single-molecule level.<sup>360</sup> Single-molecule imaging is a well-known technique for deep visualizing biological structures. Single-molecule imaging enables high specificity and sensitivity at the molecular level.<sup>368, 369</sup> The standard single-molecule localization techniques are confocal microscopy, TRIFM, and super-resolution microscopy. Confocal microscopy is the first single-molecule technique with a far-field approach. Several advanced super-resolution techniques, such as PLAM and STORM, are widely implemented for single-molecule imaging applications.<sup>152</sup> The widefield microscope also enables visualization of single UCNP from infinitely diluted dispersion. However, due to light diffraction, a tenfold of the actual size could be observed. The current achievements in detecting a single molecule are highly associated with rapid advancements in optics and electronic devices.<sup>3</sup> Selective resolution of a single emitter at the point spread function center is a primary interest in the single-molecule approach.<sup>370</sup> Single-molecule avoids background signal interference and helps to eliminate limitations associated with epi-illumination of the whole specimen.<sup>146</sup>

Single UCNP spectroscopy relies on nonlinear excitation power and crystal facet orientation.<sup>371, 372</sup> The sharp band emissions from the 4f-4f electronic transition in polarized single UCNP is more advantageous than semiconductor emissions.<sup>373</sup> In single UCNP imaging, optimizing particle size and brightness is an important issue.<sup>39, 270, 374</sup> The size compatibility of UCNP with the target intracellular component helps avoid size distortion and undesired interferences.<sup>375, 376</sup> Comprehensive efforts have been made to obtain smaller particle sizes and the brightest UCNP for super-resolution applications.<sup>377-379</sup> A successful deep tissue imaging using fully alloyed 12 nm NaYF<sub>4</sub> core-shell nanocrystals doped with Yb<sup>3+</sup> and Er<sup>3+</sup> has been reported.<sup>193</sup> The recent report shows promising progressive achievements and single UCNP developments.<sup>380</sup> Figure 42 is a timeline of recent progress in a single UCNP implementation.

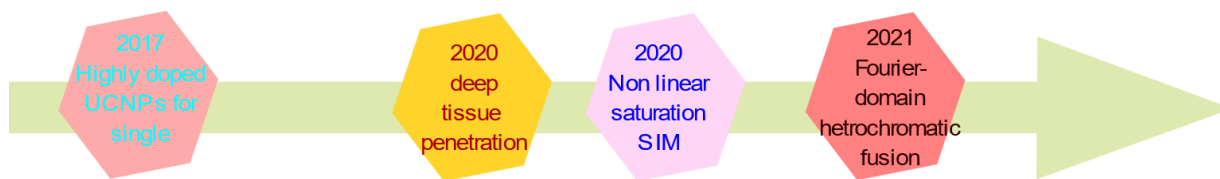


Figure 42 The progressive developments in UCNPs-based super-resolution imaging.

UCNP probes have been considerably employed in super-resolution imaging. A resolution of 82 nm from cytoskeleton UCNPs labeling has been achieved.<sup>328</sup> Using up-conversion STED, the microtubules of HeLa cells labeled with UCNPs have been super-resolved by Zhan et al.<sup>381</sup> Jin et al. found blue emission of highly doped UCNPs (8% Tm<sup>3+</sup> ions) under continuous wave (CW) 980 nm excitation can be inhibited once a CW 808 nm probe beam is applied at the same time. The electron population mechanism in the ladder-type energy levels facilitates the lanthanides in UCNPs. The approach enables the realization of low power-up conversion-based super-resolution STED at a single particle resolution of 28 nm.<sup>39, 328</sup> The upconversion-based STED is not limited to the Yb<sup>3+</sup>-Tm<sup>3+</sup> systems. It has also been explored successfully in Yb<sup>3+</sup> and Er<sup>3+</sup> co-doped UCNPs.<sup>382</sup> Liu et al. developed a deep tissue super-resolution nanoscopic imaging that can achieve sub-hundred-nanometer resolution inside tumor spheroids by using a non-diffractive Bessel beam.<sup>383</sup> The nonlinear saturation structure illumination microscopy (SIM) from near-infrared excitation and emission of UCNPs provides better deep penetration capability.<sup>384</sup> Recently, Chen et al. developed a Fourier-domain heterochromatic fusion, and a prolonged proficiency in the engineered point spread function (PFS) has been gained from diverse emission responses of UCNPs. This approach helps to gather both low- and high-frequency information to produce optimized image quality. Moreover, in a UCNPs photoavalanches investigation, a single beam super-resolution imaging with sub-70 nm spatial resolution has been achieved without any computational analysis.<sup>385</sup>

## 2.5 Conclusion

Optical imaging has tremendous potential advantages both in academic research and clinical uses. In optical imaging, fluorophores play prominent roles in optical imaging to generate high-contrast images. Although organic dyes and fluorescence proteins are the most common labeling agents, nanoprobe are emerging to address the common challenges observed with conventional probes. UCNPs are emerging as a potential biomarker in intracellular labeling and imaging. The

upconversion nanoparticles have the merits to overcome challenges observed in conventional fluorophores like photobleaching. UCNPs exhibit many exciting features, like high stability and low excitation energy. The brightness of UCNPs emission is essential in implementing the particles for intracellular application. The established standard synthesis techniques provide wide options for controlling the particles' size, composition, and morphology. Successful intracellular delivery of nanoparticles, localization, and achievement of long-term in-vivo stability are essential factors in nanoprobe's development.

Nanohybrids produced from UCNPs, polymers, and biomolecules have numerous opportunities for diverse intracellular applications, imaging, tracking, and delivery. The untapped potentials of the UCNPs could be investigated through polymer-based surface tailoring. Surface functionalization of UCNPs allows for addressing the critical challenges of nanoprobe, surface limitations, and size compatibility in cell labeling. The polymer-tailored UCNPs enable the particles to overcome nano-bio interface challenges. Polymer-based surface modification of UCNPs substantially alters their functionality and in vivo performances. The long-term in-vivo circulation and stability of UCNPs help to implement them in real-time live cell imaging applications.

The progressive advancements in polymer chemistry are a great advantage to designing specific surface-modifying polymers. Advanced polymerization techniques, like RDRP, allow for synthesizing polymers with sophisticated functionality and architecture for surface modification of UCNPs. RAFT polymerization provides an incredible role in the synthesis of polymers for nanoparticle surface functionalization. RAFT polymers are ideal for altering nanoparticle surfaces. Polymers with anchoring functionalities, such as phosphate groups, could be effectively incorporated into the inorganic particles' surfaces. The polymer-grafted nanoparticles gain multi-functional surfaces, such as reactive surfaces, that allow for the practical attachment of bioactive molecules. The surface-immobilized biomolecules are responsible for the achievement of specific targetability.

The biofunctionalized nanoparticles help to address nano-bio interface challenges. Proper selection of a polymer-nanoparticle integration is essential in producing functionalized surfaces. The 'graft to' technique helps use ready-made polymers in the surface grafting of particles. The strong surface coordination bond formation between the anchoring agent and the particle surfaces enables a

relatively stable composite. The controllability of modified particle size is essential to avoid reproducibility challenges in the implementation of nanoprobes. The polymer functionalized particle's performance could be assessed from the hydrodynamic diameter, surface zeta potential, and stability in the specified working conditions such as pH solvent polarity.

The current advancement of optical microscopy is an excellent opportunity to investigate UCNP-based intracellular labeling and imaging. Conventional imaging techniques like confocal microscopes and wellfield microscopes help to capture UCNP-based images. However, the choice of microscopic technique for UCNP probes implementation is vital in obtaining a high-resolution image. For molecular-level biological investigations, super-resolution techniques are suitable because they overcome the light diffraction challenge. UCNPs with a reasonably smaller diameter could be employed in a detailed labeling investigation of intracellular structures, including microtubules, actin filaments, and nucleolus. Moreover, the UCNPs could be utilized in monitoring intracellular dynamics, imaging freely behaving animals, and actualizing personalized medicine at the ultimate.

In a nutshell, the surface modification and functionalization of UCNPs take prominent roles in efficient intracellular labeling and imaging. In chapters 3, 4, 5, and 6, the nanoprobes development processes that includes nanoparticles synthesis, the design and development of multiple copolymers for the surface functionalization; the UCNPs surface grafting and coupling techniques, and UCNP based labeling and imaging of specific intracellular structures are presented explicitly.



# 3 | Synthesis and Characterization of Upconversion Nanoparticles

## 3.1 Preamble

This section discusses the synthesis and characterization of lanthanide (III) doped upconversion nanoparticles (UCNPs). The theoretical backgrounds and chemistry of the UCNPs are briefed. The optical properties of  $\text{Er}^{3+}$ -doped nanoparticles using fluorescence spectrometry are discussed. The use of core-shell structure in enhancing the brightness for efficient imaging is mentioned. The impacts of surface chemistry and importance of surface polymer functionality and surface density, and the possible characterization techniques used to include ATR-FTIR and TGA are mentioned. The synthesis of  $\text{Er}^{3+}$ -doped nanoparticles with core and core-shell structures and different sizes is briefed. UCNPs characterization techniques implemented to assess particle size, morphology and emissions properties.

## 3.2 Introduction

The lanthanide (III) upconversion nanoparticles attracted wide attention for their indispensable biomedical applications. The absence of background noise, for instance, is an exciting feature of the lanthanide (III) nano phosphors in nanomedicine applications. The presence of high stability, low toxicity, and sharp emission bands are the other merits of UCNPs.<sup>386</sup> The optical properties of the upconversion nanoparticles depend on the particle size, crystalline structure, and composition of the crystals. Optimization of the reaction time, temperature, host material type, and dopant type and concentration enable particle size, shapes, and crystal phase control.<sup>55, 64, 387</sup>

Structure-property manipulation is an integral approach to tuning the optical performance of nanoparticles. The interest in monodisperse and smaller-size particles for fluorescence labeling has grown since the first nano-sized  $\text{NaYF}_4$  UCNPs were conveyed.<sup>388</sup> The  $\beta\text{-NaYF}_4: \text{Yb}^{3+}/\text{Er}^{3+}$  doped UCNPs are the most attractive nanocrystals that generate an intense visible emission through NIR excitation.<sup>132</sup> Due to the excellent chemical stability, size, shape, and crystal structure control, the  $\beta\text{-NaYF}_4$  has received substantial attention.<sup>387</sup> The thermal decomposition method is the most efficient technique for developing spherical, uniform, and colloidally stable  $\beta\text{-NaYF}_4: \text{Yb}^{3+}/(\text{Er}^{3+}/\text{Tm}^{3+})$  nanocrystals.<sup>41, 134, 142 389</sup> Thus, as a part of this Ph.D. project, the  $\beta\text{-NaYF}_4:$

Yb<sup>3+</sup>/Er<sup>3+</sup> doped UCNPs synthesized and characterized. The nanoparticle is synthesized to develop functionalized UCNPs through polymer-based surface modification and biofunctionalization. Then, the functionalized nanoparticles serve to label intracellular structures and to perform imaging.

#### ➤ Optical properties of UCNPs

The optical properties of the UCNPs are the most fundamental in biomedical applications.<sup>390</sup> The electronic transition mechanisms of lanthanides occur through 4f-4f, 4f-5d, and charge transfer between ligand and metal, or vice versa.<sup>391</sup> Although the f-f electric dipole transitions are known as Laporte forbidden, doped lanthanide ions relax the rule, and an induced or forced electric dipole transition occurs.<sup>391</sup> The lanthanide-doped UCNPs produce a sharp f-f electronic transition compared to the d-d transition exhibited by conventional organic dyes. The sharp emission and fewer Stokes shift in Ln (III) ions are due to the involvement of deeper f-electrons and the closer equilibrium internuclear distance between the ground and excited states. Spectral characterization of the NaYF<sub>4</sub>: Yb<sup>3+</sup>/Er<sup>3+</sup> UCNPs is based on determination of the characteristic emission peaks. Among the multiple upconversion processes, the energy transfer mechanism is the most efficient one in lanthanide-doped nanocrystals.<sup>107</sup>

#### ➤ Determination of surface area, molecular weight, and particle number

A precise determination of surface area, molecular weight, and particle number is essential in the quantitation of UCNPs. The molecular weight of the UCNPs could be estimated from the particle volume and unit cell relationship. The number of atoms found in the individual unit cell could be used to determine the molecular weight of the particles. A detailed explanation of the molecular weight related to the particle size of UCNPs has been given by Mackenzie et al.<sup>392</sup> To simplify, the UCNPs' has been considered as a spherical shape for surface area determination. The number of particles, and their concentration, in a specified volume of solution could be estimated From Avogadro's principle and the molecular weight. The theoretical molecular weight could be determined from the relationships between the particle volume and the unit cell.

### 3.3 Experimental section

The following reagents are used for the thermal decomposition synthesis of the  $\beta$ -NaYF<sub>4</sub>:Yb<sup>3+</sup>/Er<sup>3+</sup> nanoparticles. Yttrium (III) chloride hexahydrate (99.99%, Sigma-Aldrich); Ytterbium (III)

chloride hexahydrate (99.9%, Sigma Aldrich); Erbium (III) chloride hexahydrate (99.99%, Sigma-Aldrich); Sodium hydroxide (98%, Sigma-Aldrich); Sodium chloride (99.5%, Sigma-Aldrich); Ammonium fluoride (99.99%, Sigma-Aldrich); Oleic acid (OA) (90%, Sigma-Aldrich); 1-Octadecene (ODE) (90%, Sigma-Aldrich); Cyclohexane (99%, Merck)

The analytical instruments used for characterization are Malvern Instruments Seasider, a Nano-ZS instrument equipped with a 4 mV He-Ne laser at 633 nm, which was used to determine dynamic light scattering (DLS) for hydrodynamic size determination of the as-synthesized and polymer grafted nanoparticles. The z-potential of the modified nanoparticles was assessed using the Zeta sizer. Transmission electron microscopy (TEM) and JEOL TEM-1400 at an acceleration voltage of 120 kV have been used to determine the diameter of the as-synthesized and modified UCNPs. The crystallographic analysis has been performed using Bruker D8 discover XRD. A thermogravimetric analysis (TGA), SQ600 instrument, was used to characterize the thermal properties of synthesized polymers.

### 3.3.1 Synthesis of $\beta$ -NaYF<sub>4</sub>:Yb<sup>3+</sup>/Er<sup>3+</sup> nanoparticles

Synthesis of UCNPs with the desired size and morphology requires accurately measuring precursor salts and the reaction solvents. As discussed in chapter two, several standard synthesis techniques are widely used to synthesize nanoparticles. The pre-preparation of reagents and the synthesis steps followed in the thermal decomposition-based synthesis of the lanthanide-doped up-conversion nanoparticles is schematically represented in Figure 43.

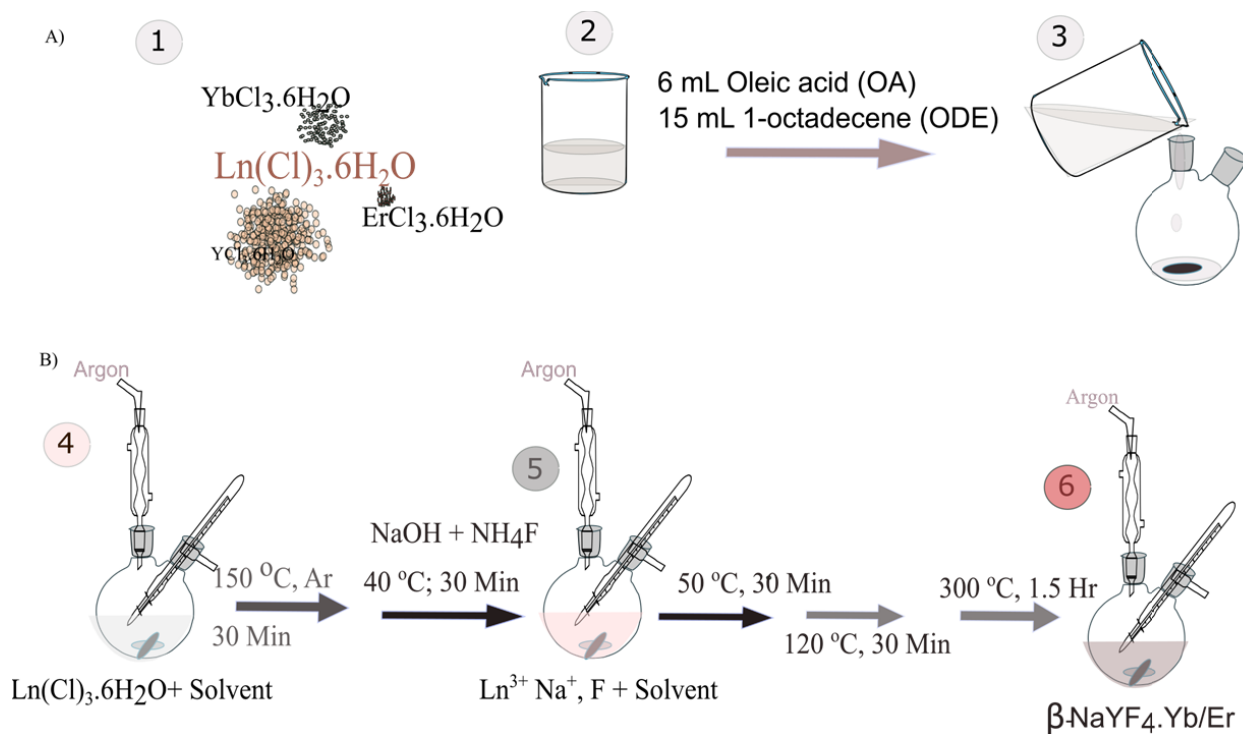


Figure 43 Schematic representation of the measurement of reagents (A) the steps 1 to 3 and the thermal decomposition synthesis of core-UCNPs (B) in steps 4 to 6.

As schematically presented in Figure 43, the UCNP synthesis was accomplished using thermal decomposition. A 6 mL of oleic acid (OA) and 15 mL of 1-Octadecene (ODE) were taken into a 50 mL capacity two-neck round bottom flask, and then a 0.56 mmol, 0.2 mmol, and 0.02 mmol of  $\text{YCl}_3 \cdot 6\text{H}_2\text{O}$ ,  $\text{YbCl}_3 \cdot 6\text{H}_2\text{O}$ , and  $\text{ErCl}_3 \cdot 6\text{H}_2\text{O}$  were added, respectively. The experimental setup was organized from a heating mantle, magnetic stirrer, and temperature controller. The round bottom flask was connected to an inert gas line, fit 320 °C capacity thermometer to monitor the reaction temperature and discharge tube at its three necks. The reaction temperature was set to 150 °C through a gradual increment of  $\sim 5$  °C/min under a continuous inert gas flow and stirring speed of 700 rpm for 30 minutes. Then, the solution was cooled to room temperature, and 5.6 mL of methanol containing 2.5 mmol of NaOH and 4.0 mmol of  $\text{NH}_4\text{F}$  was added to it; the temperature was adjusted to 50 °C and stood for 30 minutes with continuous stirring. The temperature was further raised slowly to 150 °C and proceeded at 150 °C for 20 minutes. Then, the reaction temperature was raised to 300 °C at a rate of  $\sim 15$  °C/min, string speed 400 rpm, and inert gas flow rate  $\sim 20$  mL/min. The temperature was adjusted and maintained precisely at 300 °C for 1.5 hours. The solution was cooled to room temperature and transferred into a 50 mL eppendorf tube. For the

synthesis of 20 nm particles, the same procedure was followed as mentioned for the 25 nm synthesis. The only exception was that the final reaction at 300 °C was carried out for an hour and fifteen minutes.

The synthesized nanoparticles were purified by taking 2 mL stock particle solution into a 15 mL capacity falcon tube and centrifuging at 7500 rpm for 5 minutes. The supernatant solution was discarded, 5 mL of cyclohexane was used to re-disperse precipitation, and 5 drops of oleic acid and 8 mL of ethanol were added and sonicated until a homogenized solution was obtained. Then, it was centrifuged at 7500 rpm for 5 minutes. The last procedure was repeated for a second time, and the sediment was dispersed in 3 mL of cyclohexane. The particles' complete dispersion and emission quality were assessed using a 980 nm laser tester. The particles' hydrodynamic diameter was examined by using dynamic light scattering (DLS) analysis.

The inert-shell development was performed by taking 6 mL of OA and 15 mL of ODE into a 50 mL capacity three-neck round bottom flask equipped with a magnetic rod and then a 0.56 mmol, 0.2 mmol, and 0.02 mmol of  $\text{YCl}_3 \cdot 6\text{H}_2\text{O}$ ,  $\text{YbCl}_3 \cdot 6\text{H}_2\text{O}$ , and  $\text{ErCl}_3 \cdot 6\text{H}_2\text{O}$  were added into, respectively. The reaction setup was organized as it was done in the core nanoparticles. The heating mantle, the magnetic stirrer, and the temperature controller were appropriately arranged. Then the flask was connected to argon gas at its one neck through a condenser tube, and a thermometer was fitted at its second neck and served to monitor the solution temperature. With controlled inert gas flow and continuous stirring at 600 rpm, the reaction temperature was raised to 150 °C and maintained for 30 minutes. Then after it was cooled to room temperature, a methanol solution containing 2.5 mmol of NaOH and 4.0 mmol of  $\text{NH}_4\text{F}$  was added. The temperature was adjusted to 50 °C and continuously stirred for 30 minutes. The temperature was slowly raised to 150 °C at a heating rate of  $\sim 5$  °C/min with continues stirring at 700 rpm. Finally, the solution was cooled to room temperature, then transferred into a 50 mL capacity falcon tube, and stored under 4 °C till consumed for further experiment.

The synthesis of core-shell nanoparticles was accomplished by taking 3.6 mL OA and 9.2 mL ODE, and 0.4 M of the pre-prepared core nanoparticles into a 50 mL capacity three-neck round bottom flask. Initially, the reaction proceeded at 150 °C under a controlled inert gas flow and continued stirring at 600 rpm for 30 minutes. Then, the reaction temperature was further raised to 300 °C and kept for 10 minutes. A 5 mL of pre-prepared shell-forming solution was injected into

the hot reaction solution at a rate of 0.2 mL/2 min. After the complete addition of the shell solution, the reaction was continued for an additional 10 minutes. The core-shell nanoparticles were purified and characterized using the same procedure followed with the core nanoparticles. The quality of the nanoparticles was monitored by laser test on emission intensity, DLS size analysis, and TEM characterization for morphology analysis.

### 3.4 Result and discussion

The UCNPs synthesis was performed using the thermal decomposition technique. The controlled temperature treatment transforms the cubic phase into a hexagonal crystal structure in the heat-up process. In thermal decomposition, post-annealing is not required as done with the solvo (hydro) thermal technique. The particle shape and size proper control has a fundamental effect in developing nanoprobes for intracellular imaging applications. The TEM micrograms in Figure 44 show the nanoparticles' good monodispersity and spherical morphology.

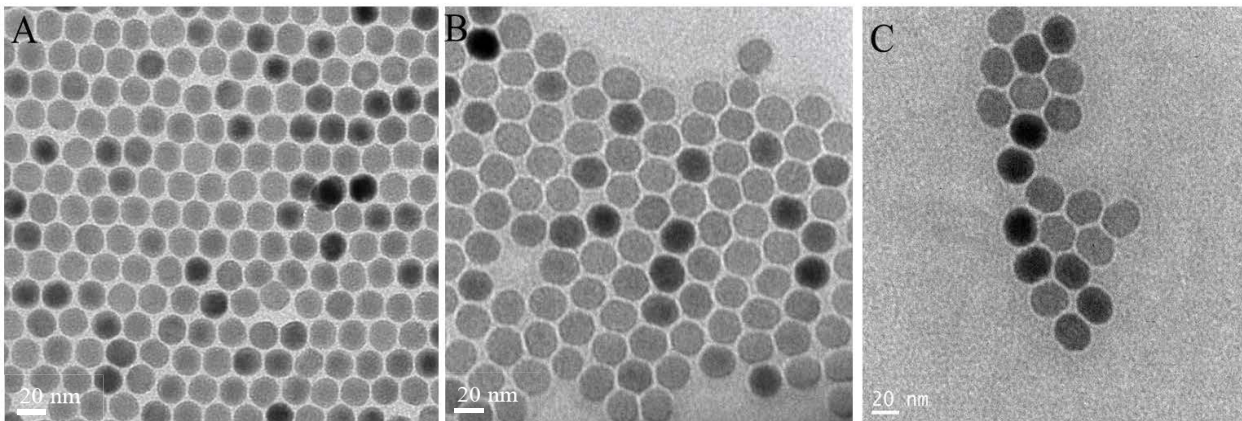


Figure 44 TEM micrograph of synthesized UCNPs (A) 20 nm, (B), 25 nm, and (C) 35 nm.

The smaller diameter UCNPs are suitable for labeling intracellular structures closer to the target site. The nanoparticle size compatibility is crucial to avoid screening and far-distance labeling. For instance, adequate labeling of the F-actin at a 7 nm target requires a comparable size nanoprobe. The purpose of the 20 nm diameter particles is to investigate the particle size effect while labeling the tiny intracellular structure. The smaller diameter particles, however, suffer from decreased emission intensity. The core-shell structure, Figure 44C, is designed to investigate the effect of the core-shell emission in intracellular imaging. Since the core-shell particles produce brighter emission compared to the core only one, a smaller number of particles would be enough to label

and image cellular structures. It avoids use of excessive nanoparticles, and consequently, it could minimize cytotoxicity.

The crystallinity of the UCNPs is an essential property of gaining bright emission.<sup>393</sup> Figure 45 displays the strong fingerprint emissions of Er<sup>3+</sup>-doped NP,  $\beta$ -NaYF<sub>4</sub>:Yb<sup>3+</sup>/Er<sup>3+</sup>, and the green and red emissions. The enhanced emissions at 510 to 540 and 645 to 655 nm are characteristic of a hexagonal UCNP structure.<sup>394</sup> The green emission spectra at 510 to 530 nm are due to  $^2H_{11/2} \rightarrow ^4I_{15/2}$  transitions. The intense 530 to 570 nm emission belongs to  $^4S_{3/2} \rightarrow ^4I_{15/2}$  transitions. The red emission at 645 to 680 nm is associated with  $^4F_{9/2} \rightarrow ^4I_{15/2}$  electronic transitions.<sup>179</sup> The Er<sup>3+</sup> doped nanoparticles are also known for their emissions at 410 nm ( $^2H_{9/2} \rightarrow ^4I_{15/2}$ ); and 1550 nm ( $^4I_{13/2} \rightarrow ^4I_{15/2}$ ).<sup>131, 395</sup>

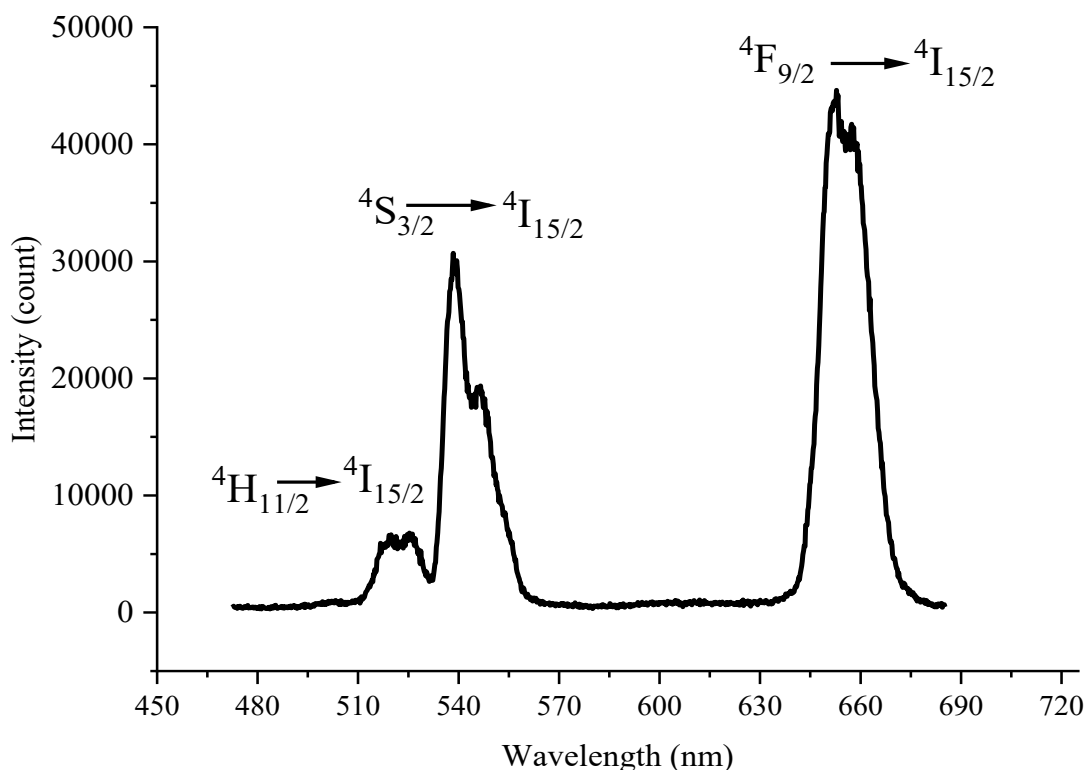


Figure 45 The spectroscopic property of  $\beta$ -NaYF<sub>4</sub>: 20% Yb<sup>3+</sup>/2% Er<sup>3+</sup>.

For XRD analysis, nanoparticle solution in cyclohexane was dried slowly on a silicon wafer. The obtained diffraction pattern shows that the nanocrystals are favored to develop a hexagonal structure.<sup>396</sup> The interest in developing hexagonal nanocrystals is due to their strong capacity to transform NIR light into visible emissions.<sup>397</sup> The obtained XRD pattern is similar to the reference

card number, confirming the high purity of the hexagonal phase.<sup>134 394 398</sup> As presented in Figure 46, the diffraction pattern corresponds with a reference card number, JCPDS 16-0334.<sup>141</sup>

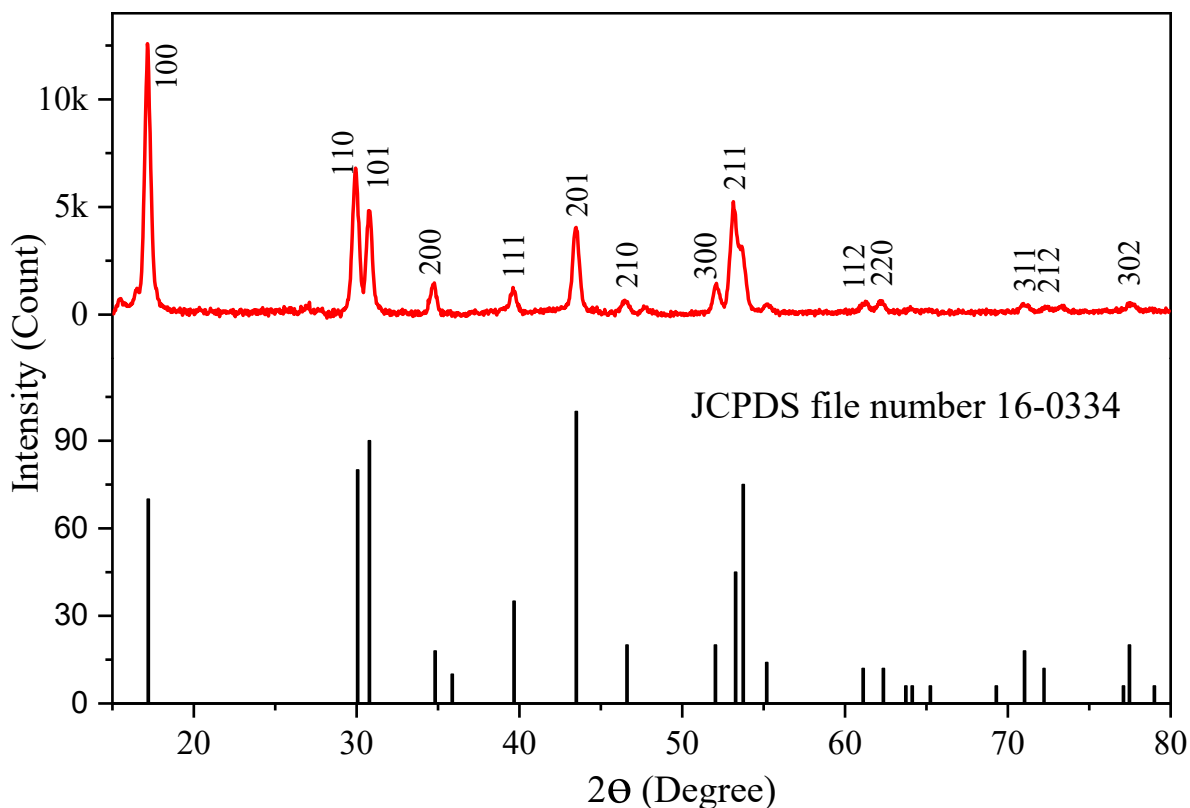


Figure 46 The XRD powder diffraction of the synthesized 25 nm  $\beta$ - $\text{NaYF}_4$ :  $\text{Yb}^{3+}$ (20%)/  $\text{Er}^{3+}$ (2 %) (Red plot) and standard (black plot).

### 3.5 Conclusion

The upconversion nanoparticles synthesis was accomplished effectively. The morphological characterizations confirm that the synthesized particles are monodispersed. The spectroscopic analysis shows the characteristic peaks of  $\text{Er}^{3+}$ -doped emissions. The purity of the hexagonal crystalline structure is confirmed by comparing the XRD of the sample with the standard. As the synthesis is favored to hexagonal structure, it produces strong fluorescence emission. Here, the quality of synthesized nanoparticles to produce well-performing probes is suitable enough. The surface preparation using polymer grafting and biofunctionalization could be performed to implement them for intracellular labeling.



# 4 | Development of RAFT Block Copolymers for UCNPs Surface Functionalization

## 4.1 Preamble

This chapter presents detailed information on the design and synthesis of different RAFT copolymers for surface grafting of the UCNPs. RAFT agents applicable in the thermal/photo-initiated radical techniques for synthesizing the copolymers are mentioned. The polymer synthesis and characterization techniques are presented in detail. The advantage of RAFT agents' end-group functionalities in controlling reactivity and amphiphilicity is discussed. The roles of MAA-functionalized copolymers in the surface grafting of UCNP surfaces are described. The benefits of the different copolymers in UCNP surface tailoring, stabilization, and functionalization are elaborated. The polymer-UCNP hybrids give superior surface performances during their intracellular targeted delivery applications, especially in overcoming nano-interface challenges. It has been concluded that RAFT block copolymers have multiple potential opportunities in advancing UCNPs' surface for various biomedical applications.

## 4.2 Introduction

The RDRP technique provides enormous opportunities to develop copolymers with desired functionality and compositions.<sup>224, 399, 400</sup> Due to its practical research feasibility, RDRP has been extensively implemented in many advanced applications.<sup>401-403</sup> RAFT polymerization is one of the robust RDRP techniques. RAFT technique is widely used in synthesizing block copolymers for drug delivery and nanoparticle functionalization.<sup>404, 405</sup> The conventional RAFT polymerization is based on thermal initiation. The recent RAFT polymerizations, such as the light, enzyme, and redox initiation techniques, offer significant improvements over the conventional RAFT methods.<sup>193, 218</sup> The visible light-mediated RAFT technique and macromolecular design by xanthates replacement (MADIX) have enormous potential in developing multifunctional copolymers for biomedical applications.<sup>75, 217, 406, 407</sup> The adaptability of polymers makes them suitable for diverse biomedical applications, including nanoparticles surface modification.<sup>193, 194</sup>

RAFT technique enables us to design of suitable polymers for surface tailoring of UCNPs. The vast monomer choices such as PEG, MPC, DPA, and MAA allow multiple copolymer synthesis.

The PEG-based copolymers are the most widely implemented to develop stable and water-dispersible colloids.<sup>403, 408</sup> Copolymers with phosphate and sulphonate anchoring moieties are widely implemented to tether polymers to the UCNP surfaces through the surface-exposed trivalent lanthanide ions.<sup>84, 273</sup> Surface grafting using stimulus-responsive polymers (i.e., pH, temperature, and salt) provides multiple advantages in intracellular applications.<sup>409-411</sup> Zwitterionic copolymers are new-generation polymers with superior surface antifouling capability.<sup>70</sup> Zwitterionic functional polymers such as phosphorylcholine have known for their antifouling and salt-responsive capacity.<sup>250, 412, 413</sup> The 2-methacryloyloxyethyl phosphorylcholine is widely used in antifouling surface development. Nanoparticle surface mimicking through attaching polymers avoids undesirable interface interactions like protein fouling.<sup>414, 415</sup>

#### 4.2.1 RAFT polymerization for the synthesis of block copolymers

RAFT polymerization is a widely implemented technique in devolving copolymers with complex architectures.<sup>225, 405</sup> RAFT agent compatibility and solvent suitability are critical factors in polymerizing monomer(s). The synthesis of RAFT block copolymers could be achieved through stepwise polymerization.<sup>399</sup> Dispersity index allows to measure chain distribution from the average molecular weight (MW) ratio to a number-average molecular weight ( $M_n$ ). Ideally, monodisperse polymers have a dispersity value of one, and polymers with a higher dispersity value are polydisperse. The degree of dispersity does not determine the effectiveness of the polymer; both high and low-dispersity polymers can exhibit unique properties.<sup>405</sup> Recently, polydispersity has gained strong consideration for its advantages in the compatibilization of copolymer blends.<sup>219</sup>

The most decisive physicochemical properties polymers', such as structural information and functionality, must be confirmed to assess the specific required parameters. The thermal property, molecular weight, dispersity, and morphology characterization are necessary investigations to tailor them to the intended application.<sup>416</sup> Various standard analytical techniques are available to gather complete information about the physicochemical properties of the polymers. The <sup>1</sup>H NMR, for instance, is considered a routine technique for monitoring the progress of polymerization and determining the theoretical MW and average chain length. The NMR characterization helps monitor polymerization progress and determine the molecular weight of polymers. Nuclei with unpaired spin possess a magnetic resonance effect. Thus, elements with unpaired nuclei, such as hydrogen (<sup>1</sup>H), carbon (<sup>13</sup>C), and phosphorus (<sup>31</sup>P), are NMR active. The polymerization of

(meth)acrylates could be monitored by their vinyl protons (at  $\delta$  5.6 and  $\delta$  5.9 ppm) and the ester protons (at  $\delta$  4.3 ppm for monomer and  $\delta$  4.1 ppm for polymer). Accordingly, the monomer conversion can be calculated using Equations 7 and 8, and polymer molecular weights can be determined using Equation 9.

$$\alpha^{Monomer} = \frac{\int_{4.1ppm}}{\int_{4.1ppm} + \int_{4.3ppm}} \dots\dots\dots(7)$$

$$\alpha^{Monomer} = \frac{\int_{6.2ppm(t,0)} - \int_{6.2ppm(t,h)}}{\int_{6.1ppm(t,h)}} \dots\dots\dots(8)$$

$$M_{n,NMR}^{Monomer} = \left\{ [\alpha^{Monomer}] / \left[ \frac{RA}{MRA} \right] \chi M_{wt}^{Monomer} + M_{wt}^{RA/MRA} \right\} \dots\dots\dots(9)$$

Where [RA] represents the molar concentration of the RAFT agent and [MRA] stands for the molar concentration of the macro-RAFT agent;  $\alpha^{Monomer}$  represents monomer conversion;  $\int_{4.1ppm}$  and  $\int_{4.3ppm}$  stands for integral areas of polymer and monomer, respectively, for methacrylate monomers. The  $\int_{6.2ppm(t,0)}$  and  $\int_{6.2ppm(t,h)}$  stand for the vinyl protons' of acrylate monomers before and after the polymerizations, respectively.<sup>417</sup>

The number average molecular weight (Mn) and weight average molecular (Mw) weight can be calculated using equations 10 and 11, respectively.

$$Mn = \frac{\sum_{i=1}^N N_i M_i}{\sum_{i=1}^N N_i} \dots\dots\dots(10)$$

$$Mw = \frac{\sum_{i=1}^N N_i M_i^2}{\sum_{i=1}^N N_i M_i} \dots\dots\dots(11)$$

The relative molecular weight of polymers is usually characterized using gel permeation chromatography (GPC) or size exclusion chromatography (SEC). The polymer concentration, structure, polarity, solubility, and chain-end groups can affect the accuracy of the obtained relative molecular weights. The dispersity of the polymer is thus calculated by equation 12.

$$PDI = \frac{\bar{M}_w}{\bar{M}_n} \dots\dots\dots(12)$$

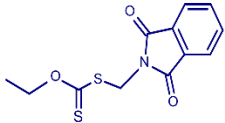
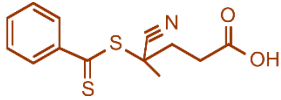
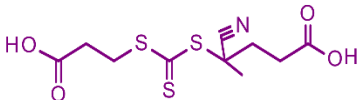
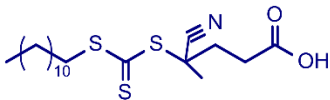
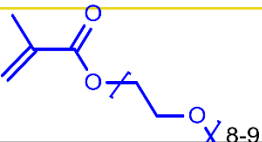
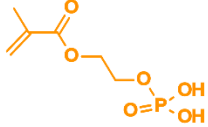
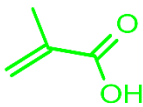
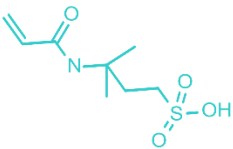
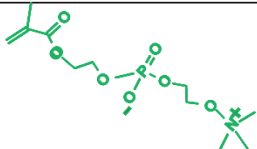
Fourier transform infrared spectroscopy (FTIR) of polymers is one of the most reliable techniques

in characterizing polymer functionalities.<sup>416</sup> Based on their bonding status, the functional groups in the polymers give specific characteristic absorption bands. Mukherjee et al. review in detail the FTIR absorption bands of different functional groups.<sup>416</sup> Thermal analysis is applicable to characterize polymers and nanoparticle's surface grafted ones.<sup>223, 418</sup> The weight loss during the thermal decomposition of the polymer gives general information on the hydrocarbon groups present. The TGA is also suitable for determining the graft density of polymer-modified nanoparticles.

### 4.3 Experimental section

O-ethyl xanthic acid potassium, potassium O-ethyl xanthate (95%, Sigma Aldrich); N- bromo phthalimide (98%, Sigma-Aldrich), hydrazine hydrate (Merck), magnesium Sulphate (Anhydrous) (Merck); cyano-4-(((dodecylthio)carbonothioyl)thio) pentanoic acid (99%, Boron molecular), 4-(((2-carboxyethyl)thio)carbonothioyl) thio)-4-cyanopentanoic acid (95%, Boron molecular); methacrylic acid (MAA) (95%, Sigma-Aldrich); 2-(methacryloxy) ethyl phosphate (MOEP); ethylene glycol methyl ether acrylate (OEGMA) ( $M_n = 500 \text{ g mol}^{-1}$ ); 2-methacryloyloxyethyl phosphorylcholine (MPC) (97%, Merck); Cyclohexane (99%, Merck); diethyl ether (Merck); brine solution; dimethylformamide (DMF) (Merck); Tetrahydrofuran (THF) (Merck); chloroform-d (99.8%, Merck), toluene (Merck), dimethyl sulfoxide-d<sub>6</sub> (DMSO-d<sub>6</sub>) (97%, Merck); inhibitor remover prepacked column (Merck) and deuterium oxide (99%, Merck); ) were used as received without further purification. Blue LED strip (460 nm); and Snakeskin dialysis tubing (3.5 K MWCO).

Table 2 Summary of RAFT agents and monomers used in the polymerization

	Structure	Abbrivation	Molecular weight	Remark
RAFT agent		OESPX	282 g mol <sup>-1</sup>	Synthesized
		CDPDB	279 g mol <sup>-1</sup>	Commercial
		CTCPA	307.4 g mol <sup>-1</sup>	Commercial
		CDCPA	403.5 g mol <sup>-1</sup>	Commercial
Monomer		OEGMA	500 g mol <sup>-1</sup>	Commercial
		MOEP	210 g mol <sup>-1</sup>	Commercial
		MAA	86 g mol <sup>-1</sup>	Commercial
		AMPS	207 g mol <sup>-1</sup>	Commercial
		MPC	295.5 g mol <sup>-1</sup>	Commercial

➤ Analytical instruments for the characterization of polymer

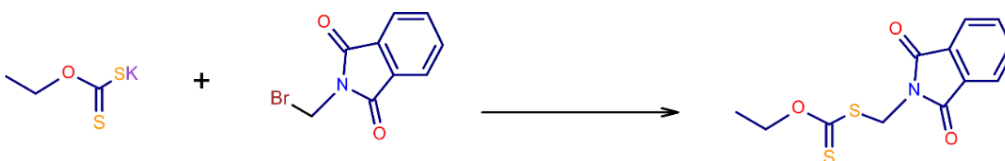
The Bruker NMR 400 MHz spectrometers were used to characterize the synthesized RAFT agents, monitor monomer conversion during polymerization, and determine the theoretical molecular

weights of the copolymers. Nicolet 6700 FT-IR spectrophotometer was used to characterize the chemical structure of the synthesized polymers and modified surfaces using the ATR technique. Thermo-gravimetric analysis (TGA), SQ600, was used to analyze the thermal property of the copolymers. Size exclusion chromatography ShimadzuRID-10A refractive index detector and an SPD-10A Shimadzu UV/Vis detector was implemented for the molecular weight and dispersity analysis.

#### 4.3.1 OESPX-based copolymer synthesis

##### ➤ O-Ethyl S-Phthalimidyl methyl Xanthate (OESPX) synthesis

The synthesis of OESPX (MW =268 g/mol) chain transfer agent (CTA) was performed according to the established procedure by Postman et al.<sup>419</sup> 1.03 g, O-Ethyl xanthic acid potassium salt (0.0064 mol) was added into a two-necked round-bottomed flask containing 20 mL of chloroform and stirred using a magnetic stirrer. 1.00 g, *N*-(bromomethyl) phthalimide (0.0042 mol) was added into a beaker containing 20 mL chloroform separately. The solution was mixed with the O-ethyl xanthic acid potassium suspension dropwise under the string. The reaction progressed for 18 hours, and the resulting mixture was diluted using 20 mL chloroform. After washing with DI water (twice, 50 mL) and brine (50 mL), the organic phase was collected and dehydrated using anhydrous MgSO<sub>4</sub>. The organic solution was then concentrated using a rotary evaporator, and the resultant products were dried under a vacuum for 48 hours. Finally, the OESPX was collected as light yellowish solids. The synthesized OESPX was characterized using <sup>1</sup>H NMR, <sup>13</sup>C NMR, FTIR, and melting point determination. The chemical reaction for synthesizing the OESPX is represented in Scheme 3.



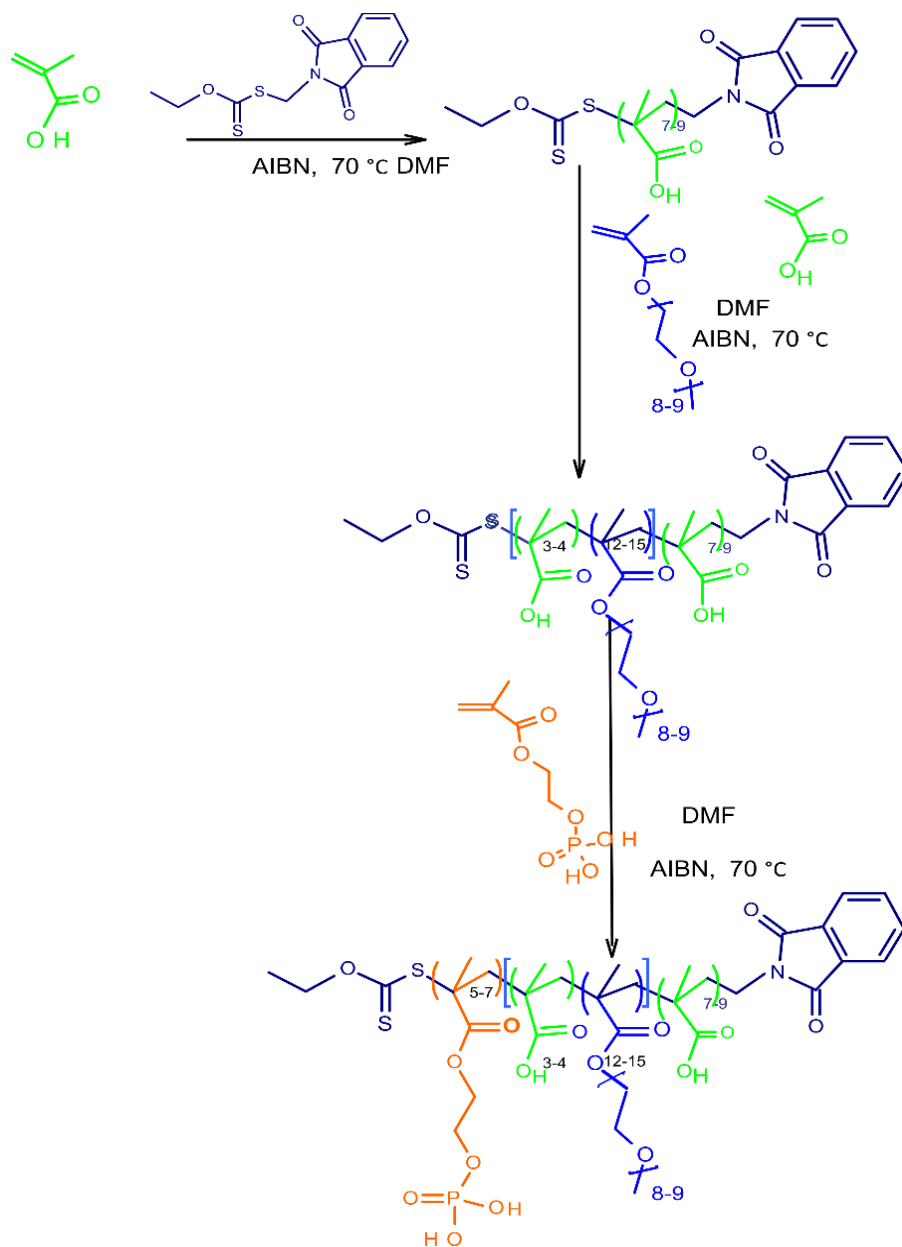
Scheme 3 The representation of the synthesis of OESPX.

##### ➤ Synthesis of OESPX-based triblock copolymer

0.18 g OESPX, 0.67 mmol, and 0.11 mg AIBN, 0.067 mmol, were added into a 50 mL round bottom flask containing 5 mL toluene. 0.35 g MAA, 4 mmol was added to the flask, and the mixture was purged with Argon gas for 30 minutes. The reaction was carried out at 70 °C for 7

hours. The progress of the reaction was monitored by using  $^1\text{H}$  NMR. At 60 to 70% MAA conversion, the reaction was stopped by quenching in an ice bath for 10 minutes. The diblock copolymer synthesis was then continued without purification of the macro-RAFT agent. The molecular weight of the macro-RAFT was calculated based on the  $^1\text{H}$  NMR result as MW= 884 g/mol and 0.4 gm, 0.45 mmol, was taken with 4.0 g OEGMA-500, 8 mmol, and 0.04 mmol AIBN was added into the mixture, and purged argon gas for 30 minutes. The polymerization was carried out at 70°C for 8 hours and stopped by quenching with an OEGMA conversion of 85%. Then the resulting products were purified via precipitation using diethyl ether as a non-solvent.

The synthesis of the diblock copolymer was performed by taking 1.2 g of the macro-RAFT agent 0.16 mmol, AIBN (0.02 mmol), and 0.25 g MOEP, 1.2 mmol were dissolved in DMF, and the mixture was purged using argon gas for 30 minutes. The polymerization was conducted at 70°C for 11 hours. The reaction was stopped by quenching in the ice bath, and the monomer conversion was 80%. The copolymer was purified by dialyzing against methanol for 24 hours using Snakeskin dialysis tubing (3.5 K MWCO), followed by lyophilization. The overall polymerization reactions of the triblock synthesis have been represented in Scheme 4. Subsequently, the OESPX-based triblock copolymer is called “Polymer ” .



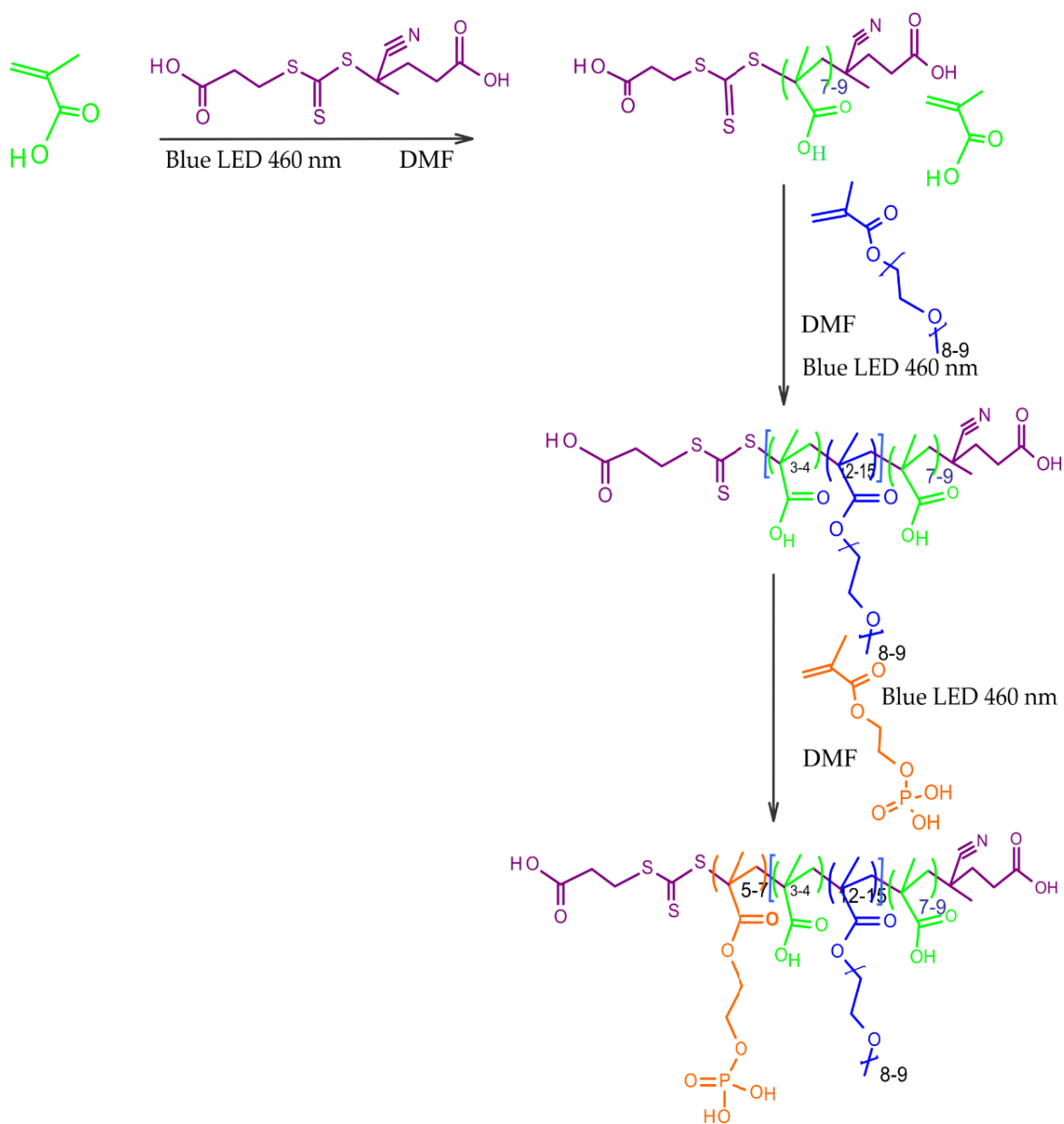
Scheme 4 Schematic illustration of the sequential synthesis of Polymer 1.

#### 4.3.2 CTCPA-based photo-induced triblock polymerization

The light-initiated polymerization was performed using a blue LED strip (460 nm). A 25 ml capacity Schleck tube was charged with 0.1 g CTCPA, 0.33 mmol, 0.7 g MAA, 8.0 mmol, and 5.0 ml DMF. The mixture was degassed through a three-cycle freeze-pump-thaw. The LED light was then ‘turned on,’ marking the start of the polymerization reaction. After 12 hours of irradiation, the polymerization was stopped at a monomer conversion of 70%. The diblock copolymer was



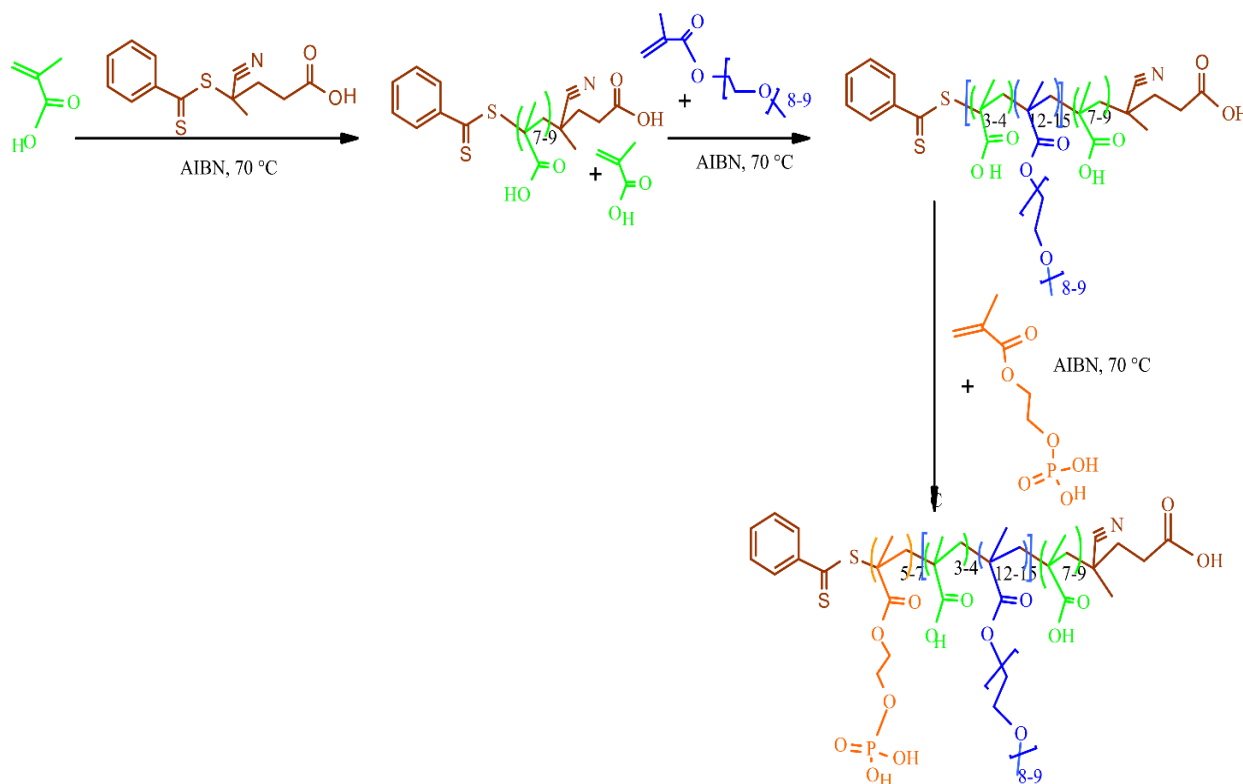
synthesized by adding 5 g OEGMA-500, 10 mmol. The mixture was degassed, reacted for 10 hours, and at 80% monomer conversion, the reaction was stopped. The polymer was precipitated in diethyl ether, and the triblock copolymer was synthesized by taking 1.5 g, 0.21 mmol, diblock with 0.3 g MOEP, 1.4 mmol, in 5.0 ml DMF. After degassing, the reaction was carried out for 11 hours, and the final tr-block polymer was purified via precipitation in diethyl ether. Subsequently, the copolymer is referred to as “Polymer 2”. Scheme 5 shows the overall reactions in the synthesis of the copolymer.



Scheme 5 Schematic representation of the synthesis of Polymer 2.

### 4.3.3 CPADB-based thermally initiated triblock polymerization

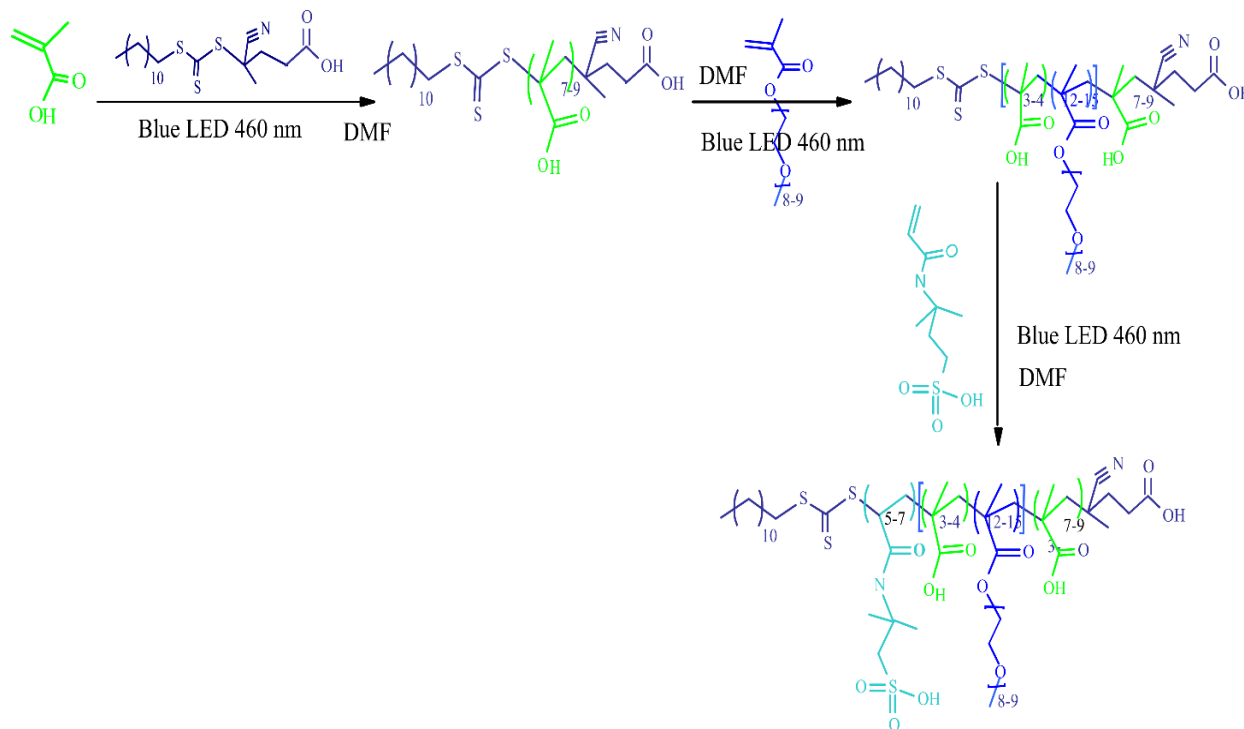
0.18 g CPADB, 0.65 mmol, and 0.11 mg AIBN, 0.067 mmol, were taken into a 50 mL capacity round bottom flask containing 5.0 mL toluene, and then 0.35 g MAA, 4 mmol, was added. The reaction progressed for 12 hours in a pre-heated oil bath at 70 °C and stopped at 70 - 80% monomer conversion. 5 g OEGMA-500, 10 mmol, was added, and purged with argon gas, for the reaction was further reacted for 8 hours. At 80% conversion, the reaction was stopped and precipitated using diethyl ether. A 1.5 g, 0.21 mmol of the second macro-RAFT was dissolved in 5.0 mL DMF, and 0.6 g MOEP, 2.8 mmol, and 0.11 mg AIBN, 0.06 mmol, were taken into and purged for 30 minutes and reacted for 11 hours at 70 °C. The resulting polymer was separated by precipitating out using diethyl ether, characterized, and stored at 4 °C till consumed for UCNPs surface modification. Subsequently, the triblock copolymer is referred to as “Polymer 3”. The sequential reactions in the macro-RAFT polymer, diblock macro-RAFT polymer, and the synthesis of the triblock copolymer are presented in Scheme 6.



Scheme 6 Schematic representation of the synthesis of Polymer 3.

#### 4.3.4 CDCPA-based photo-induced triblock polymerization

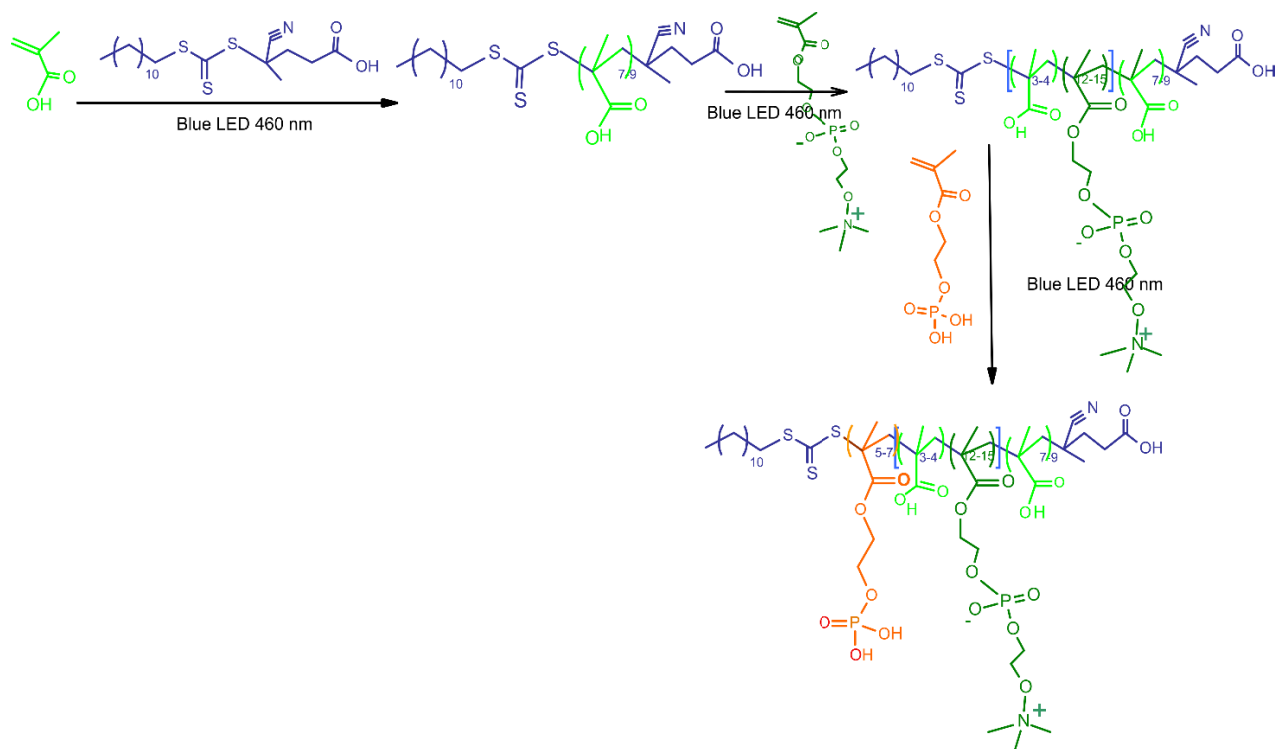
A triblock copolymer with sulphonate anchoring using 2-acrylamide-2-methylpropane sulphonic acid was synthesized as follows. A 25 ml Schleck tube was charged with 0.1 g CDCPA, 0.33 mmol, 0.35 g MAA, 4 mmol, and 5.0 ml DMF. The mixture was degassed through a three-cycle freeze-pump-thaw. The LED light was then ‘turned on, marking the start of the polymerization reaction. After 8 hours of irradiation, the polymerization was stopped at a monomer conversion of 70%. The diblock copolymer was synthesized by adding 5 g OEGMA-500, 10 mmol. The mixture was degassed, reacted for 10 hours, and at 80% monomer conversion, the reaction was stopped. The polymer was precipitated in diethyl ether, and the triblock copolymer was synthesized by taking 0.58 g AMPS, 2.7 mmol. The polymer was purified using diethyl ether and characterized using NMR and FTIR instruments. Subsequently, this triblock copolymer is called “Polymer 4”. The overall polymerization reactions for the macro-RAFT polymer, diblock macro-RAFT polymer, and triblock copolymer are given in Scheme 7.



Scheme 7 Schematic representation of the step-wise synthesis reactions for Polymer 4.

The purpose of synthesizing MPC-based triblock copolymer is to develop antifouling UCNP surfaces. In the case of AMPS-based copolymer, 0.1 g CDCPA, 0.33 mmol, and 0.35 g MAA, 5

mmol in 5.0 ml DMF was reacted. In the diblock copolymer synthesis, 2.5 g MPC, 8.5 mmol, was used instead of the OEGMA monomer. In the triblock copolymer synthesis, 1.5 g of the diblock, 0.21 mmol, and 0.4 g MOEP, 1.9 mmol, were dissolved in 5.0 mL DMF, degassed, and then reacted for 10 hours. The final polymer was purified by dialysis against methanol using Snakeskin<sup>®</sup> Dialysis tubing (3.5 K MWCO) and characterized. Subsequently, the MPC triblock copolymer is called “Polymer 5”. The overall stepwise synthesis reactions mechanism for MPC-based triblock copolymer is given in Scheme 8.

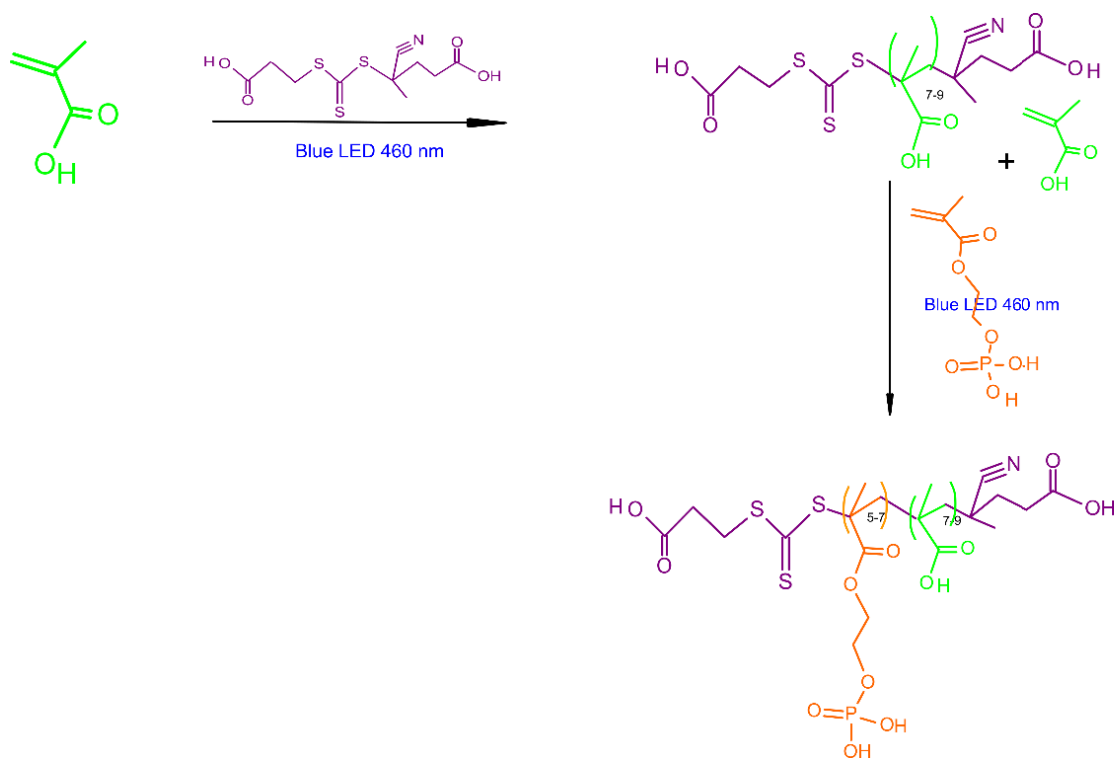


Scheme 8 Schematic illustration of the sequential synthesis of Polymer 5.

#### 4.3.5 CTCPA-based photo-induced diblock polymerization

The short branch MAA-based diblock copolymer CPCPA-p(MOEP)-b-p[(MAA)] was synthesized as follows. 0.1 g CTCPA, 0.33 mmol, and 0.35 g MAA, 0.4 mmol, were taken in 5.0 mL DMF. After the mixture was degassed, the reaction progressed under LED blue (460 nm) strip irradiation for 12 hours. At 60 to 70% monomer conversion, the reaction was stopped, and the diblock synthesis was continued by adding 0.6 g MOEP, 2.8 mmol. The mixture was degassed and allowed to react for 11 hours. The resulting copolymer was precipitated out in diethyl ether, and

subsequently, this copolymer is called “Polymer 6”. The overall synthesis reaction of the diblock copolymer is represented in Scheme 9.



Scheme 9 Schematic representation of the synthesis of Polymer 6.

## 4.4 Result and discussion

### 4.4.1 OESPX-based triblock copolymer

#### ➤ Synthesis of OESPX

O-Ethyl S-Phthalimidyl methyl xanthate (OESPX) RAFT agent (Mol. Wt. =282 g mol<sup>-1</sup>) was synthesized and characterized. A 1.01 g (86% yield) was obtained, and it has been confirmed that the compound has a melting point is 94 °C, and the obtained melting point corresponds with the previously reported value. Figure 47A, the <sup>1</sup>H NMR peaks show characteristic protons of the OESPX molecule. The peak at δ 1.47 belongs to the protons of CH<sub>3</sub>CH<sub>2</sub>-), the protons at δ 4.70 is associated with CH<sub>3</sub>CH<sub>2</sub>-O, and the protons at δ 7.75 and δ 7.85 belong to aromatic groups. In Figure 47B, the <sup>13</sup>C NMR confirms the OESPX carbons. The peak at δ 210 ppm, for instance, belongs to the dithiol group, the peak at δ 166 is due to the carbonyl carbon, and the peaks at δ 135 ppm, δ 131 ppm, and δ 124 ppm positions correspond to the ortho-, meta- and para- carbons of the

Phthalimidyl group. The peaks at  $\delta$  70 ppm are from the oxygen-connected (-C-O-) carbon triple peaks around  $\delta$  40 ppm due to the methylene group carbon attached to nitrogen, and the  $\delta$  15 ppm peak belongs to the methyl group. The  $^1\text{H}$  NMR and  $^{13}\text{C}$  NMR spectra of the OESPX are presented in Figure 47.

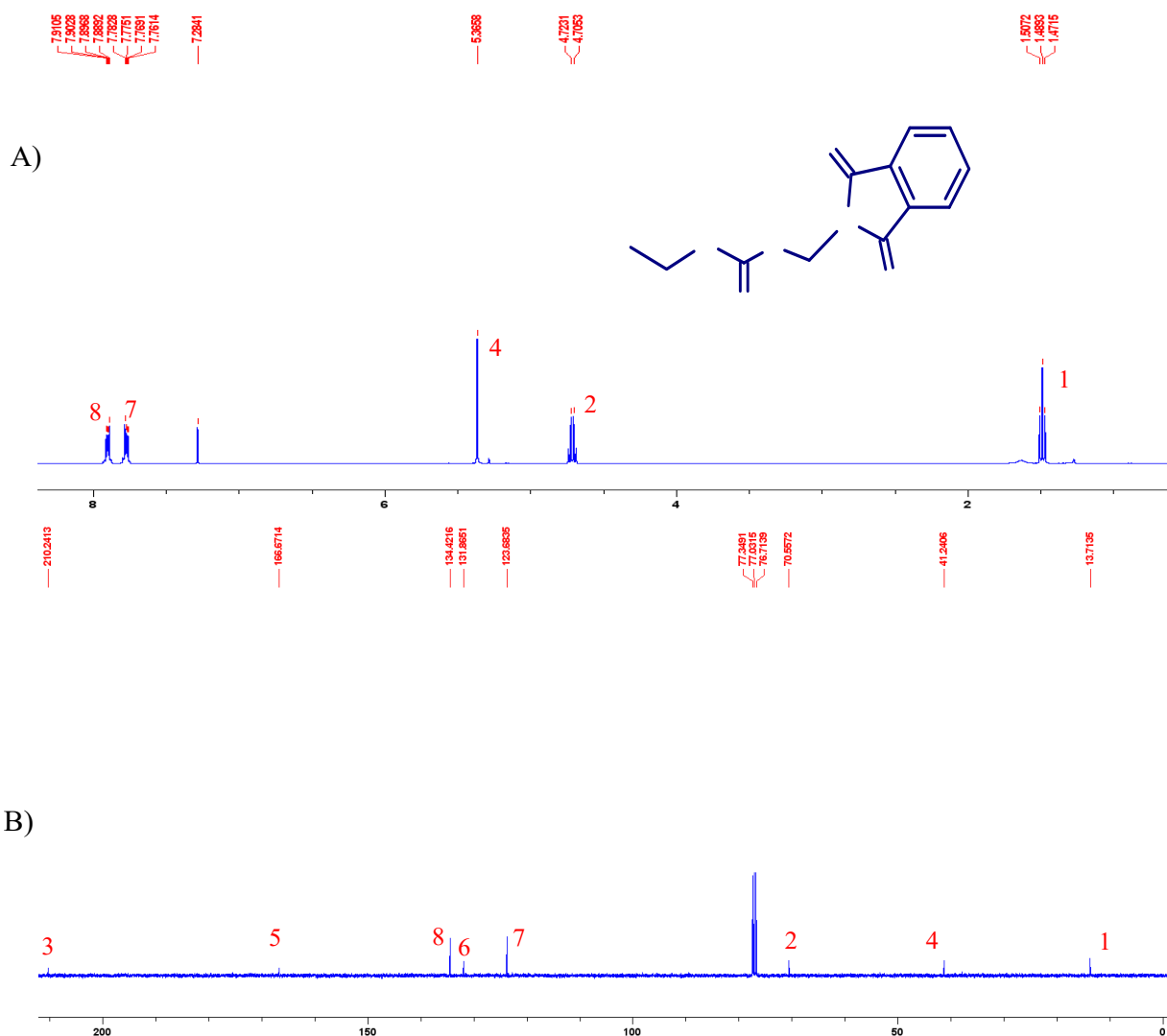


Figure 47 The  $^1\text{H}$  NMR (A) and  $^{13}\text{C}$  NMR (B) spectra of OESPX.

The synthesis of OESPX based copolymers was performed via thermal technique, using AIBN, at  $70^\circ\text{C}$ . The first macro-RAFT agent was synthesized from MAA. The carboxylic block provides high carboxylic groups and accessibility in further EDC-based functionalization. The end group modification provides a flexible amine group that could facilitate efficient coupling. Since the molecular weight of the poly (methyl acrylic acid) macro-RAFT is incredibly low, purification of

the macro-RAFT agent by solvent precipitation method and membrane dialysis was challenging. The  $^1\text{H}$  NMR spectra of the different polymers' synthesis steps are given in Figure 48.

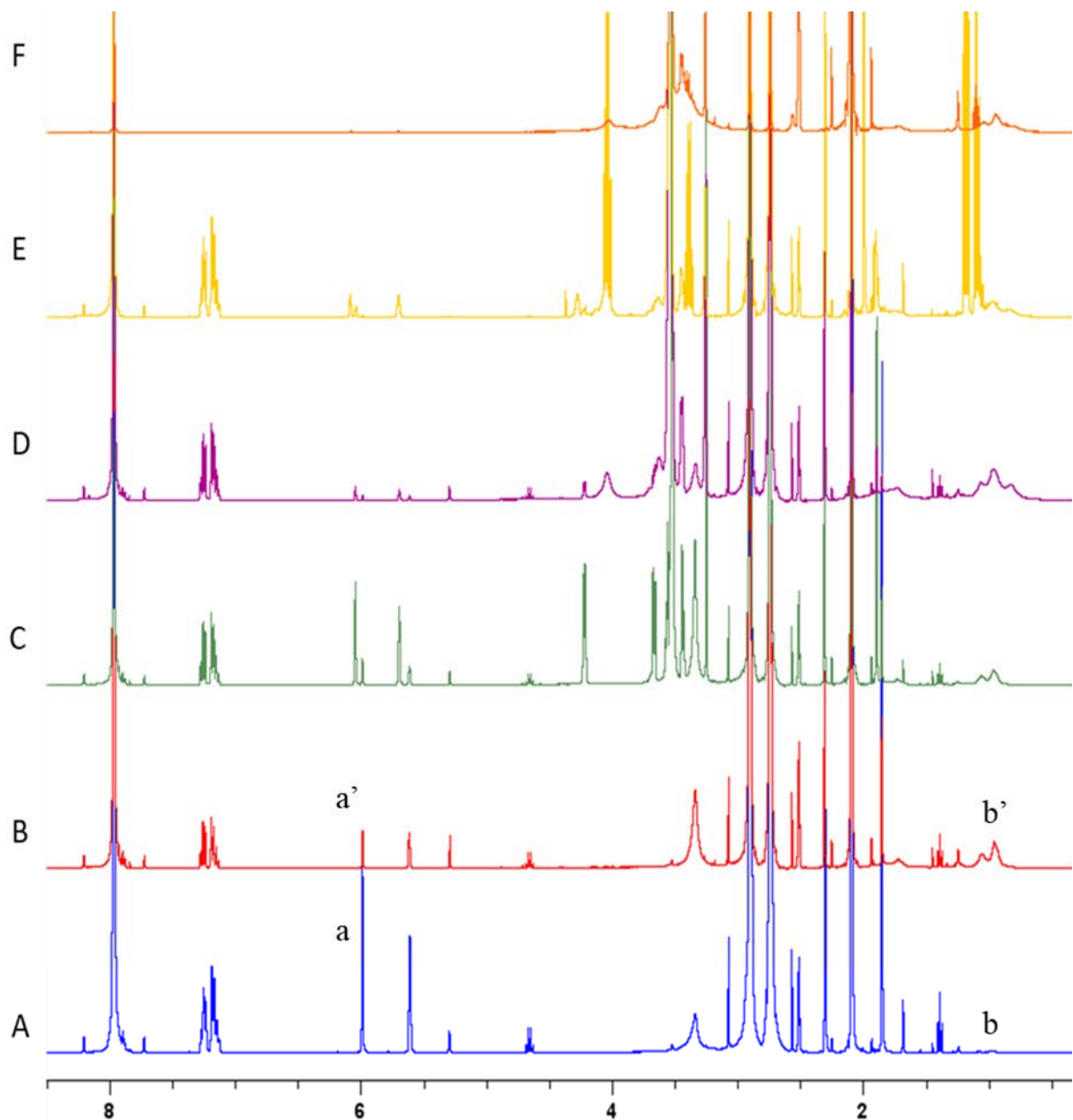


Figure 48 The  $^1\text{H}$  NMR spectra of Polymer 1: synthesis of MAA macro-RAFT agent at 0 hours (A) and 7 hours (B); synthesis of diblock at 0 hours (C) and 8 hours (D) hours; triblock synthesis at 0 hours (E) and 11 hours (F) ( $^1\text{H}$  NMR solvent:  $\text{DMSO-d}_6$ ).

The polymerization progress was assessed using  $^1\text{H}$  NMR, as presented in Figure 48. Figures 48A and B present the change in vinyl proton intensity before and after the polymerization for each

block synthesis step. At the start of the reaction, the high concentration of the vinyl protons is displayed at  $\delta$  5.6 and  $\delta$  5.9 ppm, which is indicated as a and a'. The change in the methyl group intensity around  $\delta$  . ppm i s also labeled as b and b's. Similarly, the synthesis of the diblock and the triblock copolymers was monitored, as mentioned in the synthesis of the first block, from intensity changes of monomer and polymer protons, as shown in Figures 48C to F.

The vinyl protons of the monomers are essential for monitoring the progress of polymerization. The significant change in monomer protons intensity confirms that the polymerizations have been achieved successfully. The methyl group intensity changes at  $\delta$  0.9 are the confirmation for the polymers. At the start of the reaction, Figure 48A, at the start of the polymerization, no methyl and methylene proton peaks were found at  $\delta$  1.0 to 1.9 ppm regions. However, after 8 hours, as seen in Figure 48B, the reduction in the intensity of the vinyl protons and the appearance of new broad peaks at  $\delta$  1.0 to 1.9 ppm indicates the formation of the polymer. In the subsequent synthesis, Figure 48C shows  $^1\text{H}$  NMR spectra of vinyl protons of OEGMA monomer and unreacted MAA monomer. An intense peak from the ester proton of the OEGMA monomer appears at  $\delta$  4.3 ppm. After 8 hours of reaction, an 85% monomer conversion was achieved. The monomer conversion has been observed from the diminishing of vinyl and ester protons peaks in Figure 48D. The second macro-RAFT was purified, and then the triblock synthesis was performed with MOEP. Figure 48E shows the initial vinyl and ester proton peaks of the MOEP. After 10 hours of reaction, 70% monomer conversion was achieved, and the polymer was purified through diethyl precipitation. The calculated average molecular weight for Polymer 1 is  $9230 \text{ g mol}^{-1}$ .

As the previous report indicates, a diblock with an OEGMA block with 13 units perform well in the biofunctionalization of the UCNPs.<sup>420 433</sup> The synthesized copolymers contain an average of MAA 7-10 blocks, OEGMA 13 - 15 blocks, and MOEP 5 to 7 blocks. The primary purpose of introducing MAA units in the copolymer is to improve the reactivity of the copolymer during surface grafting. The MOEP blocks are responsible for integrating the polymer into the nanoparticle surfaces. The living of the copolymerization was controlled by keeping the monomer conversion less than 85%. A compressive representation, Figure 49, has been given on the chemical structure of the triblock copolymer, its  $^1\text{H}$  NMR, ATR-FTIR, and TGA.



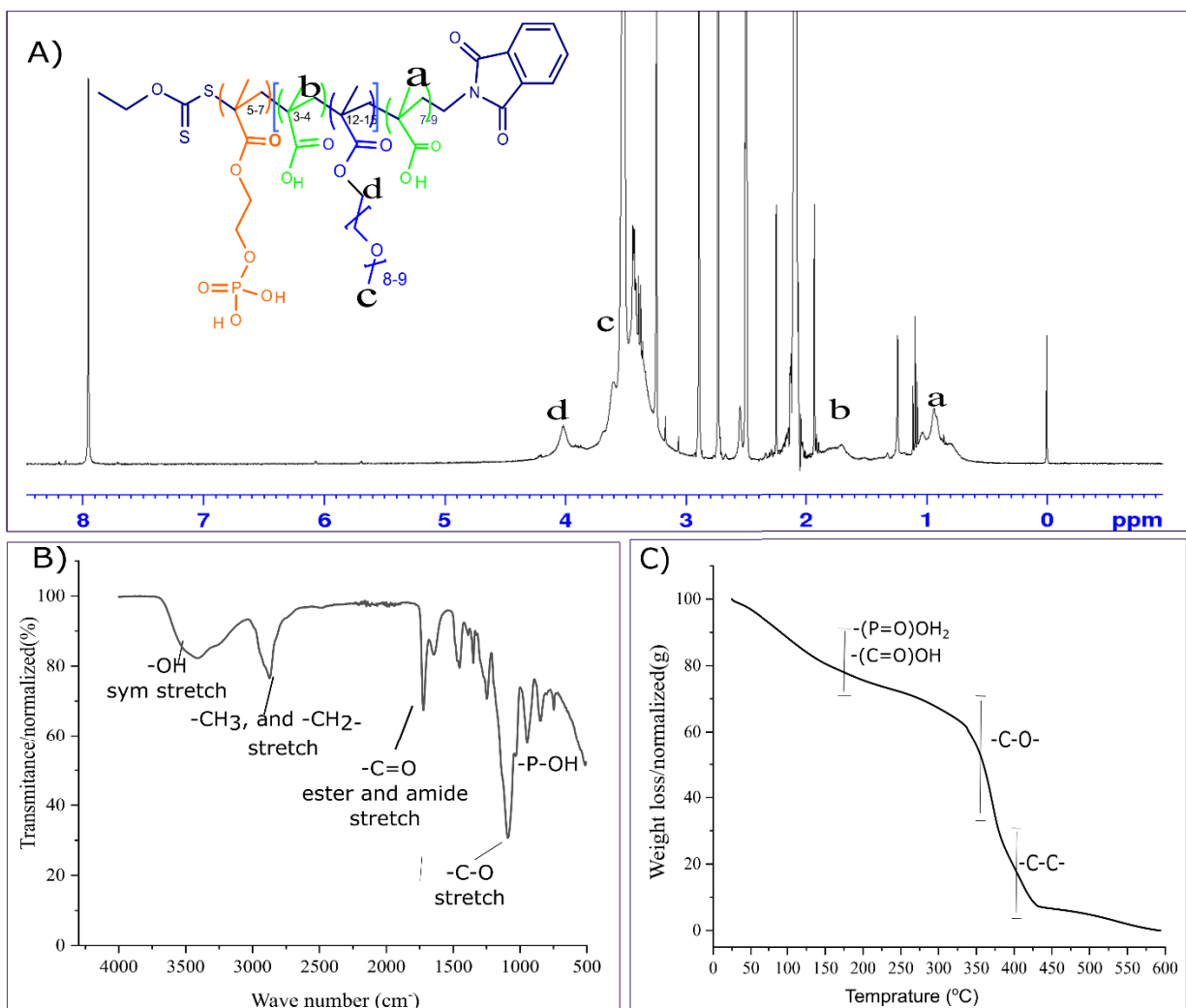


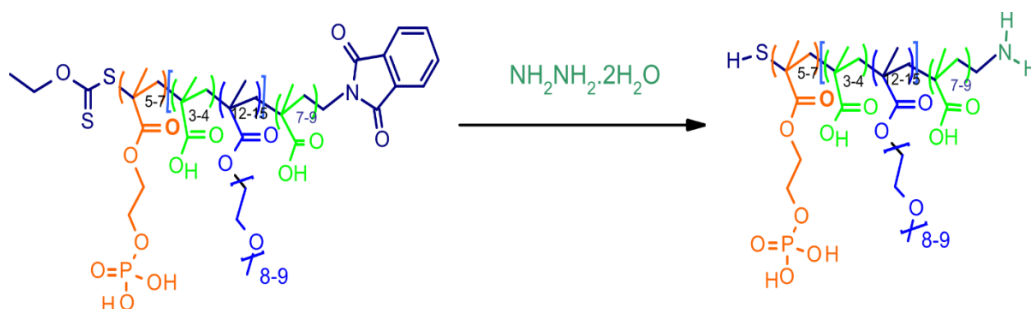
Figure 49 The <sup>1</sup>H NMR spectrum (A), ATR-FTIR spectrum (B), and TGA (C) of Polymer 1.

Figure 49A shows characteristic protons of the copolymer. As indicated in the corresponding structural representation, the proton at  $\delta$  4.0 ppm belongs to the ester protons of the OEGMA blocks. The high concentration of the methyl groups from the different blocks is indicated at  $\delta$  0.9. The different blocks of the triblock. Like the other copolymers, Polymer 3 consists of an average of seven to nine MAA units. In the polymer <sup>1</sup>H NMR, the common monomer peaks at  $\delta$  4.3,  $\delta$  4.2,  $\delta$  5.6, and  $\delta$  6.2 ppm are disappeared. It confirms that the copolymer is purified well. The intense bands at  $\delta$  0.9 to 1.2 and  $\delta$  1.8 to 2.0 ppm belong to methyl end groups and backbone protons.

The ATR-FTIR, Figure 49B, shows the main functional groups of Polymer 1. The enhanced absorption at 3500 to 3000 cm<sup>-1</sup> corresponds to hydroxyls in the carboxylic group. The absorption bands of the methyl end group, and methylene backbone of the copolymer are visible at 2800 to

2900  $\text{cm}^{-1}$ . The absorption bands at 1650 to 700  $\text{cm}^{-1}$  belong to the different carbonyl groups of the blocks. The peak at 970  $\text{cm}^{-1}$  belongs to phosphate functionality. The TGA analysis, Figure 49C, was performed from 25  $^{\circ}\text{C}$  to 600  $^{\circ}\text{C}$  at a heating rate of 10  $^{\circ}\text{C}$  min under an air atmosphere. The hydroxy group decomposition from the carboxylic and phosphate groups is visible at 100 to 150  $^{\circ}\text{C}$ , and the decomposition of carboxylate groups is visible at 250 to 300  $^{\circ}\text{C}$ . The degradation of the ether groups showed from 300 to 350  $^{\circ}\text{C}$ . The alkane backbone decomposition and the decomposition of the carbon double bonds are observed at 350 to 500  $^{\circ}\text{C}$ .

The OESPX-based copolymers have a unique advantage because the cleavable phthalimide end-group enables post-surface grafting end-group modification.<sup>211</sup> The phthalimide end group can be transformed into the desired functionalities, such as amine and sulfhydryl. Since both end groups of the OESPX chain transfer agent are cleavable, introducing amine and azido groups gives a unique advantage. The biofunctionalization of polymers is performed through EDC coupling, maleimide, and click chemistry. The end group modification hydrazinolysis gives amine and sulfhydryl group or hydrazine functionalities. The introduction of amine functionality provides an EDC coupling opportunity, and the sulfhydryl group enables maleimide coupling. The detailed mechanism of the end group transformation is shown in Scheme 10.



Scheme 10 Representation of the hydrazinolysis of Polymer 1 to introduce amine and sulfhydryl functionalities.

#### 4.4.2 CTCPA-based triblock copolymer

The CTCPA RAFT agent contains a double carboxylic acid end group. CTCPA is suitable for both traditional thermal initiation and recent photo-based initiated polymerizations. Photo-activation avoids contamination and degradation due to the exogenous initiator and high-temperature reaction. The calculated average molecular weight for Polymer 2 is 9260  $\text{g mol}^{-1}$ . The  $^1\text{H}$  NMR

analysis on the successive copolymerization during the development of Polymer 2 has been shown in Figure 50.

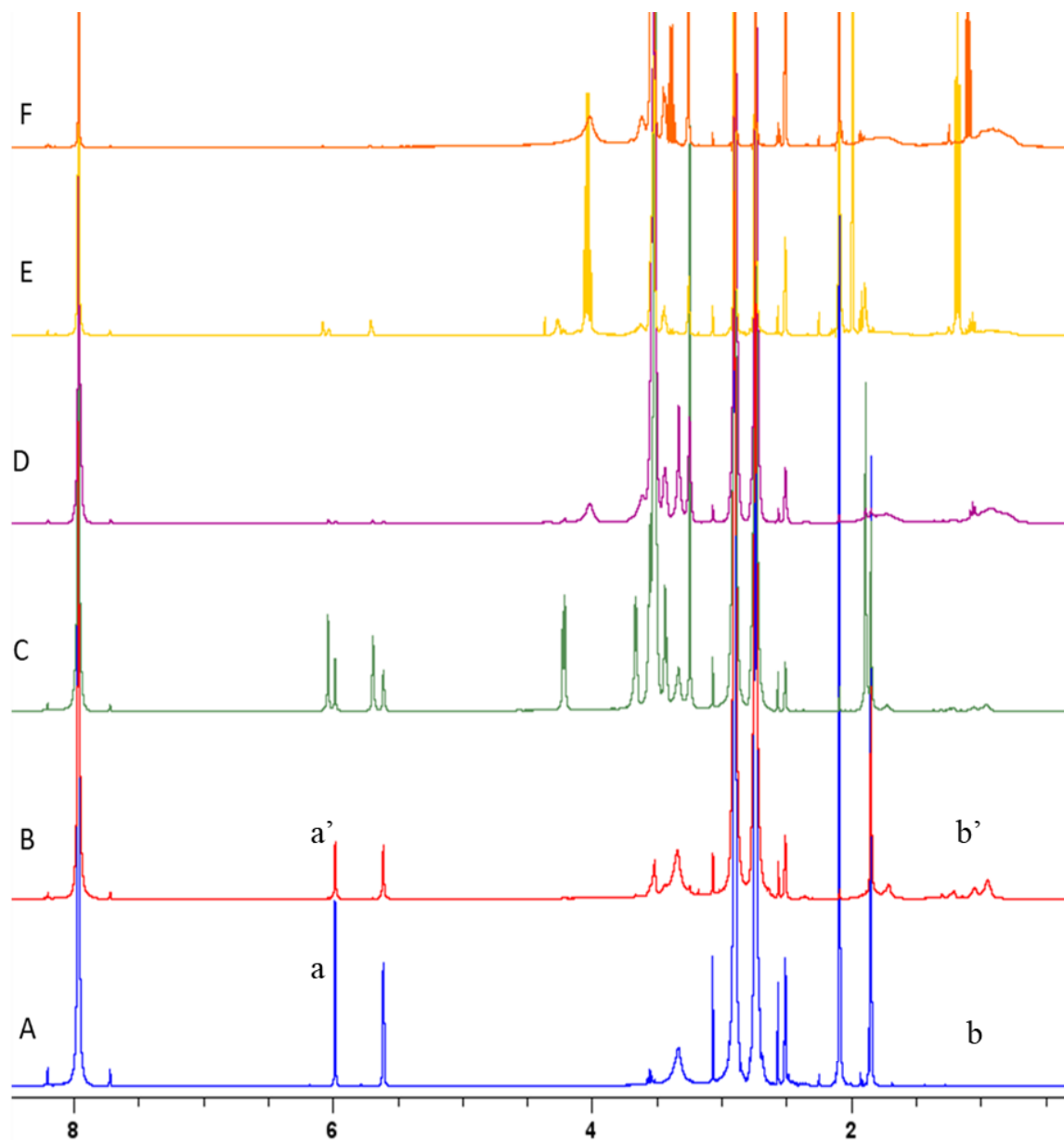


Figure 50  $^1\text{H}$  NMR spectra of Polymer 2: MAA macro-RAFT agent formation at 0-hour (A) and 12 hours (B) diblock synthesis at 0 hours (C) and 10 hours (D) hours; triblock synthesis at 0 hours (E) and 11 hours (F) (NMR solvent: DMSO- $d_6$ ).

The primary purpose of enhancing the carboxylic functionality is to improve the coupling of the surface-grafted polymers. The CTCPA-based copolymer produces enhanced surface carboxylic density compared to copolymers from RAFT agents with single carboxylic end groups. The excess

carboxylic groups from triblock grafted UCNP provide accessible reactive sites for surface coupling. The hydroxyl groups also produce a high degree of hydrophilicity. The hydrophilicity induced due to a large number of carboxylic groups improves the antifouling capacity of the surface.<sup>421</sup>

In the synthesis of Polymer 2, photo-initiated polymerization was carried out using blue LED strip (460 nm). The pi electrons of the thiocarbonyl group are susceptible to initiate radical polymerization. The tri-thiocarbonyl RAFT agents generate radicals, and the reaction proceeds through the further radical attack at the vinyl functionality monomer. The reaction progresses further till all the monomers are consumed, and a dead polymer is formed. In Figure 51, the <sup>1</sup>H NMR, ATR-FTIR, and TGA of Polymer 2 have been presented.

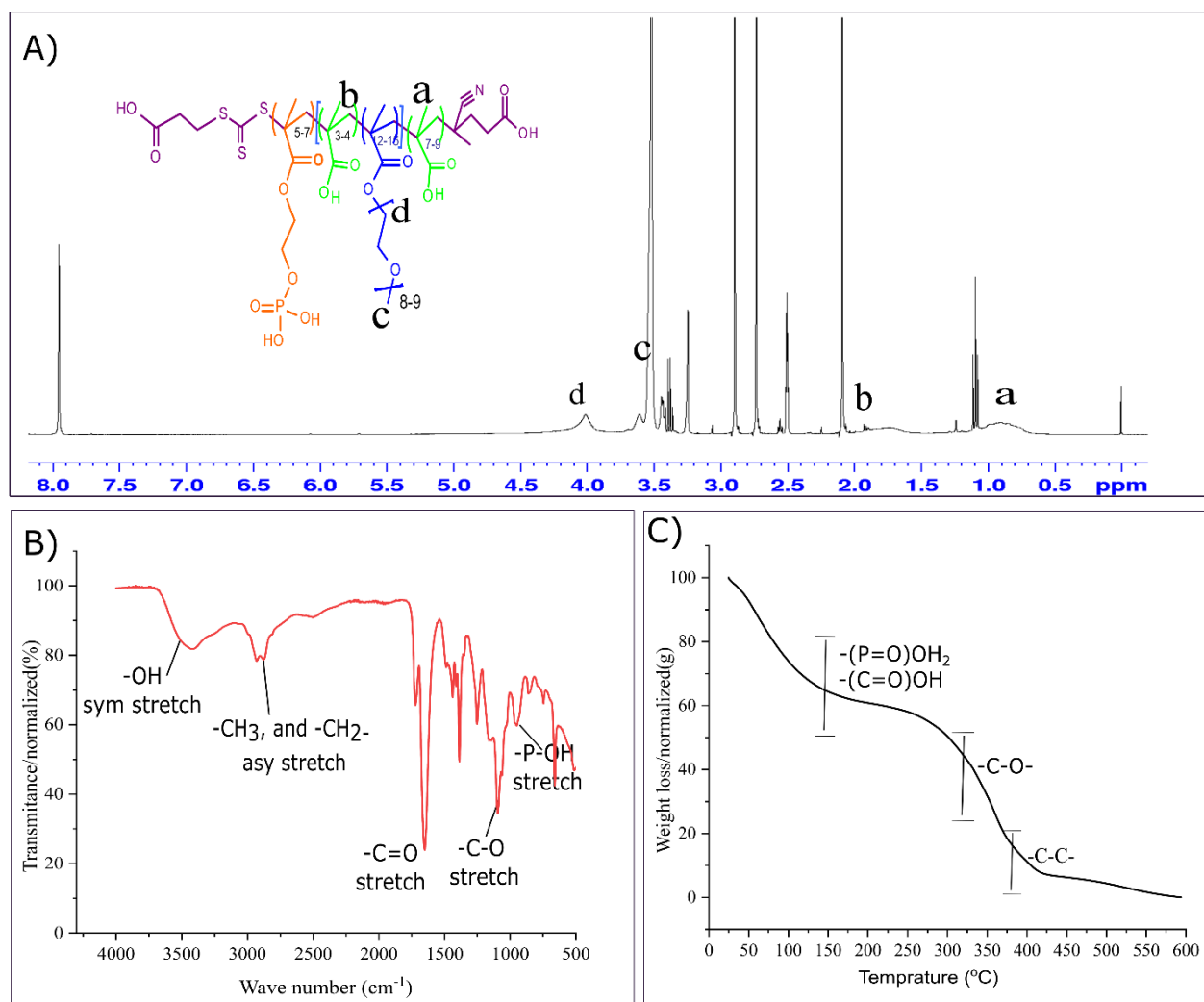


Figure 51 The <sup>1</sup>H NMR spectrum (A), ATR-FTIR spectrum (B), and TGA (C) of Polymer 2.

In Figure 5 A, the change in vinyl proton intensity at  $\delta$  5.6 and  $\delta$  5.9 ppm before and after polymerization is observed as indicated as a and a'. The change in the methyl group intensity around  $\delta$  . ppm, labeled as b and b', confirms the polymerization's effectiveness. Similarly, the diblock and the triblock synthesis were monitored from the monomer and polymer protons intensity changes. Figure 51B shows the main functional groups, and Figure 51C belongs to the TGA curve of Polymer 2.

The surface hydrophilicity of polymer-grafted particles has a vital role in the in-vivo applications of UCNPs. Copolymers composed from hydrophilic groups carboxylic, amine, or oxide groups develop enhanced UCNPs hydrophilicity. The availability of carboxylic hydroxyl and amine functionalities is responsible for surface hydrophilicity and reactivity to incorporate bioactive molecules. The hydrophilic surface generated high hydration and stabilized the modified particles by preventing protein corona during the in-vivo delivery application.<sup>62, 422</sup>

#### 4.4.3 CPADB-based triblock copolymer

The copolymers from the CPADB-RAFT agent have a relatively high degree of hydrophobicity. The amphiphilicity of those copolymers could be enhanced from MMA and OEGMA monomers. The CPADB RAFT agent had been employed in the conventional thermal synthesis in the presence of AIBN. The polymerization solvent has a vital role in facilitating the chain transfer process. A mixed solvent of 20% DMF in toluene was used to synthesize MAA macro-RAFT. The MAA macro-RAFT agent reacted with OEGMA without purification to synthesize diblock.

As presented in Figure 52, the progress of the polymerization was monitored from the change in proton intensity. In Figure 52A, the vinyl protons intensities before and after the reaction observed at  $\delta$  5.6 and  $\delta$  5.9 ppm are indicated as a and a'. The change in the methyl group intensity around  $\delta$  . ppm is also labeled as b and b's. Similarly, the diblock and the triblock synthesis were monitored from the monomer and polymer protons intensity changes, as shown in Figures 52C to F. Figures 52A and B belong to the MAA macro-RAFT agent at 0 and 12 hours. Figures 52 C and D belong to the diblock from the OEGMA and unreacted MAA, and Figures 52E and F stand for Polymer 3. The average molecular weight for Polymer 3 is estimated to be  $9232 \text{ g mol}^{-1}$ .

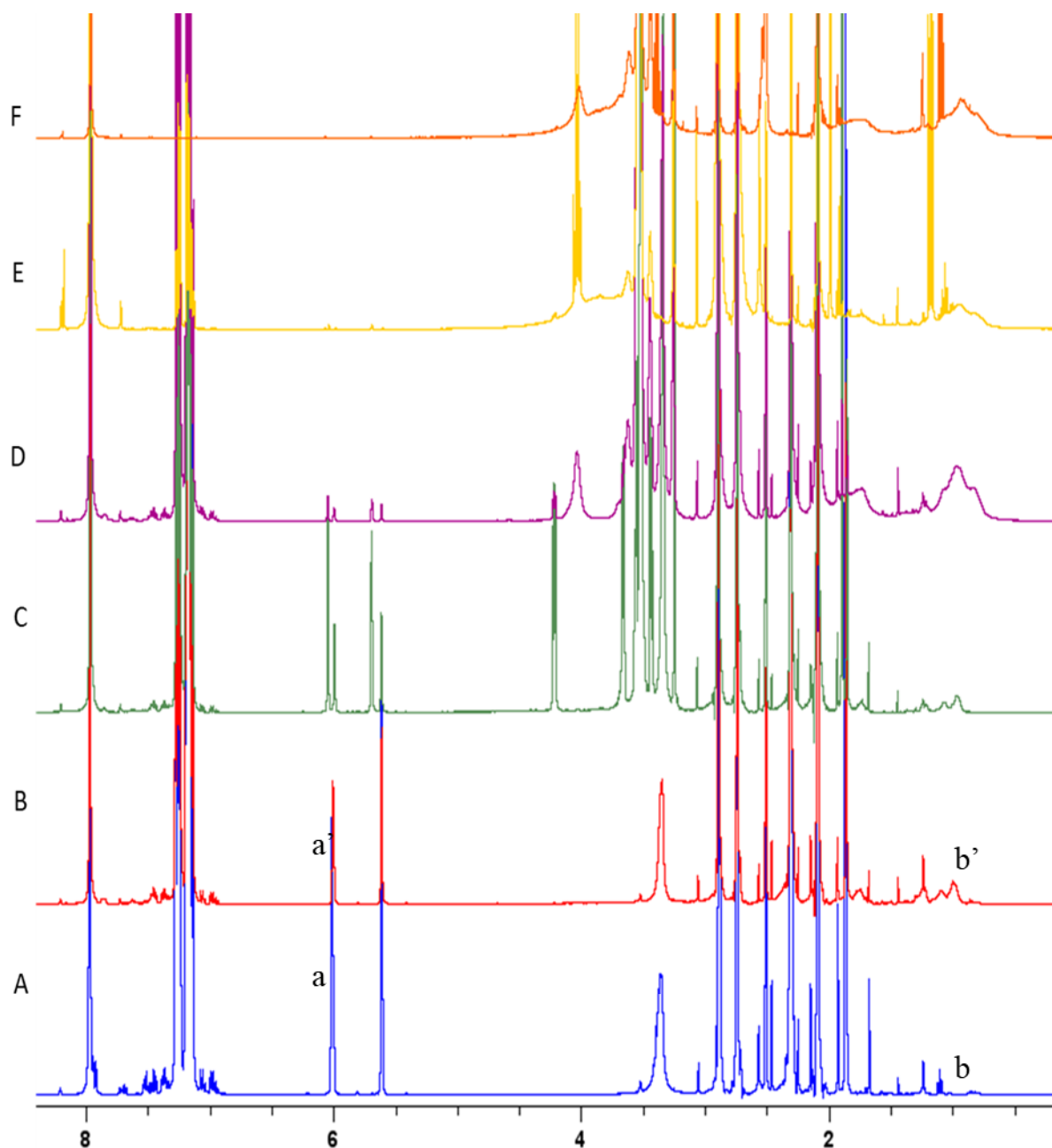


Figure 52  $^1\text{H}$  NMR spectra of Polymer 3: MAA macro-RAFT agent synthesis at 0 hours (A), and 12 hours (B); diblock synthesis at 0 hours (C) and 8 hours (D) hours; triblock synthesis at 0 hours (E) and 11 hours (F) (NMR solvent: DMSO- $d_6$ ).

Polymer 3 was characterized for its chemical functionalities and its thermal properties. As shown in Figure 53,  $^1\text{H}$  NMR, FTIR, and TGA characterization of Polymer 3 are presented. Figure 53A shows the  $^1\text{H}$  NMR spectra of Polymer 3, with its structural representation. The  $^1\text{H}$  NMR helps to

confirm the purity of the final polymer. The characteristic protons of the purified copolymer are labeled and located on the chemical structure.

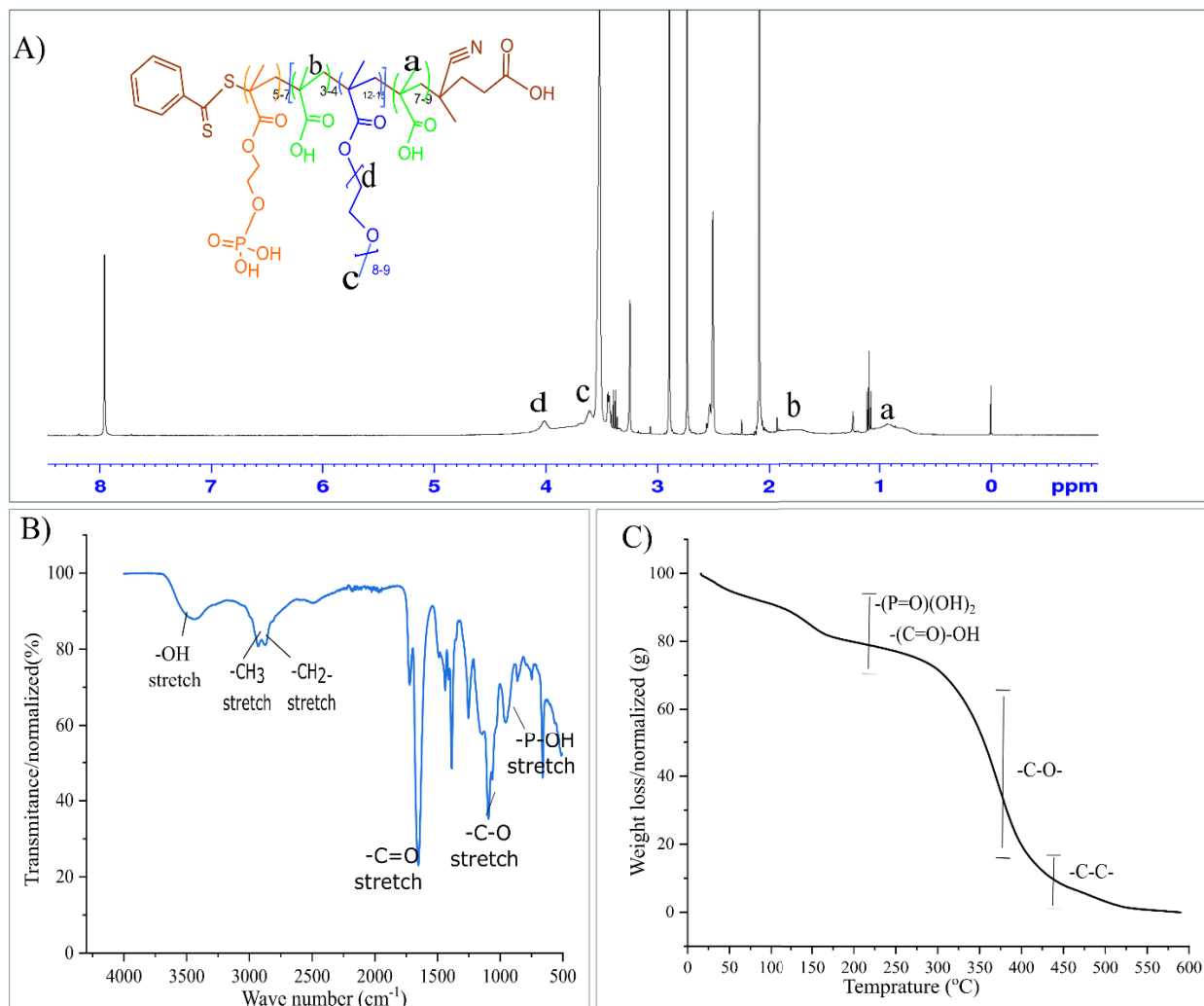


Figure 53 The <sup>1</sup>H NMR spectrum (A), ATR-FTIR spectrum (B), and TGA thermograph (C) of Polymer 3.

The ATR-FTIR spectrum of the copolymer, Figure 53B, reveals the functional groups of the purified copolymer. As discussed in the case of the polymers, the broadband peak at 3000 cm<sup>-1</sup> to 3500 cm<sup>-1</sup> regions is due to the carboxylic hydroxyl groups of the MAA units and from the RAFT agent end group. The absorption peak at 1720 cm<sup>-1</sup> belongs to carbonyl groups from each block. At 2900 cm<sup>-1</sup>, the backbone proton methyl stretch is visible, and the rise at 970 cm<sup>-1</sup> belongs to phosphate groups of the MOEP block. Figure 53C shows the decomposition curves of the different groups as described in the case of Polymer 1.

The proportion of the component blocks could control the amphiphilicity of the copolymers. The RAFT agent R-end group of Polymer 3 exhibits a high degree of hydrophobicity. The OEGMA units have a substantial role in the amphiphilicity of the final polymer. As the OEGMA block is the major component of the copolymer, the physicochemical property of the copolymer could be controlled through optimization of its amount. The MAA block has a high-water retention capacity at its carboxylic end groups. The carboxylic groups also strongly determine the physicochemical property of the grafted nanoparticles because an increased carboxylic group forms a strong hydrogen bonding and particle aggregation.

#### 4.4.4 CDCPA-based triblock copolymer

The long hydrocarbon Z-group of the CDCPA contributes a high degree of hydrophobicity in copolymer development. Here, the CDCPA was used in synthesizing two different triblock copolymers from AMPS anchoring unit (Polymer 4) and MPC monomer (Polymer 5). The synthesis of Polymer 4 is to implement sulphonate anchoring groups from the AMPS functionality. The AMPS functionalized polymers help develop UCNP surfaces that could perform at lower pH ranges. Especially the implementation of combined grafting using both the phosphate and sulphonate-containing copolymers allow the production of UCNP surfaces with better stability in ionic conditions. Figure 54 presents the  $^1\text{H}$  NMR, ATR-FTIR, and TGA of the synthesized copolymers.



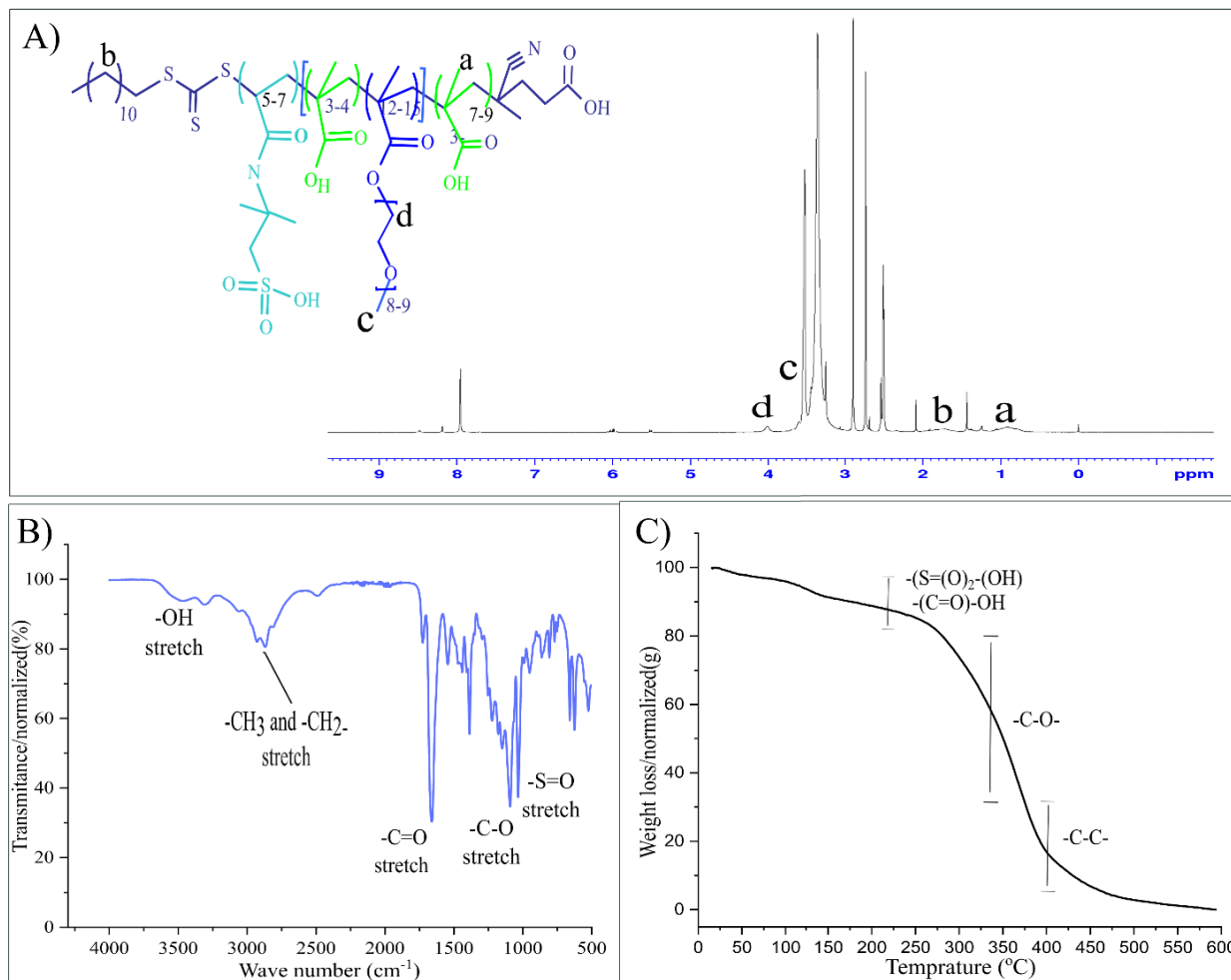


Figure 54 The <sup>1</sup>H NMR spectrum (A), ATR-FTIR spectrum (B), and its TGA thermograph (C) of Polymer 4.

The <sup>1</sup>H NMR spectra, Figure 54A, show the characteristic protons of the purified copolymer. The corresponding chemical structure of the polymer depicts the branched structure of the copolymer. The average molecular weight for Polymer 4 is estimated to be 9230 g mol<sup>-1</sup>. The ATR-FTIR spectrum, Figure 54B, indicates the functional groups of the purified copolymer. As discussed in the case of the previous polymers, the broadband peak at 3000 cm<sup>-1</sup> to 3500 cm<sup>-1</sup> regions is due to the carboxylic hydroxyl groups in the polyacrylic block and the RAFT agent end group.

The intense peak at 1720 cm<sup>-1</sup> belongs to the carbonyl groups from each block. At 2900 cm<sup>-1</sup>, the backbone proton methyl stretch is visible, and the rise at 1040 cm<sup>-1</sup> belongs to phosphate groups of the sulfite (-S=O) functionality. Figure 54C shows the decomposition curves of the different

groups as described in the case of Polymer 1. The stepwise synthesis of the triblock copolymer was monitored using  $^1\text{H}$  NMR, as presented in Figure 55.

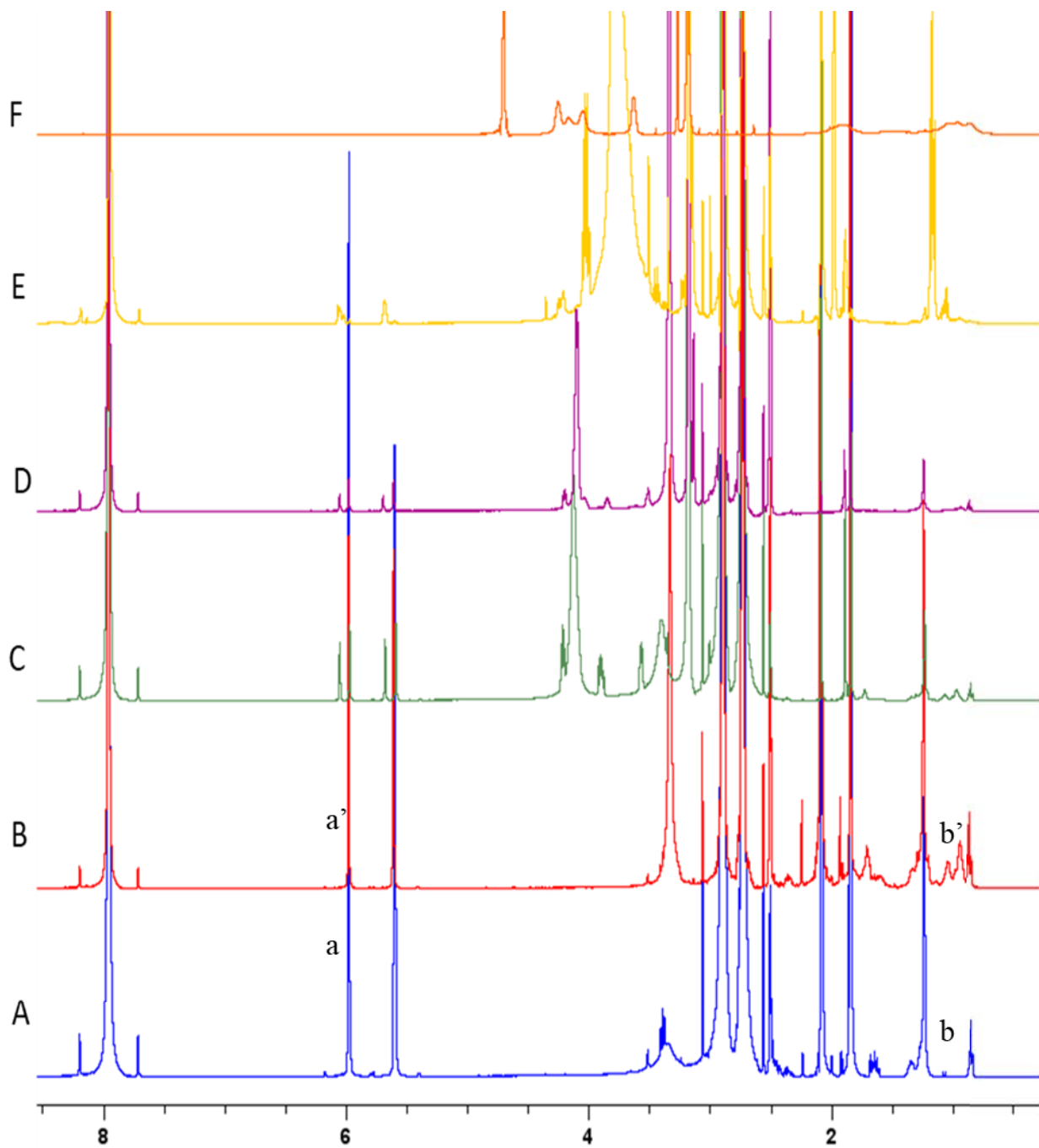


Figure 55 The  $^1\text{H}$  NMR spectra of Polymer 5: MAA macro RAFT agent formation at 0 hours (A) and 8 hours (B) diblock synthesis at 0 hours (C) and 10 hours (D) hours; triblock synthesis at 0 hours (E) and 11 hours (F) (NMR solvent: A-E DMSO- $d_6$ ; and F - in deuterated water).

The MPC-based copolymer was also synthesized using CDCPA. The CDCPA has an advantage in optimizing amphiphilicity during MPC copolymer development. The high hydrophilicity of the MPC polymers could be balanced with the hydrophobic Z- a group of the RAFT agent. The MPC copolymer is an excellent alternative to OEGMA-based copolymers. MPC copolymers have a unique advantage in developing antifouling surfaces. Surface grafting of UCNPs with MPC-based copolymers is expected to minimize protein fouling during intracellular applications. The polymer characterization was done through vinyl proton intensity assessment at  $\delta$  5.6 and  $\delta$  5.9 ppm before and after polymerization as indicated at a and a'. The peak around  $\delta$  1.0 to 0.9 ppm is due to methyl marked as b and b' to differentiate changes associated with synthesizing the first macro-RAFT agent. Similarly, the diblock and the triblock synthesis were monitored from the monomer and polymer protons intensity changes.

Characterization of the Polymer 5 was performed using NMR, FTIR, and TGA. The  $^1\text{H}$  NMR and chemical structure are represented in Figure 56A. The labeled functional groups belong to protons of the purified polymer. The calculated molecular weight of the copolymer is  $6810 \text{ g mol}^{-1}$ . The ATR-FTIR of Polymer 5, Figure 56B, is due to carboxylic hydroxyls, the intense absorption band in the region  $3300 \text{ cm}^{-1}$  and  $3600 \text{ cm}^{-1}$ .<sup>423</sup> The peaks at  $2900 \text{ cm}^{-1}$  are due to combined absorptions of the - NH and -  $\text{CH}_3$  stretch. The absorption peak at  $1060$  is due to the P-O- stretch, and the quaternary amine group of the MPC is observed at  $970 \text{ cm}^{-1}$ .<sup>424</sup> Figure 56C; the thermal decomposition curve of Polymer 5 shows the different groups, for instance the high decomposition at  $150$  to  $250$  is due to the high carboxylate and phosphonate groups of MPC and MAA.

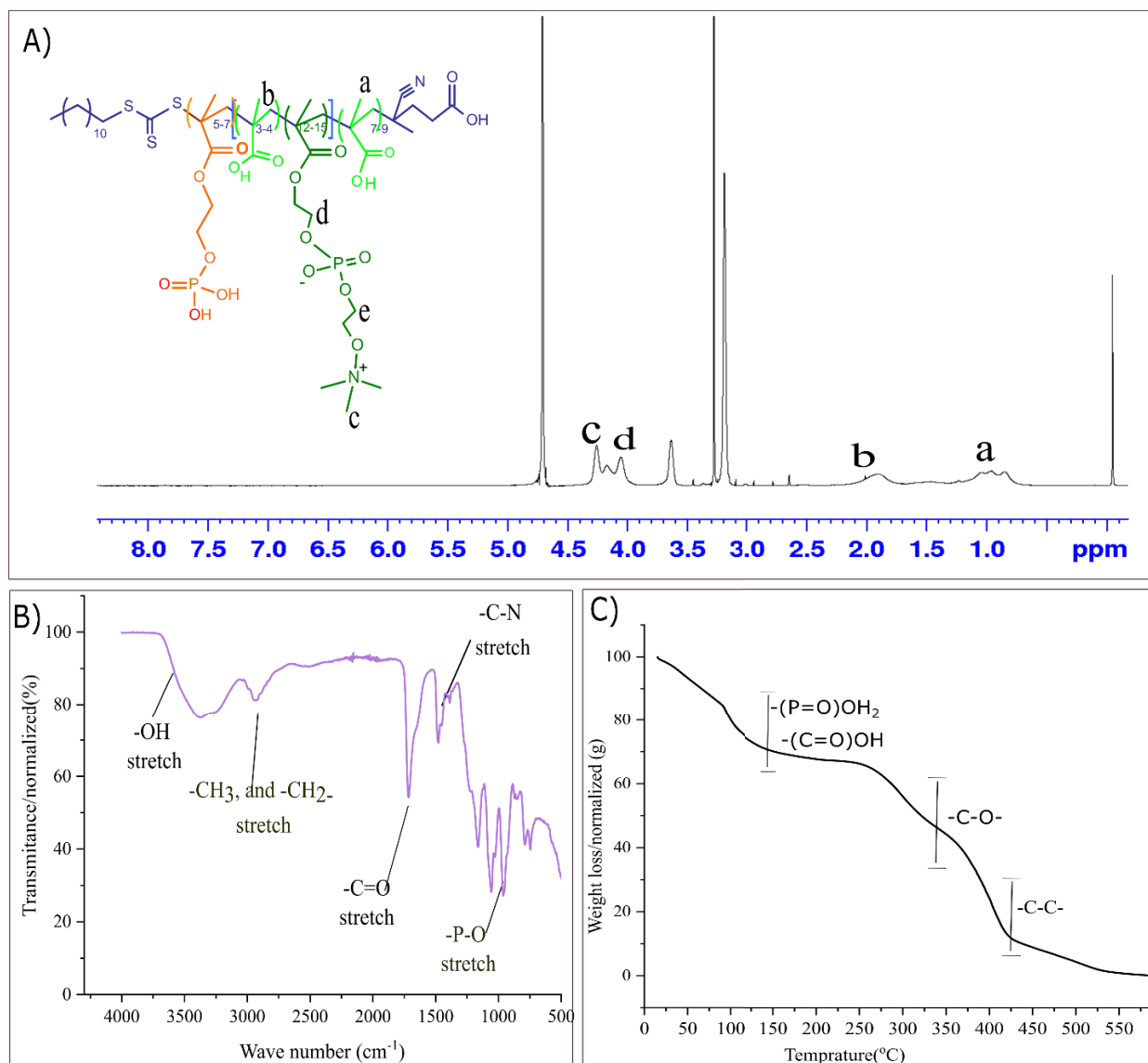


Figure 56 The  $^1\text{H}$  NMR spectrum (A), ATR-FTIR spectrum (B), and TGA thermograph (C) of Polymer 5.

#### 4.4.5 CTCPA-based diblock copolymer

The diblock copolymer, Polymer 6, was characterized using NMR, FTIR, and TGA, as presented in Figure 57A, the labeled functional groups belong to protons of the purified polymer, as shown from the  $^1\text{H}$  NMR spectrum. The calculated molecular weight of the copolymer is  $1850 \text{ g mol}^{-1}$ . In Figure 57B, the intense absorption band in the region  $3500$  to  $2500 \text{ cm}^{-1}$  belongs to the excess carboxylic group absorption. The shoulder peaks at  $2800$  to  $2900 \text{ cm}^{-1}$  are due to combined  $\text{CH}_3$  and  $\text{CH}_2$  stretch absorptions. The absorption peak at  $1060 \text{ cm}^{-1}$  is due to the P-OH. Figure 57C

shows the decomposition curves of the different components of the copolymer. The enhanced weight loss between 150 to 250 °C is due to the high carboxylic concentration.

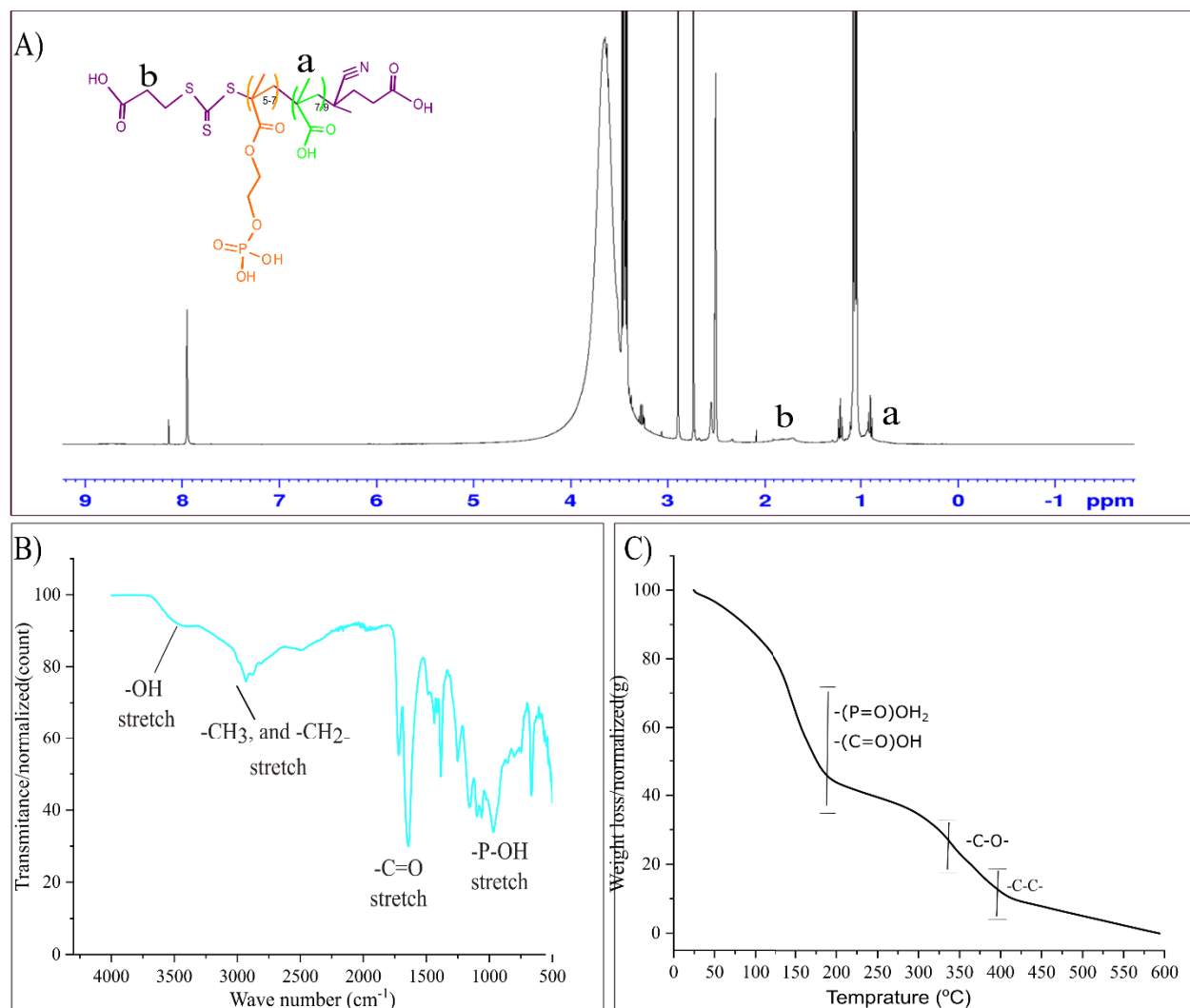


Figure 57 The <sup>1</sup>H NMR (A) FTIR (B) and TGA (C) of Polymer 6.

### ➤ GPC analysis of the Copolymers

The GPC analysis of synthesized copolymers was outsourced and performed for a few samples. The obtained GPC analysis couldn't show good results. The observed GPC characterization challenges are expected to originate from two possible conditions. First, an appropriate solvent selection is necessary to thoroughly disperse the amphiphilic copolymer components. Second, the high-branched copolymers of copolymers also need a suitable standard. The GPC sample must not be adsorbed to the stationary phase, and a suitable solvent is required to achieve complete

dissolution.<sup>425</sup> A previous review explains that long-branched copolymers significantly affect polymer separation during GPC analysis.<sup>425</sup> The interaction of copolymer carboxylic groups with the column stationary phase results in a misleading result. The high hydroxyl group concentration and local heterogeneity are the other possible factors for the unsuccessfulness of GPC analysis.

➤ Summary of RAFT copolymers in grafting of UCNP surfaces and intracellular labeling

The multiple copolymers are developed to provide wide options for the grafting of UCNPs. Polymer 1 applies to introducing multiple coupling opportunities, including UCNPs-dye hybrids development. The OESPX-RAFT agent has advantages in introducing additional functionalities through end-group modification.<sup>211, 426</sup> Polymers 2 and 3 are the most implemented polymers, and their grafted particles are very efficient in size control and stability. The relatively high hydrophilicity differences give a preferential selection for a specific application. Polymer 4 is designed to implement sulphonate-based anchoring separately or in combination, and it is expected to enable reasonable control of stability in wide pH ranges. Polymer 5 has a unique advantage in controlling protein fouling. The MPC blocks have biomimicking and antifouling capacity, making the polymer a future alternative in intracellular investigations. The MPC-based copolymers are attractive synthetic polymers for biomedical applications.<sup>427</sup> The MPC-based polymers have two potential advantages in biomedical applications: biocompatibility and antifouling capacity. MPC-based polymers are biocompatible because they comprise a synthetic phospholipid similar to the phospholipid composition of the cell membrane. The zwitterionic copolymer of MPC is well in its biocompatibility and resistance to protein adhesion.<sup>423</sup> As MPC surface coating is effective in other applications,<sup>428</sup> its implementation in the surface grafting UCNPs allows for producing a biocompatible and brush-like antifouling feature.

Polymer 6 allows for the optimization of surface graft composition and stability. The MAA-based diblock copolymers could replace the conventional PAA-based UCNPs surface modification. Implementing MAA diblock polymers has some unique advantages over the PAA-based UCNPs surface functionalization. The MAA-b-MOEP copolymer is advantageous to substitute the PAA-based UCNPs surface modification. The backbone methyl and the RAFT agent allow for amphiphilicity optimization. The solid anchoring capacity of MOEP enables the replacement of oleate ligands directly. The newly designed diblock copolymer avoids the two steps, oleate

removal, and replacement and surface grafting, and helps to minimize associated aggregation challenges. When Polymer 6 is used in combined UCNPs surface grafting, the MAA diblock is ideal for optimizing the surface graft density, nanoparticle amphiphilicity, and reactivity.

## 4.5 Conclusion

In this section, a library of polymers could be prepared for the surface functionalization of the UCNPs. The different functional copolymers are designed to meet the intense current and future needs of polymers for surface optimization of UCNPs. The current efficient synthetic routes help develop copolymers with diverse structures and connectivity, producing desired molecular architectures. The RAFT techniques, for example, provide a vast opportunity to introduce diverse functionalities through controlled (co)polymerization of interest monomers. The monomer selection, the polymerization technique implemented and designing and maintaining the block proportionating enable reasonable control in the final functionalities. The functional copolymers have unique advantages in the surface modification of the UCNPs. Combining the copolymers, such as a mix of sulphonic and phosphate anchoring groups, could help introduce various functionalities to the UCNP surfaces.

The RAFT agent selection is determined from the reaction method and based on the functionalities of the end group. The RAFT agent end groups also allow controlling amphiphilicity of the copolymer. The functionality of the copolymers has been highly regulated by the type of monomers copolymerized. For example, MAA is extensively used to introduce high reactivity. The RAFT agents' end groups functionalities also help to control reactivity and bio-coupling performances. The CDTPA and CTCPA RAFT agents have inherent carboxylic groups, for instance, the double carboxylic groups from CTCPA provide enhanced carboxylic acid access. The xanthate RAFT agent, the phthalimide end group, enables the introduction of amine functionality through further end-group modification.

The developed copolymers offer various options for controlling the physicochemical properties of UCNPs. The surface-grafted nanoparticles are aimed to gain enhanced dispersibility, stability, reactivity, and antifouling capacity. MPC copolymers are expected to improve the biological performances of UCNPs' by overcoming fouling challenges. The sulfonate anchoring ligand is advantageous for developing stable nanoparticles in wide pH ranges, specifically at lower pH, due

to the low pKa of sulfonic acid compared to the phosphoric and carboxylic acids. The responsiveness of MPC-based copolymers could be implemented as an alternative to the PEG copolymers for UCNP's surface modification. The separate and combined copolymer-based grafting of the UCNP surfaces has promising opportunities. The antifouling capacity of the phosphorylcholine zwitterionic copolymer facilitates the intracellular delivery of the UCNPs. The copolymers could be further optimized for delivery matrices and biosensing applications.



# 5 | Design and Functionalization of Upconversion Nanoparticles Surfaces

## 5.1 Preamble

This chapter emphasizes the surface design and development of the UCNPs. The different copolymers discussed in chapter four are implemented to functionalize UCNPs. Ligand exchange approaches have been implemented to transform as-synthesized hydrophobic UCNP surfaces into hydrophilic, (bio) stable, and multifunctional ones. The virtues of implementation of combined (double) copolymers in UCNP grafting to optimize surface functionalities are explained. The effects of surface functionalities in attaining improved colloidal stability, like in ionic media, are mentioned. Surface coupling of different antibodies and peptides on the UCNPs surfaces is discussed. The hybrid nanoprobe development process through coupling organic dyes to UCNPs has been discussed. The MAA functionalized triblock copolymers, and the double copolymer based UCNPs surface grafting allows to enhance surface functionality, cellular uptake, bio(stability), and intracellular targetability.

## 5.2 Introduction

Nanocomposites from combinations of polymer-metal nanoparticles are the most attractive nanomaterials in biomedical applications. They gain synergized capabilities that couldn't be achieved by using the individual components separately.<sup>429</sup> An integration of polymers into nanoparticle surfaces helps to modulate their interactions with the surrounding environment.<sup>430</sup> Surface grafting of UCNPs using specifically designed polymers helps to address the critical UCNPs' surface challenge, such as targetability. For instance, the UCNPs' surface development improves colloidal stability, surface reactivity, and biocompatibility.<sup>157</sup> Moreover, the bio-nano interaction of nanoparticles could be altered through manipulation of the surface amphiphilicity and functionalities.<sup>100</sup>

The post-synthesis UCNP surface ligand replacement helps transform the surfaces' physicochemical properties. Copolymers specifically designed and developed using RAFT polymerization are suitable for effectively controlling the surface functionalities of the nanoparticles. In the UCNPs surface transformation, the oleate ligand from as-synthesized

particles could be replaced with suitable ligands.<sup>431</sup> Due to the high acid dissociation constant, the carboxylic group of the oleate ligand easily detaches from the UCNPs surface upon exposure to strong ligands like the phosphate and sulphonate ones. Establishing strong bonding between the polymer's anchoring moieties and inorganic nanoparticles helps to develop a strong surface linkage.<sup>245</sup> To successfully implement the UCNPs in different bioanalytical applications such as in bioimaging, surface grafting provides numerous opportunities. The copolymer-based surface grafting of the UCNPs helps to optimize their physicochemical properties.<sup>259, 432</sup> The amphiphilicity of the surface grafting copolymers and their surface appearances determines the nanoparticles' dispersibility and stability. Amphiphilic surface polymers tend to extend themselves away from the particle surface and can produce a brush-like surface architecture. The extended surface appearance of grafted polymers provides enhanced nanoparticle dispersibility and improves colloidal stability.

### 5.2.1 UCNPs surface functionalization

Nanoparticle surface modification has two significant steps. The first step of surface modification involves introducing reactive surface groups. The second step is immobilizing bioactive molecules.<sup>433</sup> Surface-engineered UCNPs have several promising features in broad applications like biosensing, imaging, and therapeutics.<sup>74</sup> The polymer-based surface modification is a promising approach because the adaptability of polymers enables the development of UCNP surfaces with wide desired composition and architecture. The 'graft to' technique is the most widely implemented technique to modify UCNPs surface using pre-formed copolymers. 'Graft to' enables tuning surface features of the nanoparticles without affecting the crystal structure.<sup>245</sup> Different (co)polymers, such as PEG, are commonly investigated in the surface functionalization of the UCNPs. The first PEG-based UCNP grafting was performed in 2009 to develop water-dispersible nanoparticles.<sup>434</sup> At that time, phosphate-derivatized PEG had been implemented to replace the oleate ligand from the UCNP surfaces. Recently, copolymers from phosphate-functionalized OEGMA (short PEG monomers) have been widely tested in the surface modification of the UCNPs.<sup>85, 420, 435</sup> Maddahfar et al., for instance, investigated the effect of the OEGMA block length on antibody coupling efficiency in the functionalization of UCNPs. The study indicates that a diblock copolymer consisting of 13 units of OEGMA is found to be efficient in antibody conjugation compared to diblock copolymers composed of 35 and 55 OEGMA units.<sup>420</sup>

Copolymers from OEGMA, and other interest monomers, allow for development of polymers with a bottle brush-like architecture.<sup>436</sup> The OEGMA units in the copolymers could undertake local microphase separations from the rest polymer units, resulting in surface heterogeneity. Increasing the PEG chain length induces high hydrophobicity due to increased backbone carbons. During nanoparticle surface grafting, the achieved graft density level and the surface brush appearance determine the confirmation of the surface polymers.<sup>437</sup> The recent study from Zhang et al. indicates that UCNP surfaces grafted from copolymers made from long-chain OEGMA-300 exhibit reduced protein fouling at their low grafted density compared to the short chain ones.<sup>85</sup>

UCNPs surface modification using the MAA functionalized triblock copolymers is desirable to introduce improved surface functionality. The MAA units help to generate flexible surfaces and excess carboxylic groups that enable the development of enhanced surface reactivity, bio-coupling density, and targetability during the surface grafting of nanoparticles.<sup>307, 438, 439</sup> The OEGMA and MPC-based triblock copolymer helps to generate surfaces with good antifouling capacity. Copolymers composed of MPC units mimic the cell membrane composition and enhance cellular uptake and biocompatibility.<sup>427</sup> In Figure, a schematic representation of UCNPs surface grafting is presented.

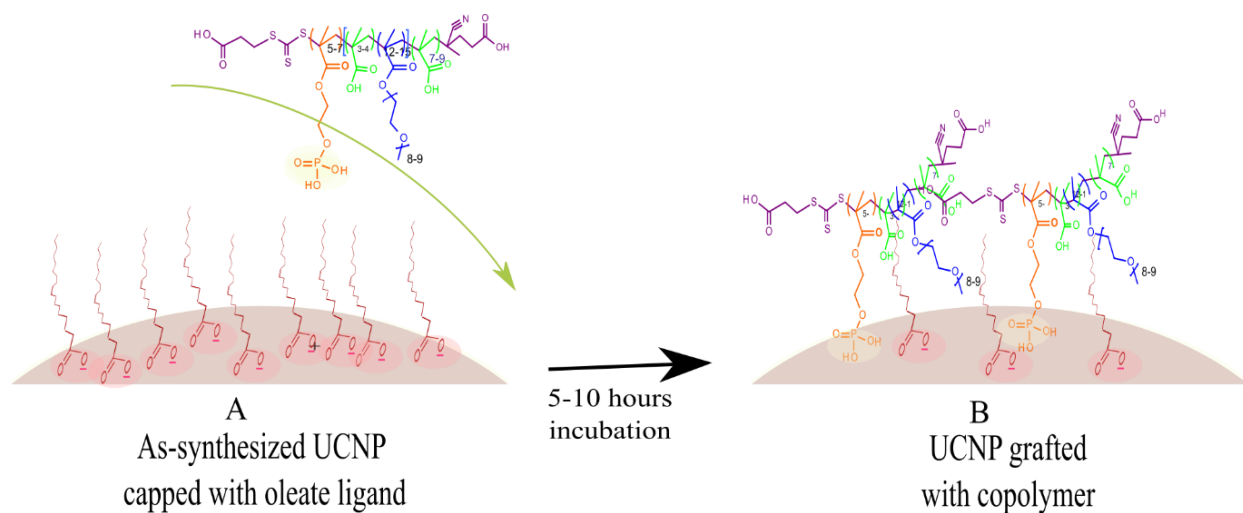


Figure 58 Schematic representation of UCNPs surfaces oleate capped as-synthesized nanoparticles(A) and copolymer grafted particles through ligand exchange (B).

The oleate ligand replacement efficiency depends on the copolymer's size and the anchoring ligand strength. The incomplete replacement of oleate ligands results in a mixed surface composition,

that consists from the newly introduced copolymers and unremoved oleate groups.<sup>440</sup> Similar challenges were reported in the surface grafting of superparamagnetic iron oxide nanoparticles.<sup>441</sup> To improve surface graft density, short and long-branch copolymers could be used in sequential grafting of the UCNP surfaces. Implementation of combined copolymers surface grafting gives more advantages compared to the separate use of copolymers. The combined surface grafting is promising to control the surface composition and overcome surface challenges, such as nonspecific binding and endosomal traps, during intracellular delivery targeting of the UCNPs.

Active targeting of nanoparticles requires incorporating biorecognition elements on the nanoparticle surfaces. The biorecognition element helps to guide the nanoparticles to the desired intracellular site. Selective targeting of interest intracellular sites could be achieved through the surface attachment of antibodies and peptides.<sup>74</sup> Surface ligand density plays a prominent role in controlling the targetability of the nanoparticles. An optimized target agent concentration is required for efficient ligand-receptor interaction and improved signal generation.<sup>442</sup> Availability of large numbers of surface targeting ligands results in multiple receptor interactions, and high consumption of receptors by fewer particles could have reduced signal strength.<sup>277</sup>

### 5.2.2 Coupling of biomolecules

The nanoparticle surface bioconjugates are one of the hottest research topics for their sensing and therapeutic application.<sup>443</sup> Since nature uses robust approaches to facilitate the intracellular delivery of materials in sophisticated biological systems, mimicking the nanoparticle's surface is essential for intracellular labeling. The primary advantage of the surface grafted UCNPs is enabling the practical attachment of biomolecules. The EDC-based surface functionalization requires accessible hydroxyl. The MAA-derivatized copolymers are ideal for the facilitation of biofouling. Intracellular targeting requires for attachment of a specific targeting agent. Antibodies are most widely implemented in cell labeling applications.<sup>444</sup> Peptides are also well known for the facilitation of intracellular delivery purposes. For example, cell-penetrating peptides (CPP) are effective in cargo delivery applications. The arginine-containing peptides are effective in improving the cellular uptake of the nanoparticles. The negatively charged cell membrane surface interacts with the positively charged peptide to obtain cell membrane access. In this project, surface grafting of the UCNP using the different synthesized RAFT copolymers has been performed to attain multifunctional and stable nanoparticles. The polymer-particle integration

allows to control the surface functionalities and immobilization of biomolecules are performed to achieve active targeting of the UCNPs.

### 5.3 Experimental section

For the preparation of the functionalized UCNP, an  $\text{Er}^{3+}$ -doped 20 nm and 25 nm core only and 35 nm core-shell particles were taken for the surface modification. THF and deionized water were used as a solvent for surface grafting, functionalization, and purification. 1 mM NaF was used to suppress the dissociation of ions from the nanocrystals. The TAT-HIV peptide, polyarginine, anti-tubulin antibody, alpha-antibody coupled with Alexa Fluor 488, FITC-SCN, anti-actin antibody, and anti-nuclear pore complex antibody (NUP-98) have been used in the bioconjugates preparation. Biomolecule coupling to nanoparticles was performed by activating carboxylic groups from the surface-grafted copolymers using EDC chemistry, followed by NHS stabilization. The hydrodynamic size, surface potential, and stability of surface grafted nanoparticles were assessed using DLS and FTIR. The grafting density of the modified particles was evaluated from their TGA profiles.

#### 5.3.1 UCNPs copolymer surface grafting

##### ➤ Separate copolymer based UCNPs surface grafting

Surface grafting of the UCNPs was performed by directly replacing the inherent oleate ligand using the specifically designed RAFT triblock copolymers. The surface grafting was performed by mixing and co-incubating as-synthesized nanoparticles with the copolymer(s). The overall ligand exchange process is schematically represented in Figure 59.

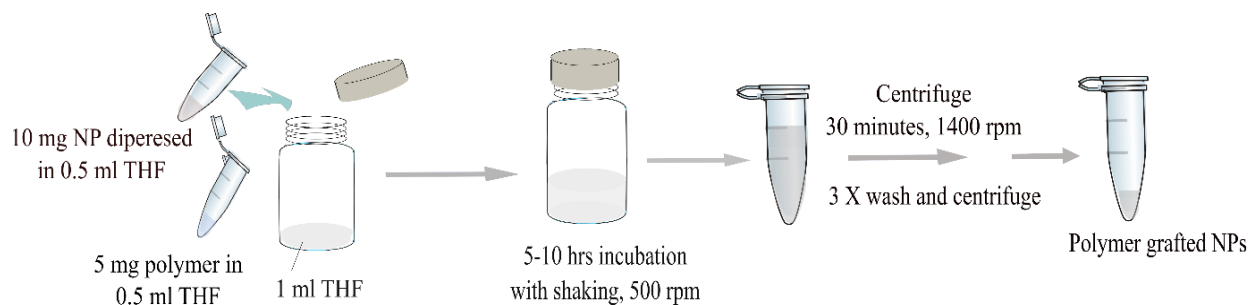


Figure 59 Flow Scheme for polymer surface grafting of the UCNPs.

Briefly, the surface grafting was performed by taking 10 mg of nanoparticles dispersed in 1 mL THF and mixing with 5 mg copolymer 1 mL THF. The mixed solution was co-incubated for five to ten hours under continuous shaking at 500 rpm. The solution was centrifuged at 14860 rpm for 30 minutes; then, after discarding the supernatant solution, sedimented particles were washed by re-suspending and centrifuging for 30 minutes at 14860 rpm. The nanoparticles were washed three times using 500  $\mu$ L THF, 250  $\mu$ L THF/250  $\mu$ L deionized water, and 500  $\mu$ L water in consecutive steps. Finally, the nanoparticles were dispersed in 300  $\mu$ L deionized water containing 1 mM NaF, DLS, and zeta potential analysis was performed. In the case of Polymer 5 and Polymer 6, since those copolymers are partially soluble in THF, 80% THF was used to get complete dispersion of the polymers during the incubation.

➤ Combined (double) copolymer UCNPs surface grafting

The combined copolymers surface grafting of UCNPs using two different copolymers was performed stepwise. After the first graft was done and the particles were purified once, as the procedure represented in Figure 60, the second copolymer grafting was performed. Then, purification and characterization were performed for grafted nanoparticles, as in the separate polymer grafting. The steric hindrance effect could be minimized using short-branch copolymers in the first graft, followed by the long-branch chains. In Figure 60, the stepwise double grafting is represented.

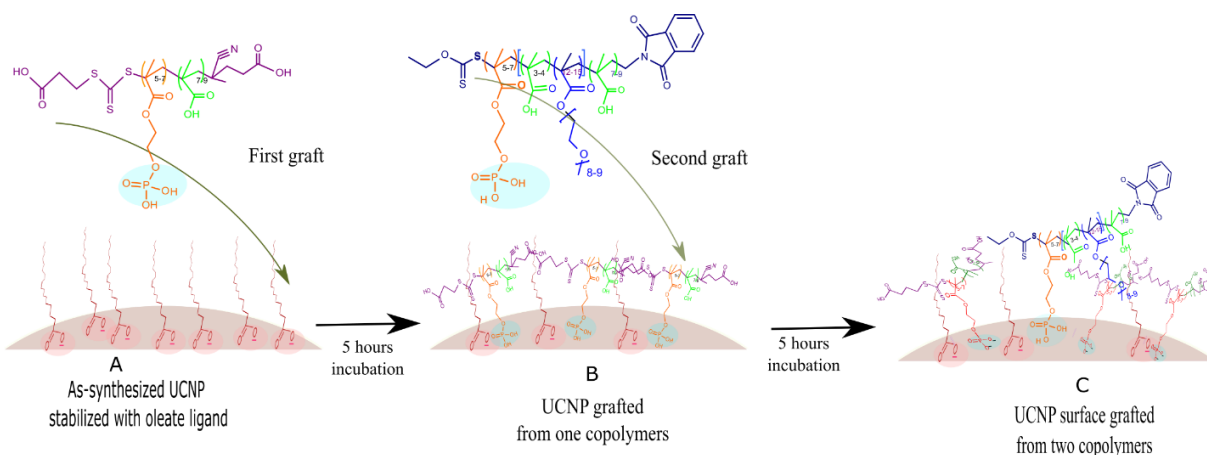


Figure 60 Pictorial representation of UCNPs surfaces (A) oleate capped, (B) first copolymer grafted, and (C) second copolymer grafted.

➤ Grafted copolymers end group modification

The functionality of the xanthate RAFT agent, in the case of Polymer 1, allows post-end group modification. Hydrazinolysis of both end groups produces sulfhydryl and amine functionalities. The introduction of the two reactive groups on the UCNP surfaces allows for implementing other coupling techniques like maleimide and amine-based EDC conjugation, in addition to the carboxylic-EDC activation-based bioconjugation. The xanthate thiol end groups are susceptible to hydrazinolysis and could be reduced to sulfhydryl functionality.

➤ Stability of copolymer grafted UCNPs in ionic medium

The stability of copolymers grafted nanoparticles was assessed in different media. The stability evaluation was performed by measuring the hydrodynamic size change of the particles in aqueous was assessed for 30 days. The 100  $\mu\text{g}$  nanoparticles taken from 4 mg/mL stock solution and dispersed in 500  $\mu\text{L}$  of deionized water for DLS size measurement. The stability of the grafted nanoparticles stored in different buffers 10 mM buffer PBS pH 7.4, MES pH 5.2, and in borate buffer pH 8.5 was analyzed. The nanoparticle stability assessment in the different buffers was performed based on NIST 2004 protocol.<sup>445</sup> The stability of nanoparticles was assessed in buffers and acidic medium for 6 hours, 12 hours, 24 hours, and 48 hours.

➤ Surface coupling of bioactive molecules and organic dyes

UCNPs surface coupling of different biomolecules was performed using EDC chemistry. 200  $\mu\text{g}$  of the copolymer grafted UCNPs were dispersed in 900  $\mu\text{L}$  of deionized water containing 1 mmol NaF, and then 100  $\mu\text{L}$  1 mg/mL EDC solution was added. The solution was incubated in an ice bath for 15 minutes with continuous shaking, and 100  $\mu\text{L}$  1 mg/mL NHS solution was added to it and further incubated for 1 hour. The EDC-activated nanoparticles were separated by centrifugation at 14860 rpm for 30 minutes and re-dispersed in 200  $\mu\text{L}$  of deionized water. Then it was mixed with a pre-prepared 800  $\mu\text{L}$  borate buffer (pH 8.5, 20 mM) containing 1  $\mu\text{g/mL}$  antibody and 1 mmol NaF. The reaction progressed for two hours under continuous shaking at room temperature. Then, functionalized nanoparticles were separated by centrifugation at 14860 rpm for 30 minutes, re-dispersed in 1  $\mu\text{g}$  of arginine 800  $\mu\text{L}$ , incubated for 15 minutes, and separated by centrifugation. Finally, the particles were dispersed in 200  $\mu\text{L}$  of deionized water containing 1 mmol NaF. The same procedure was followed for both the antibody and peptide coupling.

## 5.4 Result and discussion

### 5.4.1 Hydrodynamic size and zeta potential of surface grafted UCNPs

Surface grafting of UCNPs had performed using the different synthesized copolymers through an implementing "graft to" technique. The phosphate ligand-derivatized copolymers gain higher surface coordination capability than the carboxylate functionalized oleate ligand. The surface cations on the nanoparticles preferentially interact with electron-rich ligands. As their synthesis mentioned in chapter four, the pre-prepared RAFT copolymers have been used to utilize the unique advantages of each copolymer in surface grafting of UCNPs. The copolymers' grafted UCNPs surface has potential benefits in maintaining particle stability and improving amphiphilicity and dispersibility.

The MAA functionalized triblock copolymers help to introduce reactivity, amphiphilicity, and antifouling to the nanoparticle's surfaces simultaneously. As observed in the case of PAA-coated UCNPs, the high carboxylic functionality helps to improve their surface coupling efficiency and biocompatibility of the nanoparticles.<sup>157</sup> The copolymer grafted nanoparticles' final property relies on the functionalities of the copolymer blocks constitutes. The two grafting approaches implemented for the surface modification of UCNPs, the separate and combined copolymer surface grafting, have advantages in optimizing the surface polymer composition. The different characterization techniques confirm the achievement of the combined copolymers based UCNPs surface grafting. Separate copolymer UCNPs surface grafting enhances coupling efficiency and stability in aqueous media. The combined copolymer UCNPs surface grafting helps to improve UCNPs' performances in buffer and ionic media. Since the tri-copolymers consist of an OEGMA-500 long side chain, due to steric repulsion extent of oleate ligand replacement and grafted density is limited. However, the step-wise co-grafting short-branch copolymer grafting followed by a long-branch copolymer allows for enhanced surface grafting by replacing more oleate ligands.

#### ➤ Separate triblock copolymers grafted UCNPs

The modified particles' water dispersibility proves the accomplishment of effective UCNPs surface grafting. A 25 nm as synthesized UCNP was taken and grafted with the different copolymers. The hydrodynamic size of the different copolymers grafted UCNPs has slightly increased compared to the starting substrate particle diameter. The obtained number-weighted hydrodynamic diameter



ranges from 30 nm to 60 nm. The measured hydrodynamic diameter of the grafted UCNPs is given in Figure 61.

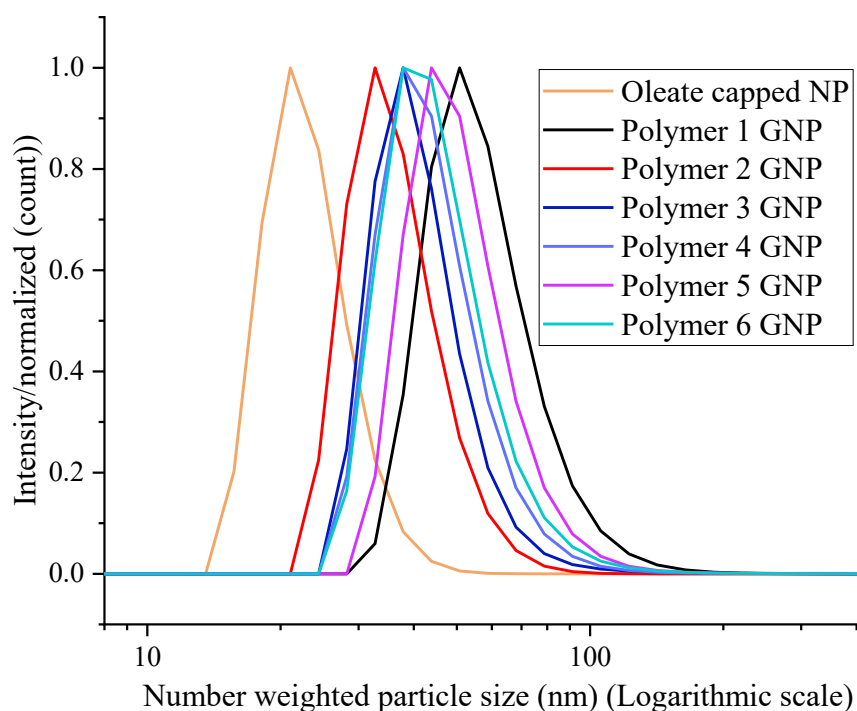


Figure 61 Number weighted DLS particle size distribution of the oleate capped and copolymers grafted UCNPs.

The different copolymers affect the stability and surface potential of the particles. Surface grafting of UCNPs has a significant effect on the physicochemical properties of the particles. The reduced size increment from copolymer-grafted particles is associated with the high dispersibility of particles. The enhanced surface hydrophilicity significantly contributes to particle dispersity and reduced size increments. The achieved hydrodynamic sizes are 30 to 60 nm in diameter, which is suitable for biomedical applications.<sup>446</sup> The Polymer 2, 3, and 4 grafted nanoparticles show a reduced size increment associated with the surface grafting; less than 10 nm number distribution weighted hydrodynamic size increment has been obtained. The low hydrodynamic size change indicates that the copolymers are good enough to control the size of copolymer-grafted particles. The minimized size increment is essential in achieving UCNPs targetability during labeling and imaging intracellular structures.

In the case of nanoparticles grafted from Polymer 1, 5, and 6, the noticeable hydrodynamic size increment might be associated with a strong force of interaction like hydrogen bonding between

the oxygen and nitrogen groups. The reduced steric hindrances in the case of Polymer 5 and 6 could be the other reason for the observed size increments. In the case of Polymer 1 modified nanoparticles, the possible hydrogen bonding arising from the hydroxyl and amine groups in the xanthate may induce nanoparticle clustering. Due to the grafted copolymers' steric and electrostatic stabilization effect, nanoparticles are highly water dispersible.

The nanoparticle grafted from the different copolymers have gained negatively charged surfaces, as presented in Table 3. All the copolymer grafted surfaces have developed highly negatively charged surfaces.<sup>447, 457</sup> A relatively reduced negative charge is observed in the case of Polymers 1 and 5 grafted particles. It is due to the monomers' functionality being RAFT agents. The surface charge of copolymer-grafted nanoparticles strongly depends on the copolymers' working pH composition. At pH 8.5, due to the high degree of carboxylic acid deprotonation, a significantly lower zeta potential,  $\sim -40$  mV, has been achieved. The UCNPs grafted from the MPC-containing triblock have shown a lower zeta potential at pH 5.5. The high surface charge associated with increased carboxylic density indicates that the surfaces of the nanoparticles are efficient in performing bio-coupling through EDC-based covalent bonding. The DLS hydrodynamic diameter and zeta potential of the copolymer-grafted nanoparticles are given in Table 3.

Table 3 Summary of the DLS particle size and zeta-potential of copolymers grafted nanoparticles.

Grafted Polymer type	Initial size (nm)	DLS size of grafted NP, (nm)	Zeta-potential (mV)	
			pH 5.5	pH 8.5
Polymer 1	25	52 $\pm$ 3	-9	-17 (- 30, 27%)
Polymer 2	25	35 $\pm$ 2	-19	-25 (- 34, 20%)
Polymer 3	25	33 $\pm$ 3	-18	-28 (-40, 15%)
Polymer 4	25	45 $\pm$ 2	-13	-25
Polymer 5	25	50 $\pm$ 3	-3	-31
Polymer 6	25	43 $\pm$ 5	-20	-32

The introduction of excess carboxylic groups grafted UCNPs' gives two potential advantages source of reactivity and amphiphilicity. For instance, the MAA and OEGMA units, in the case of Polymers 1 to 3, have a prominent role in optimizing amphiphilicity. The backbone of the

copolymers induces a high degree of hydrophobicity and helps to counterbalance the high hydrophilicity effect due to the introduced MAA units. The OEGMA block induces amphiphilicity because it consists of both hydrophobic and hydrophilic domains.<sup>436</sup> The induced amphiphilicity prevents possible aggregations between the domains. As the surface grafted copolymers have long branches, the spatial surface area coverage and the brush length would be significantly higher than the oleate ligand. The surface polymer forms a spiral structure due to the hydrophilic-hydrophobic self-interactions. In addition to the steric dispersion effect of the copolymer's long branch chains, high hydrophilicity traps more water and reduces hydrodynamic size.

The controlled surface introduction of desired copolymer(s) enables the development of optimized surface functionalities. UCNPs surfaces grafted from MAA-incorporated triblock copolymers to avoid steric hindrance from the long OEGMA side chains. The MAA group of the triblock induces high surface carboxylic density. The high carboxylic surface density enhances coupling efficiency and improves the surfaces' antifouling capacity. The possible UCNPs surface heterogeneity, such as amphiphilicity and surface zeta potential heterogeneity, can be controlled from the different surface groups of the copolymers. The various groups of the surface grafted copolymer improve the polymer compatibility by blending with similar surface components.<sup>219</sup> The surface zeta potential also depends on the local area compositions.

Although the average zeta potential is used most, which is misleading, the experimental data indicates that the different surface regions could exhibit local zeta potentials.<sup>448</sup> The surface consists of high carboxylic groups, which induces increased surface charge density and zeta potential. Multiple zeta potentials appear due to the local surface charge differences. The average zeta potential agrees with a previously reported zeta potential of the PAA-coated UCNPs.<sup>394</sup> The partially charged ether functionality in the OEGMA blocks contributes to the negative surface zeta potential. Local surfaces dominated by the OEGMA groups produce a lower zeta potential, -6.6 mV, as seen in Figure 62. The high surface zeta potential from the copolymers grafted nanoparticles indicates the presence of high electrostatic stabilization, in addition to the steric stabilization from the long surface brushes. The demonstrated surface charge heterogeneity from Polymer 3 grafted nanoparticles is presented in Figure 63 as an example.

	Mean (mV)	Area (%)	St Dev (mV)
<b>Zeta Potential (mV): -17.7</b>	<b>Peak 1: -6.60</b>	66.4	6.27
<b>Zeta Deviation (mV): 17.2</b>	<b>Peak 2: -40.0</b>	33.6	7.48
<b>Conductivity (mS/cm): 0.518</b>	<b>Peak 3: 0.00</b>	0.0	0.00

Result quality : **Good**

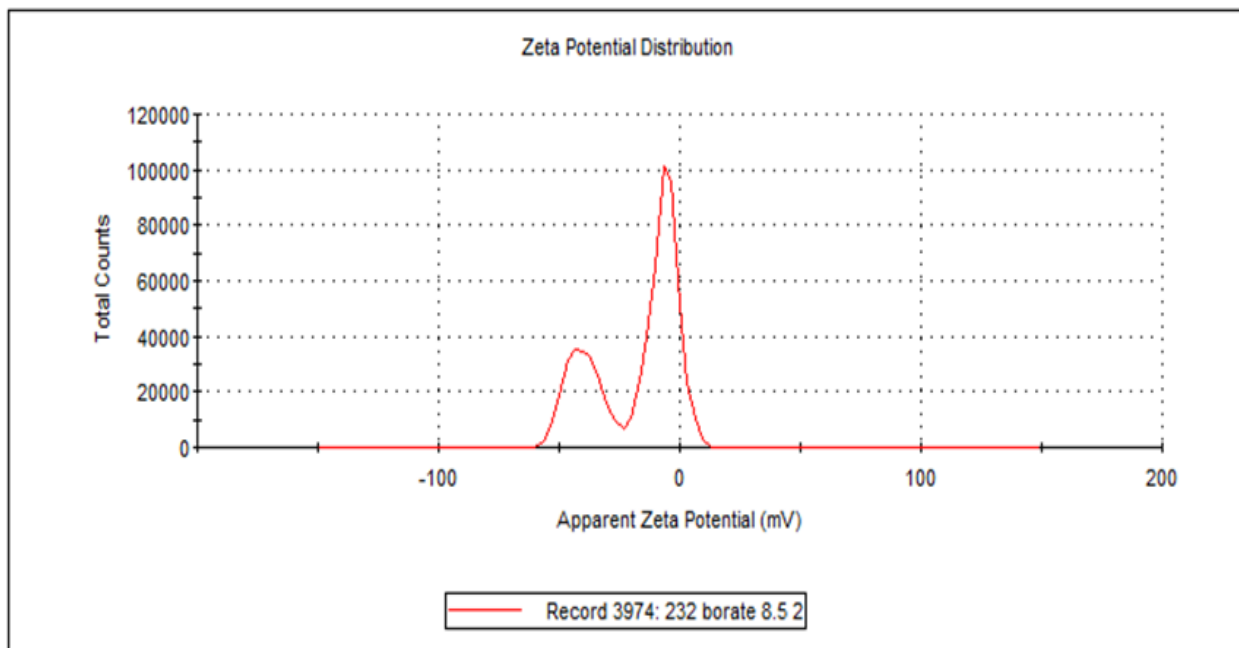


Figure 62 Zeta potential of Polymer 3 modified heterogeneous nanoparticle surfaces at pH 8.5.

➤ Combined (double) copolymers grafted UCNPs surfaces

Combined or double copolymer surface grafting of UCNPs was implemented to improve the performances of UCNP surfaces by optimizing surface composition. The introduction of two polymers enables the generation of surfaces with multiple functionalities. Selected combinations of copolymers have been investigated for double grafting of UCNPs. Double copolymer co-grafting is advantageous as optimization is optimizing graft density and stability. Surface heterogeneity could be introduced by co-grafting nanoparticles using various copolymers. The stepwise surface grafting using two different copolymers creates an alternate surface appearance of the copolymers grafting and allows variations in surface brush chain length, amphiphiles, and charge distribution. Combining the copolymers was performed by considering composition, branch size, and anchoring ligand type. The combinations of high molecular weight polymers with

low-branched polymers have been investigated. The long-branch copolymers were co-grafted with the short-branch copolymer, Polymer 6. Figure 63 shows the DLS hydrodynamic size of modified particles through combined copolymer grafting.

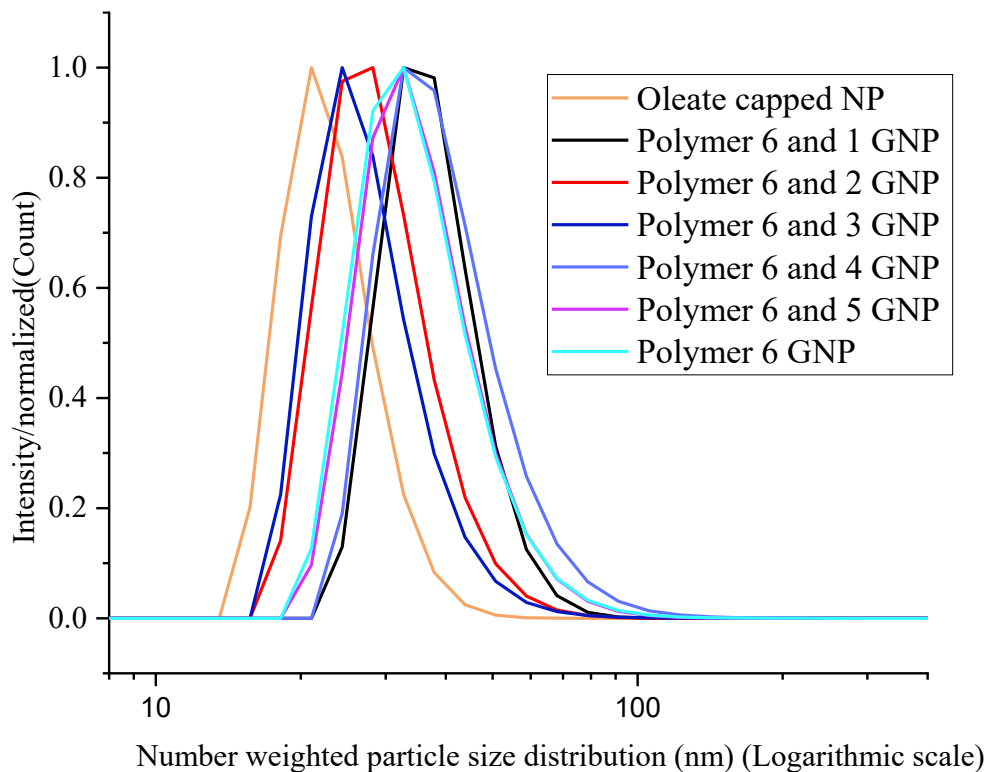


Figure 63 Number weighted DLS hydrodynamic size of the oleate capped, separate Polymer 6 grafted and double copolymer grafted UCNPs.

The combined copolymers UCNPs grafting gives advantages, such as optimization of graft density and improvement of nanoparticles stability. The OEGMA copolymers' long branch induces steric stabilization and more extended blood circulation.<sup>7</sup> However, the copolymers with the long OEGMA-500 branch surfaces produce a steric hindrance effect to stabilize the nanoparticles. The surfaces between two grafted copolymers could not be further accessible and remain capped with inherent oleate ligands. The surfaces between two grafted copolymers could not be further accessible and remain capped with inherent oleate ligands. Those surfaces gain a mixed surface composition from the newly introduced copolymers and the residual oleate ligands.<sup>182</sup> One main reason for the instability of copolymer-modified UCNPs in PBS is the displacement of residual oleate ligands with competitive ions like the phosphate ions in PBS. The ejection of oleate molecules tends to interact with the hydrophobic chains of the grafted copolymer, and they interact

with themselves due to the strong hydrophobic effect. The interaction of surface detached oleate with phospholipid of the cell membrane had been reported by Das et al.<sup>182, 184</sup>

Combined copolymer grafting of UCNPs produces surface heterogeneity. The presence of possible interactions, like hydrogen bonding and electrostatic interactions between the grafted copolymers, enable the production of miscible surface composition. Combined anchoring ligands-based surface grafting like phosphate and sulphonate anchoring groups may enable anisotropy. Surface co-grafting has the advantage of optimizing the physicochemical properties of the nanoparticles. Implementing different copolymers with various molecular sizes, chain compositions, and end-group functionalities produces localized surface features. The possible polymer chain length variations and differences in functional groups, induces surface heterogeneity, and anisotropy. As the copolymers take their preferential anchoring sites to attain a thermodynamically stable arrangement, Once the first grafted copolymers occupy the preferred surface sites, second graft copolymers have ample chances to take the unoccupied sites and form an alternative graft pattern. Table 4 presents data on size dispersity and z-average of the separate and copolymer grafted nanoparticles.

Table 4 Comparative hydrodynamic sizes of the separate and double copolymer grafted 25 nm substrate UCNPs.

Grafted polymer(s)	Size	PDI	Z-average	Amphiphilicity
Polymer 6	46	0.14	80	high
Polymer 1	54	0.20	97	Average
Polymer 6&1	38	0.18	72	Average
Polymer 2	33	0.2	60	high
Polymer 6&2	28	0.13	59	high
Polymer 3	31	0.18	59	Average
Polymer 6&3	28	0.19	59	Average
Polymer 4	30	0.17	46	Average
Polymer 6&4	34	0.18	69	Average
Polymer 5	45	0.12	60	high
Polymer 6&5	37	0.17	60	high

The copolymer-grafted surfaces show a reduced hydrodynamic size compared to the corresponding single polymer-grafted particles. The observed property might be due to the dispersity effect of the combined extended and short-branched surface groups. The analysis indicates that different surface functionalities could be introduced to the UCNPs, as confirmed through FTIR and TGA analysis in Figures 66 and 68, respectively.

#### 5.4.2 Stability of copolymers grafted UCNPs surfaces

The nanoparticles' stability relies on the surface-grafted copolymer's surface charge, steric effect, and hydration capacity. Surface with high hydration capacity forms a hydrogel layer that encapsulates the surfaces. Surface functionalities like carboxylic, amine, or oxide groups induce a high degree of hydrophilicity and stabilize the modified surfaces by preventing protein corona during the in-vivo delivery of the nanoparticles.<sup>62, 422</sup> The MPC-incorporated copolymers give a short branch brush-like surface architecture and require less surface area than the OEGMA-based copolymers. The hydration capacity of the MPC groups allows the surfaces to retain a large amount of water and forms a hydration layer. The surface hydration layer protects particles from non-specific interactions during biological application.<sup>449</sup> The nanoparticle stability was assessed for 28 days; the results are presented in Figure 64.

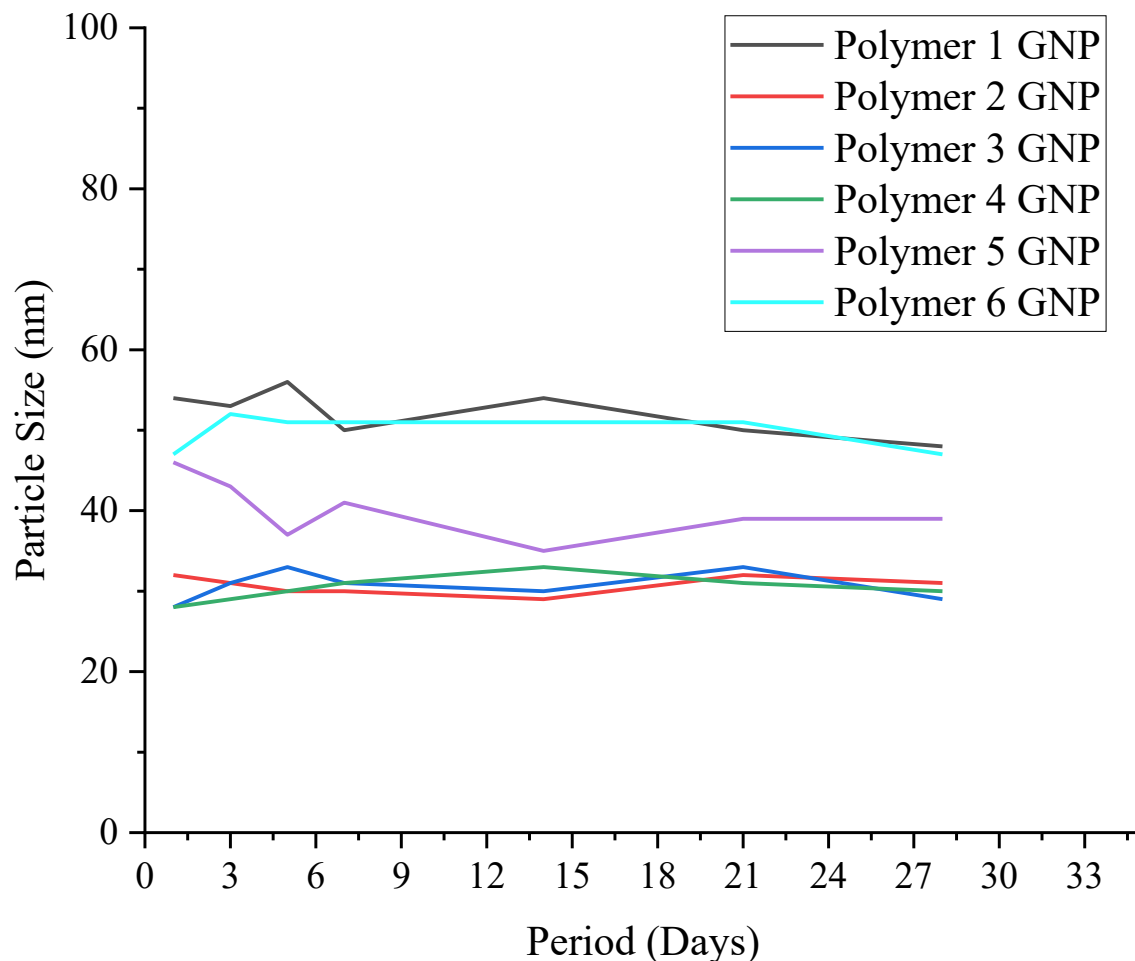


Figure 64 shows the stability of the different copolymers grafted nanoparticles stability in deionized water.

In Figure 64, the number weighted hydrodynamic size for the stability of copolymers' grafted nanoparticles shows the stability of the particles. The result indicates that hydrodynamic size remains stable for a more extended period in an aqueous medium. The change in z-average and PDI change in most of the grafted particles is insignificant. The z-average and PDI of the modified particles are stable. In the case of Polymer 1, the first day PDI and z-average values are 0.20 and 109 nm, respectively, and on the 28<sup>th</sup> day, the PDI and z-average are 0.32 and 106 nm, respectively. A gradual decrease in from the Polymer 1, 3, and 4, a gradual decrease in z-average is observed. The hydrophobic functionalities, mainly from the end groups of are. The Polymer 4 grafted particles show a high PDI of 0.48, which indicates the relative instability of the sulphonate-coordinated particles compared to phosphate-grafted ones. The observed slight fluctuations in hydrodynamic sizes are suspected from possible electrostatic and hydrophobic interactions that



lead to particle clustering. The nanoparticles grafted from copolymers with hydrophobic end groups show a gradual decrease in hydrodynamic size which might result from the shrinkage and tight attachment of the hydrophobic units on the particle's surfaces.

The slight variations in hydrodynamic diameter with time are associated with the possible interactions between surface polymer chains and the clustering of particles. Surfaces high graft with combinations of PEG units and hydrophobic end groups induce overlapped surface appearances than the formation of extended surface brush structures.<sup>242</sup> Nanoparticles grafted with MPC-containing copolymers, for example, produce brush-like surface architecture that induces a high degree of surface hydration.<sup>449</sup> The hydrophobic backbone carbons of the OEGMA blocks tend to reside on the particle surfaces by forming overlapped surface appearance. As a result, a reduced hydrodynamic size could be observed from surfaces containing a high proportion of hydrophobic surface groups.<sup>242</sup> The presence of amine groups in Polymers 1 grafted nanoparticles could induce a strong hydrogen bonding that could lead to the clustering of nanoparticles.

The nanoparticle stability assessment allows the evaluation of the long-term performance of copolymer-grafted nanoparticles. The stability of the particles is associated with steric repulsion effects from long-chain grafted copolymers. The electrostatic repulsion from the charged groups of the colloidal dispersion also has a significant role in the nanoparticles' colloidal stability.<sup>450</sup> Electrostatic stabilization is confirmed from the z-potential analysis, and all modified particles exhibit high surface potentials. The MAA units are vital in achieving enhanced surface charge and zeta potentials. The combined effects from possible steric hindrances and electrostatic repulsions help to keep the nanoparticles stable.<sup>450</sup>

The ATR-FTIR of copolymer grafted nanoparticles confirms for functionalities of copolymers from the modified UCNPs surfaces. Variations in the intensity of FTIR absorptions before and after copolymer grafting confirm that surface grafting had been achieved effectively. In Figure 64, the main functionalities of the oleate ligand and other copolymers are observed at 3010, 2920, 2815, and 1548  $\text{cm}^{-1}$ . The broad absorption bands at 3500 to 2500  $\text{cm}^{-1}$  reveal the presence of high carboxylic density. The pronounced absorption from the carboxylic groups obscures the absorption effect of the rest functionalities in the 3500 to 2500  $\text{cm}^{-1}$ . The oleate-capped nanoparticle surfaces show an intense absorption band around 2920  $\text{cm}^{-1}$  due to the oleate methyl end groups. The absorption bands at 2850  $\text{cm}^{-1}$  in the case of Polymers 2, 4, and 5 grafted nanoparticles are

significantly high. The alkane groups of the RAFT agents contribute to the strong absorption bands at  $2850\text{ cm}^{-1}$ , in addition to methylene groups of the OEGMA.

The overlapped absorption at  $1100\text{ cm}^{-1}$  belongs to ether groups which are significantly high in all copolymers except Polymers 5 and 6. The absorptions at  $1720\text{ cm}^{-1}$  and  $1700\text{ cm}^{-1}$  are due to carboxylic and ester carbonyl absorptions, respectively. The intense absorption at  $1650\text{ cm}^{-1}$  belongs to the carbon double bond of the oleate ligands. The different grafted copolymers enable the development of improved UCNP performances due to the different functionalities and surface composition. Figure 65 shows FTIR spectra of different copolymer grafted UCNPs.

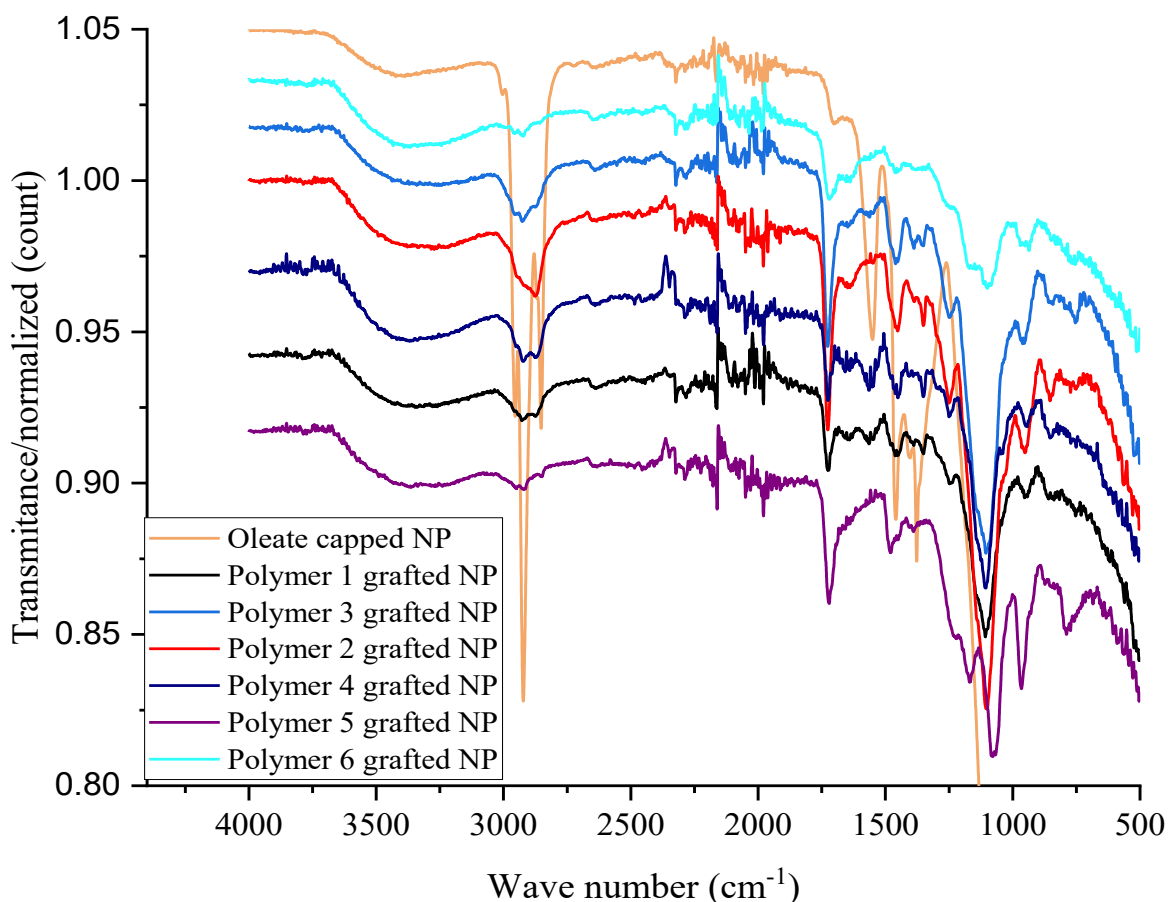


Figure 65 ATR-FTIR spectra of the oleate capped, and copolymers modified nanoparticles.

The combined copolymer-grafted surface functionalities are assessed from observed variations in absorption peaks between the first copolymer-grafted and second-grafted nanoparticle's surfaces. The FTIR spectra show different functionalities like hydroxyl, methyl, methylene, and carbonyl, confirming that the double copolymer grafting had been done successfully. Enhanced

absorbances are observed in the FTIR spectra with the thorough grafting of the second copolymers. The absorption at  $1720\text{ cm}^{-1}$  belongs to the second grafted copolymer. In the case of Polymers 1 and 2, double-grafted surfaces have an intense absorption peak at  $1100\text{ cm}^{-1}$ , compared to the single copolymer grafted surfaces. The observed difference in surface functionalities is associated with the newly introduced ether groups of OEGMA units. The enhanced intensity at  $1720\text{ cm}^{-1}$  is due to carboxylic carbonyl, indicating the surface gained high carboxylic density. The absorption peak at  $1700\text{ cm}^{-1}$  belongs to ester carbonyls. In Figure 66, nanoparticles grafted through combined copolymers are compared to separate Polymer 6 grafted surfaces.

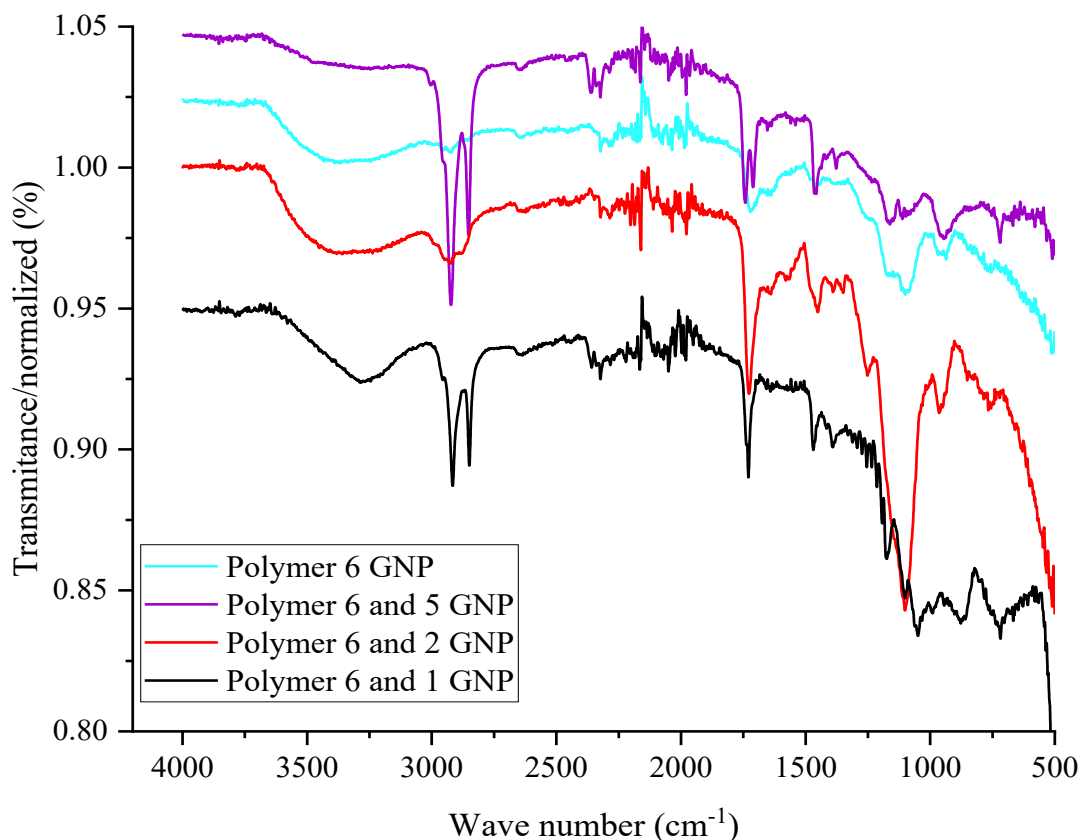


Figure 66 ATR-FTIR spectrum of combined copolymers grafted UCNPs.

The Polymer 6 grafted surfaces have a lower absorption band than the combined copolymer grafted ones. In the Polymer 5 co-grafted surfaces, carbonyl absorption from MPC and the copolymerized monomer is observed at  $1650$  and  $1720\text{ cm}^{-1}$ . The strong absorption bands at  $2800$  and  $2900\text{ cm}^{-1}$  in the case of Polymer 6 and 1 and Polymers 6 and 2 co-grafted surfaces are due to methyl groups end groups of the OEPSX and MPC units, respectively. The change in methyl and methylene

absorption is a good indication of the achievement of double grafting. For instance, the methyl and methylene absorptions are highly pronounced in the case of Polymer 5 and 1 grafted surface. However, the Polymer 6 and 2 and Polymer 6 only grafted surfaces show insignificant methyl absorption.

The combined copolymers-based grafting of the UCNPs enables control of surface composition and graft density. For instance, enhancing reactivity for further coupling has some significant advantages of the combined polymers' surface grafting. Surface graft density improvement opens new opportunities in the roles of UCNPs in nanomedicine. Multiple functionalities through combined sequential grafting could be introduced. The efficient replacement of the oleate ligand minimizes nanoparticle aggregation and toxicity that arise from a gradual detachment of the less stable carboxylate ligand.<sup>182</sup> In drug delivery application of UCNPs, the loading capacity of the surface is dependent on the surface composition and graft density.

➤ Stability of the copolymers grafted UCNPs in different buffers

The observed stability of the surface grafted nanoparticles in different buffers indicates that the grafted surface resists replacement with the buffer competitive ions. The stability of Polymer 1 grafted nanoparticles, for instance, in the borate buffer is better than in the PBS and MES buffers. As presented in Table 5, the double copolymer grafted particles show relatively low hydrodynamic sizes PDI. The low PDI from the combined copolymer grafted nanoparticles shows improved stability compared to different corresponding separate copolymer grafted nanoparticles. The instability UCNPs in buffer media is associated with interference of the buffer component ions to the surface anchoring ions and their possible chemical reaction with the crystal component cations. The phosphate ions originate from the PBS buffer could displace the residual oleate ligands.

Achievement of high graft density through efficient exchange of oleate ligands helps to secure improved nanoparticle stability. Optimization of surface graft density enhances the stability of the particles in PBS. The performed preliminary investigation shows that the double-grafted nanoparticles show relatively better stability. The UCNPs surfaces contain relatively large amounts of residual oleate chains in low surface graft density conditions. An increase in the number (footprint) of surface-anchored moieties improves the stability of UCNPs in the presence of competitive ions.<sup>146</sup> Tong et al. confirm multidentate tetraphosphate derivatized ligands based

surface grafting effectively stabilizing the nanoparticles in PBS buffer.<sup>451</sup> The stability of those surfaces originates from the introduction of sufficient phosphate attachment to the nanoparticles.

Table 5 The stability of different copolymers obtained from separated and double-grafted nanoparticles in different buffer solutions.

Grafted copolymer	Hydrodynamic size (nm/PDI)											
	6 Hours			12 Hours			24 Hours			48 Hours		
	MES (pH=5.2)	PBS (pH=7.4)	Borate (pH=8.5)	MES (pH=5.2)	PBS (pH=7.4)	Borate (pH=8.5)	MES (pH=5.2)	PBS (pH=7.4)	Borate (pH=8.5)	MES (pH=5.2)	PBS (pH=7.4)	Borate (pH=8.5)
Polymer 1	69/ 0.7	70/ 0.7	52/ 0.3	46/ 0.4	118/ 0.7	50/ 0.7	42/ 0.4	690/ 0.7	58/ 0.4	50/ 0.4	416/ 1.0	51/ 0.4
Polymer 2	34/ 0.6	37/ 0.4	41/ 0.4	35/ 0.6	41/0 .5	42/ 0.5	35/ 0.6	45/ 0.7	39/ 0.5	413/ 0.6	41/0 .7	41/ 0.5
Polymer 3	52/ 0.8	38/ 0.3	42/ 0.7	42/ 0.8	34/0 .7	52/ 0.6	47/ 0.7	41/ 0.5	44/ 0.6	46/ 0.7	389/ 0.4	58/ 0.6
Polymer 5	55/ 0.5	33/ 0.7	54/ 0.7	45/ 0.6	315/ 0.5	56/ 0.6	40/ 0.5	340/ 0.6	40/ 0.5	52/0 .8	400/ 0.6	52/ 0.8
Polymer 6 and 2	-	40/ 0.4	-	-	39/0 .4	-	-	33/ 0.4	-	-	37/ 0.3	-
Polymer 6 and 3	-	30/ 0.4	-	-	36/ 0.5	-	-	39/ 0.5	-	-	49/ 0.6	-

Table 5 shows a preliminary result on the stability of the copolymers grafted nanoparticles. The data indicates that the double copolymer grafted nanoparticles gained smaller hydrodynamic size and lower dispersity in PBS than the corresponding separate copolymer grafted nanoparticles. Relatively the co-grafted nanoparticles have better stability in PBS; for instance, Polymer 6 and 2 and Polymer 6 and 3 exhibit relatively small hydrodynamic sizes and high dispersity. Relative to the MES and borate buffers, most grafted nanoparticles are unstable in the PBS buffer. The phosphate ion from PBS buffers displaces the weak carboxylate residuals ligands. The displaced oleate ligands pend with in the particle suspensions and strongly impact the longer-period stability of the nanoparticles.

#### 5.4.3 Determination of surface graft density of modified nanoparticles

Determining graft density for the copolymers modified nanoparticles allows determining the amount of surface attached polymer per particle. The TGA analysis was conducted from 20 to 600 °C in atmospheric conditions. In Figure 67, the TGA weight loss clearly shows that the grafted

nanoparticles surfaces have gained different compositions. Most TGA curves of the grafted copolymers have similar appearances because they are made from similar monomers and block proportions. The copolymer's TGA curves of the individual copolymers corresponds pure polymers presented in Chapter 4.

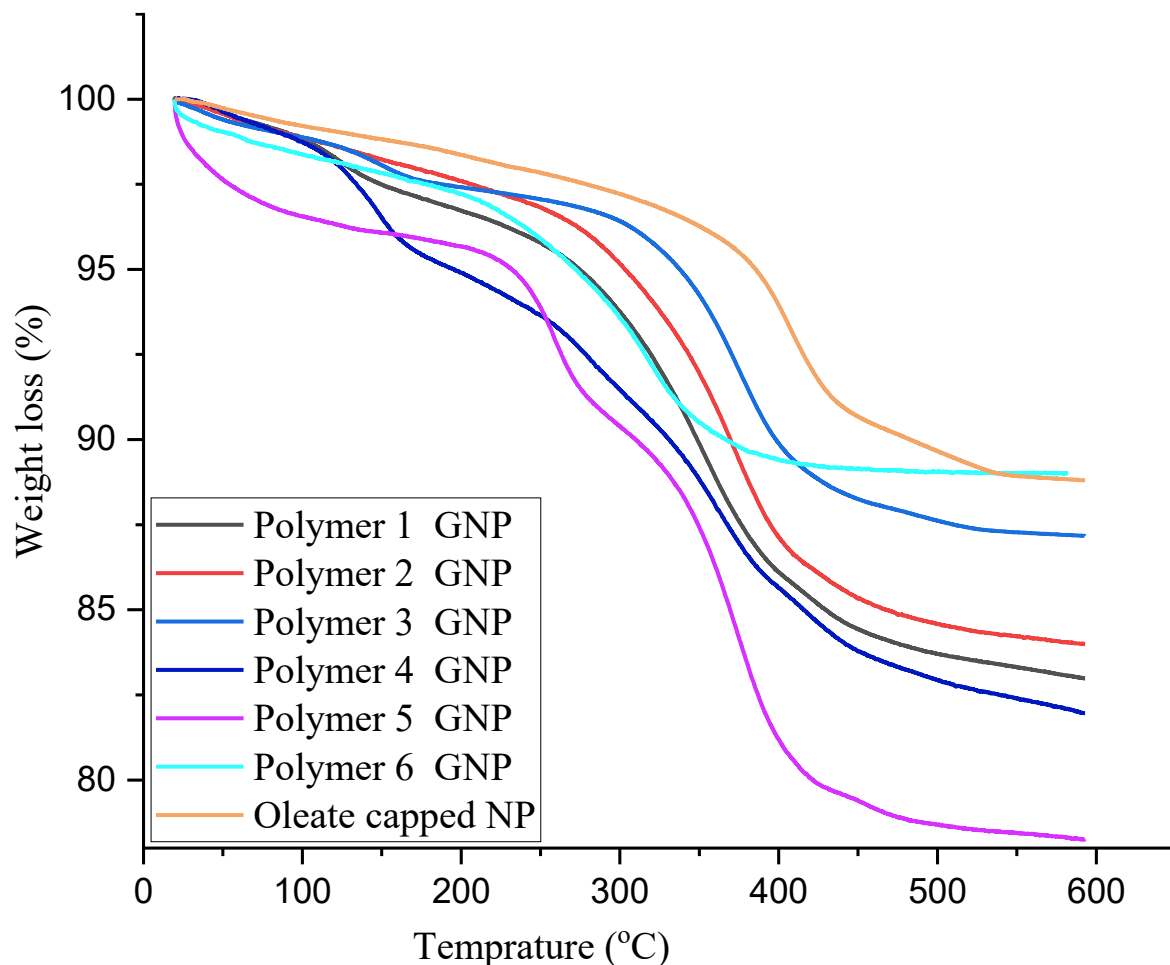


Figure 67 TGA thermograph of the as-synthesized oleate capped and copolymers grafted UCNPs. The TGA curves consist of form six major weight loss regions. Weight losses below 100 °C are due to impurities. The change in weight at 100 to 150 °C is associated with de-hydroxylation from the carboxylic, phosphate, and sulphonate hydroxyls. The hydroxyl weight losses are significantly pronounced in the copolymers modified nanoparticles compared to the oleate ligand.<sup>394</sup> The weight at 180 to 250 °C is due to decarboxylation and the RAFT agent decomposition.<sup>452</sup> The weight at temperatures of 250 to 300 °C belongs to the decomposition of the PEG ether groups.<sup>452</sup> The weight loss at 350 to 450 °C belongs to the decomposition of backbone chains. The pronounced

degradation curve in the case of oleate-capped particles is due to the long alkane chains. The weight loss at 450 to 600 °C is associated with the carbon double bonds, which are more visible in the double bonds containing polymers, such as the oleate ligand, Polymers 1 and 3. conditions. Compared to oleate-capped nanoparticles, the copolymer grafted particles, the rapid and high weight losses at 150 to 300 °C are associated with the carboxylate and hydroxyl weight losses. In the case of oleate-capped surfaces, however, a slow and reduced change in weight is due to the lower concentration of the carboxylic groups. The carboxylic group weight loss in the Polymer 6 grafted surfaces is almost double that of the rest copolymers, and this shows the presence of a relatively high graft density.

The observed differences in TGA curves for the grafted surfaces are due to monomer type and RAFT agent composition differences. In the case of Polymers 4 and 5 grafted nanoparticles, the TGA curves significantly differ from the rest due to the AMPS and MPC monomers.<sup>453</sup> The Polymer 5 grafted nanoparticles show significant dehydration and dihydroxylation loss. The weight loss at 150 to 350 °C is related to the sulphonate group.<sup>454</sup> The slight variations in molecular weight, block number, and end group functionalities from the different RAFT agents are expected to have slight variations in the GTA curves. The nanoparticles grafted from Polymers 3 and 5 show high graft densities because those polymers are composed of short branch chains. The reduced steric repulsions allow for the introduction of large molecules to the nanoparticle surface.

The graft density determination has been done by considering the particles to have a spherical shape to simplify the surface area determination. The TEM 25 nm diameter provides a surface area of 1962.5 nm<sup>2</sup> and the mass of one particle is determined from its volume (V) and density (d) (2.41 g/cm<sup>3</sup>) relationship, as represented in equations 8 and 9. The total number of copolymers (ligand) per sample and the number of ligands per particle are calculated according to equations 10 and 11, respectively.<sup>141</sup>

$$V_{UCNP} = \frac{4}{3}\pi\left(\frac{d}{2}\right)^3 \dots\dots\dots(8)$$

$$N_{UCNP} = \frac{m_{UCNP}}{m_{UCNP}} \dots\dots\dots(9)$$

$$N_{Lignd} = \frac{m_{loss}}{M_{Ligand}} N_A \dots\dots\dots(10)$$

$$\frac{N_{Ligand}}{UCNP^P} = \frac{N_{Ligand}}{N_{UCNP^P}} \dots\dots\dots(11)$$

Where UCNP<sup>P</sup> represents plain UCNP, and NA stands for Avogadro number. The weight loss, number of chains, and graft density for the different copolymers are summarized in Table 5.

Table 6 TGA data on weight loss and graft density of a 25 nm oleate capped and polymer grafted nanoparticles.

Grafted Copolymer type	Initial weight	Final weight	Change in weight (%)	No. of poly/NP	No. of Poly. molecule/nm <sup>2</sup>
Polymer 1 GNP	1.545090	1.271153	17.73	724	0.37
Polymer 2 GNP	1.675639	1.398559	16.54	663	0.34
Polymer 3 GNP	1.302671	1.052638	19.19	797	0.41
Polymer 4 GNP	1.579716	1.375124	12.95	499	0.25
Polymer 5 GNP	1.163484	0.887984	23.67	1410	0.72
Polymer 6 GNP	1.948788	1.791814	8.10	1465	0.75
Oleate capped NP	3.876565	3.447454	11.07	13684	6.95

The oleate ligand density for the 25 nm UCNP is determined to be 6.95 molecules per nanometre square. The determined weight loss from the oleate-capped nanoparticles corresponds with previously reported values.<sup>223</sup> The UCNPs accommodate fewer oleate ligands than smaller molecule ligands. The possible oleate desorption during the purification of the nanoparticles also reduces the measured graft density. The extended surface appearance of the long branch chain copolymers hinders coordinating sites for further coordination, and only a few copolymers could be introduced to the surface. However, the ligand density calculation is performed by considering a complete ligand exchange is accomplished.<sup>440</sup> The surface oleate ligand replacement is done through the nucleophilic substitution (S<sub>N</sub>2) mechanism. The surface introduction of the new ligand is achieved when the existing ligand leaves out the surface. The accessibility of the surface coordination sites determines the number of copolymers that could be introduced. Direct ligand exchange enables low graft density because the steric repulsion from long-branched block copolymers limits the number of polymers introduced. The residual oleate ligands strongly affect the stability of the nanoparticles in ionic media including buffer and solutions.

The architecture and size of the copolymer were implemented to determine graft density. Copolymers that consist of OEGMA blocks exhibit an extended surface area coverage and steric hindrance. The oleate residing in the nearby surface regions is protected from ligand replacement



and remains unreplaced. The introduced copolymer number and composition determine the dispersibility and stability of the copolymer-grafted nanoparticles. The amphiphilic surface groups extend out, and colloidal dispersibility could be achieved in the aqueous and biological media. Although a few copolymers are attached to the surfaces of the particles, the introduced amphiphilicity enables the production of water nanoparticles.

The double copolymer UCNP grafting enables high control of the surface features.<sup>455</sup> The nanoparticle surface can accommodate many smaller molecules than larger ones. Combined surface grafting from short-branched and long-branched copolymers co-grafting enables high graft density surface production. The presence of diminished steric and electrostatic repulsions in the short-branch copolymers allows the introduction of many chains to strip out the oleate ligands. The smaller branch size polymers like Polymer 5 and 6 are ideal candidates to occupy the inter-spaces between the long-branched copolymers such as Polymers 1 to 4.<sup>455</sup> Particles grafted from short branch copolymers, for example, in the case of Polymer 5, a relatively high graft density. The copolymers with hydrophobic end groups have high graft density; for instance, nanoparticles grafted from Polymers 2 and 3, in the same conditions, achieved 16.54 and 19.9 % graft densities are achieved. A possible reason for the enhanced graft density in the case of Polymer 3 could be due to strong hydrophobic interactions between the hydrophobic end groups and the nanoparticle surfaces.

The combined copolymers based UCNPs grafting have potential opportunities to introduce a new surface feature. The mixed copolymers' surface compositions can provide multiple functionalities and physicochemical properties. The multiple synthesized copolymers are advantageous to obtain comprehensive options from possible combinations for the grafting of the UCNP. The multiple surfaces could be designed to provide vast opportunities that could not be addressed here under this project's scope. In Figure 68, the normalized TGA curves clearly show differences in the UCNPs' surface composition for separate and co-grafted surfaces.

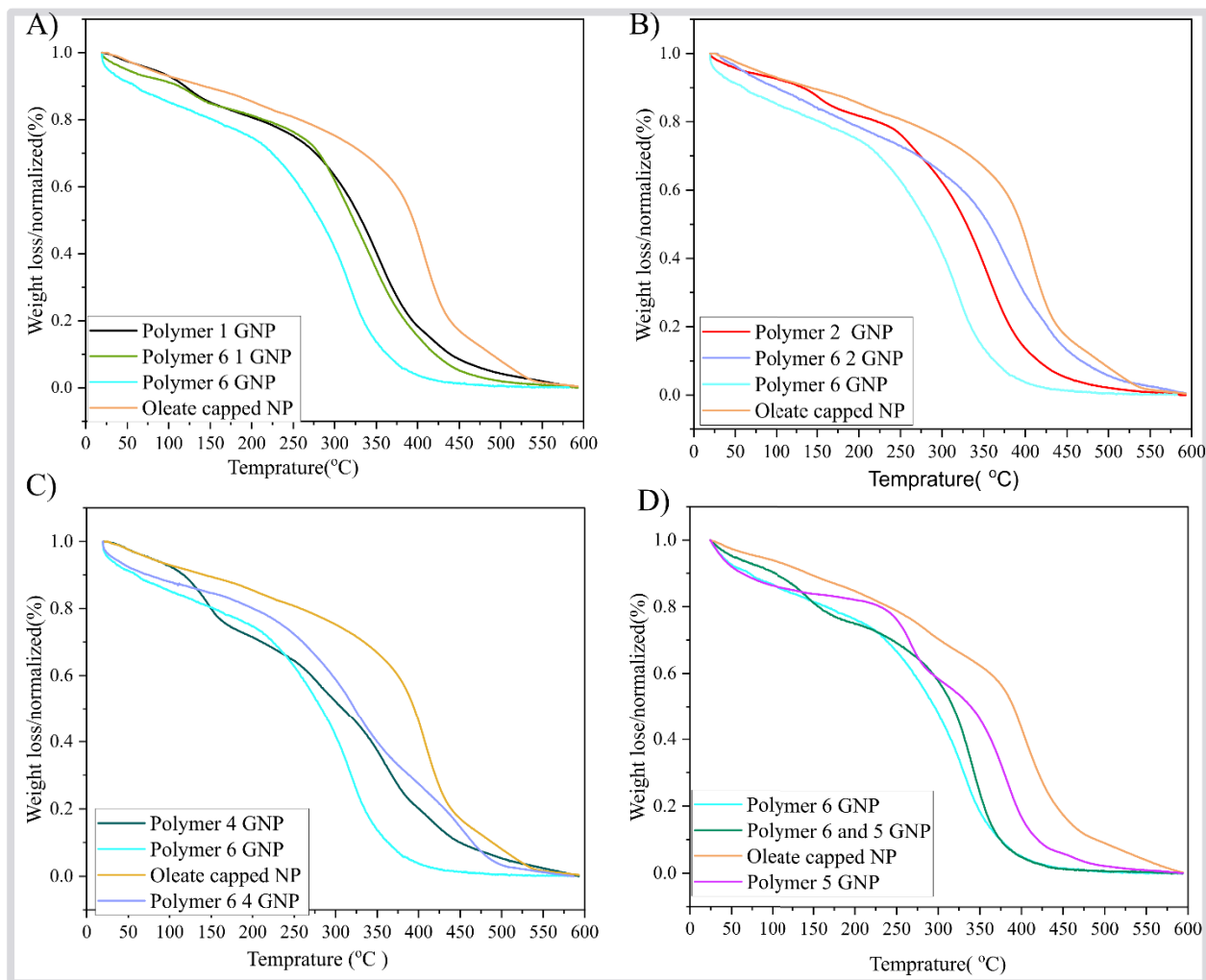


Figure 68 Thermograph of the combined copolymers grafted UCNPs.

The combined copolymer surface grafting approach affects both graft density and surface compositions. The TGA curves of the double copolymer co-grafted particles are entirely different from the corresponding separate copolymer-grafted ones. The Polymer 6 grafted nanoparticles show a high weight loss at 100 to 250 °C, confirming the presence of significant carboxylic group loss achieved through double grafting. It indicates that surface grafting using Polymer 6 enables the introduction of large amounts of hydroxyl groups to the surface. As seen in Figure 68A-D, the combined copolymers grafted nanoparticles have shown an average hydroxyl and carboxylate weight loss compared to the corresponding separate copolymer grafted ones. Introducing the highly branched copolymers reduces the surface hydroxyl and carboxylate group density. The long-branched copolymers achieve a lower phosphate surface footprint, and the short-branch polymers give high graft density.

➤ Surface grafted copolymer end-groups modification

The OEPSX-based Polymer 1 copolymer has an attractive potential advantage by modifying its two end groups. Hydrazinolysis of the grafted copolymer through hydrazine treatment allows the introduction of additional functionalities. As shown in Figure 69, amine and sulfhydryl functionalities could be introduced from the hydrazinolysis. In addition to the excessive carboxylic groups from the MAA blocks, sulfhydryl and amine functionalities could be introduced as an alternative coupling site. The introduction of sulfhydryl reactive sites enables to implementation of maleimide coupling, and the amine serves for EDC-based coupling. Furthermore, the sulfhydryl functionality implements the copolymers for gold particle functionalization. The MAA functionality provides a high degree of flexibility from its hydrophilic nature, allowing for enhanced biomolecule attachment to the particle surfaces.

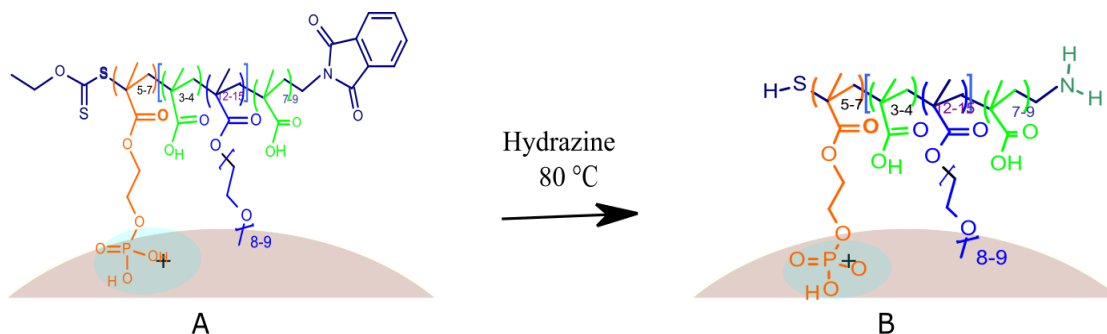


Figure 69 Schematic illustration of an end-group modification of the OEPSX copolymers, where (A) before and (B) after end-group modification.

The OEPSX end-group modification has an advantage in the functionalization of the UCNP. Biomolecule coupling through amine-EDC activation or by maleimide chemistry through the sulfhydryl group. The hybrids from UCNP-FITC covalent coupling keep the FITC molecule very close to the nanoparticle surfaces, 5-10 nm, which gives an additional advantage to implementing the FRET sensing application.<sup>456, 457</sup> The FITC-NCS could be coupled at the functionalities of the sulfhydryl or amine end group.<sup>458</sup> The xanthate RAFT agent-based graft polymers could serve as an all-in-one coupling platform. The carboxylic groups could also be further derivatized to azido functionality, which is not under the project's scope. The UCNP-FITC integration was performed through covalent coupling. The hybrid nanoprobe is useful in cell labeling and imaging using microscopes with NIR and visible excitation approaches. The coupling of UCNP with FITC NCS has been performed as schematically illustrated in Figure 70.

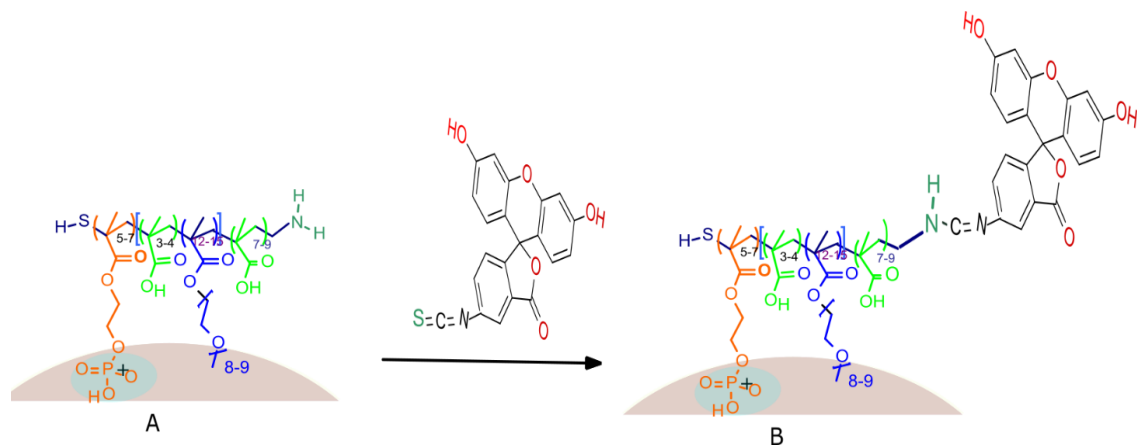


Figure 70 Schematic illustration of the coupling of FITC-NCS at the amine (A) and sulfhydryl of the modified end groups and (B) FITC-coupled surfaces.

➤ The functionality of the copolymer's grafted and modified surfaces

ATR-FTIR analysis was performed to assess change in end group functionality of the OESPX polymers modified particles. As displayed in Figure 70, the generated surfaces show different functionalities. The observed surface functionality differences from FTIR analysis performed before and after hydrazine treatment indicates that the end group modification is accomplished. These modified functionalities have enormous potential to serve in the UCNPs-dye integrated probes development for intracellular labeling and imaging. The various copolymers could be used in co-graft form for UCNP dye probe development.

The absorption peak at  $1540\text{ cm}^{-1}$  is due to the hydrazide C-N stretch, and the relatively broader peak at  $3500\text{ cm}^{-1}$  regions is due to the NH stretch. The amide II absorption at  $1470\text{ cm}^{-1}$  indicates the achievement of antibody-surface polymer covalent bonding.<sup>459</sup> The FITC coupled surfaces are identified with enhanced carbonyl absorption associated with the FITC carbonyl. Compared to the polymer-grafted and hydrazine-treated surfaces, the FITC-coupled surfaces show a slightly increased hydroxyl absorption at  $3500\text{ cm}^{-1}$ .

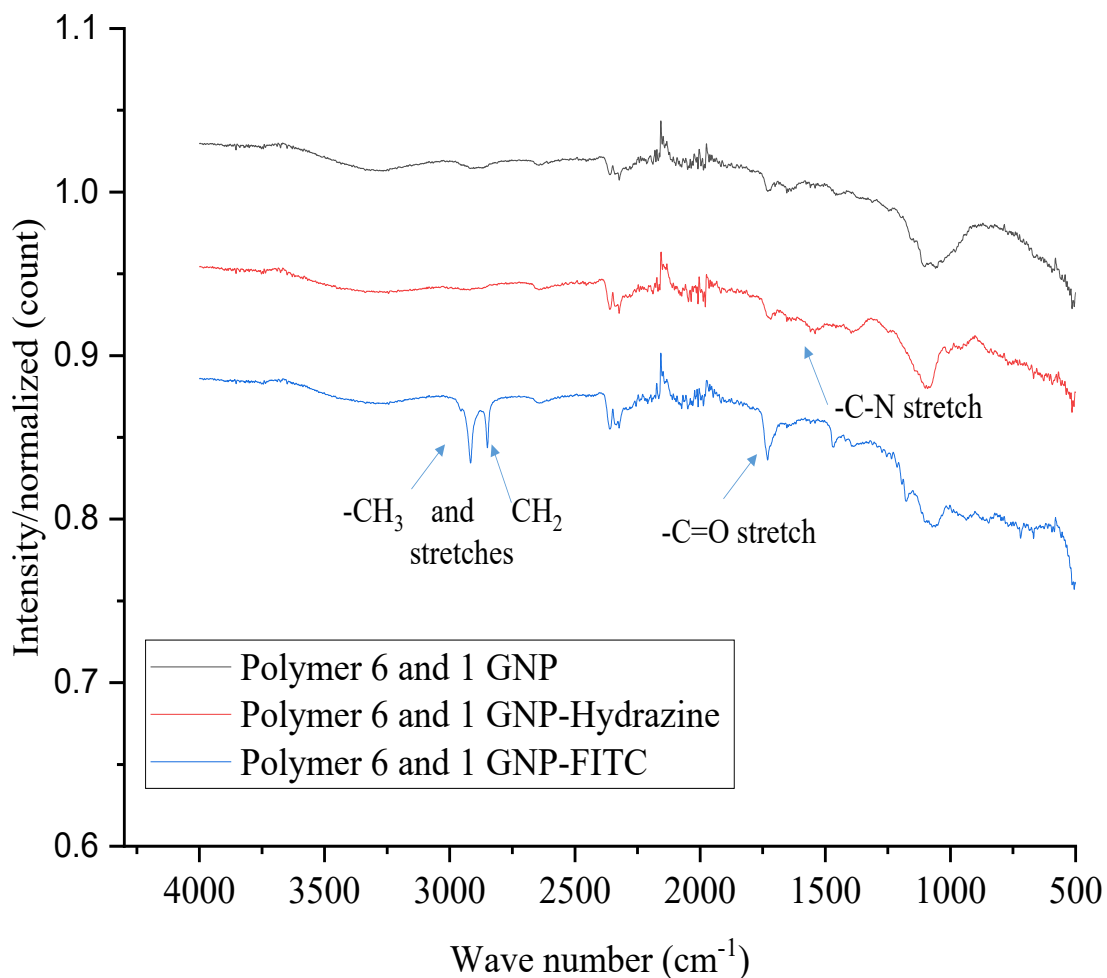
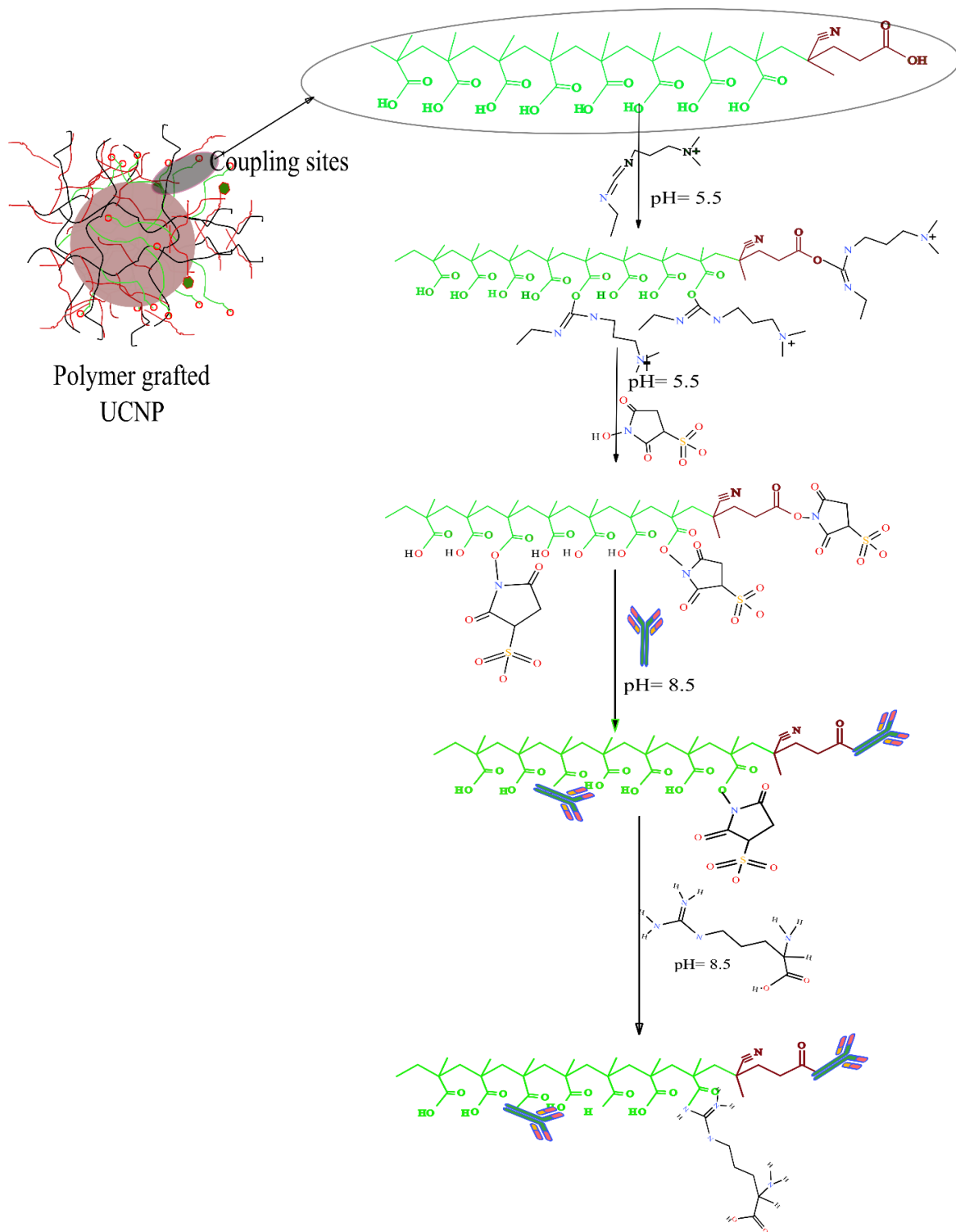


Figure 71 FTIR spectra of post-surface graft end group modified surfaces (black spectrum); with hydrazine treatment (red spectrum) and FITC coupled surfaces (blue spectrum).

#### 5.4.4 Coupling of biomolecules and organic dyes

The MAA functionalized particle surfaces are helpful in successfully introducing bioactive molecules. Conjugation of bioactive molecules to the nanoparticle surfaces allows for imparting biological features to the synthetic material.<sup>460</sup> The nanoparticle-antibody coupling has been performed using EDC chemistry as represented in Scheme 11.



Scheme 11 Mechanisms of EDC/NHS activation and stabilization, and antibody coupling.

The increased surface carboxylic density and the associated high degree of flexibility of peripheral groups allow for achieving enhanced coupling efficiency and improved targetability through

easing ligand-receptor interaction. The arginine treatment is done after coupling has two main advantages. It deactivates EDC-activated but non-coupled sites and avoids gradual self or cross-coupling. The surface-attached arginine facilitates cellular uptake of the nanoparticles. The DLS analysis shows the difference in nanoparticle size with different antibody concentrations, Figure 72. The hydrodynamic particle size changes from 28 nm to 38 nm with the coupling of 1  $\mu\text{g/mL}$  and 2  $\mu\text{g/mL}$  of antibody, and the PDI and z-average values are 0.14 and 60, respectively. Nanoparticles coupled with 3  $\mu\text{g/mL}$  antibody gained a hydrodynamic size is 45-50 nm, and their PDI and z-average values are 0.29 and 111, respectively. The significant hydrodynamic size increment with the 3  $\mu\text{g/mL}$  coupling is close to two antibody size increments. A similar study by Byzora et al. reported the effect ratio of antibodies conjugated on gold nanoparticles and the nanoparticle's stability.<sup>442</sup> The analysis indicates the surface saturates by conjugating 2 to 3  $\mu\text{g/mL}$  antibody. The 1 and 2  $\mu\text{g/mL}$  antibodies were used in the cell labeling. An optimum lower antibody density allows for reduced particle size increment and high labeling density.

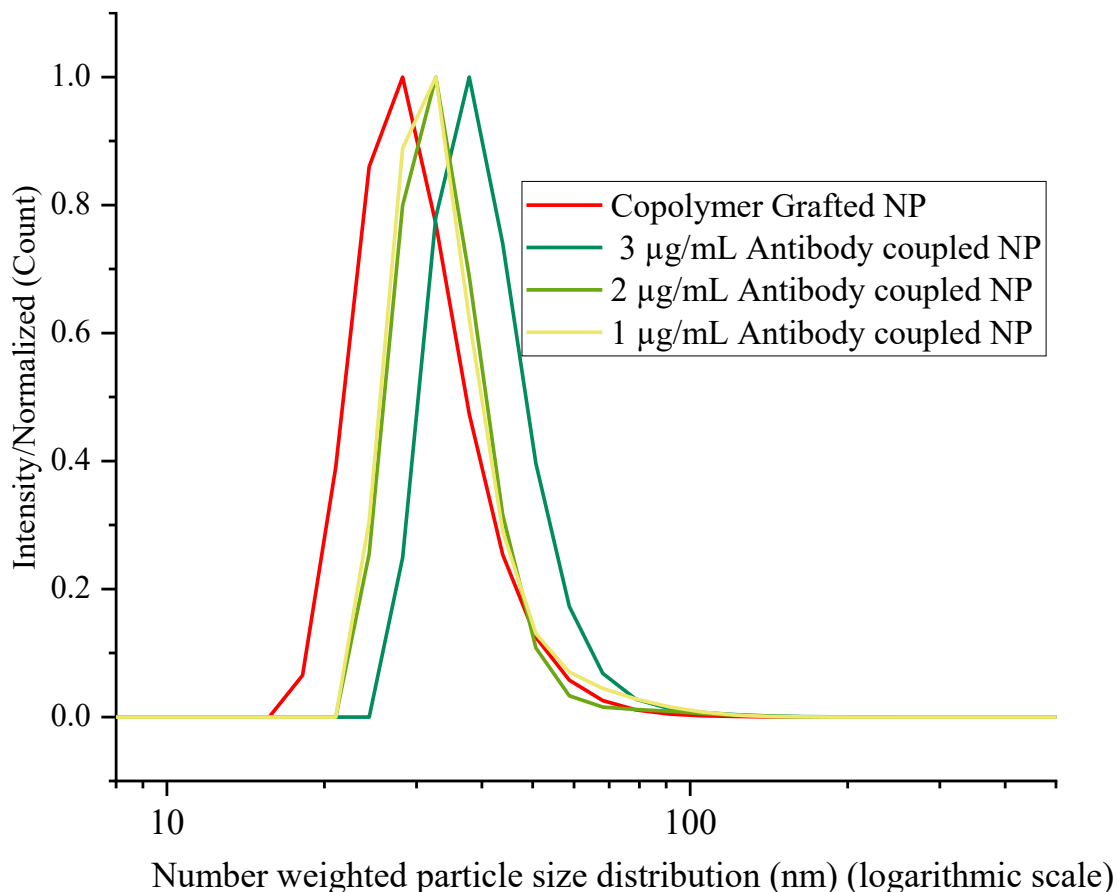


Figure 72 DLS hydrodynamic size of different antibody concentration coupled UCNPs.

A significant change in the zeta potential is observed with the coupling of antibody-to the nanoparticles. The initial zeta potential polymer of grafted nanoparticles is - 23 mV. After antibody coupling, the nanoparticles' zeta potential is reduced to - 11 mV. A similar previous result from studies of antibodies coupled to magnetic nanoparticles has been reported.<sup>461</sup> The zeta potential for coupling different antibody concentrations has shown an insignificant difference. The zeta potential of the EDC-activated and NHS-stabilized nanoparticles was measured and was found to be -6 mV. It indicates that the extent of the EDC/NHS activation and stabilization determines the final zeta potential. The carboxylic groups are already reacting with EDC/NHS, and the zeta potential of the functionalized nanoparticles is found to be low. The carboxylic groups in the surface grafting polymers are vital in achieving effective antibody coupling. The MAA-incorporated copolymers give multiple advantages in improving the coupling efficiency of UCNP surfaces. The RAFT agent, carboxylic end groups gain high flexibility and overcome the possible hindrance effect of the OEGMA blocks.

The availability of excess carboxylic groups from MAA units produces high hydrophilicity. The high carboxylic density also induces pronounced surface hydration and antifouling capacity. The surface carboxylic functionality increases along with the copolymers' graft density. The surface gains a low negative zeta potential when many carboxylic groups are activated or deprotonated. The amount of EDC used for the carboxylate activation determines zeta-potentials. Deactivation of the remaining NHS stabilized groups avoids gradual reactions of the antibody and aggregation. As arginine-based peptides are known for facilitating cellular uptake, the arginine UCNPs have additional advantages in facilitating cellular uptake during the delivery of the NPS. Combining FITC-UCNPs through surface covalent coupling allows for developing hybrid nanoprobe in cell labeling and imaging using microscopes with NIR and visible excitation approaches.

The change in the nanoparticles' hydrodynamic diameter after peptide immobilization is insignificant. As done during the antibody coupling, polyarginine and TAT peptides coupled had been performed as described in the antibody coupling procedure. As shown in Figure 73, the peptides' functionalized nanoparticles have gained diminished hydrodynamic size. Due to the small size of peptides, the polyarginine and TAT-HIV functionalized particles have a slight change in particle size. The reduced hydrodynamic size increase is essential in controlling particle size for nucleolus labeling. Nucleolus labeling requires smaller size particles that pass through the nuclear



complex. The arginine rich peptide-functionalized particles are found good enough to implement UCNPs-based nucleolus labeling and imaging effectively. The hydrodynamic size of the polyarginine-functionalized particles is 38 nm with a PDI of 0.18, and the z-average is about 65 nm. The TAT-HIV functionalized particles are 37 nm with a PDI of 0.17, and the z-average is 60 nm. The peptide-functionalized nanoparticles exhibit a low increment in hydrodynamic size, as presented in Figure 73.

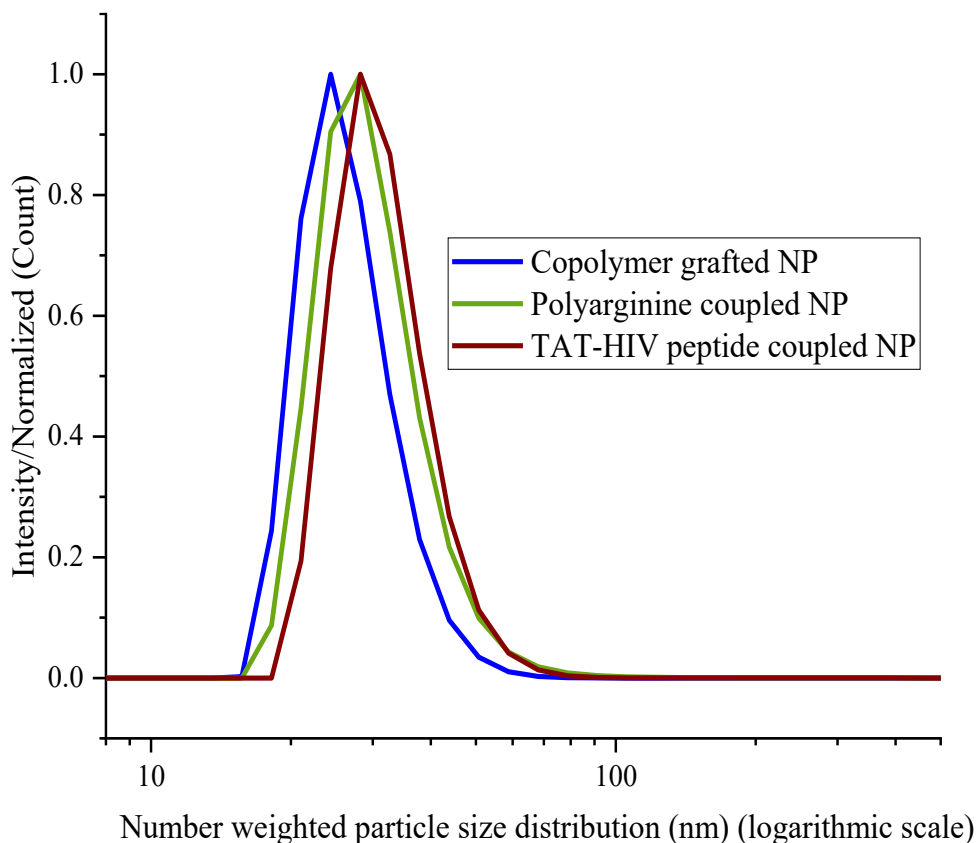


Figure 73 The hydrodynamic size of poly arginine and TAT-HIV peptide coupled UCNPs.

The FTIR of the antibody functionalized nanoparticles clearly shows that the antibody is coupled to the surface. The antibody peak dominated the grafted polymer. In Figure 74, the double peaks in the  $1710$  and  $1740\text{ cm}^{-1}$  regions are due to carbonyl stretch from the amid functionalities.<sup>462</sup> The amide functionality peaks attest to the attachment of antibodies to the nanoparticle surfaces. The strong band in  $2900$  to  $2850\text{ cm}^{-1}$  regions is due to the dominance of symmetric and asymmetric stretches of methylene and methyl groups. The amid I at  $1670\text{ cm}^{-1}$  and amid II at  $1570\text{ cm}^{-1}$  peaks confirm the antibody and peptides are coupled to the nanoparticle surfaces.<sup>461, 459</sup> The intense

absorption bands at 3000 to 3300  $\text{cm}^{-1}$  are due to -NH and the absorption at 2900  $\text{cm}^{-1}$  belongs to methylene groups of the antibody and the peptides.

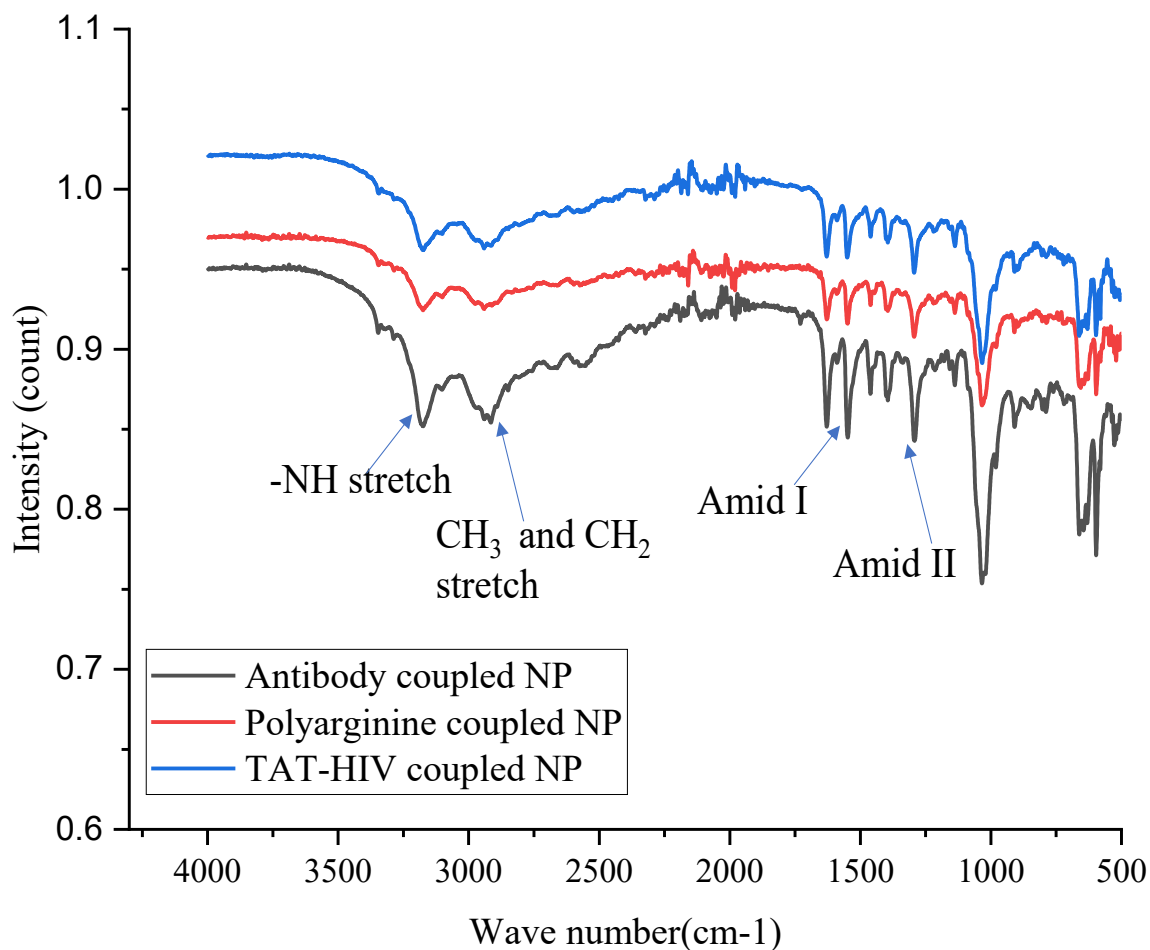


Figure 74 FTIR spectra of Antibody, Polyarginine, and TAT-HIV peptide-functionalized UCNPs.

## 5.5 Conclusions

The design and functionalization of UCNP using two copolymers enables the production of multifunctional surfaces with improved biocompatibility. The composition of copolymers used in surface grafting has a significant role in achieving improved UCNPs surface functionalities. The MAA-incorporated triblock RAFT copolymers have been successfully developed with the concept of advancing the performance of the surface graft polymers. Implementing the triblock copolymers in combined or separate surface grafting in surface modification of the UCNPs helps to introduce synergized functionalities and performances. The excess carboxylic groups in each copolymer and the MPC units are potential functionalities to enhance the biocompatibility of the particles. The

separate and combined copolymer based UCNPs surface grafting has been explored to advance the particles' surfaces. The implemented different grafting approaches enable good control of surface composition and functionality.

The impression in implementing the MAA functionalized triblock copolymers in UCNPs surface tailoring is due to the high flexibility and accessibility of the excessive groups. The combined outcomes from the reactivity MAA units and the excellent steric stabilization potential of OEGMA chains are the main reasons for observed good performances. The RAFT agent end groups and the type of monomers are critical factors in controlling the surface functionalities of polymer-grafted particles; for instance, the Polymer 2 grafted particles gained high labeling efficiency. Copolymers developed from OEPSX-based RAFT agents, MPC-incorporated triblock copolymers, and MAA-based diblock copolymers are good alternatives in the surface functionalization of the UCNPs. The OEPSX-modified particles allow for the surface introduction of sulfhydryl, amine, and carboxylic coupling sites.

The MPC-containing copolymers are ideal for developing antifouling surfaces. The deep-rooted challenge associated with protein fouling on the surface of the nanoparticles and loss of functionality needs an efficient solution. The MAA diblock could be an alternative for the PAA-based UCNPs surface modification. The current MPC-incorporated polymer-nanoparticle surface grafting helps to address the challenge. However, the effectiveness of the MPC functionalized particles requires further detailed investigation.

The combined copolymer UCNPs grafting is an innovative approach to further advance the surface grafting of UCNPs. It allows for simultaneously introducing multiple functionalities, such as MPC-based polymers with carboxylic functionalized diblock, to nanoparticle surfaces. The combined surface grafting using selected copolymers has many potential opportunities to achieve high multifunctionality UCNPs surfaces. Through implementing the different polymers, an optimization of graft density, improvement of anchoring efficiency from combined anchoring groups, and diversification of surface functionalities like responsiveness and reactivity could be enabled effectively.

A combined synergic effect from combining different branch chain length copolymers, molecular weights, and anchoring efficiencies helps optimize graft density and particle stability. As the short-branch copolymers cover a smaller surface area, a greater number of oleate ligands could be

replaced compared to those with long branches. In this Ph.D. project, however, few investigations are performed on cell labeling potentials of polymer functionalized particles. The potential of the multiple copolymers and devised co-grafting approach needs further study to utilize their immense potential in advancing UCNPs-based bio applications.

# 6 | Upconversion Nanoparticles in Intracellular Labeling and Imaging

## 6.1 Preamble

This section presents intracellular labeling of the HeLa cell using a pre-designed UCNP probe. The UCNP probes were utilized to label microtubules, actin filaments, nucleolus, and the nuclear pore complex. The effects of the different labeling agents in the delivery and active targeting of UCNPs have been noted. The targetability of the nanoparticles at the microtubules, F-actin, the nucleus, and the nuclear pore complex are confirmed from the images taken by confocal and widefield microscopes. The benefits and limitations of the various imaging techniques to obtain high-resolution images have been mentioned. The effectiveness of the overall nanoparticle fabrication approaches, including surface modification and functionalization, is mentioned. The results indicate potential opportunities for implementing the UCNPs in single molecule and live cell imaging. The functionalized UCNPs are proven for their promising potential to realize UCNP-based nanomedicine applications, including personalized treatment.

## 6.2 Introduction

Biomedical imaging has a prominent role in clinical and scientific explorations.<sup>353</sup> Molecular-level biological events provide essential information to understand the structure and dynamics of cellular behaviors. Direct observation and monitoring of intracellular structures and dynamics provide enormous benefits in life science.<sup>328</sup> Molecular imaging is a well-known technique in fundamental biological investigations. Cellular and subcellular characterization at the high temporal resolution is a pre-request to understand the molecular level structures and dynamics.<sup>463</sup> Molecular imaging techniques, such as optical imaging, provide many opportunities to advance diagnostics and therapeutic approaches.

An optical microscope is one of the most powerful techniques in subcellular studies. Among the number of optical imaging techniques, label-based imaging requires suitable fluorophores. Fluorescence imaging is a noninvasive technique to perform real-time imaging with high resolution.<sup>353</sup> Organic dyes are the most widely implemented probes in labeling subcellular structures. Organelle-specific fluorescent probes are powerful tools for exploring intracellular

structures and dynamics.<sup>301</sup> Fluorescent probes are essential element of an optical microscope to observe biological events at the cellular and subcellular level.<sup>118, 385</sup> They help visualize, monitor, and manipulate intracellular structures and dynamics at the molecular level. Moreover, the advancements in fluorescence imaging provide many opportunities like biomedicine and bioanalysis.

The advancements in materials science and nanotechnology play critical roles in developing various nanoprobess.<sup>107</sup> Since organic dyes suffer from photobleaching, broad emission spectra, and background fluorescence<sup>464</sup>, a new and efficient nanoprobess development is vital to advance biomedical imaging. Inorganic nanoparticles such as upconverting, iron oxide, and quantum dots play essential roles in magnetic and optical theranostic applications.<sup>245</sup> Nanoparticles-based intracellular labeling and imaging is a recent approach in fluorescent imaging. UCNPs have numerous attractive features to be utilized as fluorescence probes for intracellular imaging.<sup>465</sup>

Besides intracellular labeling and visualization, implementing nanoprobess in targeted theranostic allows for precise and effective management of life-treating diseases.<sup>106</sup> An achievement of a single platform through the integration of imaging and therapy helps to realize personalized medicine.<sup>179</sup> In nanomedicine, however, precise delivery and targeting of nanoprobess to a specific intracellular site remain a significant challenge.<sup>355</sup> The controllability of the nanoparticle's hydrodynamic size is essential to disclose the nanometer scale structural features and monitor the activities of biological targets.<sup>466</sup> Since the first UCNPs-based biometric application was implemented by Zijlmans et al. in 1999s<sup>467</sup>, they have been widely used in diverse intracellular applications. The specific UCNPs' NIR light absorption capability and the subsequent visible emissions make their best choices in intracellular imaging.

#### ➤ UCNPs probes in sub-cellular labeling

The lanthanide phosphors are widely explored as nanoprobess in diverse super-resolution imaging techniques.<sup>465-468</sup> The unique optical features of UCNPs, for instance, the sharp and multiple emissions, non-photo bleaching, and photo blinking properties in biological tissues, have made them preferable in multiple nanomedicine applications.<sup>74</sup> The low energy UCNPs excitation requirement avoids cell death and tissue autofluorescence, which is observed in the case of conventional dyes.<sup>464, 465</sup> The longer wavelength nonlinear emissions from UCNPs help achieve

highly resolved images. So far, the maximum resolution from implementing the UCNPs in cytoskeleton labeling is 82 nm.<sup>328, 381</sup> UCNPs' based sub-cellular labeling and imaging are at their fundamental stage, compared to the conventional dyes in super-resolution imaging.

The intracellular use of UCNPs requires pre-preparation of their surface features. The nanoparticle's biocompatibility, dispersibility, surface reactivity, and targetability are crucial in intracellular applications. The targetability of nanoparticles mainly relies on their surface functionalities. Surface integration of biorecognition elements is a typical approach to achieve active targeting. The covalent attachment of biomolecules to the nanoparticles introduces controlled orientation and better stability. The immobilized biorecognition element allows the nanoparticles to gain biological identity and improves targetability. Hybrid nano-biomaterials provide combined properties suitable for specific labeling of intracellular structures. In Figure 75, a schematic illustration of the integration of antibodies to the UCNPs has been given.

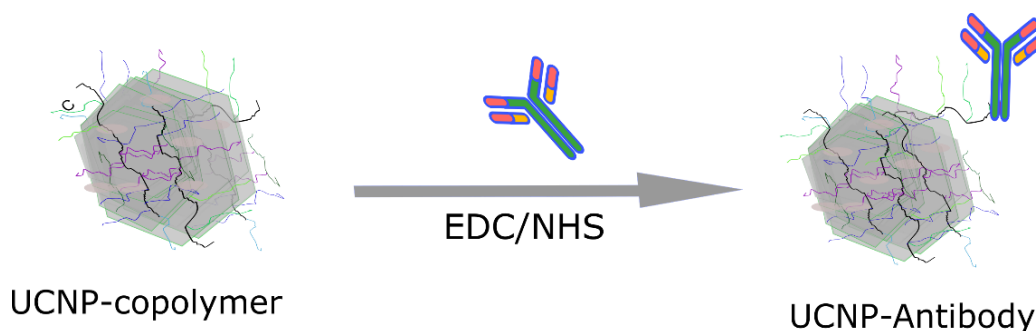


Figure 75 Representation of the integration of antibody to polymer grafted UCNPs.

The eukaryotic cells consist of specialized subunits called organelles.<sup>118</sup> The organelles are enclosed by a lipid bilayer and separated from the rest of the cell. UCNP-based organelle-specific labeling and imaging have vital roles in their diverse bioanalytical applications. Specific labeling and imaging of organelles help to understand their structure and activities. Fluorescence imaging of subcellular units also enables monitoring of the intracellular dynamics and allows to undertake of clinical interventions during abnormalities.

The individual organelle has its physicochemical characteristics and functions.<sup>301, 385</sup> The nucleus, for example, comprises a nuclear membrane, nucleolus, and nuclear scaffolds. The nucleus is separated from the cytoplasm with a nuclear membrane. The nuclear membrane involves the active

transportation of materials into and out of the nucleus through the nuclear pore complex (NPC). The nuclear pore complex is also called nucleoporin. The NPC is one of the most complex supramolecular structures. The NPC comprises different nucleoporins like the NUP58, NUP60, NUP97, NUP153, and NUP200. It is the highly curved structure of the nuclear membrane consisting of the inner nuclear membrane (INM) and the outer nuclear membrane (ONM).<sup>469</sup> The average number of nuclear pore complexes per nucleus is estimated to be 2000 to 4000, over 60 pores/mm<sup>2</sup>.<sup>470</sup> Thus, NPC imaging allows monitoring of gene expression and disease cure developments.<sup>357</sup>

The nucleolus is the densest and most dynamic structure of the cell. The nucleolus is the biogenesis site for ribosome subunit <sup>471</sup> and serves as a transcription and storage center for rDNA.<sup>472</sup> When the cell undergoes mitosis, the nucleolus stops transcription and disassembles.<sup>471</sup> Human diseases such as genetic disorders and cancer are linked to the nucleolus. The nucleoli are responsible for average cell growth.<sup>471</sup> It involves the cell cycle, and several proteins accumulate in the nucleolus during cell division. Proteins with a minimum of 6 arginine units have a strong capability to accumulate in the nucleolus. Nucleolar labeling using UCNPs enables the investigation of gene expression and cellular proliferation.<sup>472, 473</sup> However, particle size control is important to obtain enhanced cellular uptake, nuclear membrane passage and targetability.<sup>474</sup>

Cytoskeletons have the function of controlling cell migration by exerting contractile and protrusive forces. The cytoskeleton is namely composed of microtubules and actin microfilaments.<sup>475, 476</sup> The F-actin structures are ~6 nm wide fibrous structures identified in most dense meshwork zones called lamellipodia and filopodia.<sup>475</sup> The actin filaments are actively involved in the protrusion of cells during polymerization. Microtubules are capable of resisting high compressive forces to maintain the cell shape.<sup>477</sup> Microtubules are 25 nm width polymers with dimers of  $\alpha$ -tubulin and  $\beta$ -tubulins.<sup>476 477</sup> Labeling of the cytoskeleton allows monitoring of the cellular dynamics such as cell proliferation, differentiation, motility, and apoptosis.<sup>478</sup>

#### ➤ Microscopic techniques in subcellular imaging

The microscopic technique in investigating the intracellular structures determines the final image quality. Conventional fluorescence imaging techniques enormously suffer from diffraction limits. Advanced imaging techniques like SMLM can capture images at an axial resolution level of ~80



nm. The distance between the fluorophore and the interest target is one major factor in attaining high resolution. Accurate localization of fluorophores helps to enhance imaging quality.<sup>3</sup> Nanoparticles with controlled diameters could be produced through nanoparticle grafting using multifunctional copolymers and EDC-based zero-length coupling. These days, the UCNPs have become the potential choices in wide super-resolution imaging techniques.<sup>466, 479</sup> Figure 76 depicts the image qualities of different imaging techniques, including the confocal and the super-resolution techniques like SIM, STED, and SMLM on, and the different nanoparticles in the images.<sup>479</sup>

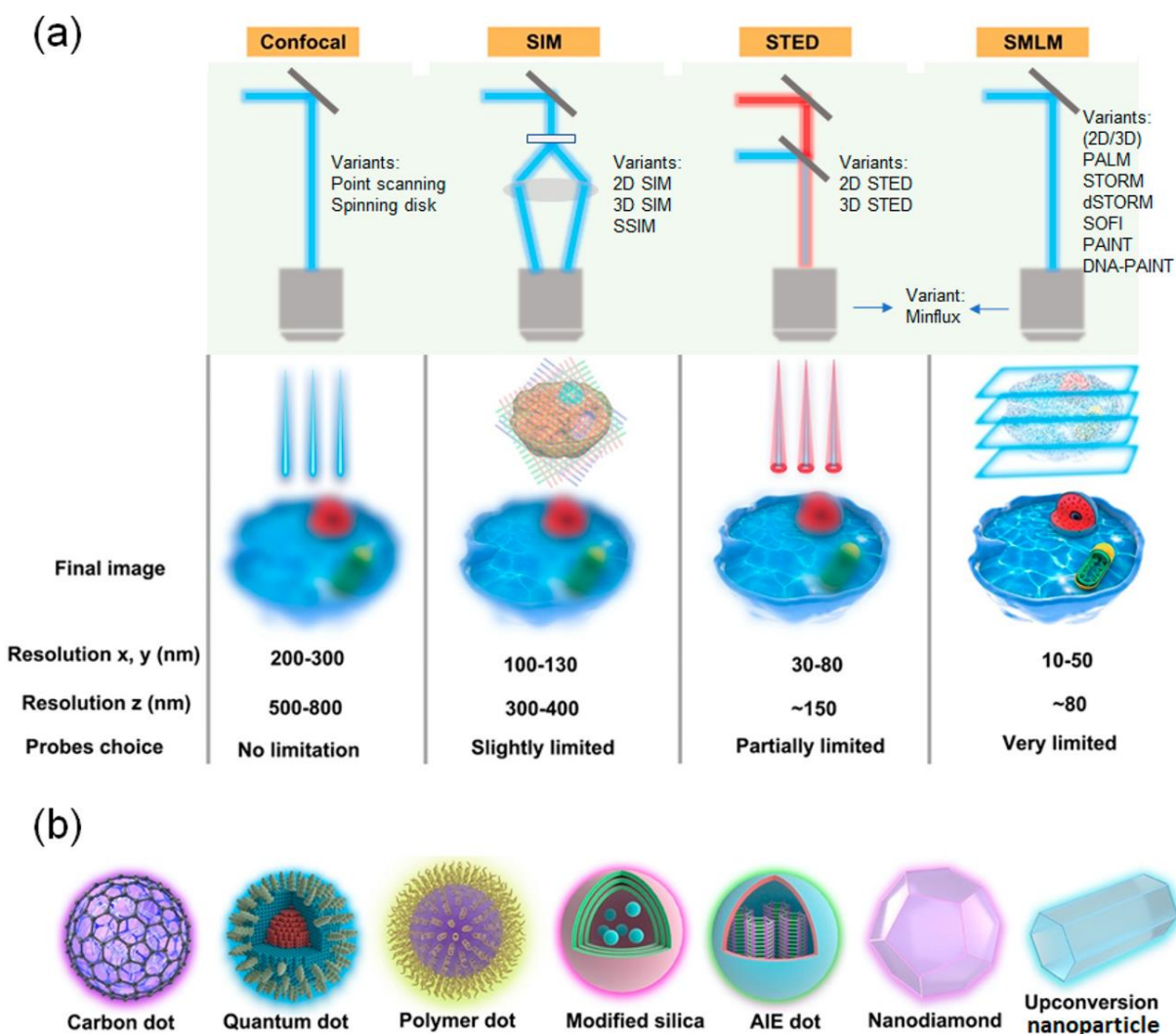


Figure 76 Schematic visualization of different fluorescence imaging techniques in intracellular imaging (a) and nanoparticles in use by those instruments (b). Reprinted with permission<sup>479</sup> © 2022 American Chemical Society.

Each fluorescence imaging technique requires suitable probes to achieve the highest resolution imaging to their best performances. As a part of the Ph.D. project, here, the pre-functionalized UCNPs, as discussed in chapter 5, have been used in the labeling and imaging of the microtubules, actin, nuclear pore complex, and nucleolus of the Hella cell line. Homemade widefield and TIRF-confocal microscopes have been used in most of the imaging, and the Lecia Stellaris confocal microscopy has been implemented for comparison. A hybrid nanoprobe from combinations of UCNPs-dye has been implemented to capture images using both microscope techniques.

### 6.3 Experimental section

#### 6.3.1 Materials and methods

The biofunctionalized UCNPs, as their design and preparation have been described in chapter five, were implemented for intracellular labeling and imaging. Hela cell line was borrowed from a researcher at the bioscience laboratory, UTS. Cell culture DMEM medium, trypsin, PBS buffer, antibiotics, FBS, MTT, and PFA were used in the cell sample preparation and fixation. The nanoprobe of UCNPs grafted from different copolymers, both separately and in combination, that are functionalized with suitable targeting agents were implemented for cell labeling. In Figure 77, list of pre-prepared, peptide and antibody functionalized, and hybrid nanoprobe are presented.

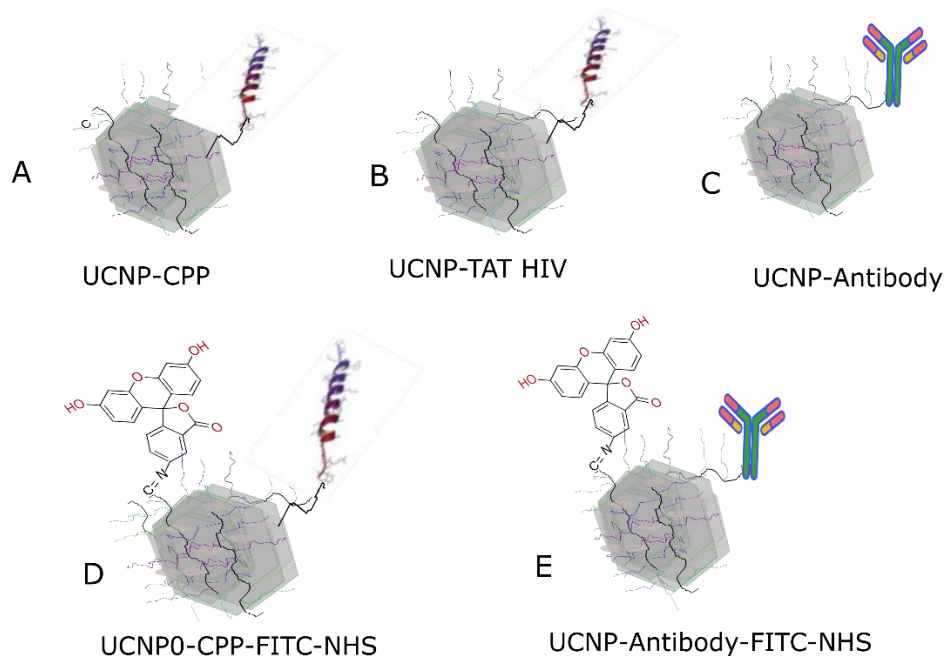


Figure 77 Functionalized UCNPs, and hybrid nanoprobe, for intracellular labeling and imaging.

### 6.3.2 The HeLa cell line UCNPs labeling

The HeLa cell line has been used for all the experimental investigations of UCNP intracellular labeling and imaging. The cell culture was performed using a 75T culture flask. The cell culture was achieved by taking  $0.7 \times 10^6$  cells/mL in a 10 mL cell culture media (DMEM) containing 10% FBS and 1% antibiotic. The cells were cultured in an incubator at 37 °C and 5% CO<sub>2</sub> for three days. At 70% cell confluent, the cells were split using trypsin and centrifuged for 5 minutes at 125 g. The sedimented cells were resuspended in 10% FBS DMEM media, and  $0.3 \times 10^6$  cell/mL, 2 mL media, were taken and cultured in a 35 mm fluoro dish for 24 hours. The functionalized UCNPs at concentrations of 50 µg/mL, 60 µg/mL, 75 µg/mL and 100 µg/mL, 150 µg/mL, and 200 µg/mL were dispersed in 10% FBS DMEM was co-cultured depending on the organelle labeled, as specifically mentioned in each organelle labeling sections. The overall procedures on the cell culturing and nanoparticle labeling is given in Figure 78.

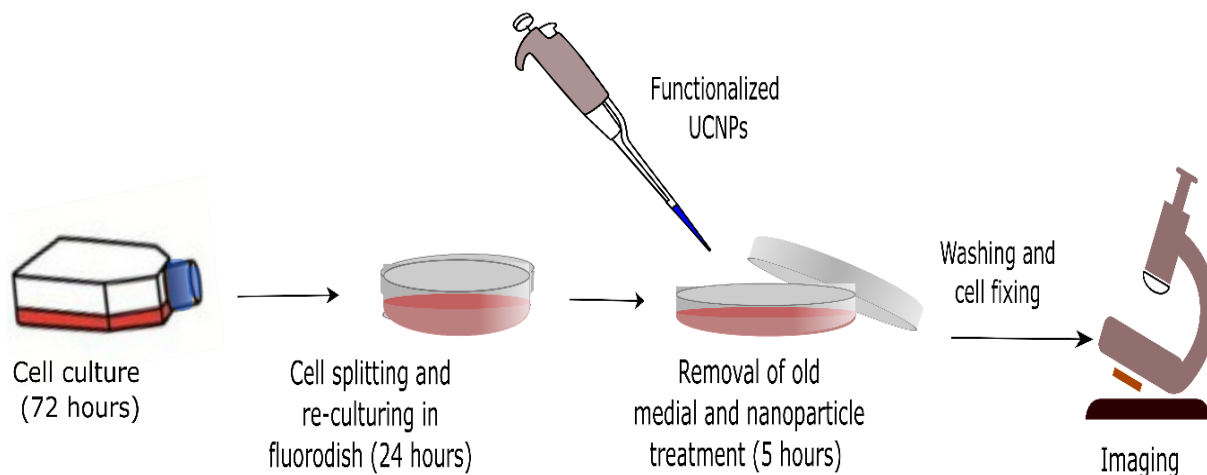


Figure 78 Overall procedure on cell culture and nanoparticles labeling of the intracellular structures.

#### ➤ Labeling and imaging of the nucleolus and the nuclear pore complex

Cell-penetrating peptides (CPP), specifically polyarginine and TAT-HIV peptides coupled with UCNPs, were used to label the nucleolus. The cell culture was performed as the flow scheme schematically represented in Figure 78. The nanoparticles were functionalized with rabbit monoclonal antibody (NUP98) (Figure 76C) at concentrations of 60 µg/mL, 75 µg/mL, and 100 µg/mL for the NPC labeling. The nucleolus was labeled using hybrid nanoprobe by integrating

UCNPs with polyarginine and FTIC (Figure 76D). The UCNPs-based imaging was performed using a homemade widefield and confocal microscope at 980 nm excitation. In the case of hybrid nanoprobe labeled specimen, in addition to the 980 nm excitation microscopes, Lecia Stellaris confocal microscope was used at 488 nm excitation.

The widefield microscope setup is reproduced as shown in Figure 79. It is composed of the sample loading stage; collimation lens: lens 1 (L1): collimation lens; lens 2 (L2): tube lenses; dichroic mirrors (DM); objective lens (Obj); collection lens (L3); short pass filter (SPF); and flexible mirror.

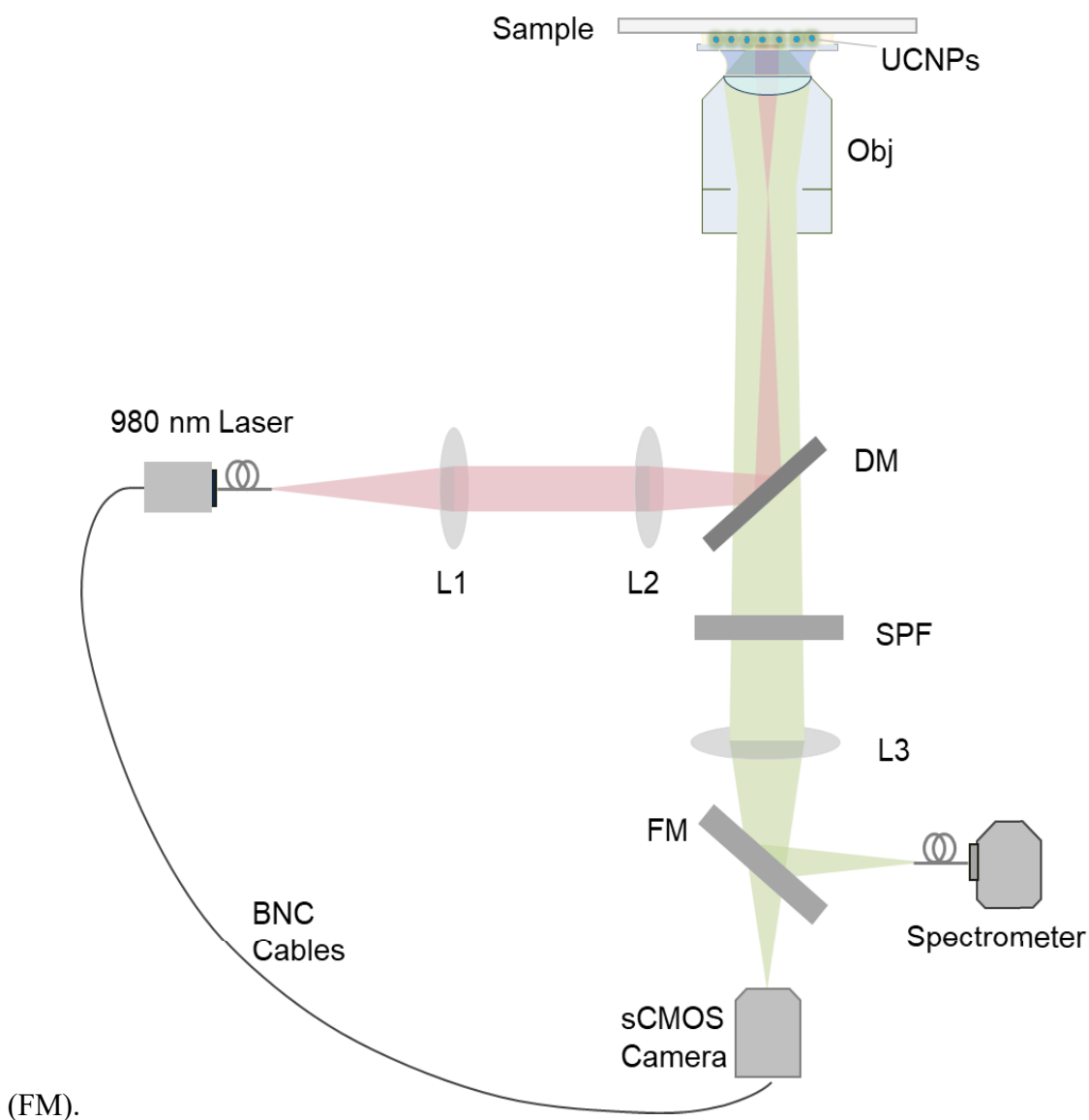


Figure 79 Schematic visualization of layout of the wide-field microscope.

### ➤ Labeling and imaging of microtubules and actin filaments

The microtubule labeling was performed using 60  $\mu\text{g/mL}$ , 100  $\mu\text{g/mL}$ , and 200  $\mu\text{g/mL}$ ; anti-tubulin antibody functionalized UCNPs were co-incubated with the pre-cultured Hella cell line cell for 5 hours, as shown in Figure 75. After nanoparticle labeling, the cell was washed three times and fixed using 0.4 mL 4% PFA for 15 minutes. The PAF was discarded, and the fixed cell was washed two times; the imaging was done using a widefield microscope that operates at 980 nm excitation. The mentioned procedures here were implemented in all the rest experiments unless stated. The same procedure was performed using hybrid nanoprobe to label the actin structures and the microtubules and take images from Lecia Stellaris confocal microscope.

### ➤ The effects of nanoparticles size and concentration and grafted copolymers

To investigate the nanoparticle size effect, 20, 25 nm, and 35nm nanoparticles had used for labeling the nucleolus and the nuclear pore complex. The Anti-tubulin antibody functionalized UCNPs at a concentration of 6  $\mu\text{g/mL}$ , 5  $\mu\text{g/mL}$ , and 2  $\mu\text{g/mL}$  was dispersed in 2 mL of media with 1 mmol NaF. As described before, the cells were pre-cultured in a 35 mm fluoro dish, and a pre-prepared anti-actin antibody (ab179467) functionalized UCNPs 75 and 5  $\mu\text{g/mL}$  were used to target actin structure. The rest cell preparations procedure, nanoparticle delivery, and imaging approaches were performed the same as it was done in the case of microtubes labeling and imaging.

## 6.4 Result and discussion

### 6.4.1 UCNPs nanoprobe for intracellular labeling

#### ➤ Labeling and imaging of the nucleolus

The nucleolus labeling was performed using UCNPs-CPP. As described in Chapter 5, CPP, polyarginine, and TAT-HIV peptides were covalently coupled to the nanoparticle's surfaces to produce stable conjugation and facilitate intracellular delivery. The polyarginine-rich peptides are efficient in the delivery and targeting of particles to the nucleolus. The delivery and targeting of the nanoparticles to the nucleolus requires successful passage of the plasma and nuclear membranes. The main challenge with labeling nucleolus arises from the nuclear delivery of the particles because the particles should pass the strong screening procedure of the nuclear pore complex. The nuclear pore complex, a 40 nm nuclear gate, is exceptionally tight to permit the

transfer of materials into and outside the cell. Here, the surface-coupled cell-penetrating peptides are advantageous in facilitating the nuclear membrane passage and targetability of the UCNPs. Figure 80 shows TIRF confocal microscope images of the nucleolus from delivery and specific targeting UCNPs. The TIRF enables capturing highly resolved images through thin sectioning.

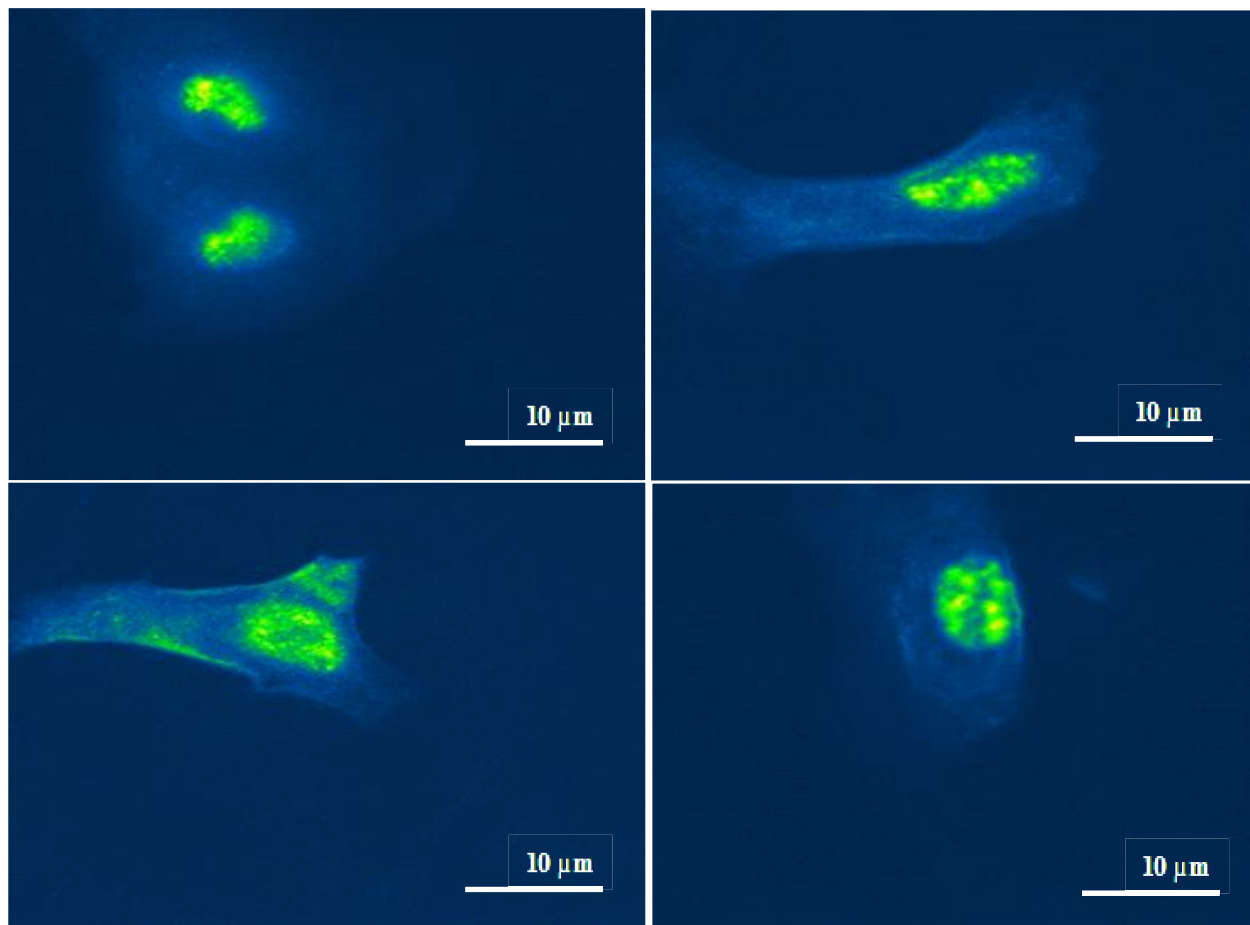


Figure 80 The TIRF confocal images from UCNPs-polyarginine labeled nucleolus at particle dose 100  $\mu\text{g}/\text{mL}$  @980 nm excitation.

In Figure 80, the images are captured from UCNPs-polyarginine labeling of the nucleolus of the HeLa cell line. Here, a green color code differentiates the nucleolus labeling from other organelles labeling. The displayed images confirm that the UCNPs could effectively deliver to those located at the nucleolus. The images are collected at different focal planes showing dense labeling of the nucleolus. The uniformly distributed emissions prove the high localization of the UCNPs to the nuclear region. A previous study on labeling nuclear using organic dyes has shown a similar

image.<sup>480</sup> The nuclear pore complex blockage has been observed in Figures 80 B, C, and D. The dense yellowish discrete spots are due to stacked UCNPs at the nuclear gates.

The labeling and imaging of the nuclear were also performed using a homemade widefield microscope; In Figure 81, images of the nucleolus of the HeLa cell labeled from 60  $\mu\text{g}/\text{mL}$  and 100  $\mu\text{g}/\text{mL}$  UCNPs-TAT-HIV functionalized probes are presented.

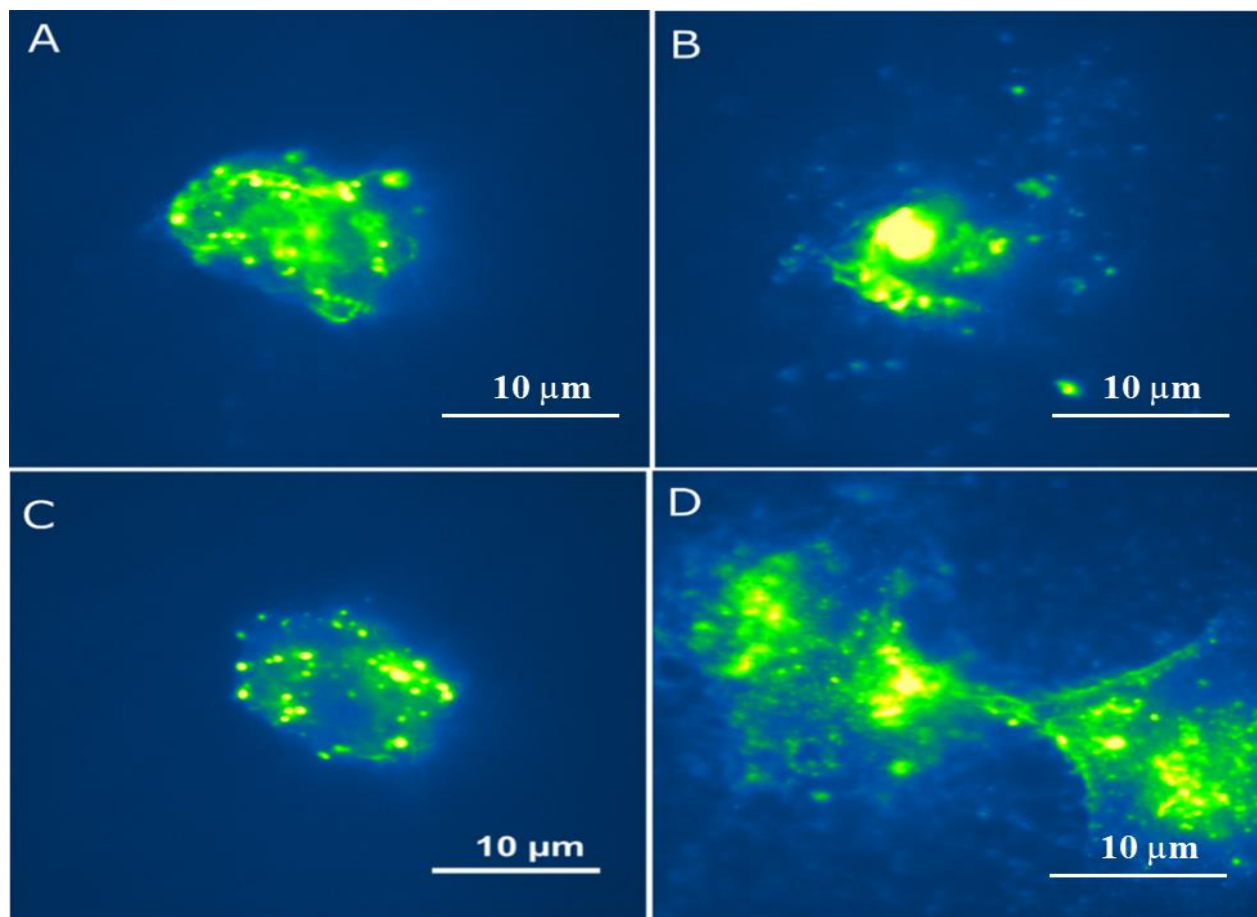


Figure 81 Widefield microscope images of nucleolus labeled with UCNPs-TAT HIV at particle dose of 60  $\mu\text{g}/\text{mL}$  (A), (B), and (C), and at 100  $\mu\text{g}/\text{mL}$  (D) @980 nm excitation.

In Figure 81B, the particles are localized at the center of the cell. The green color code is used to differentiate the nucleolus labeling from other organelles labeling. The cumulation of the nanoparticles at the nuclear pore complex is observed in Figures 81A, B, and C. It indicates that the size of the nanoparticles has an impact on nuclear delivery. A high number of nanoparticles are accumulated in the nuclear complex nuclear sites. The epi-illumination in a widefield microscope strongly affects the resolution of the images. Figure 81D shows the progression of the

nuclear division during cell mitosis. The specific labeling and visualization of the nuclear division process indicate the efficiency of UCNPs in monitoring cell proliferation. In Figures 81D and B, the presence of nonspecific interaction is observed. It indicates that the nanoparticles exhibit high interactions with the non-target intracellular sites. The non-specificity of the particles could be addressed through further optimization of the surface polymer composition and grafting density and efficient bio-coupling.

The inherent functions of the TAT-HIV and polyarginine in intracellular cargo delivery of materials could be borrowed to deliver particles to the nucleolus. Through mimicking the UCNPs surfaces with those peptides, intracellular delivery and nuclear targeting of the UCNPs is aspiring. The immobilization of the peptides to the UCNPs allows for the delivery of the particles into the cell. The nanoparticle labeling in Figure 81 is intended to target the nucleolus using the TAT-HIV peptide. The high-density labels in the nuclear region indicate that the nanoparticles could be delivered to the nuclear areas. The nuclear imaging was performed using homemade confocal and widefield microscopes. The nuclear labeling observed here is distinctly different from the UCNP labels for microtubules and F-actins.

#### ➤ Labeling and imaging of the nuclear pore complex

The anti-NUP98 antibody functionalized UCNPs specifically targeted the nuclear pore complex. In Figure 82, images clearly show that UCNPs are effectively located at the NPC sites. The concentration of the nanoparticles used to label the cells has a prominent effect on the quality of the captured images. The image taken from the 60  $\mu\text{g}/\text{mL}$  labeling provides a clear image, and the NPC labeling is visible. High labeling density has been shown in the 75  $\mu\text{g}/\text{mL}$  labeled cells. The high label density obscures the specifically labeled NPC structures. The labeling density was controlled by the number of particles per cell that should be investigated and needs to quantify precisely for the number of particles loaded and the labeled cells. Optimizing the nanoparticle's concentration allows for minimizing the light diffraction challenges that arise from high-density labeling. Quantifying the number of particles delivered into the cell is vital to estimate the labeling density per cell.<sup>277</sup>



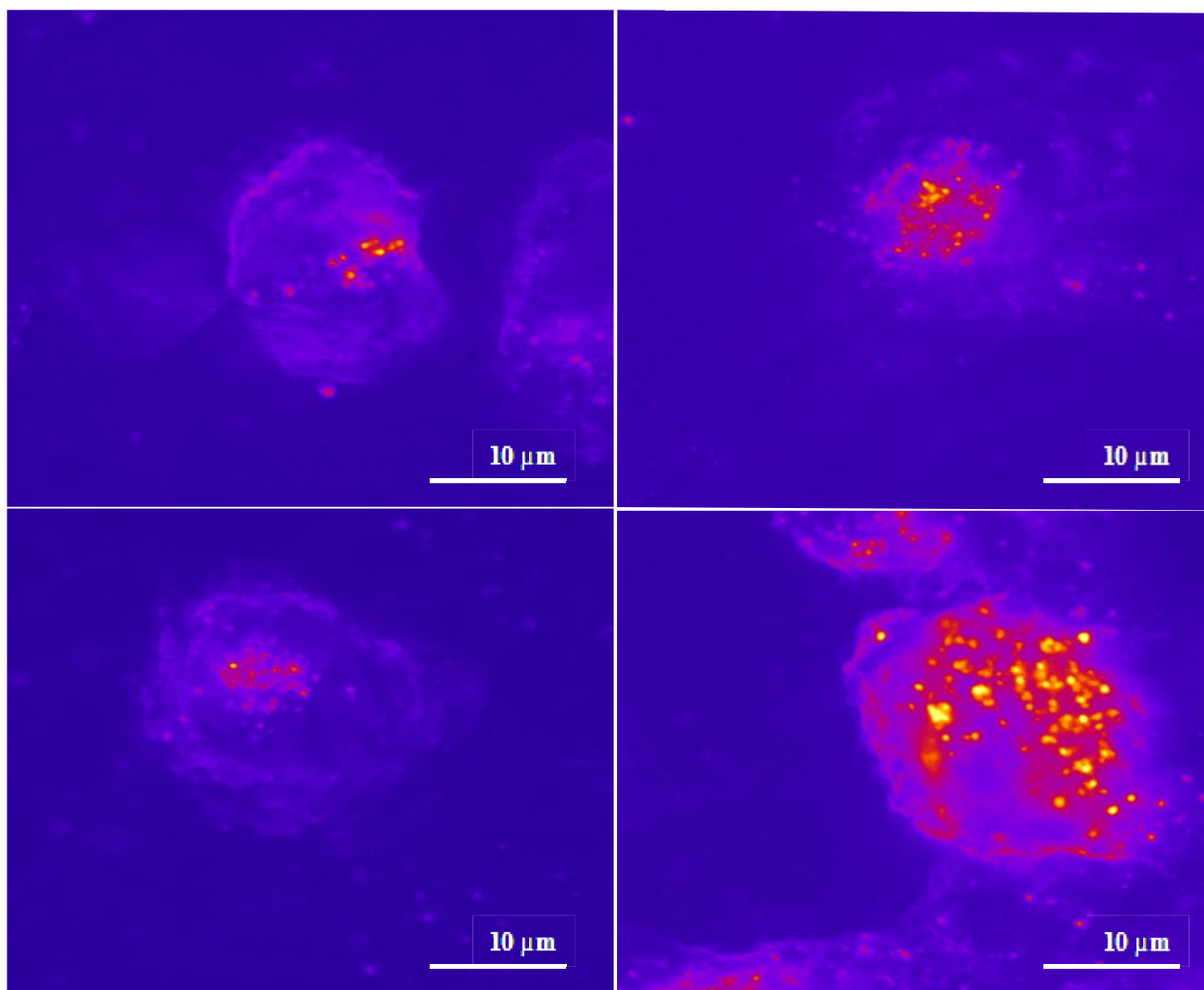


Figure 82 Widefield microscope images of NPC labeled with UCNP-NUP98 at a concentration of 60  $\mu\text{g/mL}$  (A) – (C), and 75  $\mu\text{g/mL}$  (D) @980 nm excitation.

In Figure 82, red color coding indicates the NPC labeling. The red spots in all the images show that the UCNP-NUP98 functionalized probes are specifically targeted to the nuclear pore complex sites. The variations in color in the different intracellular regions of the structures are due to the emission intensity difference between the targeted and non-target regions. The yellowish colors indicate dense particle labels, and the red spots indicate moderately labeled NPC structures. The accumulation of the nanoparticles in a distinct area is due to the high localizability of the particles at the NPC's outer part, called the luminal ring. The nuclear region has gained a higher label density than the other intracellular structures. The coupled antibody effectively guided nanoparticles to the intended specific site.

The intense emission from highly labeled intracellular sites is prone to diffraction effect. Since the target sites could accommodate limited nanoparticles, the remaining excess particles reside nearby. The intense overlapped emissions from specifically targeted and nontargeted particles obscure from visualization of target structures effectively. Here, the diffraction limit is the major challenge in obtaining a clear image, especially in the case of the widefield microscope. An optimized labeling density allows closer nanoparticle distance labeling, which helps get valuable information from the captured images. In the NPC labeling, the 60  $\mu\text{g/mL}$  UCNPs labeled NPC have gained improved visibility. However, the optimal nanoparticle concentration could vary depending on the number of cells labeled and on the uniformity of nanoparticles cell uptake and biodistribution. Quantifying the number of nanoparticles in the cell labeling would give a better understanding of the nanomedicine applications of the UCNPs.

➤ Labeling and imaging microtubules

The widefield images obtained from the different experiments show the effective intracellular delivery of the nanoparticles. In the labeling of the microtubules using 50  $\mu\text{g/mL}$ , 70  $\mu\text{g/mL}$ , 100  $\mu\text{g/mL}$ , 150  $\mu\text{g/mL}$ , and 200  $\mu\text{g/mL}$  have been investigated. The high nanoparticle concentration, 200  $\mu\text{g/mL}$ , shows intense labeling. Since the microtubules are large portions of the intracellular structure, a relatively high nanoparticle concentration is needed to attain enough labeling and brightness compared to the NPC. The high concentration of intracellular labeling significantly impacts the cell's viability. The high concentration nanoparticle concentration affects the visibility of the target site, especially in the case of widefield imaging. In Figure 83, a pink color code is used to identify the microtubes labeling.

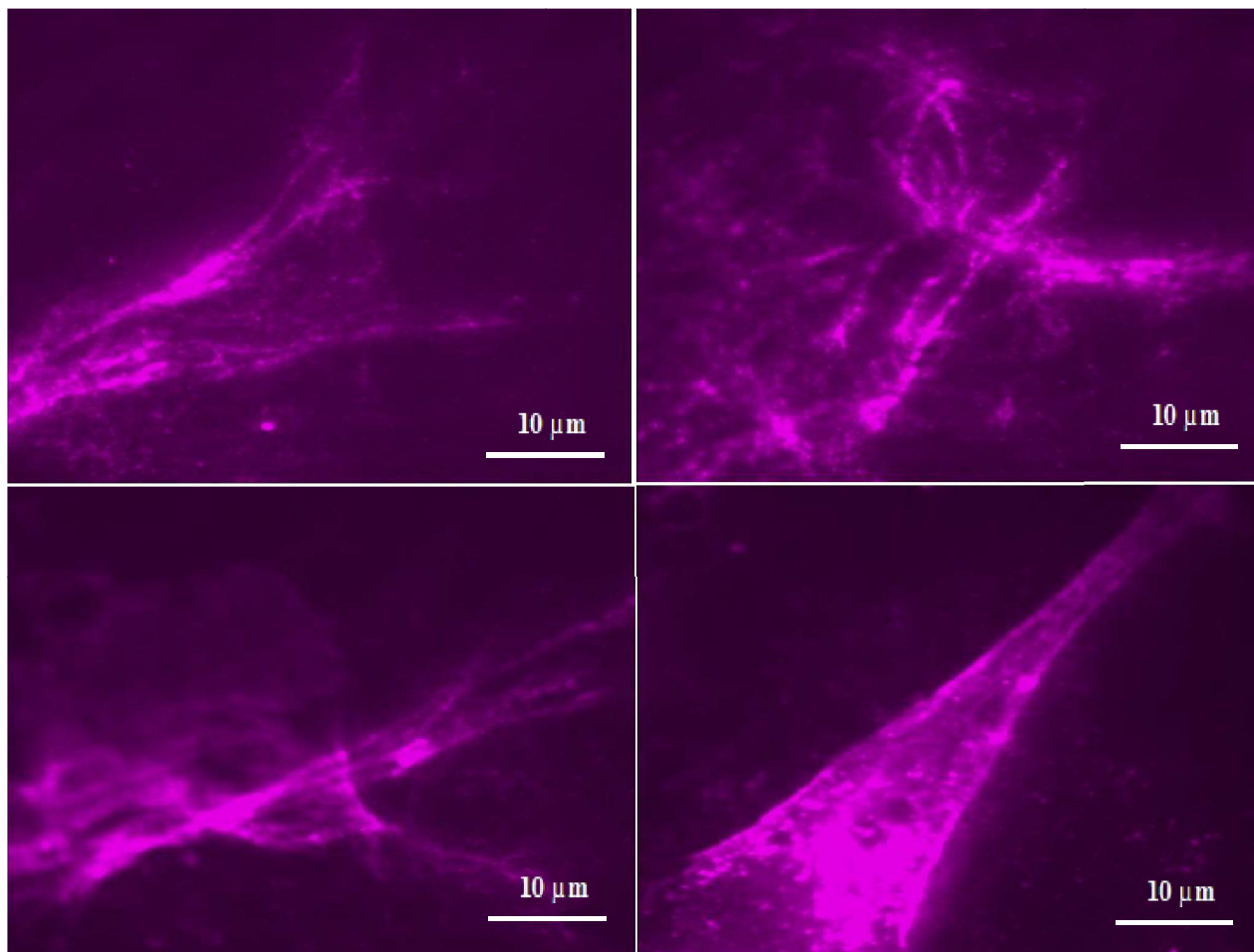


Figure 83 Wide-field images of microtubules labeled with UCNP-anti-tubulin antibody at particle doses of 100  $\mu\text{g}/\text{mL}$  (A) & (B), 200  $\mu\text{g}/\text{mL}$  (C) & (D) @980 nm excitation.

➤ Labeling and imaging of actin filaments

In Figure 83, the actin filaments of the HeLa cells are presented. The images show adequate labeling of the actin filaments using UCNPs. The effective concentration of the nanoparticle on the image's quality has been investigated. The F-actin labeling is identified using a light blue color code. Figure 84A, for instance, shows dense labeling of the actin structures. Since F-actin are tiny filaments, the widefield imaging technique is unsuitable for achieving detailed visualization.

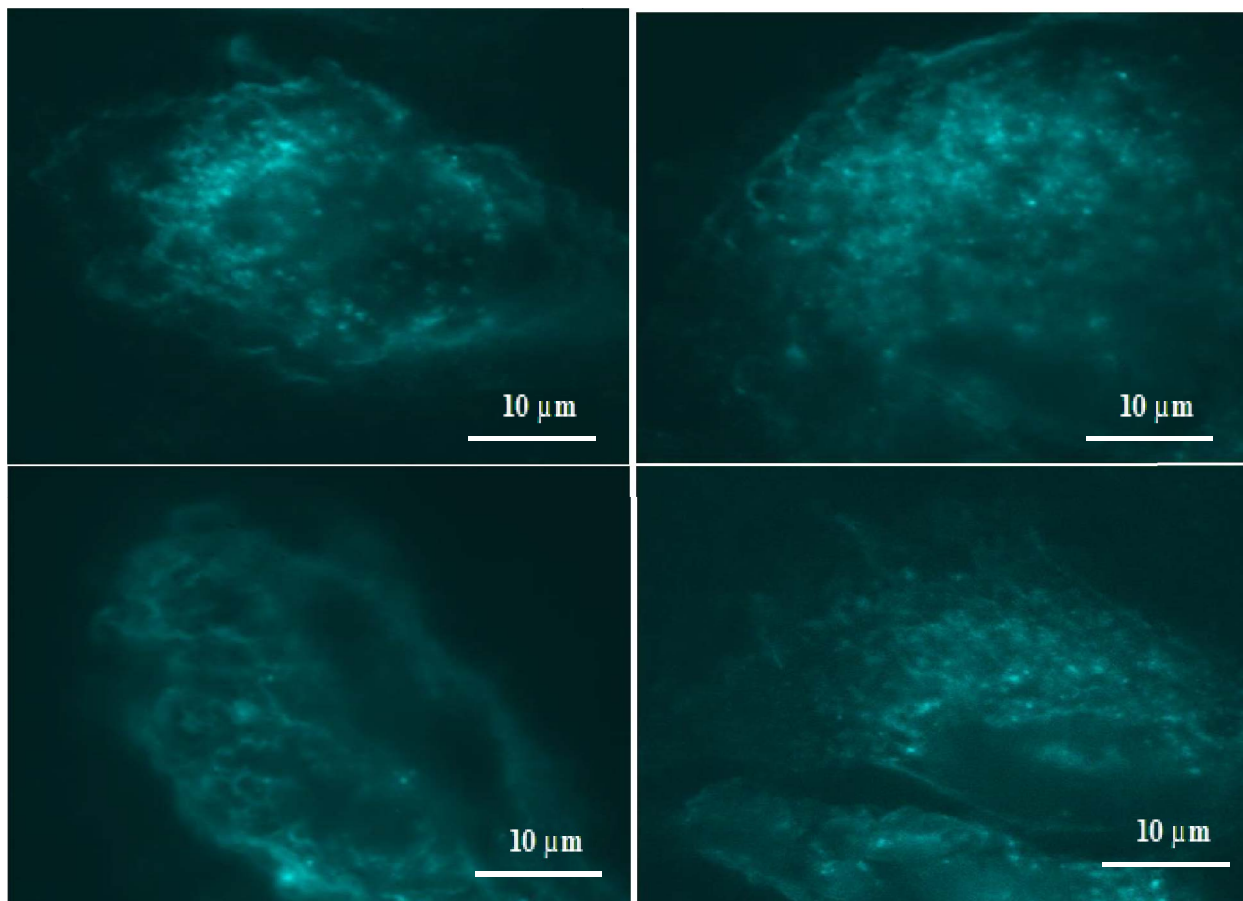


Figure 84 Widefield images of Polymer 2 grafted UCNPs-anti actin antibody labeling with particle concentration of 60  $\mu\text{g}/\text{mL}$  (A) & (B), and 75  $\mu\text{g}/\text{mL}$  (C) & (D), @980 nm excitation.

The sheet-like appearance and folding at the peripheral regions of the cellular parts are due to the dense actin mesh structures. The observed high-density label closer to the nuclear region might be from overlapped labeling and shrinkage of the cell towards the center during fixation and drying. Figure 84A, for instance, shows dense labeling of the actin structures. Since the actin is tiny structures  $\sim 7$  nm, achieving high-resolution images and detail visualization using a widefield microscope could be challenging. The homogeneous bright distribution from labeled structures indicates high biodistribution and targetability of the nanoparticles. The consistent sheet-like emission appearance shows the uniformity of the labeling. The folding-like regions are due to the dense actin mesh at peripheral regions of the cell. The observed high label density close to the nuclear region might be from overlapped labeling and shrinkage effects of the cell towards the center during fixation. The nanoparticles concentration has a significant effect on the final images.

As seen in Figures 84C and D, the images from 60  $\mu\text{g}/\text{mL}$  nanoparticle labeling show a less intense emission than the 75  $\mu\text{g}/\text{mL}$  labeled ones.

#### 6.4.2 UCNPs-dye hybrid probes for intracellular labeling and imaging

The images captured using Lecia Stellaris confocal microscope @488 nm are displayed in Figure 85. The hybrid nanoprobe from UCNPs-FITC-TAT integration are implemented to label the nucleolus in Figures 85A and B. In the case of the microtubule's images, Figure 85C and D, nano-hybrid labeling using UCNPs-FITC anti-tubulin-antibody was implemented.

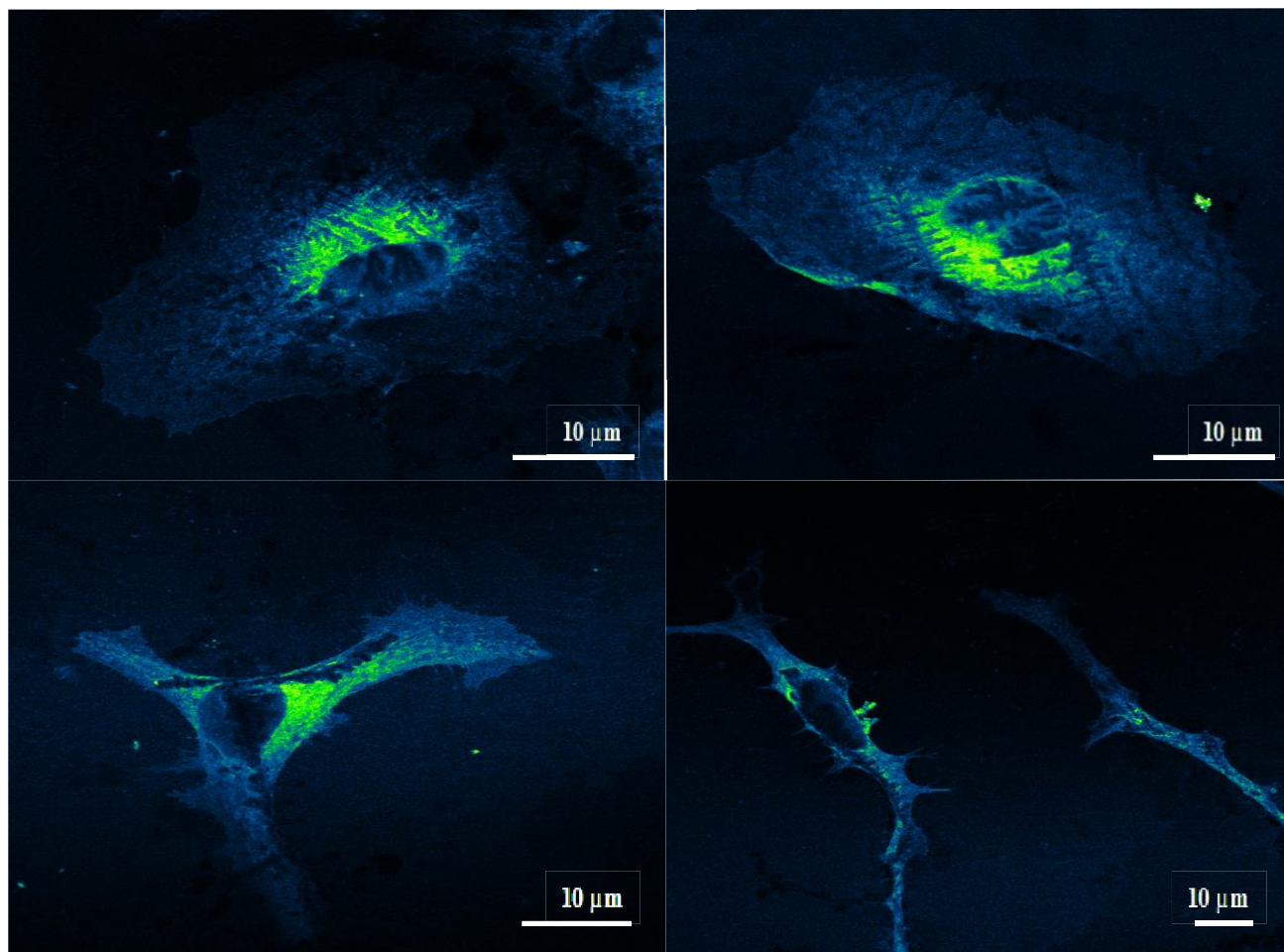


Figure 85 Images captured from UCNPs-FITC-TAT labeled nucleolus (A) and (B), and UCNPs-FITC anti-tubulin antibody labeled microtubules (C) and (D) @488 nm excitation.

In Figures 85A and B, images of microtubules captured using Stellaris confocal are presented. The images show that the nanoparticles mainly resided on the nuclear membrane. Even though labeling of the nucleolus was performed well, most nanoparticles are cumulated at the nuclear membrane.



It indicates that the nanoparticles are trapped in the nuclear membrane and can't reach the nucleolus.<sup>481</sup> The nuclear membrane pass gate, the nuclear pore complex, is a narrow hole is about 40 nm, and nanoparticles with a greater diameter cannot enter the nucleus. The images in Figures 85A and B show significant nonspecific interactions, even though efficient nuclear membrane targeting is achieved. The primary challenge in nucleolus and NPC labeling is the need for the nanoparticles to cross the cytoplasm effectively to reach the target site. In this regard, achieving effective delivery and targeting demands high specificity and stable nanoparticles.

The images on the microtubule labeling, Figures 85C and D, show relatively high labeling density. In the case of microtubule labeling, the nuclear regions are not labeled. It indicates the high specificity of the nanoparticles to the microtubules. The nonspecific interaction is insignificant here, in the case of the microtubules labeled images. The microtubules labeling particles were not shown in the nuclear region, indicating high specific interactions between the targeting agent and the receptors.

➤ UCNPs-FITC integrated NPC labeling and imaging

The NPC is an efficient molecular sieve to control the transportation of materials into and out of the nucleus.<sup>482</sup> In the hybrid UCNPs-based nanoprobe, the commercial Alexa-Fluor coupled antibody is integrated using EDC chemistry. Figure 86 contains images from UCNPs excitation (Figure 86A and B) and excitation of Alexa Fluor 488 hybrid nanoprobe (Figure 86C and D). Approximately 200 labeled spots are visible in Figures 83A and B, which are the nuclear pore complexes. However, since nuclear power is highly porous, the number of nuclear pore complexes per nucleus is estimated at 2000 to 4000. The resolution capacity of the traditional confocal and wide field techniques is limited, and it couldn't allow for detailed visualization of pore structure. Schlichthaerle et al.,<sup>483</sup> reported on a comparative study on the labeling of NPC using different probes, and the images agree with the one obtained in this experiment. In a recent report, 3D images of NPC labeled with GFP depict the appearance of the NPC structures.<sup>356</sup> The NUP96-Halo labeled image using 3D DNA-PAINT indicates NPC's appearance on the nuclear membrane. The challenge in Alexa-Fluor-Antibody hybrid nanoprobe gains significant size increment.

Depending on the antibody labeling density, the coupled antibody results in a 12 to 24 nm diameter increment. The antibody-nanoparticle coupling has a substantial limitation from random and far-

distance placement of the fluorophore nanoparticle from the target site.<sup>444</sup> Nanobodies are ten times smaller than antibodies and are recommended for targeting smaller-size probes.<sup>444</sup>

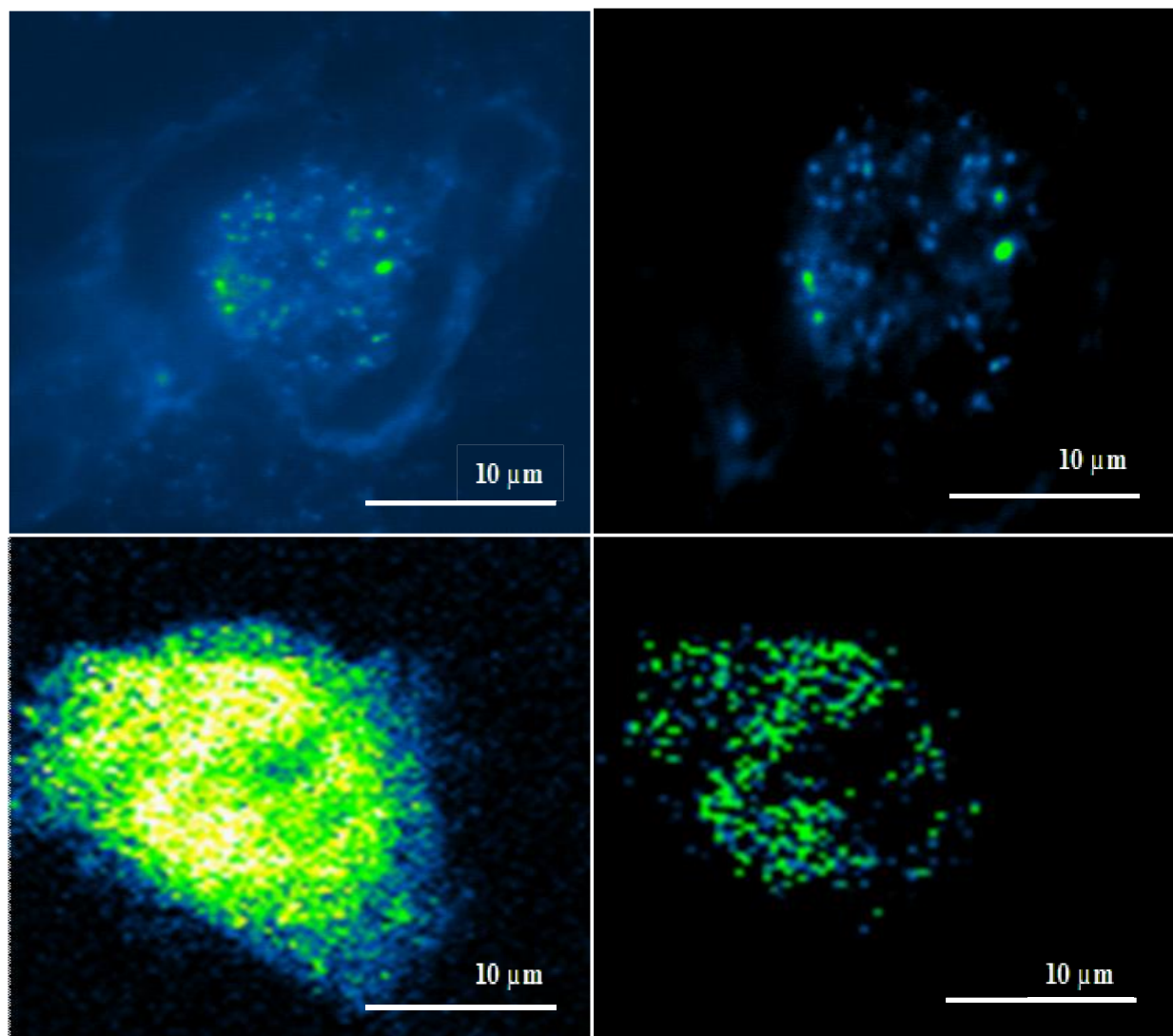


Figure 86 Images of NPC labeled from UCNPs-FITC-NUP98 antibody @980 nm excitation (A) and (B) using a homemade widefield microscope; @488 nm excitation using Lecia Stellaris Confocal microscopy.

➤ UCNPs-Alexa Fluor 488 hybrid probe for microtubules labeling and imaging

In Figure 87, the UCNP-dye hybrid nanoprobe has been used to label the microtubules. The images show an effective biodistribution of nanoparticles. Figure 87A belongs to the UCNPs-based excitation widefield image, and Figure 87B is a Stellaris confocal image from Alexa Fluor 488 excitation. The widefield images from UCNPs-based excitation are blurry. It is due to out-of-

focus radiation, which is resulted from the epi-illumination in the widefield microscopy, compared to the confocal pin hole-based imaging. The confocal images from the Alexa-Fluor 488 show uniform and high labeling density in the cytoplasm region. The improved nanoparticle distribution is associated with the adequate labeling capacity of the nanoparticles.

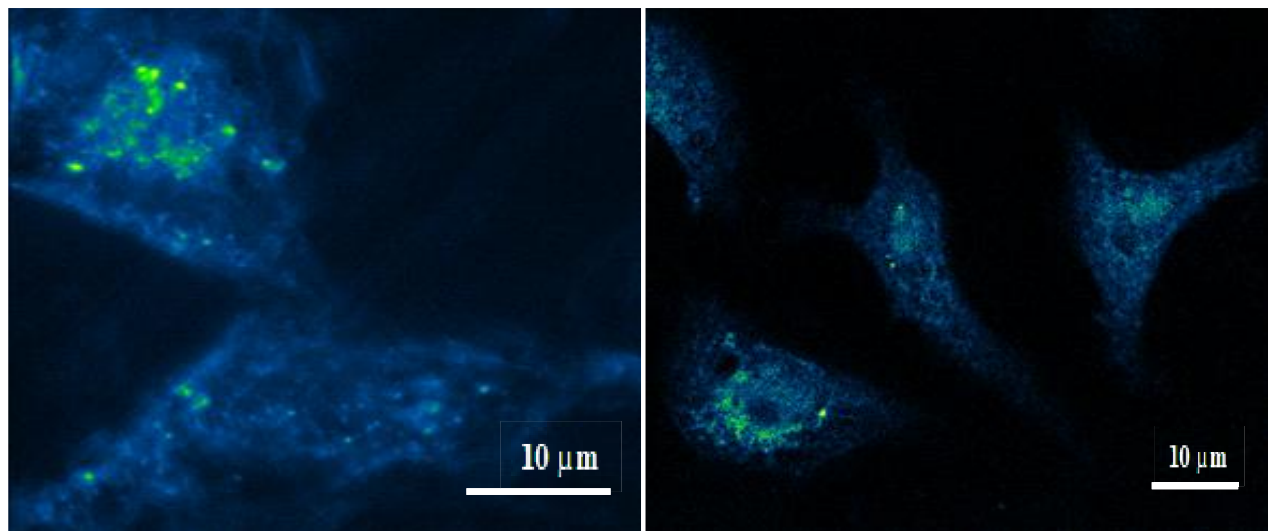


Figure 87 Imaging of microtubules from UCNP-Alexa Fluor 488-Antibody labeled cell (A) using a home-made widefield microscope @980 nm UCNPs excitation and (B) using Lecia Stellaris confocal microscopy @488 nm Alexa-Fluor excitation (B).

Here, the Stellaris images from the excitation of coupled organic dyes allow efficient evaluation of the UCNPs labeling. The uniform distribution of the fluorophores indicates that the nanoparticles distribution and localization have been done effectively. The UCNP nanoprobe work well if implemented in confocal and super-resolution imaging. An efficient UCNP-based intracellular labeling gives potential advantages for their use in live cells and animal imaging.

#### ➤ Effects of UCNPs size and concentration

The intracellular structures labeled with 20 and 25 nm were investigated for the nanoparticles' size effect. The concentration of the nanoparticles used for the labeling is 75  $\mu\text{g}/\text{mL}$ . Figure 88 shows an effective biodistribution of nanoparticles during the F-actins and the NPC labeling using the 20 nm UCNPs. The images from widefield, Figure 88A, and confocal microscopes, Figure 88B, indicate that smaller UCNPs are good enough to label delicate structures. The smaller diameter UCNPs are suitable for marking complicated intracellular systems. The main challenge in implementing the smaller UCNPs is reduced emission efficiency.



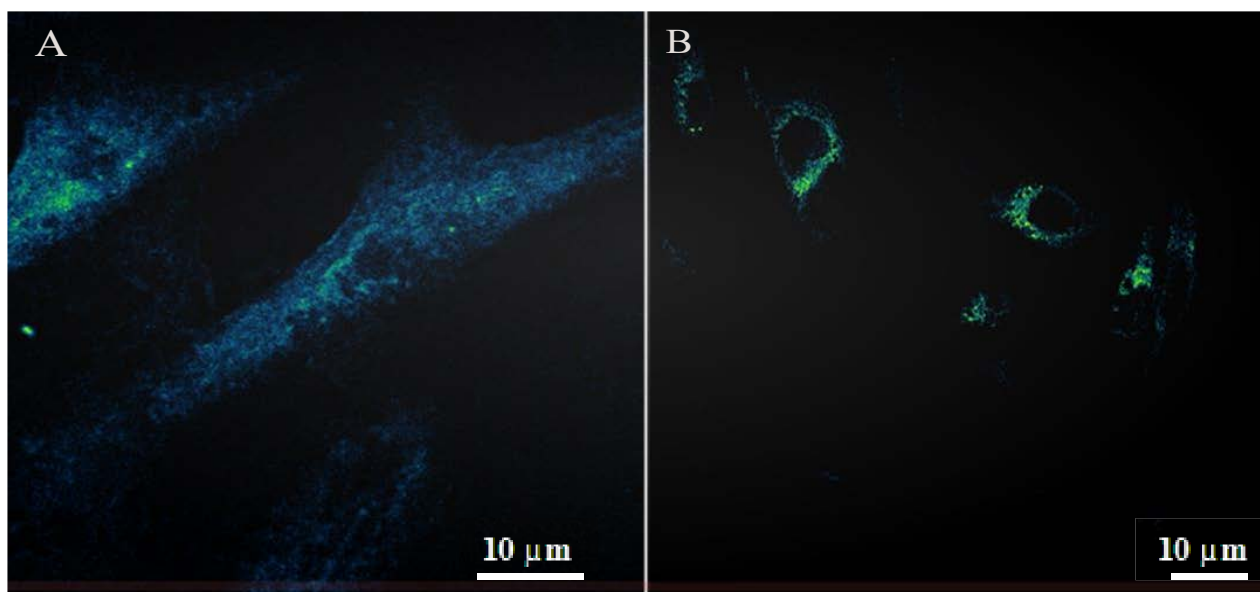


Figure 88 Labeling of F-actin using UCNPs-alpha antibody (A) labeling of NPC using UCNPs-FITC-NUP98 (B) @488 nm using Lecia Stellaris confocal microscopy.

The nanoparticle concentration plays a vital role in obtaining a quality image. In Figure 88 B, 60  $\mu\text{g}/\text{mL}$  UCNPs have been used to label the NPC structures. Highly localized delivery of particles to the nuclear pore complex sites is achieved. High-density labeling has been observed from the 75  $\mu\text{g}/\text{mL}$  UCNPs labeling; the image is not presented here. The observed uniform particle distribution in UCNP cell labeling is one of the significant challenges in intracellular labeling. This indicates the lower size particles in the size ranges of 20 to 25 nm are good enough to label the intracellular structure effectively. The controlled delivery and labeling of specific intracellular sites enable high-precision imaging. The high brightness of the core-shell nanoparticles in cell labeling has been observed in the NPC labeling.

➤ The roles of the surface grafted copolymers in UCNP intracellular delivery

The surface-grafted copolymers are the key to the successful delivery and specific targeting of intracellular structures. All polymers used in nanoparticle grafting work well in cell labeling and imaging. Polymer 1 is the most applicable in introducing multiple coupling opportunities and developing UCNP-dye nanohybrids. The double grafts from polymer 1 allow for reduced particle size and efficient labeling. Polymers 2 and 3 are common, and their grafted particles are very efficient in size control and stability. In Polymer 4, sulphonate anchoring is introduced to implement the UCNP surface grafting in combination with other polymers. Polymer 5 labeled

images show high biodistribution and labeling efficiency. Significantly, the combined graft of polymer 5 gives an improved labeling efficiency. The MPC blocks biomimicking and antifouling capacity, making Polymer 5 the future polymer in intracellular investigations. Polymer 6 allows for the optimization of surface graft composition and stability.

Furthermore, the MAA-based diblock copolymers could replace the conventional PAA-based UCNPs surface modification. Polymer 6 has a high anchoring capacity from the phosphate groups and optimized amphiphilicity from the backbones and RAFT agent end groups. As the concepts are deep, all the mentioned polymers require further detailed studies. Although this project is wind-up here, due to time limitations, several future research opportunities from each section and integration could be developed.

## 6.5 Conclusion

The UCNPs' intracellular delivery and targeting of the nucleolus, microtubules, actin, and nuclear pore complex has been achieved well. It indicates that copolymer grafted and functionalized UCNPs efficiently realize targetability and localized imaging. The images taken using the different microscopes prove that the functionalized UCNPs could be targeted to intended specific sites effectively. The high targetability of the nanoparticles indicates that the surface-grafted polymers are suitable to keep the nanoparticles stable during incubation and reach the intended target site. The nonspecific interactions are the reasons for off-target delivery, which still requires further surface composition optimization.

The UCNPs' surface reactivity has enabled the effective coupling of targeting ligands. The targetability of the nanoparticles attests to the surface coupling of the antibodies and peptides effectively. The specific targeting of UCNPs to the nucleolus, the nuclear pore complex, the microtubules, and the actin structures had been performed. The EDC chemistry is good enough to immobilize agents, peptides, and antibodies through the specifically designed surface polymers. The surface-grafted copolymers have prominent roles in defending the surfaces from the adsorption of proteins and other biological components. The reduced nonspecific interactions, and the high biodistribution, are due to the high performance of the surface-grafted polymers.

The surface grafting copolymers have multiple advantages in UCNP cell labeling and imaging. The surface copolymers' mixed functionalities allow the surface to be compatible with various

ionic and physiological conditions. The surface polymers facilitate the successful delivery and targeting of the nanoparticles to specific intracellular targets. The poly(meth)acrylic acid block has multiple benefits in governing the final physicochemical properties of the nanoparticle's surfaces. The specificity of the nanoparticles is associated with the surface coupling efficiency.

The separate and combined copolymer grafting techniques are suitable for controlling the particle size and labeling the intracellular structures. The combined surface grafted nanoparticles have been used extensively. Since Polymer 1 and 5 grafted nanoparticles have large hydrodynamic sizes, the integrated approach has been used to control the nanoparticles lower. The advantage of the combined grafting is expected to be high; however, investigation of the specific benefits in terms of nano-bio interaction would be a vast and independent research project. The nanoparticles are improved by implementing the different copolymers in the UCNPs' surface grafting. The nanoparticles grafted from separate individual copolymers and the combined grafted surfaces surface perform well in cellular labeling. The multiple functionalities on the surfaces of the nanoparticles obtained from surface-grafted copolymers, like carboxylic and phosphocholine, play vital roles in cellular uptake and achieving enhanced (bio) distribution.

The resolution capacity of the microscopic in use determines the image resolution. The imaging of the labeled structures was collected using homemade confocal and widefield microscopes at widefield at 980 nm excitation. For comparison, the Lecia Stellaris microscope, a hydride dye, was implemented using UCNP-dye hybrid nanoprobe. The widefield microscope is suitable for capturing images from all parts of the cell. The widefield images, however, are affected by diffracted lights. The images captured from radiation collected at different angles and label depths generate blurry images. The homemade TIRF microscope is good enough to obtain improved-resolution images. The capability of the confocal microscope in sectioned image formation significantly improves the axial resolution compared to the widefield microscopes. The UCNPs-dye integration replaces the colocalization. As the dyes are integrated with the UCNPs, the labeling efficiency and targetability of the functionalized UCNPs could be indirectly assessed from the images taken using the commercial Lecia Stellaris microscope. The full potential of the prepared functionalized UCNPs would be investigated using super-resolution imaging techniques.

In conclusion, the produced functionalized UCNPs are suitable enough to achieve nanometer precision targeting and to implement super-resolution imaging. The nanoparticles' stability,

dispersity, and targetability in the biological environment suit intracellular-specific labeling. Even though the delivery and targeting of the UCNPs are good, the observed degree of non-specificity requires further consideration. The remaining non-specificity challenges could be addressed by further optimization of surface grafted copolymers' composition and graft density. The functionalized UCNPs are expected to capture better microtubules and NPC if done with super-resolution techniques. In the future, implementing the functionalized UCNPs in super-resolution imaging techniques could help realize effective single-molecule and live-cell imaging. Thus, the investigation done in these projects confirms that UCNPs can label and image intracellular structures effectively. The current achievement in specific targeting and imaging of the different subcellular structures opens vast future opportunities for implementing UCNPs in biosensing, light-guided drug delivery, and tracking and tweezing applications.

# 7 | Summary of the Overall Ph.D. Project results

## 7.1 Preamble

This section summarizes the different experimental works performed throughout the project. The results from the synthesis and characterization of the UCNPs have been enlightened. The major synthesis steps and the potential advantages of the synthesized copolymers have been elaborated. The benefits of the MAA-incorporated copolymers in advancing the surface coupling efficiency and in the optimization of amphiphilicity have been discussed. The potential advantages of the surface grafting approaches and implemented biofunctionalization technique have been explained. The promising performance of copolymer-grafted and functionalized particles in specific targeting of selected organelles is mentioned. Overall, the practical implementation of functionalized UCNPs in intracellular labeling and imaging of subcellular structures and future opportunities are pointed out.

## 7.2 The UCNPs synthesis and characterization

Thermal synthesis has been used to develop the different sizes of NaYF<sub>4</sub>: Yb<sup>3+</sup>/Er<sup>3+</sup> UCNPs. A monodisperse and hexagonal structure of nanoparticles was designed. The NaYF<sub>4</sub> is the most efficient matrix for synthesizing bright Er<sup>3+</sup> doped nanocrystals and is implemented. The monodispersity of the nanoparticles has been assessed from the TEM analysis. The crystallinity of the nanoparticles was characterized by their XRD patterns. The obtained XRD pattern confirms that the hexagonal structure is effectively favored through controlled synthesis. The achievement of hexagonal structures is to gain strong emission for intracellular imaging. The hexagonal phase is the most recommended crystal structure for high contrast bioimaging application. The dispersity of the nanoparticles has been assessed from the TEM analysis. The XRD patterns allow for assessing the crystallinity of the nanoparticles. The obtained XRD pattern confirms that the hexagonal structure is effectively favored through controlled synthesis. The production of particles with hexagonal structures allows to generate strong emission for intracellular imaging structure. The intense emission capacity of the hexagonal structures is due to lower C<sub>1</sub> symmetry in the hexagonal structure compared to the cubic system's octahedral (Oh) symmetry. The enhanced emission capability of the hexagonal structure is due to the short distance between neighboring

lanthanide ions compared to the cubic form.<sup>484</sup> The luminescence capacity of the UCNPs also depends on the crystal structure of the matrix.

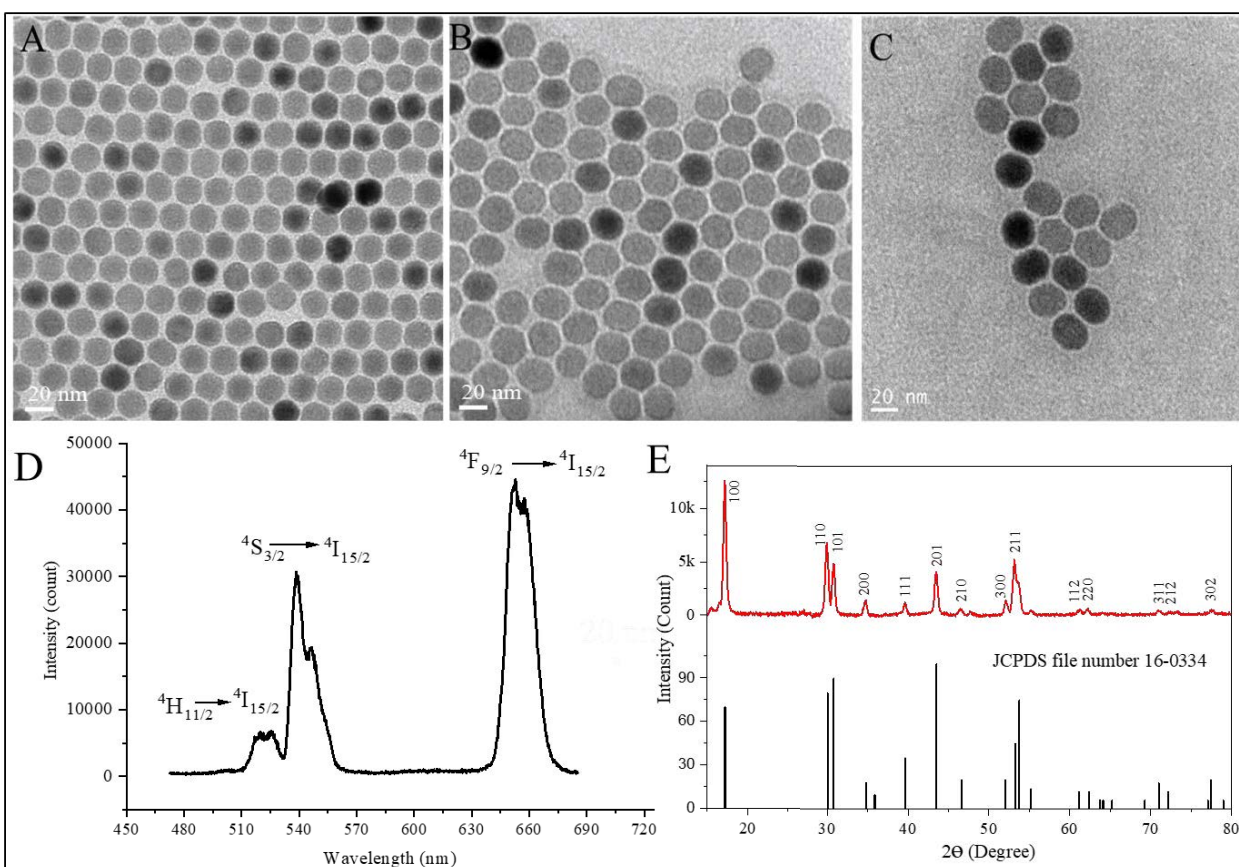


Figure 89 The TEM micrographs (A-C), electronic emission properties (D), and the XRD pattern of the synthesized UCNPs (E).

The synthesized nanoparticles are aimed to provide efficient brightness to image intracellular structures. The attractiveness of the UCNPs in bioimaging arises from their unique optical features. The electronic property of the UCNPs is determined from their multiple and sharply visible emissions. As presented in Figure 89 D, the  $\text{Er}^{3+}$ -doped UCNPs display two primary characteristic emission peaks at about 650 nm and 525 nm during NIR excitation at 976 nm. The visible emissions from the UCNPs help to brighten the deep intracellular structure and allow for visualization using the proper microscope techniques. The different particle sizes are synthesized to investigate the size effect in the intracellular labeling. Nanoparticle size control is critical in achieving efficient intracellular labeling. The smaller diameter UCNPs are preferable in subcellular labeling because they give better size compatibility and labeling density. They could

effectively label the tiny details of biological structures without inducing significant interference. The larger diameter nanoparticles, on the other hand, give an advantage of attaining bright fluorescence. The core-shell structure nanoparticles are aimed to generate intense brightness. The smaller diameter, 15 to 20 nm, highly doped core-shell nanoparticles may help to meet the size compatibility and brightness simultaneously.

The high hydrophobicity of the oleate capping ligand in as-synthesized UCNPs is a major driving factor for post-synthesis surface modification. Oleate ligand has limited functionalities to further functionalization and is unsuitable for direct-use bio-applications. The transformation of the surface chemical composition of the UCNPs gives multiple advantages besides the improvement in hydrophilicity. The copolymers based UCNPs surface grafting provides vast opportunities to use them in advanced applications. The surface grafted UCNPs gain improved dispersibility, biocompatibility, and stability. Different functional copolymers have been developed to produce UCNP surfaces with high reactivity and functionalities.

### 7.3 The synthesis of RAFT copolymers

RAFT polymerization is one of the advanced RDRP techniques in the development of block copolymers for UCNPs surface modification. As the UCNPs surface functionalization aims to introduce specific and desired surface features, the RAFT-based copolymers are ideal for producing a readymade polymer to perform surface grafting. The design and development of multiple RAFT copolymers for UCNP stabilization and functionalization have been done successfully. The RAFT technique gives potential opportunities in controlling functionalities through the RAFT AGENT USED and the type and amount of monomer inserted. The availability of wide monomer options commercially helps to select the suitable functional monomer. The possibility of controlled insertions of desired monomers makes the RAFT technique more attractive in developing copolymers with controlled physicochemical properties. With this project, The RAFT block MAA-based copolymers are developed to improve reactivity towards coupling agents and, in parallel, enhance dispersibility and maintain colloidal stability. Figure 90 presents the structures of the multiple block copolymers developed from different RAFT agents and monomers.

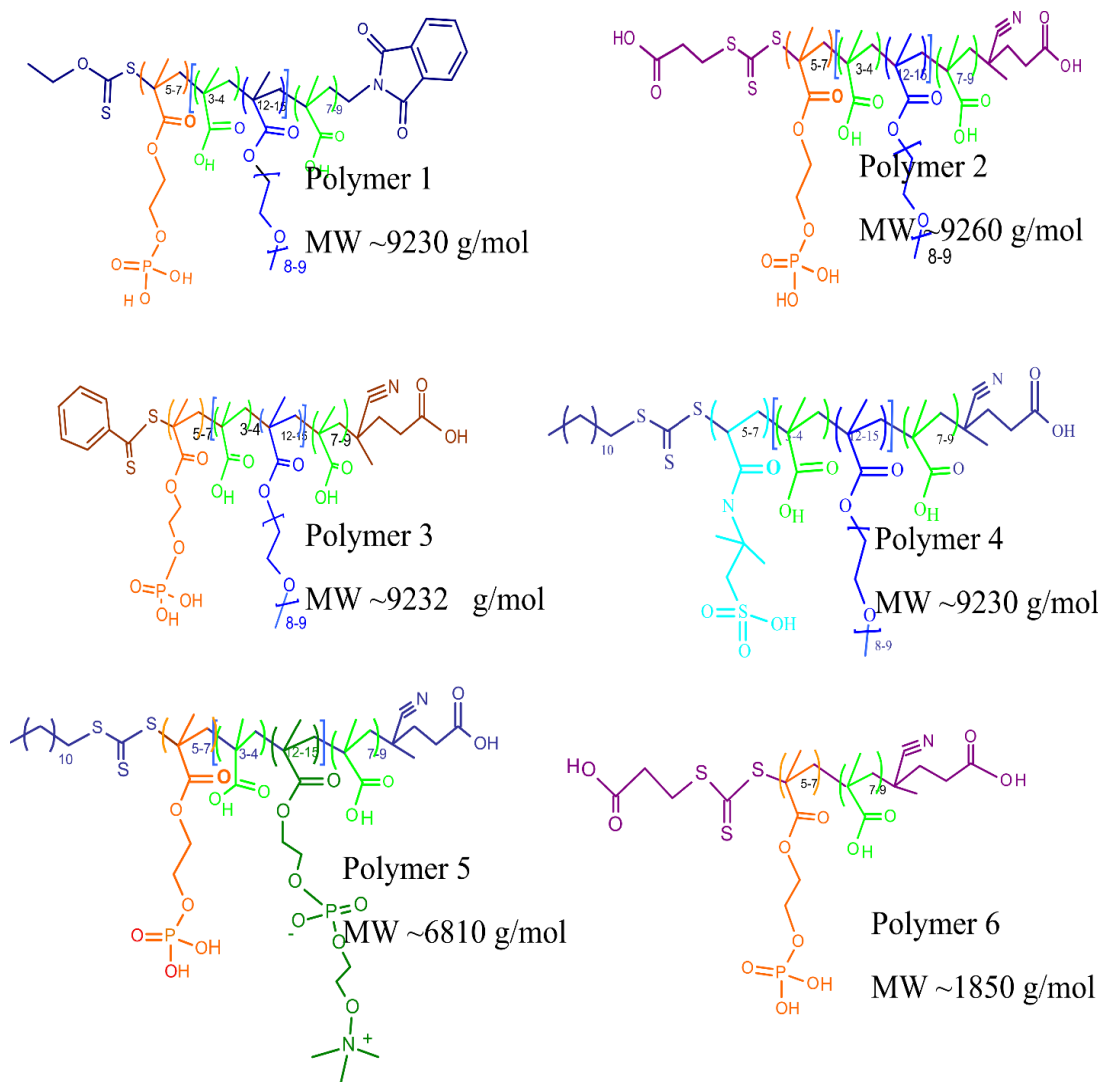
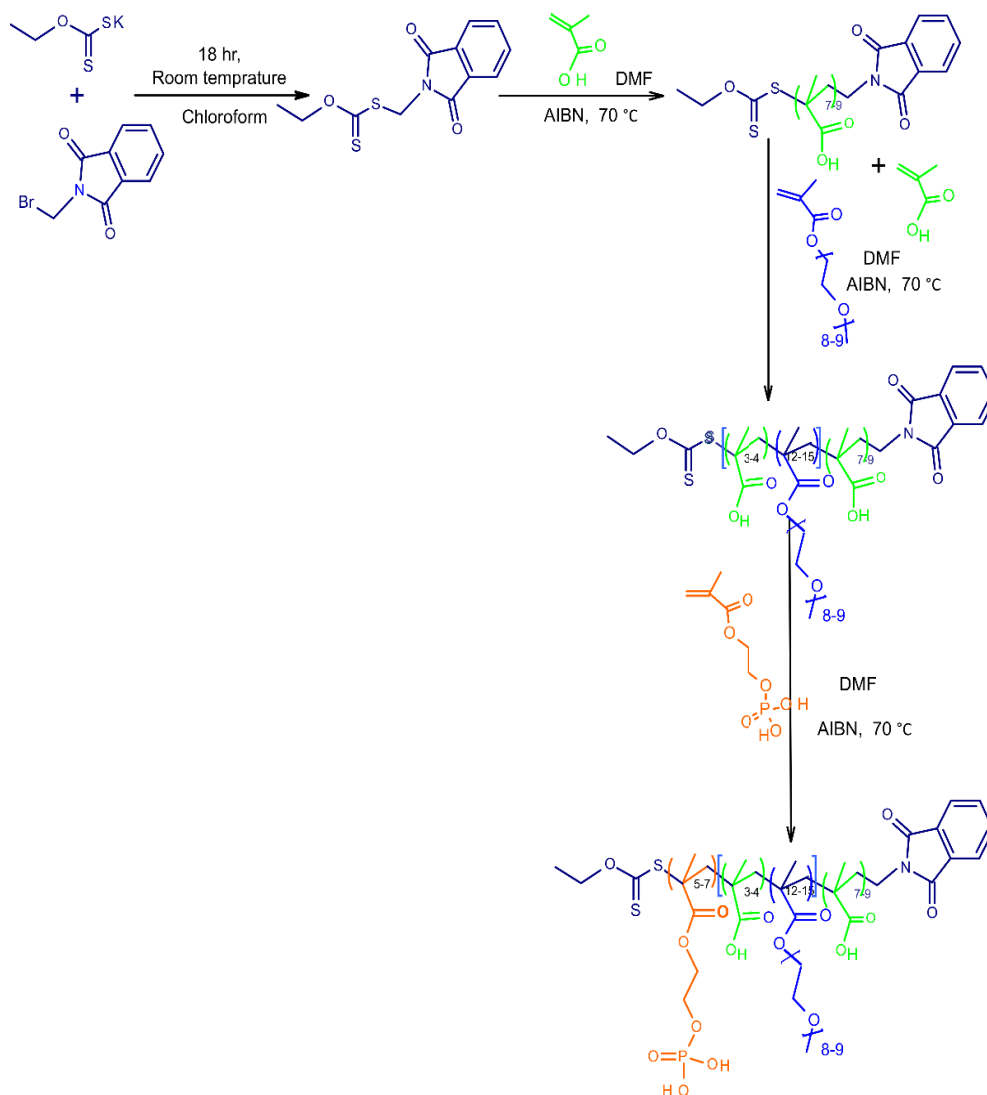


Figure 90 List of copolymers developed using the RAFT copolymerization technique.

The different polymers are synthesized using traditional and modern radical initiation techniques. The monomer and RAFT agent selection have determinant roles in the success of polymerization. The monomer choice has been made based on the functionalities in need to functionalize nanoparticle surfaces. Depending on the RAFT agent employed, thermal and photo-induced polymerizations are effectively implemented in the sequential synthesis of copolymers. The traditional thermal radical initiation was implemented in synthesizing Polymers 1 and 3 from OESPX and dithiol carbonate RAFT agents, respectively. The tri-thiol RAFT agents, CTCPA and CDTPA, are implemented in photo-polymerization utilizing a blue LED strip (460 nm) as an initiator for synthesizing Polymers 2, 4, 5, and 6. The sequential synthesis of the copolymers gives advantages in controlling the functionality and amphiphilicity of the final polymer.



Polymer 1 began from OESPX (MADIX) RAFT agent synthesis. The RAFT agent synthesis was performed based on an established protocol.<sup>419</sup> The synthesized RAFT agent characterization was performed to check for chemical and physical properties using <sup>1</sup>H NMR, <sup>13</sup>C NMR, and melting point. The NMR analysis and melting point values agree with previously reported ones. The OESPX RAFT agent and the subsequent copolymer polymerization reactions are schematically represented as shown in Scheme 12.



Scheme 12 Schematic illustration of the synthesis of the xanthate RAFT agent and subsequent development of Polymer 1.

In the case of Polymer 1, the OESPX RAFT agent-based copolymer has unique advantages in developing UCNP surfaces. The OESPX-based polymer synthesis was performed through radical

thermal initiation. Post-synthesis modification of the phthalimide end group was performed to introduce reactive sites. An end-group modification through hydrazinolysis of the phthalimides group produces amine and sulfhydryl functionalities. The amine from the post-modification has been used as a coupling site for organic dyes to obtain hybrid nanoprobe. The sulfhydryl functionality allows performing maleimide coupling as an alternative to functionalizing UCNPs. The MAA's carboxylic acid units allow for improved bio coupling using EDC chemistry. The synthesis of the rest copolymers was performed similarly, except for type monomer changes and the implementation of photo-based initiation in the case of tri-thiol RAFT agents.

Polymer 2 is a highly hydrophilic copolymer developed using the CTCPA RAFT agent. The two carboxylic end groups of the CTCPA are responsible for the hydrophilicity and reactivity of the copolymer. In addition to the RAFT agent carboxylic groups, the MAA block significantly enhances the hydrophilicity of the polymers. Incorporating the MMA units helps to produce flexible and easily accessible carboxylic groups. The increased carboxylic acid availability and their flexible appearances improve coupling efficiency. The OEGMA units are responsible for the optimization of amphiphilicity and miscibility. The triblock copolymers have copolymers designed with 7 to 9 DP of MAA, 13 to 15 DP of OEGMA, and 5 to 7 DP of MOEP maintained in all polymer synthesis cases. Polymer 3 is based on thermal synthesis using CDBPA. The Z-end group of Polymers 3 is highly hydrophobic and helps to counterbalance the high hydrophilicity generated due to the MAA units. One advantage of amphiphilic copolymers is the achievement of high dispersibility in THF, the most common solvent in the UCNPs' surface grafting.

Polymers 4 and 5 are based on CTCPA and CDTPA RAFT agents which are suitable for performing photo-initiated polymerization. Polymer 4 is helpful in modifying surfaces with sulphonate anchoring functionality to produce stable particles at lower pH. The MPC copolymers exhibit a high degree of hydrophilicity. Polymer 5 is MPC based copolymer for the development of antifouling surfaces. The high hydrophilicity from the MPC could be counterbalanced with the hydrophobic end group of the RAFT agent. The long alkane chain of the CDTPA is also vital to synthesizing the MAA-based diblock for combined copolymer grafting applications. Polymer 6 has been designed from CDTPA to introduce hydrophobicity to produce from its Z-end group. The amphiphilicity optimization helps obtaining THF dispersible polymer to perform single-step surface modification.

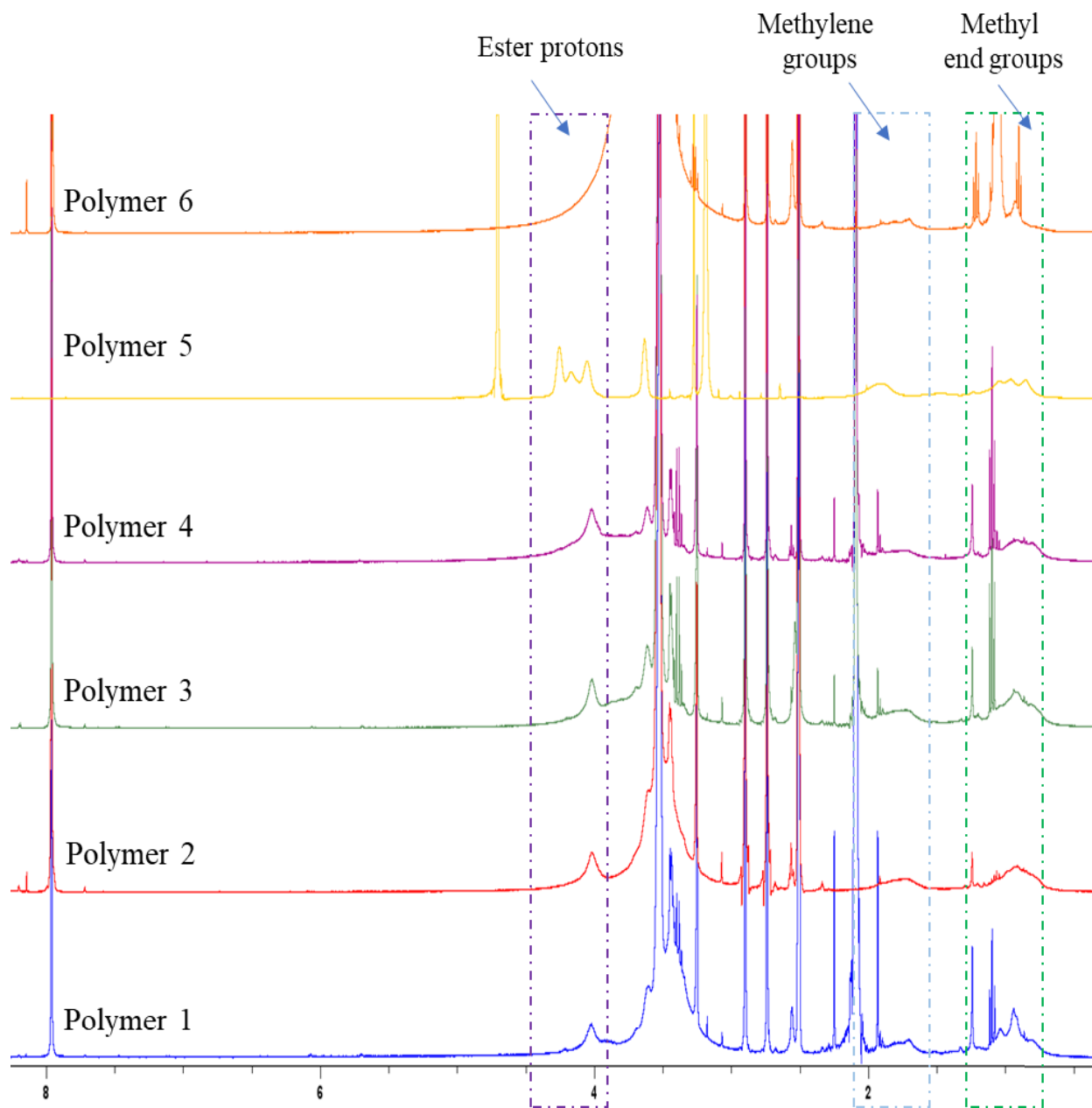


Figure 91 The  $^1\text{H}$  NMR of the different purified final copolymers (NMR solvent: Polymer 5 run using deuterated water; and the rest run in  $\text{DMSO-d}_6$ ).

Figure 91 presents the  $^1\text{H}$  NMR spectra of the purified copolymers. All the  $^1\text{H}$  NMR spectra show three primary characteristic intensities at  $\delta$  4.0,  $\delta$  1.9, and  $\delta$  0.9 ppm. The monomer proton peaks at  $\delta$  5.6 and  $\delta$  5.9 ppm that belong to the vinyl protons, and the  $\delta$  4.3 and  $\delta$  4.2 ppm peaks from the ester protons disappeared. It confirms that the polymer is purified and free from the residual monomer. The intense peaks close to  $\delta$  4.0 ppm belong to the ester proton of the copolymer, and

the broad peaks at  $\delta$  1.9 and  $\delta$  0.9 ppm are due to the increased methylene backbone and methyl end groups, respectively. In the case of Polymer 6, since the source ester protons are from the few MOEP units, a very low intensity has been observed at  $\delta$  4.0 ppm. In the case of Polymer 5, the triple peaks are due to ester groups of MPC and MOEP blocks.

#### 7.4 Surface grafting and functionalization of the UCNPs

The ligand exchange process is a replacement of oleate ligands from as-synthesized UCNPs. The primary aim of ligand exchange-based surface modification is to introduce functional polymers and to attain water-dispersible particles. The phosphate-derivatized copolymers are efficient in ejecting out the carboxylate ligands of oleate polymers. The strong basicity of phosphate and sulphonate ligands allows them to replace the carboxylate ligands preferentially. The surface cations from partially coordinated UCNPs are interactive sites to connect the polymer to the nanoparticles. The positively charged nanoparticle preferentially coordinates with the available electron-rich ligands for better stability. The formation of strong electrostatic interaction between the ligand and the nanoparticle's surface keeps them stable enough. The oleate ligand replacement is highly dependent on the copolymer size and composition. The copolymer with hydrophobic RAFT end groups has shown an enhanced graft density achievement during the UCNPs surface modification. It might be associated with hydrophobic interaction between the nanoparticle surface and the copolymer z-end groups. A closer association between the surface and the copolymer's end groups increases ligand replacement and could be from physical adsorption effects.

The hydrodynamic size of surface-grafted nanoparticles' is one of the significant parameters in evaluating the effectiveness of surface grafting. The hydrodynamic diameter of the copolymer-grafted UCNPs is between 30 to 60 nm. The observed number of weighted distribution hydrodynamic size increments and surface grafting are expected to be less than 20 nm. The Polymer 2 and 3 grafted nanoparticles have gained reduced hydrodynamic sizes. The surface grafted 25 nm UCNPs have gained 33 to 35 nm final hydrodynamic size. The weak hydrogen bonding and the steric stabilization capability of the OEGMA units are the possible reasons for the reduced hydrodynamic sizes. The Polymer 1 and 5 grafted nanoparticles have 45 to 55 nm hydrodynamic size, which is comparatively high. The presence of amine functionalities in those copolymers could induce hydrogen bonding, leading to nanoparticle clustering.

The amount of replaced ligand is directly proportional to the number of phosphate groups coordinated to the nanoparticle surface. The highly branched copolymers induce a high hindrance effect, limiting the number of phosphates attached to the surfaces. Intercalation of less branched copolymers on surfaces grafted in the highly branched copolymers, or vice versa, helps to produce heterogeneous hierarchical surfaces. The short-branched grafts reside closer to the surface, and the long-branch copolymers align at the peripheral regions.

The stability of copolymers grafted UCNPs were assessed from the long-term retention of their hydrodynamic size in aqueous media. The practical covalent attachment of polymers through ligand exchange gives better crystal stability and helps to minimize aggregation effects. The colloidal stability of the particles is due to the steric effect of the grafted polymers and the electrostatic repulsion of the highly charged surfaces. Most of the copolymers grafted UCNPs surfaces have surfaces that have high negative surface zeta-potentials. The MAA units are the primary source of surface charge for the copolymer's grafted nanoparticles. The OEGMA blocks are known for their steric stabilization of colloidal dispersions. The grafted copolymers' brush-like surface appearances serve as a barrier to keep nanoparticles far apart.

The degree of oleate ligand exchange determines the long-term stability of the nanoparticles in ionic environments. The carboxylate-based surface anchoring group, such as the oleate ligand, has a higher pKa than the phosphate and sulphonate groups. The oleate ligands are easily displaced from the surface when the nanoparticles are exposed to ionic conditions such as PBS buffer. The competitive ions, such as the PBS buffer's phosphate ion, replace the residual oleate ligands. Achieving reduced residual oleate is the primary solution to obtaining better nanoparticle stability.

The concept of combined copolymers surface grafting has two main advantages. First, it allows for a mix-up of different polymers to obtain various surface features. Second, it enables the management of graft density, surface charge, and functionalities. The composite graft incorporates other functional monomers and anchoring ligands to generate and address surface anisotropy. The achieved surface double grafted surface was assessed using FTIR and TGA. The investigations indicate that combined copolymer surface grafting is effectively implemented in the surface modification of the UCNPs. In the TGA experiment, as seen in Figure 92, the different grafted nanoparticles have shown their specific thermograph profile curves. The high weight loss in the 50 to 150 °C ranges is due to water loss from highly hydrated MPC units and the

dihydroxylations of phosphate hydroxyls from the MPC and anchoring phosphate. The Polymer 6 grafted nanoparticles also show significant weight loss from the enormous number of phosphates anchoring groups. Combining the two copolymers with branch length and functionalities produces improved surface performances.

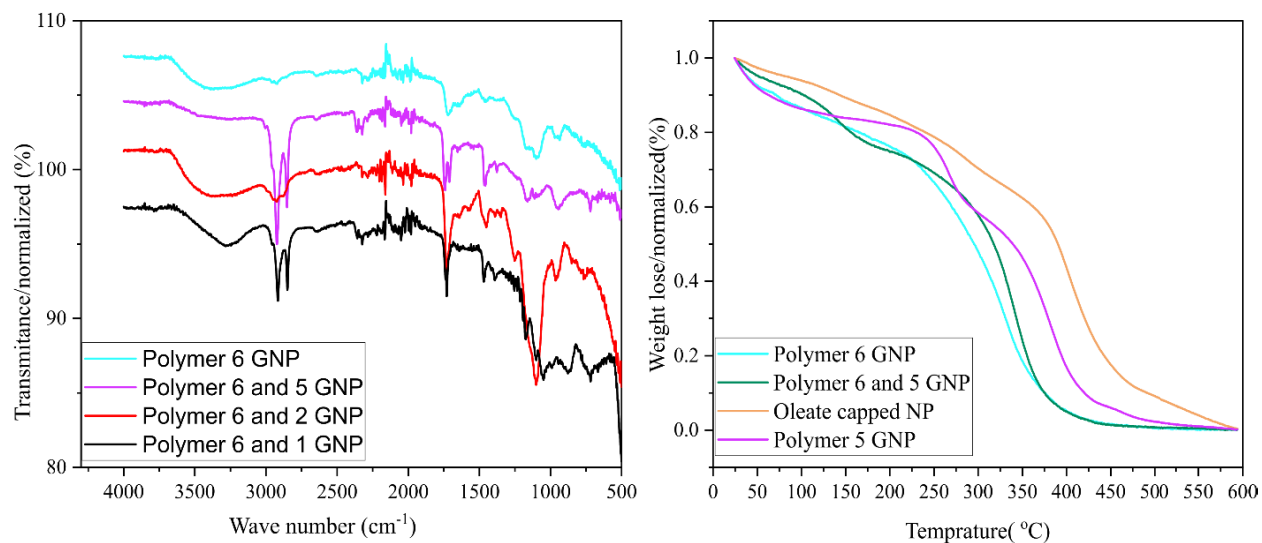


Figure 92 Thermograph of combined copolymers grafted UCNPs.

The co-grafting has potential promising features in advancing the surface functionalization of the UCNPs. Surface heterogeneity could be achieved, which helps gain multifunctional surfaces. With combined copolymers grafting, besides the local heterogeneity in surface charge and amphiphilicity from MAA, MPC, and OEGMA blocks, the introduction of chain length variation produces additional advantages like hierarchical surface appearances. The surface copolymers' composition and architecture govern the colloidal stability and dispersibility of the nanoparticles. The combined surface grafting based on copolymers' chain length and branch size introduces many surface variations.<sup>224</sup>

The main advantage of the MAA-incorporated triblock-copolymers is the enhancement of surface reactivity. The triblock copolymers allow addressing the limited surface reactivity observed in commonly used di blocks copolymers during surface grafting of UCNPs. The composition of grafted copolymers determines the efficiency of surface coupling. The copolymer-grafted surfaces effectively immobilize peptides, antibodies, and organic dyes. The high carboxylic acid density and their extended surface appearance are the possible reasons for an effective EDC-based bioactive molecules immobilization to the UCNPs surface attached polymers. The reduced zeta

potential values show the successful EDC activation of the carboxylates and, in parallel, the high coupling performance. The integration of biorecognition elements into the UCNP surfaces enormously boosts their potential in nanomedicine applications. The UCNP probes intracellular imaging targetability is the critical factor in precisely localizing the particles. The undesired nano-bio interaction and off-target delivery could be minimized through surface-grafted copolymers and from the immobilized biomolecules.

### 7.5 UCNPs in intracellular labeling and imaging

Adequate visualization of the microtubules, actin, nuclear pore complex, and nucleolus is performed using UCNPs. The demonstrated UCNP probes-based subcellular labeling shows efficient labeling of the tiny intracellular structures. The images captured in Figure 92 prove that the UCNPs are successfully delivered and targeted to specific sites. Multiple UCNPs-based nanomedicine opportunities could be gained through targeted intracellular delivery and imaging of the UCNPs. The success in targeted delivery and imaging of the particles enables to performance of other intracellular applications like single particle tracking, biosensing, and monitoring of delivery applications. The images in Figure 93 confirm that the UCNPs could be explicitly targeted at the desired intracellular sites specifically.

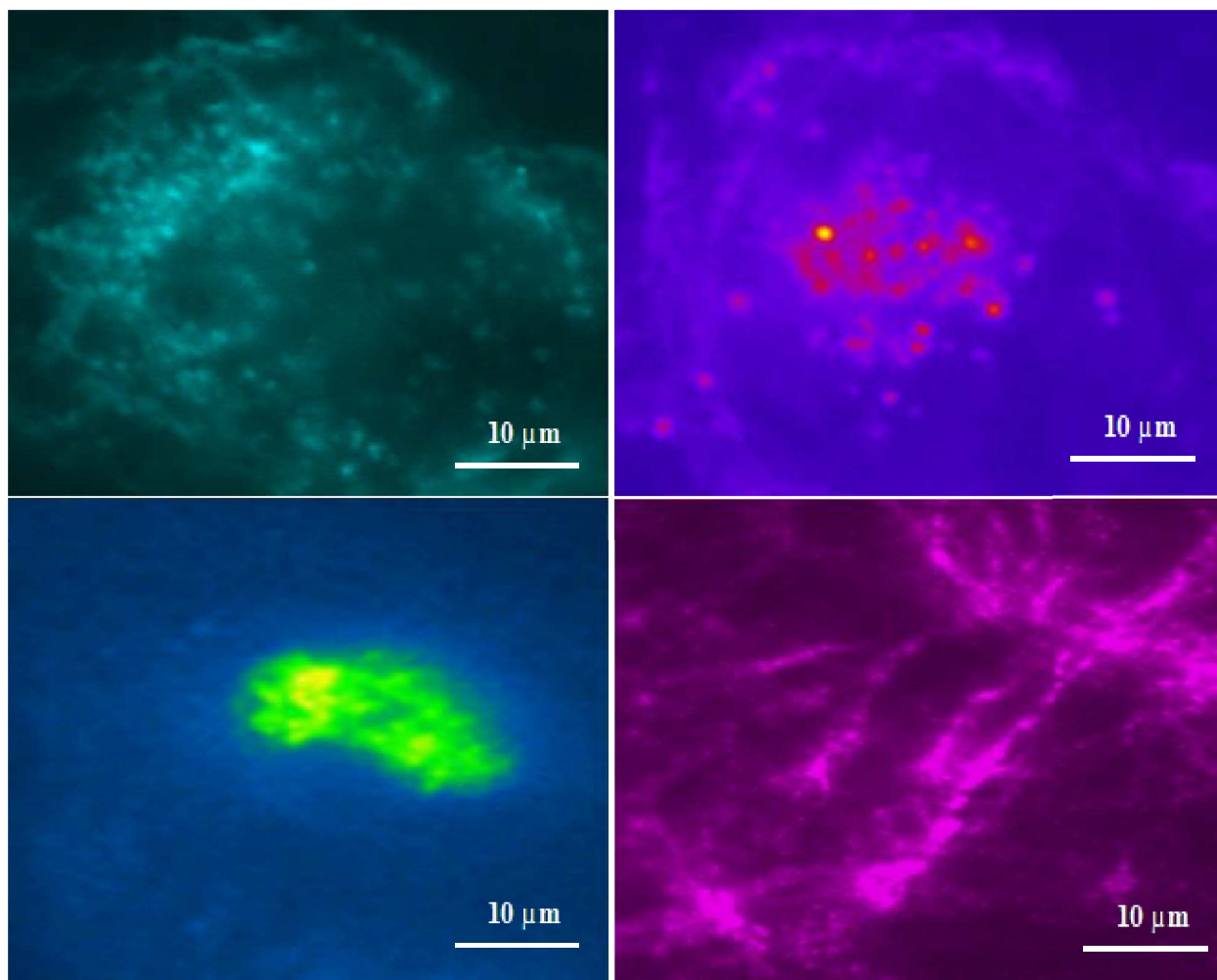


Figure 93 Images captured from UCNP probes labeling of F-actin (A), NPC (B), nucleolus (C), and microtubules (D).

The hybrid UCNP-dye probes serve to image the intracellular structure by implementing dual-wavelength excitation, for example, visible excitation for the dyes and NIR excitation for the UCNPs.<sup>103</sup> The hybrid labeling could replace the need for colocalization to cross-check the nanoparticle's targetability with the established dye-based labeling. The comparative studies performed on hybrid nanoprobe help to assess the efficiency of the UCNPs in specific targeting. The effectiveness of nanoparticle delivery and targeting could be monitored from the well-established dye-based advanced imaging facilities and the NIR UCNPs excitation.

The overall experimental outcomes indicate that the UCNPs are potential alternatives for dye-based intracellular labeling. The targetability of the nanoparticles is associated with proper size control of the modified particles. The capability in UCNPs specific targeting has numerous



advantages in diverse fluorescence imaging applications. The resolution of the images captures strongly dependent on the microscopic techniques. Light diffraction impacts the qualities of images captured using the confocal and widefield microscopes. As future work, further optimization of surface grafting and precise control of surface chemical groups gives multiple opportunities to use them in super-resolution imaging techniques.

## 7.6 Conclusion

The results from the cumulative experimental approaches indicate that the UCNPs could be effectively implemented in detail intracellular labeling and imaging. UCNP probes are successfully implemented in fluorescence labeling and imaging multiple intracellular structures. The numerous attractive features of the UCNPs could be exploited using the potential advantages of the surface-grafted copolymers. The already-established thermal synthesis has been implemented to produce monodisperse and different-diameter UCNPs. The synthesized nanoparticles are suitable enough to design and develop the UCNP surfaces for intracellular imaging. The surface development with desired size and shape has been achieved successfully. The UCNPs surfaces have been developed using copolymer grafting and implemented in precisely delivering, targeting, and imaging multiple intracellular structures.

The synthesized copolymers are found suitable to empower the UCNP surfaces for intracellular application. The UCNPs surface optimization has opened new opportunities to utilize them effectively in intracellular and other bioanalytical applications. The intracellular imaging performance of the UCNPs is determined by their effective delivery, targetability, and stability in the physiological environment. The physiological system is dynamic, and the possible nano-bio interactions are unpredictable. The possible solution considered in this project work is the enhancement of UCNPs surface performances from effective integration of the nanoparticle's polymers and biomolecules.

Multiple copolymers with various physicochemical properties have been produced and implemented in the surface functionalization of the UCNPs. RAFT polymerization is one of the most advanced RDRP techniques to develop block copolymers in a controlled manner. The availability of vast monomer choices is advantageous in designing and synthesizing copolymers with exciting properties. The different RAFT agents could be implemented through thermal- or

photo-initiation-based polymerization. Direct photo-initiated polymerization avoids the use of exogenous initiation to develop copolymers. The functionalities of the copolymer could be controlled from the RAFT agent end groups and the specific monomers introduced in the copolymers.

The monomers functionality has played vital plays in the performance of the functionalized. Surface. The MAA-based triblock copolymers introduce optimized carboxylic functionality to the UCNP surfaces. The employment of MPC copolymer further advances the UCNP surfaces to develop antifouling capacity and helps to minimize protein adsorption and nanoparticle entrapment. The OESPX RAFT, agent-based copolymers synthesis, has produced potential advantages in introducing surface coupling sites. The post-polymer end group modification gives amine and sulfhydryl functionalities. Here, the amine functionalities are extensively used in developing hybrid nanoprobes. The surface-integrated polymer helps to bridge and transfer the UCNPs effectively into the physiological system.

The performed surface grafting techniques are specifically designed to control the performance of the functionalized particles. The graft period and polymer-particle ratios are optimized. The combined surface grafting has been investigated for the development of mixed multi-functionalities. The combination of short and long-branch copolymers was assessed for their performance in size control and intracellular labeling efficiency. The TGA curves of the combined copolymers grafted surfaces confirm that combined surface grafting is achieved effectively. Overall, particle synthesis and surface development have been accomplished effectively. The performance of the functionalized UCNPs has been confirmed by imaging of microtubules, f-actin, nucleolus, and complex nuclear structures. The MAA functionalized copolymers are efficient in coupling biomolecules, and they could be utilized in the preparation of UCNPs for single-molecule and live-cell imaging applications.

## 8 | Conclusion and Perspectives

Overall, a substantial scientific understanding of UCNP surface functionalization and intracellular labeling and imaging has been gained from the Ph.D. training. The multidisciplinary approach implemented in developing UCNP probes gives enormous opportunities in their intracellular applications. The surface functionalization of the UCNPs has played determinant roles in the labeling and imaging of specific organelles. The inherent luminescence potentials of the nanoparticles could be retained and effectively employed for intracellular applications through polymer-based surface functionalization and stabilization. The polymers are the main actors in governing the interactions at the surfaces of the nanoparticles. The vast options in synthesizing copolymers are an excellent opportunity to implement diverse polymers for the surface grafting of the nanoparticles. The integration of polymers to the UCNP surfaces gives numerous opportunities to optimize the performance of the nanoparticles.

The MAA functionalized copolymers developed using different RAFT agents are the key role players in realizing the objectives of the Ph.D. project. The commonly used surface grafting copolymers could provide a limited reactive site for the coupling of biomolecules. The MAA functionalized copolymers enable the surface introduction of excessive carboxylic functionalities. The surface introduction of excessive carboxylic groups provides accessible reactive sites for the achievement of effective EDC-based coupling. The different blocks of the copolymer have their own contributions to the overall performance of the nanoparticle's surfaces. The OEGMA units serve to improve amphiphilicity and water dispersibility. The MOEP blocks are responsible for the coordination of the polymer to the particle's surfaces. The RAFT agents' end groups are taken as an advantage in choosing the implemented synthesis approach and the final functionalities. Conventional thermal initiation and photopolymerization are implemented to prepare the different polymers. The amphiphilicity and dispersibility of the particles could be tuned from the proper choices of the RAFT agents. The newly designed copolymers are advantageous in the development of UCNP surfaces with new functionalities. The OESPX RAFT agent and MPC monomers-based copolymers provide new surface advantages with their surface grafting of UCNPs. The OESPX allows for the introduction of amine and sulfhydryl functionality through end-group modification.

The MPC copolymers help develop antifouling surfaces to address the nano-bio interface challenges.

The surface grafting techniques determine the effectiveness of UCNPs surface functionalization. The ligand exchange techniques help to replace the oleate ligand through the displacement process. The replacement of the oleate ligand could be achieved when the new copolymer ligand could access the particle surfaces. Surface co-grafting using two copolymers with different allows introduction of a more significant number of polymers to the surface. The stepwise UCNP grafting using di-block copolymers followed by a triblock copolymer has enabled the development of the optimized surface composition. The mixed copolymer grafting has promising features in advancing the functionalities of UCNP surfaces.

The developed UCNP-polymer-biomolecule hybrid probes have revolutionary potential in their future biomedical roles. The high intracellular targetability and imaging capability of produced UCNP probes provide tremendous opportunities in super-resolution imaging and other intracellular purposes. Although the scope of the current project is limited to developing the UCNPs surfaces for intracellular labeling and imaging, the effective surface functionalization and localization of the nanoparticles is also essential in intracellular delivery and biosensing applications. The well functionalized UCNPs are advantageous in rapid screening of pathogens, drugs, and food poisoning are the other potential bio applications.

In conclusion, throughout the Ph.D. training, a comprehensive and multidisciplinary experience has been developed. The experimental works have been performed in different laboratories using cutting-edge research facilities at UTS. The nanoparticles synthesis, RAFT copolymers development, the different grafting techniques and functionalization, cell culture and nanoparticles labeling, and intracellular imaging are the major lessons from the Ph.D. study. The advanced materials characterization techniques and the industrial internship taken have broad opportunities to gain hands-on skills in the fabrication of functionalized particles. Besides the specific research experiences, the vast opportunities gained in personal development, teamwork, and project management have profound impacts on creating future career opportunities.

## Appendix

### Internship Project work:

#### Materials Chemistry and scaling-up of nanoparticles fabrication

##### 1. Introduction

The potential of UCNPs is not only limited to intracellular labeling and imaging. The UCNPs could be employed in diverse bioanalytical sensing applications. UCNPs are applicable in detecting and screening analytes from different biological and environmental samples.<sup>51, 74, 457</sup> It is widely implemented in vitro diagnosis and environmental and food safety monitoring.<sup>485, 486</sup> The portable paper-based immunoassay tests have received substantial attention in the onsite detection of drug abuse.<sup>487</sup> These days, different signal labels, such as colour luminescence and electrochemical signals, are employed, and the choice of nanoparticles is essential in all LFA platforms. Lateral flow immunoassay (LFA) is the most typical representative point-of-care (POC) device.<sup>488</sup> Advanced analytical instruments, like liquid chromatography and gas chromatography-mass spectroscopy, accurately measure analytes. However, they are expensive and unsuitable for use in on-the-spot field detection. Although RT-PCR is considered a gold-standard technique in viral nucleic acid, it demands sophisticated laboratories and skilled professionals to operate.<sup>488</sup> The LFA is a fast-growing technique and advantageous regarding shorter detection time, lower production cost, and comprehensive population coverage compared to sophisticated analytical techniques.

The UCNPs are ideal for developing LFA devices for timely and on-site screening of analytes such as small molecules and nucleic acids. Nanoparticles serve as signal amplifiers in LFA, and they determine the sensitivity and accuracy of the measurement.<sup>489</sup> The WHO criteria, ASSURED (affordable, sensitive, specific, user-friendly, rapid and robust, equipment-free, and deliverable to end users) are very crucial in the development of LFA devices.<sup>490</sup> The nanoparticles are also employed as antibody carriers and signal tags. The nanoparticle development approach strongly determines the performance of the LFA technique.<sup>488</sup> The UCNPs surface functionalization is a promising approach to enhance sensitivity, specificity, and reproducibility. An effective UCNP surface development meets the ASSURED criteria and enables the development of LFA testing devices for in vitro diagnosis, environmental, food quality, and safety evaluation.

## 2. Activities performed and experiences.

The development of fluorescent nanoparticles (UCNPs) for SARS-COV-2 antigen testing has been performed. Nanoparticles with core- and core-shell structures with good monodispersity have been developed and characterized. Bi-functional ligands were synthesized for nanoparticle surface modification. Surface modification of the nanoparticles was performed through ligand exchange, and the hydrodynamic size of the nanoparticles was characterized using the DLS instrument. Coupling of biomolecules has been performed, and the preparation of test strips and kits assembly and sample testing for SARS-COV-2 antigen were performed with the Alcolizer research team.

The internship was an excellent opportunity to gain industrial exposure for a 4-month stay. I have developed invaluable skills regarding technical and administrative aspects. I have gained excellent experience in how research ideas could be transferred into a valuable product, SARS-COV-2 antigen strip development. I could implement most of my Ph.D. topics, such as fabrication of fluorescent nanoparticles, polymer synthesis, surface modification, and functionalization, into the internship work. Working in an advanced manufacturing company allowed me to experience their research laboratory handling and cleanroom production. The professional development opportunity was immense. I gained invaluable teamwork experience in a fast-paced system. In conclusion, the program helped me develop technical and leadership skills, helped to prepare me well to meet the future demand of industrial experts, and enhanced my employability.

## 3. Conclusion

The internship had vast learning opportunities regarding the industrial translation of UCNPs for rapid screening of SARS-COV-2 antigen. My involvement in the technology transfer was a great experience, besides the main project, UCNPs intracellular and imaging. The extensive experience gained from my project helped me fabricate the nanoparticles for the LFA application. The vast number of developed copolymers and the available different grafting and coupling approaches give comprehensive options to design the UCNP surfaces considering amphiphilicity, functionality, and coupling efficiency for developing efficient LFA testing devices.

## Bibliography

1. Kargozar, S.; Mozafari, M., Nanotechnology and Nanomedicine: Start small, think big. *Materials Today: Proceedings* **2018**, 5 (7), 15492-15500.
2. Feynman, R. P., There's plenty of room at the bottom [data storage]. *Journal of microelectromechanical systems* **1992**, 1 (1), 60-66.
3. Kwon, J.; Elgawish, M. S.; Shim, S. H., Bleaching - Resistant Super - Resolution Fluorescence Microscopy. *Advanced Science* **2022**, 9 (9), 2101817.
4. Martinez-Negro, M.; Gonzalez-Rubio, G.; Aicart, E.; Landfester, K.; Guerrero-Martinez, A.; Junquera, E., Insights into colloidal nanoparticle-protein corona interactions for nanomedicine applications. *Adv Colloid Interface Sci* **2021**, 289, 102366.
5. Wang, Y.; Song, S.; Zhang, S.; Zhang, H., Stimuli-responsive nanotheranostics based on lanthanide-doped upconversion nanoparticles for cancer imaging and therapy: current advances and future challenges. *Nano Today* **2019**.
6. Ahmed, T.; Liu, F.-C. F.; Lu, B.; Lip, H.; Park, E.; Alradwan, I.; Liu, J. F.; He, C.; Zetrini, A.; Zhang, T., Advances in Nanomedicine Design: Multidisciplinary Strategies for Unmet Medical Needs. *Molecular Pharmaceutics* **2022**.
7. Li, P.; Wang, D.; Hu, J.; Yang, X., The role of imaging in targeted delivery of nanomedicine for cancer therapy. *Advanced Drug Delivery Reviews* **2022**, 114447.
8. Krukemeyer, M.; Krenn, V.; Huebner, F.; Wagner, W.; Resch, R., History and possible uses of nanomedicine based on nanoparticles and nanotechnological progress. *J. Nanomed. Nanotechnol* **2015**, 6 (6), 336.
9. Prasad, M.; Lambe, U. P.; Brar, B.; Shah, I.; Manimegalai, J.; Ranjan, K.; Rao, R.; Kumar, S.; Mahant, S.; Khurana, S. K., Nanotherapeutics: an insight into healthcare and multi-dimensional applications in medical sector of the modern world. *Biomedicine & Pharmacotherapy* **2018**, 97, 1521-1537.
10. Chen, G.; Roy, I.; Yang, C.; Prasad, P. N., Nanochemistry and Nanomedicine for Nanoparticle-based Diagnostics and Therapy. *Chem Rev* **2016**, 116 (5), 2826-85.
11. Jain, K. K., *The Handbook of Nanomedicine*. Humana Press: 2017.
12. Woźniak, M.; Płoska, A.; Siewczyk, A.; Dobrucki, L. W.; Kalinowski, L.; Dobrucki, I. T., Molecular Imaging and Nanotechnology—Emerging Tools in Diagnostics and Therapy. *International journal of molecular sciences* **2022**, 23 (5), 2658.
13. Mohammadi, M. R.; Sun, W.; Inayathullah, M.; Rajadas, J., Nanoparticles hybridization to engineer biomaterials for drug delivery. In *Nanobiomaterials Science, Development and Evaluation*, Elsevier: 2017; pp 147-161.
14. Riehemann, K.; Schneider, S. W.; Luger, T. A.; Godin, B.; Ferrari, M.; Fuchs, H., Nanomedicine--challenge and perspectives. *Angew Chem Int Ed Engl* **2009**, 48 (5), 872-97.

15. Shetty, Y.; Prabhu, P.; Prabhakar, B., Emerging vistas in theranostic medicine. *International Journal of Pharmaceutics* **2019**, *558*, 29-42.
16. Zhang, Q.; O'Brien, S.; Grimm, J., Biomedical applications of lanthanide nanomaterials, for imaging, sensing and therapy. *Nanotheranostics* **2022**, *6* (2), 184.
17. Nguyen, T. D. T.; Marasini, R.; Aryal, S., Re-engineered imaging agent using biomimetic approaches. *Wiley Interdisciplinary Reviews: Nanomedicine and Nanobiotechnology* **2022**, *14* (1), e1762.
18. Massoud, T. F.; Gambhir, S. S., Molecular imaging in living subjects: seeing fundamental biological processes in a new light. *Genes & development* **2003**, *17* (5), 545-580.
19. Jokerst, J. V.; Gambhir, S. S., Molecular imaging with theranostic nanoparticles. *Accounts of chemical research* **2011**, *44* (10), 1050-1060.
20. Baggerman, J.; Smulders, M. M.; Zuilhof, H. J. L., Romantic Surfaces: A Systematic Overview of Stable, Biospecific, and Antifouling Zwitterionic Surfaces. **2019**, *35* (5), 1072-1084.
21. Xing, H.; Bu, W.; Ren, Q.; Zheng, X.; Li, M.; Zhang, S.; Qu, H.; Wang, Z.; Hua, Y.; Zhao, K., A NaYbF<sub>4</sub>: Tm<sup>3+</sup> nanoprobe for CT and NIR-to-NIR fluorescent bimodal imaging. *Biomaterials* **2012**, *33* (21), 5384-5393.
22. Zhang, Z.; Rayabharam, A.; Martis, J.; Li, H.-K.; Aluru, N. R.; Majumdar, A., Prospects for sub-nanometer scale imaging of optical phenomena using electron microscopy. *Applied Physics Letters* **2021**, *118* (3).
23. Diaspro, A.; Bianchini, P., Optical nanoscopy. *La Rivista del Nuovo Cimento* **2020**, *43* (8), 385-455.
24. James, M. L.; Gambhir, S. S., A molecular imaging primer: modalities, imaging agents, and applications. *Physiol Rev* **2012**, *92* (2), 897-965.
25. Wickline, S. A.; Lanza, G. M., Nanotechnology for molecular imaging and targeted therapy. Am Heart Assoc: 2003.
26. Liu, J.; Lécuyer, T.; Seguin, J.; Mignet, N.; Scherman, D.; Viana, B.; Richard, C., Imaging and therapeutic applications of persistent luminescence nanomaterials. *Advanced drug delivery reviews* **2019**, *138*, 193-210.
27. Bünzli, J.-C. G., Lanthanide light for biology and medical diagnosis. *Journal of Luminescence* **2016**, *170*, 866-878.
28. Lei, P.; Feng, J.; Zhang, H., Emerging biomaterials: Taking full advantage of the intrinsic properties of rare earth elements. *Nano Today* **2020**, *35*, 100952.
29. Algar, W. R.; Massey, M.; Rees, K.; Higgins, R.; Krause, K. D.; Darwish, G. H.; Peveler, W. J.; Xiao, Z.; Tsai, H. Y.; Gupta, R.; Lix, K.; Tran, M. V.; Kim, H., Photoluminescent Nanoparticles for Chemical and Biological Analysis and Imaging. *Chem Rev* **2021**, *121* (15), 9243-9358.
30. Schouw, H.; Huisman, L.; Janssen, Y.; Slart, R.; Borra, R.; Willemsen, A.; Brouwers, A.; van Dijl, J.; Dierckx, R.; van Dam, G., Targeted optical fluorescence imaging: a meta-



narrative review and future perspectives. *European Journal of Nuclear Medicine and Molecular Imaging* **2021**, *48* (13), 4272-4292.

31. Zhao, J.; Chen, J.; Ma, S.; Liu, Q.; Huang, L.; Chen, X.; Lou, K.; Wang, W., Recent developments in multimodality fluorescence imaging probes. *Acta Pharmaceutica Sinica B* **2018**, *8* (3), 320-338.
32. Ni, M.; Zhuo, S.; So, P. T.; Yu, H., Fluorescent probes for nanoscopy: four categories and multiple possibilities. *J Biophotonics* **2017**, *10* (1), 11-23.
33. Wang, M.; Abbineni, G.; Cleverger, A.; Mao, C.; Xu, S. J. N. N., Biology; Medicine, Upconversion nanoparticles: synthesis, surface modification and biological applications. **2011**, *7* (6), 710-729.
34. Dunst, S.; Tomancak, P., Imaging Flies by Fluorescence Microscopy: Principles, Technologies, and Applications. *Genetics* **2019**, *211* (1), 15-34.
35. Song, C.; Zhang, S.; Zhou, Q.; Hai, H.; Zhao, D.; Hui, Y., Upconversion nanoparticles for bioimaging. *Nanotechnology Reviews* **2017**, *6* (2), 233-242.
36. Son, J.; Yi, G.; Yoo, J.; Park, C.; Koo, H.; Choi, H. S., Light-responsive nanomedicine for biophotonic imaging and targeted therapy. *Advanced drug delivery reviews* **2019**, *138*, 133-147.
37. Sedlmeier, A.; Gorris, H. H., Surface modification and characterization of photon-upconverting nanoparticles for bioanalytical applications. *Chem Soc Rev* **2015**, *44* (6), 1526-60.
38. Klier, D. T.; Kumke, M. U., Analysing the effect of the crystal structure on upconversion luminescence in Yb<sup>3+</sup>, Er<sup>3+</sup>-co-doped NaYF<sub>4</sub> nanomaterials. *Journal of Materials Chemistry C* **2015**, *3* (42), 11228-11238.
39. Jin, D.; Xi, P.; Wang, B.; Zhang, L.; Enderlein, J.; van Oijen, A. M. J. N. m., Nanoparticles for super-resolution microscopy and single-molecule tracking. **2018**, *15* (6), 415.
40. Yao, J.; Huang, C.; Liu, C.; Yang, M., Upconversion luminescence nanomaterials: A versatile platform for imaging, sensing, and therapy. *Talanta* **2020**, *208*, 120157.
41. Zhu, X.; Zhang, J.; Liu, J.; Zhang, Y., Recent Progress of Rare-Earth Doped Upconversion Nanoparticles: Synthesis, Optimization, and Applications. *Adv Sci (Weinh)* **2019**, *6* (22), 1901358.
42. Sharma, P.; Brown, S.; Walter, G.; Santra, S.; Moudgil, B., Nanoparticles for bioimaging. *Adv Colloid Interface Sci* **2006**, *123-126*, 471-85.
43. Xu, J.; Gulzar, A.; Yang, P.; Bi, H.; Yang, D.; Gai, S.; He, F.; Lin, J.; Xing, B.; Jin, D., Recent advances in near-infrared emitting lanthanide-doped nanoconstructs: Mechanism, design and application for bioimaging. *Coordination Chemistry Reviews* **2019**, *381*, 104-134.
44. Huang, Y.; He, S.; Cao, W.; Cai, K.; Liang, X.-J., Biomedical nanomaterials for imaging-guided cancer therapy. *Nanoscale* **2012**, *4* (20), 6135-6149.
45. Reja, S. I.; Minoshima, M.; Hori, Y.; Kikuchi, K., Near-infrared fluorescent probes: a next-generation tool for protein-labeling applications. *Chem Sci* **2020**, *12* (10), 3437-3447.

46. Chen, X.; Peng, D.; Ju, Q.; Wang, F., Photon upconversion in core-shell nanoparticles. *Chemical Society Reviews* **2015**, *44* (6), 1318-1330.
47. Malhotra, K.; Hrovat, D.; Kumar, B.; Qu, G.; Houten, J. V.; Ahmed, R.; Piunno, P. A.; Gunning, P. T.; Krull, U. J., Lanthanide-Doped Upconversion Nanoparticles: Exploring A Treasure Trove of NIR-Mediated Emerging Applications. *ACS Applied Materials & Interfaces* **2023**.
48. Francés-Soriano, L.; Ferrera-González, J.; González-Béjar, M.; Pérez-Prieto, J., Near-infrared excitation/emission microscopy with lanthanide-based nanoparticles. *Analytical and Bioanalytical Chemistry* **2022**, 1-20.
49. Hahn, M. A.; Singh, A. K.; Sharma, P.; Brown, S. C.; Moudgil, B. M., Nanoparticles as contrast agents for in-vivo bioimaging: current status and future perspectives. *Analytical and bioanalytical chemistry* **2011**, *399*, 3-27.
50. Padmanabhan, P.; Kumar, A.; Kumar, S.; Chaudhary, R. K.; Gulyás, B., Nanoparticles in practice for molecular-imaging applications: An overview. *Acta biomaterialia* **2016**, *41*, 1-16.
51. Kumar, B.; Malhotra, K.; Fuku, R.; Van Houten, J.; Qu, G. Y.; Piunno, P. A. E.; Krull, U. J., Recent trends in the developments of analytical probes based on lanthanide-doped upconversion nanoparticles. *TrAC Trends in Analytical Chemistry* **2021**, *139*.
52. Lin, Y.; Nienhaus, K.; Nienhaus, G. U., Nanoparticle Probes for Super-Resolution Fluorescence Microscopy. *ChemNanoMat* **2018**, *4* (3), 253-264.
53. Liu, Z.; Liu, J.; Wang, X.; Mi, F.; Wang, D.; Wu, C., Fluorescent Bioconjugates for Super-Resolution Optical Nanoscopy. *Bioconjug Chem* **2020**, *31* (8), 1857-1872.
54. Oliveira, H.; Bednarkiewicz, A.; Falk, A.; Frohlich, E.; Lisjak, D.; Prina-Mello, A.; Resch, S.; Schimpel, C.; Vrcek, I. V.; Wysokinska, E.; Gorris, H. H., Critical Considerations on the Clinical Translation of Upconversion Nanoparticles (UCNPs): Recommendations from the European Upconversion Network (COST Action CM1403). *Adv Healthc Mater* **2019**, *8* (1), e1801233.
55. Sun, C.; Gradzielski, M., Advances in fluorescence sensing enabled by lanthanide-doped upconversion nanophosphors. *Adv Colloid Interface Sci* **2021**, 102579.
56. Rostami, I.; Alanagh, H. R.; Hu, Z.; Shahmoradian, S. H., Breakthroughs in medicine and bioimaging with up-conversion nanoparticles. *International Journal of Nanomedicine* **2019**, *14*, 7759.
57. Wang, F.; Banerjee, D.; Liu, Y.; Chen, X.; Liu, X., Upconversion nanoparticles in biological labeling, imaging, and therapy. *Analyst* **2010**, *135* (8), 1839-54.
58. Ranjan, S.; Jayakumar, M. K. G.; Zhang, Y., Luminescent lanthanide nanomaterials: an emerging tool for theranostic applications. *Nanomedicine* **2015**, *10* (9), 1477-1491.
59. Ning, Y.; Zhu, M.; Zhang, J.-L., Near-infrared (NIR) lanthanide molecular probes for bioimaging and biosensing. *Coordination Chemistry Reviews* **2019**, *399*, 213028.
60. Generalova, A.; Chichkov, B.; Khaydukov, E., Multicomponent nanocrystals with anti-Stokes luminescence as contrast agents for modern imaging techniques. *Advances in colloid and interface science* **2017**, *245*, 1-19.

61. Ansari, A. A.; Parchur, A. K.; Chen, G., Surface modified lanthanide upconversion nanoparticles for drug delivery, cellular uptake mechanism, and current challenges in NIR-driven therapies. *Coordination Chemistry Reviews* **2022**, *457*, 214423.
62. Liang, G.; Wang, H.; Shi, H.; Wang, H.; Zhu, M.; Jing, A.; Li, J.; Li, G., Recent progress in the development of upconversion nanomaterials in bioimaging and disease treatment. *Journal of Nanobiotechnology* **2020**, *18* (1), 1-22.
63. Jethva, P.; Momin, M.; Khan, T.; Omri, A., Lanthanide-Doped Upconversion Luminescent Nanoparticles—Evolving Role in Bioimaging, Biosensing, and Drug Delivery. *Materials* **2022**, *15* (7), 2374.
64. Tiwari, S. P.; Maurya, S. K.; Yadav, R. S.; Kumar, A.; Kumar, V.; Joubert, M.-F.; Swart, H. C., Future prospects of fluoride based upconversion nanoparticles for emerging applications in biomedical and energy harvesting. *Journal of Vacuum Science & Technology B, Nanotechnology and Microelectronics: Materials, Processing, Measurement, and Phenomena* **2018**, *36* (6), 060801.
65. Yan, C.; Zhao, H.; Perepichka, D. F.; Rosei, F., Lanthanide ion doped upconverting nanoparticles: synthesis, structure and properties. *Small* **2016**, *12* (29), 3888-3907.
66. Altavilla, C., *Upconverting nanomaterials: perspectives, synthesis, and applications*. CRC Press: 2016.
67. Xu, Y.; Xu, R.; Wang, Z.; Zhou, Y.; Shen, Q.; Ji, W.; Dang, D.; Meng, L.; Tang, B. Z., Recent advances in luminescent materials for super-resolution imaging via stimulated emission depletion nanoscopy. *Chemical Society Reviews* **2021**, *50* (1), 667-690.
68. Singh, A.; Amiji, M. M., Application of nanotechnology in medical diagnosis and imaging. *Current opinion in biotechnology* **2022**, *74*, 241-246.
69. Labrador-Páez, L.; Ximendes, E. C.; Rodríguez-Sevilla, P.; Ortgies, D. H.; Rocha, U.; Jacinto, C.; Rodríguez, E. M.; Haro-González, P.; Jaque, D., Core-shell rare-earth-doped nanostructures in biomedicine. *Nanoscale* **2018**, *10* (27), 12935-12956.
70. Gu, Y.-H.; Liu, H.-W.; Dong, X.-H.; Ma, Z.-Z.; Li, Y.-X.; Li, L.; Gan, D.-L.; Liu, P.-S.; Shen, J., Zwitterionic-phosphonate block polymer as anti-fouling coating for biomedical metals. *Rare Metals* **2022**, *41* (2), 700-712.
71. Sun, L.; Wei, R.; Feng, J.; Zhang, H., Tailored lanthanide-doped upconversion nanoparticles and their promising bioapplication prospects. *Coordination Chemistry Reviews* **2018**, *364*, 10-32.
72. Zhang, Y.-W.; Sun, X.; Si, R.; You, L.-P.; Yan, C.-H., Single-crystalline and monodisperse LaF<sub>3</sub> triangular nanoplates from a single-source precursor. *Journal of the American Chemical Society* **2005**, *127* (10), 3260-3261.
73. Wilhelm, S., Perspectives for Upconverting Nanoparticles. *ACS Nano* **2017**, *11* (11), 10644-10653.
74. Li, Y.; Chen, C.; Liu, F.; Liu, J., Engineered lanthanide-doped upconversion nanoparticles for biosensing and bioimaging application. *Microchimica Acta* **2022**, *189* (3), 1-28.

75. Parkatzidis, K.; Wang, H. S.; Truong, N. P.; Anastasaki, A., Recent Developments and Future Challenges in Controlled Radical Polymerization: A 2020 Update. *Chem* **2020**.
76. Kopeček, J.; Yang, J., Polymer nanomedicines. *Advanced Drug Delivery Reviews* **2020**.
77. Jeon, I.-Y.; Baek, J.-B., Nanocomposites derived from polymers and inorganic nanoparticles. *Materials* **2010**, 3 (6), 3654-3674.
78. Nam, J.; Won, N.; Bang, J.; Jin, H.; Park, J.; Jung, S.; Jung, S.; Park, Y.; Kim, S., Surface engineering of inorganic nanoparticles for imaging and therapy. *Adv Drug Deliv Rev* **2013**, 65 (5), 622-48.
79. Liu, G.; Sun, X.; Li, X.; Wang, Z., The Bioanalytical and Biomedical Applications of Polymer Modified Substrates. *Polymers* **2022**, 14 (4), 826.
80. Asai, M.; Zhao, D.; Kumar, S. K., Role of grafting mechanism on the polymer coverage and self-assembly of hairy nanoparticles. *ACS nano* **2017**, 11 (7), 7028-7035.
81. Boyer, C.; Bulmus, V.; Davis, T. P.; Ladmiral, V.; Liu, J.; Perrier, S. J. C. r., Bioapplications of RAFT polymerization. **2009**, 109 (11), 5402-5436.
82. Moad, C. L.; Moad, G., Fundamentals of reversible addition–fragmentation chain transfer (RAFT). *Chemistry Teacher International* **2021**, 3 (2), 3-17.
83. Moad, G.; Rizzardo, E., *RAFT Polymerization: Methods, Synthesis, and Applications*. John Wiley & Sons: 2021.
84. Yan, J.; Bockstaller, M. R.; Matyjaszewski, K., Brush-modified materials: Control of molecular architecture, assembly behavior, properties and applications. *Progress in Polymer Science* **2020**, 100, 101180.
85. Zhang, L.; Chen, C.; Tay, S. S.; Wen, S.; Cao, C.; Biro, M.; Jin, D.; Stenzel, M. H., Optimizing the polymer cloak for upconverting nanoparticles: an evaluation of bioactivity and optical performance. *ACS Applied Materials & Interfaces* **2021**, 13 (14), 16142-16154.
86. Lelek, M.; Gyparaki, M. T.; Beliu, G.; Schueder, F.; Griffié, J.; Manley, S.; Jungmann, R.; Sauer, M.; Lakadamyali, M.; Zimmer, C., Single-molecule localization microscopy. *Nature Reviews Methods Primers* **2021**, 1 (1).
87. Gonzalez-Bejar, M.; Frances-Soriano, L.; Perez-Prieto, J., Upconversion Nanoparticles for Bioimaging and Regenerative Medicine. *Front Bioeng Biotechnol* **2016**, 4, 47.
88. Aime, S.; Barge, A.; Gianolio, E.; Pagliarin, R.; Silengo, L.; Tei, L., *Molecular Imaging: 1*. Springer: 2008.
89. Hong, G.; Antaris, A. L.; Dai, H., Near-infrared fluorophores for biomedical imaging. *Nature Biomedical Engineering* **2017**, 1 (1).
90. Zhang, K.; Sun, Y.; Wu, S.; Zhou, M.; Zhang, X.; Zhou, R.; Zhang, T.; Gao, Y.; Chen, T.; Chen, Y., Systematic imaging in medicine: a comprehensive review. *European Journal of Nuclear Medicine and Molecular Imaging* **2021**, 48 (6), 1736-1758.
91. Bond, C.; Santiago-Ruiz, A. N.; Tang, Q.; Lakadamyali, M., Technological advances in super-resolution microscopy to study cellular processes. *Molecular Cell* **2022**, 82 (2), 315-332.

92. Chávez García, D.; Juárez-Moreno, K.; Campos, C. H.; Alderete, J. B.; Hirata, G. A., Functionalized up conversion rare earth nanoparticles for bio imaging of cancer cells. **2017**.
93. Malik, A.; Khan, J. M.; Alhomida, A. S.; Ola, M. S.; Alshehri, M. A.; Ahmad, A., Metal nanoparticles: biomedical applications and their molecular mechanisms of toxicity. *Chemical Papers* **2022**, 1-23.
94. Domingues, C.; Santos, A.; Alvarez-Lorenzo, C.; Concheiro, A.; Jarak, I.; Veiga, F.; Barbosa, I.; Dourado, M.; Figueiras, A., Where Is Nano Today and Where Is It Headed? A Review of Nanomedicine and the Dilemma of Nanotoxicology. *ACS nano* **2022**.
95. Sweeney, A. E., Nanomedicine concepts in the general medical curriculum: initiating a discussion. *International journal of nanomedicine* **2015**, *10*, 7319.
96. Duncan, R.; Kreyling, W.; Biosseau, P.; Cannistraro, S.; Coatrieux, J.; Conde, J.; Hennick, W.; Oberleithner, H.; Rivas, J., ESF scientific forward look on nanomedicine. *Eur. Sci. Found. Policy Brief* **2005**, 1-6.
97. Abdellatif, A. A.; Mohammed, H. A.; Khan, R. A.; Singh, V.; Bouazzaoui, A.; Yusuf, M.; Akhtar, N.; Khan, M.; Al-Subaiyel, A.; Mohammed, S. A., Nano-scale delivery: A comprehensive review of nano-structured devices, preparative techniques, site-specificity designs, biomedical applications, commercial products, and references to safety, cellular uptake, and organ toxicity. *Nanotechnology Reviews* **2021**, *10* (1), 1493-1559.
98. Fadeel, B.; Alexiou, C., Brave new world revisited: Focus on nanomedicine. *Biochemical and Biophysical Research Communications* **2020**.
99. Bayda, S.; Adeel, M.; Tuccinardi, T.; Cordani, M.; Rizzolio, F., The history of nanoscience and nanotechnology: From chemical–physical applications to nanomedicine. *Molecules* **2019**, *25* (1), 112.
100. Zhao, H.; Wang, Y.; Bao, L.; Chen, C., Engineering Nano–Bio Interfaces from Nanomaterials to Nanomedicines. *Accounts of Materials Research* **2022**.
101. Zhang, W.; Taheri-Ledari, R.; Ganjali, F.; Afruzi, F. H.; Hajizadeh, Z.; Saeidirad, M.; Qazi, F. S.; Kashtiaray, A.; Sehat, S. S.; Hamblin, M. R., Nanoscale Bioconjugates: A review of the structural attributes of drug-loaded nanocarrier conjugates for selective cancer therapy. *Heliyon* **2022**, e09577.
102. Sindhwani, S.; Chan, W. C., Nanotechnology for modern medicine: next step towards clinical translation. *Journal of internal medicine* **2021**, *290* (3), 486-498.
103. Sanner, M. F.; Stolz, M.; Burkhard, P.; Kong, X.-P.; Min, G.; Sun, T.-T.; Driamov, S.; Aebi, U.; Stoffler, D., Visualizing nature at work from the nano to the macro scale. *NanoBiotechnology* **2005**, *1* (1), 7-21.
104. Khan, S.; Mansoor, S.; Rafi, Z.; Kumari, B.; Shoaib, A.; Saeed, M.; Alshehri, S.; Ghoneim, M. M.; Rahamathulla, M.; Hani, U., A review on nanotechnology: Properties, applications, and mechanistic insights of cellular uptake mechanisms. *Journal of Molecular Liquids* **2021**, 118008.
105. Siddique, S.; Chow, J. C., Application of Nanomaterials in Biomedical Imaging and Cancer Therapy. *Nanomaterials* **2020**, *10* (9), 1700.

106. Wang, Z.; Han, Q.; Zhao, X.; Xie, X.; Wang, Z.; Lin, J.; Xing, B., Near-infrared photocontrolled therapeutic release via upconversion nanocomposites. *Journal of Controlled Release* **2020**.
107. Tan, G. R.; Wang, M.; Hsu, C. Y.; Chen, N.; Zhang, Y., Small Upconverting Fluorescent Nanoparticles for Biosensing and Bioimaging. *Advanced Optical Materials* **2016**, *4* (7), 984-997.
108. Lv, R.; Raab, M.; Wang, Y.; Tian, J.; Lin, J.; Prasad, P. N., Nanochemistry advancing photon conversion in rare-earth nanostructures for theranostics. *Coordination Chemistry Reviews* **2022**, *460*, 214486.
109. Freise, A. C.; Wu, A. M., In vivo imaging with antibodies and engineered fragments. *Molecular immunology* **2015**, *67* (2), 142-152.
110. Singh, G.; Gott, M.; Pietzsch, H.-J.; Stephan, H., Nuclear and optical dual-labelled imaging agents. *Nuklearmedizin* **2016**, *55* (02), 41-50.
111. Wan, H.; Du, H.; Wang, F.; Dai, H., Molecular Imaging in the Second Near - Infrared Window. *Advanced Functional Materials* **2019**, *29* (25), 1900566.
112. Lee, H.; Kim, J.; Kim, H.-H.; Kim, C.-S.; Kim, J., Review on Optical Imaging Techniques for Multispectral Analysis of Nanomaterials. *Nanotheranostics* **2022**, *6* (1), 50-61.
113. Suárez, P. L.; García-Cortés, M.; Fernández-Argüelles, M. T.; Encinar, J. R.; Valledor, M.; Ferrero, F. J.; Campo, J. C.; Costa-Fernández, J. M. J. A. c. a., Functionalized phosphorescent nanoparticles in (bio) chemical sensing and imaging—a review. **2019**, *1046*, 16-31.
114. Khair - Fernández, N.; Macicior, J.; Marcos - Ramiro, B.; Ortega - Gutiérrez, S., Chemistry for the Identification of Therapeutic Targets: Recent Advances and Future Directions. *European Journal of Organic Chemistry* **2021**, *2021* (9), 1307-1320.
115. Reineck, P.; Gibson, B. C., Near-Infrared Fluorescent Nanomaterials for Bioimaging and Sensing. *Advanced Optical Materials* **2017**, *5* (2).
116. Conde, J.; Dias, J. T.; Grazú, V.; Moros, M.; Baptista, P. V.; de la Fuente, J. M., Revisiting 30 years of biofunctionalization and surface chemistry of inorganic nanoparticles for nanomedicine. *Frontiers in chemistry* **2014**, *2*, 48.
117. Wei, P.; Wang, Q.; Yi, T., From Fluorescent Probes to the Theranostics Platform. *Chinese Journal of Chemistry* **2022**, *40* (16), 1964-1974.
118. Zhu, H.; Fan, J.; Du, J.; Peng, X., Fluorescent probes for sensing and imaging within specific cellular organelles. *Accounts of Chemical Research* **2016**, *49* (10), 2115-2126.
119. Liu, Z.; Liu, J.; Wang, X.; Mi, F.; Wang, D.; Wu, C., Fluorescent Bioconjugates for Super-Resolution Optical Nanoscopy. *Bioconjugate Chemistry* **2020**, *31* (8), 1857-1872.
120. Sun, X.; Li, Y.; Liu, T.; Li, Z.; Zhang, X.; Chen, X., Peptide-based imaging agents for cancer detection. *Advanced drug delivery reviews* **2017**, *110*, 38-51.

121. Chen, Z.-Y.; Wang, Y.-X.; Lin, Y.; Zhang, J.-S.; Yang, F.; Zhou, Q.-L.; Liao, Y.-Y., Advance of molecular imaging technology and targeted imaging agent in imaging and therapy. *BioMed research international* **2014**, 2014.
122. Wang, W.; Mattoussi, H., Engineering the Bio–Nano Interface Using a Multifunctional Coordinating Polymer Coating. *Accounts of Chemical Research* **2020**.
123. Wen, S.; Zhou, J.; Zheng, K.; Bednarkiewicz, A.; Liu, X.; Jin, D., Advances in highly doped upconversion nanoparticles. *Nat Commun* **2018**, 9 (1), 2415.
124. Liao, J.; Yang, L.; Wu, S.; Yang, Z.; Zhou, J.; Jin, D.; Guan, M., NIR-II emissive properties of 808 nm-excited lanthanide-doped nanoparticles for multiplexed in vivo imaging. *Journal of Luminescence* **2022**, 242, 118597.
125. May, P. B.; Suter, J. D.; May, P. S.; Berry, M. T., The dynamics of nanoparticle growth and phase change during synthesis of  $\beta$ -NaYF<sub>4</sub>. *The Journal of Physical Chemistry C* **2016**, 120 (17), 9482-9489.
126. Wang, F.; Liu, X., Recent advances in the chemistry of lanthanide-doped upconversion nanocrystals. *Chemical Society Reviews* **2009**, 38 (4), 976-989.
127. Ma, C.; Xu, X.; Wang, F.; Zhou, Z.; Liu, D.; Zhao, J.; Guan, M.; Lang, C. I.; Jin, D., Optimal sensitizer concentration in single upconversion nanocrystals. *Nano letters* **2017**, 17 (5), 2858-2864.
128. Jurga, N.; Przybylska, D.; Kamiński, P.; Grzyb, T., Improvement of ligand-free modification strategy to obtain water-stable up-converting nanoparticles with bright emission and high reaction yield. *Scientific reports* **2021**, 11 (1), 1-10.
129. Kostiv, U.; Farka, Z. k.; Mickert, M. J.; Gorris, H. H.; Velychkivska, N.; Pop-Georgievski, O.; Pastucha, M. j.; Odstrčil kov , E. k.; Skládal, P.; Horák, D., Versatile bioconjugation strategies of PEG-modified upconversion nanoparticles for bioanalytical applications. *Biomacromolecules* **2020**, 21 (11), 4502-4513.
130. Andresen, E.; Resch-Genger, U.; Sch ferling, M., Surface modifications for photon-Upconversion-based energy-transfer Nanoprobes. *Langmuir* **2019**, 35 (15), 5093-5113.
131. Zheng, B.; Fan, J.; Chen, B.; Qin, X.; Wang, J.; Wang, F.; Deng, R.; Liu, X., Rare-Earth Doping in Nanostructured Inorganic Materials. *Chemical Reviews* **2022**.
132. Pawade, V.; Pawar, N.; Dhoble, S., Upconversion in Some Fluoride Crystal System–A Review. *Infrared Physics & Technology* **2022**, 104148.
133. Tu, D.; Liu, Y.; Zhu, H.; Li, R.; Liu, L.; Chen, X., Breakdown of crystallographic site symmetry in lanthanide - doped NaYF<sub>4</sub> crystals. *Angewandte Chemie* **2013**, 125 (4), 1166-1171.
134. Radunz, S.; Schavkan, A.; Wahl, S.; Würth, C.; Tschiche, H. R.; Krumrey, M.; Resch-Genger, U., Evolution of size and optical properties of upconverting nanoparticles during high-temperature synthesis. *The Journal of Physical Chemistry C* **2018**, 122 (50), 28958-28967.
135. Chen, G.; Qiu, H.; Prasad, P. N.; Chen, X. J. C. r., Upconversion nanoparticles: design, nanochemistry, and applications in theranostics. **2014**, 114 (10), 5161-5214.

136. Xu, S.; Huang, S.; He, Q.; Wang, L., Upconversion nanophosphores for bioimaging. *TrAC Trends in Analytical Chemistry* **2015**, *66*, 72-79.
137. Bhattacharjee, S., DLS and zeta potential—what they are and what they are not? *Journal of controlled release* **2016**, *235*, 337-351.
138. Modena, M. M.; Ruhle, B.; Burg, T. P.; Wuttke, S., Nanoparticle Characterization: What to Measure? *Adv Mater* **2019**, *31* (32), e1901556.
139. Sanita, G.; Carrese, B.; Lamberti, A., Nanoparticle Surface Functionalization: How to Improve Biocompatibility and Cellular Internalization. *Front Mol Biosci* **2020**, *7*, 587012.
140. Mudunkotuwa, I. A.; Al Minshid, A.; Grassian, V. H., ATR-FTIR spectroscopy as a tool to probe surface adsorption on nanoparticles at the liquid–solid interface in environmentally and biologically relevant media. *Analyst* **2014**, *139* (5), 870-881.
141. Himmelstoß, S. F.; Hirsch, T., Long - Term Colloidal and Chemical Stability in Aqueous Media of NaYF<sub>4</sub> Type Upconversion Nanoparticles Modified by Ligand - Exchange. *Particle & Particle Systems Characterization* **2019**, *36* (10).
142. Li, Z.; Zhang, Y., An efficient and user-friendly method for the synthesis of hexagonal-phase NaYF<sub>4</sub>: Yb, Er/Tm nanocrystals with controllable shape and upconversion fluorescence. *Nanotechnology* **2008**, *19* (34), 345606.
143. Budijono, S. J.; Shan, J.; Yao, N.; Miura, Y.; Hoye, T.; Austin, R. H.; Ju, Y.; Prud'homme, R. K., Synthesis of stable block-copolymer-protected NaYF<sub>4</sub>: Yb<sup>3+</sup>, Er<sup>3+</sup> up-converting phosphor nanoparticles. *Chemistry of Materials* **2010**, *22* (2), 311-318.
144. Hudry, D.; Howard, I. A.; Popescu, R.; Gerthsen, D.; Richards, B. S., Structure–property relationships in lanthanide - doped upconverting nanocrystals: recent advances in understanding core–shell structures. *Advanced Materials* **2019**, *31* (26), 1900623.
145. Brar, S. K.; Verma, M., Measurement of nanoparticles by light-scattering techniques. *TrAC Trends in Analytical Chemistry* **2011**, *30* (1), 4-17.
146. Hlaček, A.; Farka, Z.; Mickert, M. J.; Kostiv, U.; Brandmeier, J. C.; Horák, D.; Skládal, P.; Foret, F.; Gorris, H. H., Bioconjugates of photon-upconversion nanoparticles for cancer biomarker detection and imaging. *Nature Protocols* **2022**, *17* (4), 1028-1072.
147. de Kanter, M.; Meyer-Kirschner, J.; Viell, J.; Mitsos, A.; Kather, M.; Pich, A.; Janzen, C., Enabling the measurement of particle sizes in stirred colloidal suspensions by embedding dynamic light scattering into an automated probe head. *Measurement* **2016**, *80*, 92-98.
148. Lin, P.-C.; Lin, S.; Wang, P. C.; Sridhar, R., Techniques for physicochemical characterization of nanomaterials. *Biotechnology advances* **2014**, *32* (4), 711-726.
149. Liu, X.; Deng, R.; Zhang, Y.; Wang, Y.; Chang, H.; Huang, L.; Liu, X., Probing the nature of upconversion nanocrystals: instrumentation matters. *Chemical Society Reviews* **2015**, *44* (6), 1479-1508.



150. Zhu, X.; Zhang, J.; Liu, J.; Zhang, Y., Recent Progress of Rare - Earth Doped Upconversion Nanoparticles: Synthesis, Optimization, and Applications. *Advanced Science* **2019**, *6* (22), 1901358.
151. Gargas, D. J.; Chan, E. M.; Ostrowski, A. D.; Aloni, S.; Altoe, M. V. P.; Barnard, E. S.; Sanii, B.; Urban, J. J.; Milliron, D. J.; Cohen, B. E., Engineering bright sub-10-nm upconverting nanocrystals for single-molecule imaging. *Nature nanotechnology* **2014**, *9* (4), 300-305.
152. Dong, H.; Sun, L. D.; Yan, C. H., Lanthanide-Doped Upconversion Nanoparticles for Super-Resolution Microscopy. *Front Chem* **2020**, *8*, 619377.
153. Wang, Y.; Zheng, K.; Song, S.; Fan, D.; Zhang, H.; Liu, X., Remote manipulation of upconversion luminescence. *Chemical Society Reviews* **2018**, *47* (17), 6473-6485.
154. Li, H.; Wang, X.; Huang, D.; Chen, G., Recent advances of lanthanide-doped upconversion nanoparticles for biological applications. *Nanotechnology* **2020**, *31* (7), 072001.
155. Zheng, X.; Kankala, R. K.; Liu, C.-G.; Wang, S.-B.; Chen, A.-Z.; Zhang, Y., Lanthanides-doped near-infrared active upconversion nanocrystals: Upconversion mechanisms and synthesis. *Coordination Chemistry Reviews* **2021**, 438.
156. Xin, N.; Wei, D.; Zhu, Y.; Yang, M.; Ramakrishna, S.; Lee, O.; Luo, H.; Fan, H., Upconversion nanomaterials: a platform for biosensing, theranostic and photoregulation. *Materials Today Chemistry* **2020**, *17*, 100329.
157. Jia, F.; Li, G.; Yang, B.; Yu, B.; Shen, Y.; Cong, H., Investigation of rare earth upconversion fluorescent nanoparticles in biomedical field. *Nanotechnology Reviews* **2019**, *8* (1), 1-17.
158. Smith, A. M.; Johnston, K. A.; Crawford, S. E.; Marbella, L. E.; Millstone, J. E., Ligand density quantification on colloidal inorganic nanoparticles. *Analyst* **2016**, *142* (1), 11-29.
159. Lunardi, C. N.; Gomes, A. J.; Rocha, F. S.; De Tommaso, J.; Patience, G. S., Experimental methods in chemical engineering: Zeta potential. *The Canadian Journal of Chemical Engineering* **2021**, *99* (3), 627-639.
160. Kamble, S.; Agrawal, S.; Cherumukkil, S.; Sharma, V.; Jasra, R. V.; Munshi, P., Revisiting Zeta Potential, the Key Feature of Interfacial Phenomena, with Applications and Recent Advancements. *ChemistrySelect* **2022**, *7* (1), e202103084.
161. Pedota, M.; Machesky, M. L.; Wesolowski, D. J., Molecular origins of the zeta potential. *Langmuir* **2016**, *32* (40), 10189-10198.
162. Pochapski, D. J.; Carvalho dos Santos, C.; Leite, G. W.; Pulcinelli, S. H.; Santilli, C. V., Zeta potential and colloidal stability predictions for inorganic nanoparticle dispersions: Effects of experimental conditions and electrokinetic models on the interpretation of results. *Langmuir* **2021**, *37* (45), 13379-13389.
163. Jayawardena, H. S. N.; Liyanage, S. H.; Rathnayake, K.; Patel, U.; Yan, M., Analytical methods for characterization of nanomaterial surfaces. *Analytical chemistry* **2021**, *93* (4), 1889-1911.

164. Kamiya, H.; Iijima, M., Surface modification and characterization for dispersion stability of inorganic nanometer-scaled particles in liquid media. *Science and Technology of Advanced Materials* **2010**.
165. Huang, B.; Yang, Z.; Fang, S.; Li, Y.; Zhong, Z.; Zheng, R.; Zhang, J.; Wang, H.; Wang, S.; Zou, Q., Amphoteric natural starch-coated polymer nanoparticles with excellent protein corona-free and targeting properties. *Nanoscale* **2020**, *12* (10), 5834-5847.
166. Li, B.; Jain, P.; Ma, J.; Smith, J. K.; Yuan, Z.; Hung, H.-C.; He, Y.; Lin, X.; Wu, K.; Pfaendtner, J., Trimethylamine N-oxide-derived zwitterionic polymers: A new class of ultralow fouling bioinspired materials. *Science advances* **2019**, *5* (6), eaaw9562.
167. Sanchez-Cano, C.; Carril, M., Recent Developments in the Design of Non-Biofouling Coatings for Nanoparticles and Surfaces. *International Journal of Molecular Sciences* **2020**, *21* (3), 1007.
168. Gee, A.; Xu, X., Surface functionalisation of upconversion nanoparticles with different moieties for biomedical applications. *Surfaces* **2018**, *1* (1), 96-121.
169. Sedlmeier, A.; Gorris, H. H. J. C. S. R., Surface modification and characterization of photon-upconverting nanoparticles for bioanalytical applications. **2015**, *44* (6), 1526-1560.
170. Chan, W. C., Nanomedicine 2.0. *Accounts of chemical research* **2017**, *50* (3), 627-632.
171. Donahue, N. D.; Acar, H.; Wilhelm, S. J. A. d. d. r., Concepts of nanoparticle cellular uptake, intracellular trafficking, and kinetics in nanomedicine. **2019**, *143*, 68-96.
172. Jiang, Z.; He, H.; Liu, H.; Thayumanavan, S., Cellular Uptake Evaluation of Amphiphilic Polymer Assemblies: Importance of Interplay between Pharmacological and Genetic Approaches. *Biomacromolecules* **2019**.
173. Zhou, T.; Zhu, Y.; Li, X.; Liu, X.; Yeung, K. W. K.; Wu, S.; Wang, X.; Cui, Z.; Yang, X.; Chu, P. K., Surface functionalization of biomaterials by radical polymerization. *Progress in Materials Science* **2016**, *83*, 191-235.
174. Sun, J.; Ma, Q.; Xue, D.; Shan, W.; Liu, R.; Dong, B.; Zhang, J.; Wang, Z.; Shao, B., Polymer/inorganic nanohybrids: An attractive materials for analysis and sensing. *TrAC Trends in Analytical Chemistry* **2021**, *140*.
175. Nsubuga, A.; Sgarzi, M.; Zarschler, K.; Kubeil, M.; Hübner, R.; Steudtner, R.; Graham, B.; Joshi, T.; Stephan, H., Facile preparation of multifunctionalisable 'stealth'upconverting nanoparticles for biomedical applications. *Dalton Transactions* **2018**, *47* (26), 8595-8604.
176. Raliya, R.; Singh Chadha, T.; Haddad, K.; Biswas, P., Perspective on nanoparticle technology for biomedical use. *Current pharmaceutical design* **2016**, *22* (17), 2481-2490.
177. Albanese, A.; Tang, P. S.; Chan, W. C., The effect of nanoparticle size, shape, and surface chemistry on biological systems. *Annual review of biomedical engineering* **2012**, *14*, 1-16.
178. Foroozandeh, P.; Aziz, A. A., Insight into cellular uptake and intracellular trafficking of nanoparticles. *Nanoscale research letters* **2018**, *13* (1), 339.

179. Chen, G.; Qiu, H.; Prasad, P. N.; Chen, X., Upconversion nanoparticles: design, nanochemistry, and applications in theranostics. *Chem Rev* **2014**, *114* (10), 5161-214.
180. Grubbs, R. B., Roles of polymer ligands in nanoparticle stabilization. *Polymer Reviews* **2007**, *47* (2), 197-215.
181. Duan, C.; Liang, L.; Li, L.; Zhang, R.; Xu, Z. P., Recent progress in upconversion luminescence nanomaterials for biomedical applications. *J Mater Chem B* **2018**, *6* (2), 192-209.
182. Grebenik, E. A.; Kostyuk, A. B.; Deyev, S. M., Upconversion nanoparticles and their hybrid assemblies for biomedical applications. *Russian Chemical Reviews* **2016**, *85* (12), 1277.
183. Kostiv, U.; Farka, Z.; Mickert, M. J.; Gorris, H. H.; Velychkivska, N.; Pop-Georgievski, O.; Pastucha, M.; Odstreilikova, E.; Skladal, P.; Horak, D., Versatile Bioconjugation Strategies of PEG-Modified Upconversion Nanoparticles for Bioanalytical Applications. *Biomacromolecules* **2020**, *21* (11), 4502-4513.
184. Das, G. K.; Stark, D. T.; Kennedy, I. M., Potential toxicity of up-converting nanoparticles encapsulated with a bilayer formed by ligand attraction. *Langmuir* **2014**, *30* (27), 8167-8176.
185. Pearson, R. G., Hard and soft acids and bases. *Journal of the American Chemical society* **1963**, *85* (22), 3533-3539.
186. Sun, H.; Kabb, C. P.; Sims, M. B.; Sumerlin, B. S. J. P. i. P. S., Architecture-transformable polymers: Reshaping the future of stimuli-responsive polymers. **2019**, *89*, 61-75.
187. Peng, W.; Cai, Y.; Fanslau, L.; Vana, P., Nanoengineering with RAFT polymers: From nanocomposite design to applications. *Polymer Chemistry* **2021**.
188. Gao, Y.; Wei, M.; Li, X.; Xu, W.; Ahiabu, A.; Perdiz, J.; Liu, Z.; Serpe, M. J., Stimuli-responsive polymers: Fundamental considerations and applications. *Macromolecular Research* **2017**, *25* (6), 513-527.
189. Lutz, J.-F.; Lehn, J.-M.; Meijer, E.; Matyjaszewski, K., From precision polymers to complex materials and systems. *Nature Reviews Materials* **2016**, *1* (5), 1-14.
190. Matyjaszewski, K.; Müller, A. H., *Controlled and living polymerizations: from mechanisms to applications*. John Wiley & Sons: 2009.
191. Russell, A. J.; Baker, S. L.; Colina, C. M.; Figg, C. A.; Kaar, J. L.; Matyjaszewski, K.; Simakova, A.; Sumerlin, B. S., Next generation protein - polymer conjugates. *AIChE Journal* **2018**, *64* (9), 3230-3245.
192. Pearson, S.; St Thomas, C.; Guerrero-Santos, R.; d'Agosto, F., Opportunities for dual RDRP agents in synthesizing novel polymeric materials. *Polymer Chemistry* **2017**, *8* (34), 4916-4946.
193. Tian, X.; Ding, J.; Zhang, B.; Qiu, F.; Zhuang, X.; Chen, Y., Recent Advances in RAFT Polymerization: Novel Initiation Mechanisms and Optoelectronic Applications. *Polymers (Basel)* **2018**, *10* (3).

194. Perrier, S.; Takolpuckdee, P., Macromolecular design via reversible addition–fragmentation chain transfer (RAFT)/xanthates (MADIX) polymerization. *Journal of Polymer Science Part A: Polymer Chemistry* **2005**, *43* (22), 5347-5393.
195. Garni, M.; Wehr, R.; Avsar, S. Y.; John, C.; Palivan, C.; Meier, W., Polymer membranes as templates for bio-applications ranging from artificial cells to active surfaces. *European Polymer Journal* **2019**, *112*, 346-364.
196. Tawfik, S. M.; Elmasry, M. R.; Lee, Y.-I., Recent advances on amphiphilic polymer-based fluorescence spectroscopic techniques for sensing and imaging. *Applied Spectroscopy Reviews* **2019**, *54* (3), 204-236.
197. Keddie, D. J.; Moad, G.; Rizzardo, E.; Thang, S. H. J. M., RAFT agent design and synthesis. **2012**, *45* (13), 5321-5342.
198. Sun, W.; Liu, W.; Wu, Z.; Chen, H., Chemical Surface Modification of Polymeric Biomaterials for Biomedical Applications. *Macromol Rapid Commun* **2020**, *41* (8), e1900430.
199. Moad, G.; Rizzardo, E.; Thang, S. H., Living Radical Polymerization by the RAFT Process – A Third Update. *Australian Journal of Chemistry* **2012**, *65* (8).
200. Perrier, S., 50th Anniversary Perspective: RAFT Polymerization—A User Guide. *Macromolecules* **2017**, *50* (19), 7433-7447.
201. Wang, M.; Jiang, X.; Luo, Y.; Zhang, L.; Cheng, Z.; Zhu, X., Facile synthesis of poly (vinyl acetate)-b-polystyrene copolymers mediated by an iniferter agent using a single methodology. *Polymer Chemistry* **2017**, *8* (38), 5918-5923.
202. Gökteş, M., Synthesis and characterization of temperature-responsive block copolymers using macromonomeric initiator. *Chemical Papers* **2020**, 1-11.
203. An, Z., 100th Anniversary of Macromolecular Science Viewpoint: Achieving Ultrahigh Molecular Weights with Reversible Deactivation Radical Polymerization. *ACS Macro Letters* **2020**, *9*, 350-357.
204. Hortigüela, V.; Larrañaga, E.; Lagunas, A.; Acosta, G. A.; Albericio, F.; Andilla, J.; Loza-Alvarez, P.; Martínez, E., Large-area biomolecule nanopatterns on diblock copolymer surfaces for cell adhesion studies. *Nanomaterials* **2019**, *9* (4), 579.
205. Chiefari, J.; Chong, Y.; Ercole, F.; Krstina, J.; Jeffery, J.; Le, T. P.; Mayadunne, R. T.; Meijs, G. F.; Moad, C. L.; Moad, G., Living free-radical polymerization by reversible addition–fragmentation chain transfer: the RAFT process. *Macromolecules* **1998**, *31* (16), 5559-5562.
206. Montoya-Villegas, K. A.; Licea-Claverie, Á.; Zapata-González, I.; Gómez, E.; Ramírez-Jiménez, A., The effect in the RAFT polymerization of two oligo (ethylene glycol) methacrylates when the CTA 4-cyano-4-(propylthiocarbonothioylthio) pentanoic acid is auto-hydrolyzed to its corresponding amide. *Journal of Polymer Research* **2019**, *26* (3), 71.
207. Tian, Y.; Zhou, S., Advances in cell penetrating peptides and their functionalization of polymeric nanoplateforms for drug delivery. *Wiley Interdiscip Rev Nanomed Nanobiotechnol* **2021**, *13* (2), e1668.

208. Nothling, M. D.; Fu, Q.; Reyhani, A.; Allison - Logan, S.; Jung, K.; Zhu, J.; Kamigaito, M.; Boyer, C.; Qiao, G. G., Progress and perspectives beyond traditional RAFT polymerization. *Advanced Science* **2020**, *7* (20), 2001656.
209. Wanasinghe, S. V.; Sun, M.; Yehl, K.; Cuthbert, J.; Matyjaszewski, K.; Konkolewicz, D., PET-RAFT Increases Uniformity in Polymer Networks. *ACS Macro Letters* **2022**, *11* (9), 1156-1161.
210. Allegrezza, M. L.; Konkolewicz, D., PET-RAFT Polymerization: Mechanistic Perspectives for Future Materials. *ACS Macro Letters* **2021**, *10* (4), 433-446.
211. Bingham, N. M.; Abousalman-Rezvani, Z.; Collins, K.; Roth, P. J., Thiocarbonyl chemistry in polymer science. *Polymer Chemistry* **2022**, *13* (20), 2880-2901.
212. Perrier, S. b. J. M., 50th Anniversary Perspective: RAFT Polymerization • A User Guide. **2017**, *50* (19), 7433-7447.
213. Feng, H.; Lu, X.; Wang, W.; Kang, N.-G.; Mays, J. W., Block copolymers: Synthesis, self-assembly, and applications. *Polymers* **2017**, *9* (10), 494.
214. Xia, X.; Rossi, J. J., RAFTing Towards the Shore of Nanotherapeutic. *Current Drug Delivery* **2018**, *15* (8), 1084-1086.
215. Barner-Kowollik, C., *Handbook of RAFT polymerization*. John Wiley & Sons: 2008.
216. Opiyo, G.; Jin, J., Recent progress in switchable RAFT agents: Design, synthesis and application. *European Polymer Journal* **2021**, *159*, 110713.
217. McKenzie, T. G.; Fu, Q.; Wong, E. H.; Dunstan, D. E.; Qiao, G. G., Visible light mediated controlled radical polymerization in the absence of exogenous radical sources or catalysts. *Macromolecules* **2015**, *48* (12), 3864-3872.
218. Corrigan, N.; Jung, K.; Moad, G.; Hawker, C. J.; Matyjaszewski, K.; Boyer, C., Reversible-deactivation radical polymerization (Controlled/living radical polymerization): From discovery to materials design and applications. *Progress in Polymer Science* **2020**, *111*.
219. Self, J. L.; Zervoudakis, A. J.; Peng, X.; Lenart, W. R.; Macosko, C. W.; Ellison, C. J., Linear, Graft, and Beyond: Multiblock Copolymers as Next-Generation Compatibilizers. *JACS Au* **2022**, *2* (2), 310-321.
220. Moad, G.; Rizzardo, E.; Thang, S. H., Living radical polymerization by the RAFT process—a first update. *Australian Journal of Chemistry* **2006**, *59* (10), 669-692.
221. Meiser, W., Investigation of the Kinetics and Mechanism of RAFT Polymerization via EPR Spectroscopy. **2013**.
222. Yang, R.; Wang, X.; Yan, S.; Dong, A.; Luan, S.; Yin, J., Advances in design and biomedical application of hierarchical polymer brushes. *Progress in Polymer Science* **2021**, *118*.
223. Duong, H. T. T.; Chen, Y.; Tawfik, S. A.; Wen, S.; Parviz, M.; Shimoni, O.; Jin, D., Systematic investigation of functional ligands for colloidal stable upconversion nanoparticles. *RSC Advances* **2018**, *8* (9), 4842-4849.

224. Li, D.; Xu, L.; Wang, J.; Gautrot, J. E., Responsive Polymer Brush Design and Emerging Applications for Nanotheranostics. *Advanced Healthcare Materials* **2020**, 2000953.
225. Semsarilar, M.; Abetz, V., Polymerizations by RAFT: Developments of the Technique and Its Application in the Synthesis of Tailored (Co)polymers. *Macromolecular Chemistry and Physics* **2020**, 222 (1).
226. Jeong, W.-j.; Bu, J.; Kubiawicz, L. J.; Chen, S. S.; Kim, Y.; Hong, S., Peptide-nanoparticle conjugates: a next generation of diagnostic and therapeutic platforms? *Nano convergence* **2018**, 5 (1), 38.
227. Zein, R.; Sharrouf, W.; Selting, K., Physical Properties of Nanoparticles That Result in Improved Cancer Targeting. *J Oncol* **2020**, 2020, 5194780.
228. Wu, A.; Gao, Y.; Zheng, L., Zwitterionic amphiphiles: their aggregation behavior and applications. *Green Chemistry* **2019**, 21 (16), 4290-4312.
229. Yao, X.; Qi, C.; Sun, C.; Huo, F.; Jiang, X., Poly (ethylene glycol) alternatives in biomedical applications. *Nano Today* **2023**, 48, 101738.
230. Cao, Z.; Jiang, S., Super-hydrophilic zwitterionic poly (carboxybetaine) and amphiphilic non-ionic poly (ethylene glycol) for stealth nanoparticles. *Nano Today* **2012**, 7 (5), 404-413.
231. Guerrini, L.; Alvarez-Puebla, R. A.; Pazos-Perez, N. J. M., Surface modifications of nanoparticles for stability in biological fluids. **2018**, 11 (7), 1154.
232. Schubert, J.; Chanana, M., Coating matters: Review on colloidal stability of nanoparticles with biocompatible coatings in biological media, living cells and organisms. *Current Medicinal Chemistry* **2019**, 25 (35), 4556.
233. Paschke, S.; Lienkamp, K., Polyzwitterions: From Surface Properties and Bioactivity Profiles to Biomedical Applications. *ACS Applied Polymer Materials* **2020**, 2 (2), 129-151.
234. Li, Z.; Wang, Y.; Zhu, J.; Zhang, Y.; Zhang, W.; Zhou, M.; Luo, C.; Li, Z.; Cai, B.; Gui, S.; He, Z.; Sun, J., Emerging well-tailored nanoparticulate delivery system based on in situ regulation of the protein corona. *J Control Release* **2020**, 320, 1-18.
235. Ladd, J.; Zhang, Z.; Chen, S.; Hower, J. C.; Jiang, S., Zwitterionic polymers exhibiting high resistance to nonspecific protein adsorption from human serum and plasma. *Biomacromolecules* **2008**, 9 (5), 1357-1361.
236. Mahmoudi, M.; Bertrand, N.; Zope, H.; Farokhzad, O. C., Emerging understanding of the protein corona at the nano-bio interfaces. *Nano Today* **2016**, 11 (6), 817-832.
237. Gao, S.; Guisan, J. M.; Rocha-Martin, J., Oriented immobilization of antibodies onto sensing platforms - A critical review. *Anal Chim Acta* **2022**, 1189, 338907.
238. Sapsford, K. E.; Algar, W. R.; Berti, L.; Gemmill, K. B.; Casey, B. J.; Oh, E.; Stewart, M. H.; Medintz, I. L., Functionalizing nanoparticles with biological molecules: developing chemistries that facilitate nanotechnology. *Chem Rev* **2013**, 113 (3), 1904-2074.
239. Korde, J. M.; Kandasubramanian, B., Fundamentals and effects of biomimicking stimuli-responsive polymers for engineering functions. *Industrial & Engineering Chemistry Research* **2019**, 58 (23), 9709-9757.

240. Cupic, K. I.; Rennick, J. J.; Johnston, A. P.; Such, G. K., Controlling endosomal escape using nanoparticle composition: current progress and future perspectives. *Nanomedicine* **2019**, *14* (2), 215-223.
241. Mout, R.; Moyano, D. F.; Rana, S.; Rotello, V. M., Surface functionalization of nanoparticles for nanomedicine. *Chemical Society Reviews* **2012**, *41* (7), 2539-2544.
242. Delille, F.; Pu, Y.; Lequeux, N.; Pons, T., Designing the Surface Chemistry of Inorganic Nanocrystals for Cancer Imaging and Therapy. *Cancers* **2022**, *14* (10), 2456.
243. Yadav, D.; Dewangan, H. K., PEGYLATION: an important approach for novel drug delivery system. *Journal of Biomaterials Science, Polymer Edition* **2021**, *32* (2), 266-280.
244. Harris, J. M.; Chess, R. B., Effect of pegylation on pharmaceuticals. *Nature reviews Drug discovery* **2003**, *2* (3), 214-221.
245. Huang, X.; Hu, J.; Li, Y.; Xin, F.; Qiao, R.; Davis, T. P., Engineering Organic/Inorganic Nanohybrids through RAFT Polymerization for Biomedical Applications. *Biomacromolecules* **2019**, *20* (12), 4243-4257.
246. Zheng, L.; Sundaram, H. S.; Wei, Z.; Li, C.; Yuan, Z. J. R.; Polymers, F., Applications of zwitterionic polymers. **2017**, *118*, 51-61.
247. Cui, J.; Ding, F.; Yang, S.; Gao, Z.; Guo, J.; Zhang, P.; Qiu, X.; Li, Q.; Dong, M.; Hao, J., Antifouling and pH-responsive poly (carboxybetaine)-based nanoparticles for tumor cell targeting. *Frontiers in Chemistry* **2019**, *7*, 770.
248. Lin, P.; Ding, L.; Lin, C.-W.; Gu, F., Nonfouling property of zwitterionic cysteine surface. *Langmuir* **2014**, *30* (22), 6497-6507.
249. Li, M.; Zhuang, B.; Yu, J., Functional Zwitterionic Polymers on the Surface: Structures and Applications. *Chemistry—An Asian Journal* **2020**.
250. Erfani, A.; Seaberg, J.; Aichele, C. P.; Ramsey, J. D., Interactions between biomolecules and zwitterionic moieties: a review. *Biomacromolecules* **2020**.
251. Bhuchar, N.; Deng, Z.; Ishihara, K.; Narain, R., Detailed study of the reversible addition–fragmentation chain transfer polymerization and co-polymerization of 2-methacryloyloxyethyl phosphorylcholine. *Polymer Chemistry* **2011**, *2* (3), 632-639.
252. Leng, C.; Sun, S.; Zhang, K.; Jiang, S.; Chen, Z., Molecular level studies on interfacial hydration of zwitterionic and other antifouling polymers in situ. *Acta Biomaterialia* **2016**, *40*, 6-15.
253. Shrestha, S.; Wang, B.; Dutta, P., Nanoparticle processing: Understanding and controlling aggregation. *Adv Colloid Interface Sci* **2020**, *279*, 102162.
254. Yao, C.; Wang, P.; Zhou, L.; Wang, R.; Li, X.; Zhao, D.; Zhang, F. J. A. c., Highly biocompatible zwitterionic phospholipids coated upconversion nanoparticles for efficient bioimaging. **2014**, *86* (19), 9749-9757.
255. Liu, N.; Tang, M.; Ding, J., The interaction between nanoparticles-protein corona complex and cells and its toxic effect on cells. *Chemosphere* **2020**, *245*, 125624.

256. Kojima, C.; Katayama, R.; Nguyen, T. L.; Oki, Y.; Tsujimoto, A.; Yusa, S.-i.; Shiraishi, K.; Matsumoto, A., Different Antifouling Effects of Random and Block Copolymers Comprising 2-Methacryloyloxyethyl Phosphorylcholine and Dodecyl Methacrylate. *European Polymer Journal* **2020**, 109932.
257. Wolfram, J.; Yang, Y.; Shen, J.; Moten, A.; Chen, C.; Shen, H.; Ferrari, M.; Zhao, Y., The nano-plasma interface: Implications of the protein corona. *Colloids and surfaces B: biointerfaces* **2014**, *124*, 17-24.
258. Wang, L.; Dai, W.; Yang, M.; Wei, X.; Ma, K.; Song, B.; Jia, P.; Gong, Y.; Yang, J.; Zhao, J., Cell membrane mimetic copolymer coated polydopamine nanoparticles for combined pH-sensitive drug release and near-infrared photothermal therapeutic. *Colloids and Surfaces B: Biointerfaces* **2019**, *176*, 1-8.
259. Ma, S.; Zhang, X.; Yu, B.; Zhou, F., Brushing up functional materials. *NPG Asia Materials* **2019**, *11* (1), 1-39.
260. Li, J.; Mao, H.; Kawazoe, N.; Chen, G., Insight into the interactions between nanoparticles and cells. *Biomater Sci* **2017**, *5* (2), 173-189.
261. Zoppe, J. O.; Ataman, N. C.; Mocny, P.; Wang, J.; Moraes, J.; Klok, H. A., Surface-Initiated Controlled Radical Polymerization: State-of-the-Art, Opportunities, and Challenges in Surface and Interface Engineering with Polymer Brushes. *Chem Rev* **2017**, *117* (3), 1105-1318.
262. Wieszczycka, K.; Staszak, K.; Woźniak-Budych, M. J.; Litowczenko, J.; Maciejewska, B. M.; Jurga, S., Surface functionalization – The way for advanced applications of smart materials. *Coordination Chemistry Reviews* **2021**, 436.
263. Kobayashi, K.; Wei, J.; Iida, R.; Ijiro, K.; Niikura, K., Surface engineering of nanoparticles for therapeutic applications. *Polymer journal* **2014**, *46* (8), 460-468.
264. Wright, T. A.; Page, R. C.; Konkolewicz, D., Polymer conjugation of proteins as a synthetic post-translational modification to impact their stability and activity. *Polymer chemistry* **2019**, *10* (4), 434-454.
265. Kang, T.; Li, F.; Baik, S.; Shao, W.; Ling, D.; Hyeon, T., Surface design of magnetic nanoparticles for stimuli-responsive cancer imaging and therapy. *Biomaterials* **2017**, *136*, 98-114.
266. Thanh, N. T.; Green, L. A., Functionalisation of nanoparticles for biomedical applications. *Nano Today* **2010**, *5* (3), 213-230.
267. Chen, M.; Briscoe, W. H.; Armes, S. P.; Cohen, H.; Klein, J., Polyzwitterionic brushes: Extreme lubrication by design. *European Polymer Journal* **2011**, *47* (4), 511-523.
268. Chakraborty, A.; Dalal, C.; Jana, N. R., Colloidal nanobioconjugate with complementary surface chemistry for cellular and subcellular targeting. *Langmuir* **2018**, *34* (45), 13461-13471.
269. Nel, A. E.; Mädler, L.; Velegol, D.; Xia, T.; Hoek, E. M.; Somasundaran, P.; Klaessig, F.; Castranova, V.; Thompson, M., Understanding biophysicochemical interactions at the nano–bio interface. *Nature materials* **2009**, *8* (7), 543-557.
270. Zhou, B.; Shi, B.; Jin, D.; Liu, X., Controlling upconversion nanocrystals for emerging applications. *Nature nanotechnology* **2015**, *10* (11), 924.



271. Finbloom, J. A.; Sousa, F.; Stevens, M. M.; Desai, T. A., Engineering the drug carrier biointerface to overcome biological barriers to drug delivery. *Advanced Drug Delivery Reviews* **2020**.
272. Tang, Z.; He, C.; Tian, H.; Ding, J.; Hsiao, B. S.; Chu, B.; Chen, X., Polymeric nanostructured materials for biomedical applications. *Progress in Polymer Science* **2016**, *60*, 86-128.
273. Chen, Y.; D'Amario, C.; Gee, A.; Duong, H. T.; Shimoni, O.; Valenzuela, S. M., Dispersion stability and biocompatibility of four ligand-exchanged NaYF<sub>4</sub>: Yb, Er upconversion nanoparticles. *Acta Biomaterialia* **2020**, *102*, 384-393.
274. Ahmad, A.; Khan, J. M.; Haque, S., Strategies in the design of endosomolytic agents for facilitating endosomal escape in nanoparticles. *Biochimie* **2019**.
275. Lim, E.-K.; Kim, T.; Paik, S.; Haam, S.; Huh, Y.-M.; Lee, K., Nanomaterials for theranostics: recent advances and future challenges. *Chemical reviews* **2015**, *115* (1), 327-394.
276. Lin, M.; Zhao, Y.; Wang, S.; Liu, M.; Duan, Z.; Chen, Y.; Li, F.; Xu, F.; Lu, T. J. B. a., Recent advances in synthesis and surface modification of lanthanide-doped upconversion nanoparticles for biomedical applications. **2012**, *30* (6), 1551-1561.
277. Alkilany, A. M.; Zhu, L.; Weller, H.; Mews, A.; Parak, W. J.; Barz, M.; Feliu, N., Ligand density on nanoparticles: A parameter with critical impact on nanomedicine. *Adv Drug Deliv Rev* **2019**, *143*, 22-36.
278. Reuter, K. G.; Perry, J. L.; Kim, D.; Luft, J. C.; Liu, R.; DeSimone, J. M., Targeted PRINT hydrogels: the role of nanoparticle size and ligand density on cell association, biodistribution, and tumor accumulation. *Nano letters* **2015**, *15* (10), 6371-6378.
279. Yuan, H.; Zhang, S., Effects of particle size and ligand density on the kinetics of receptor-mediated endocytosis of nanoparticles. *Applied Physics Letters* **2010**, *96* (3), 033704.
280. Chen, S.; Liang, X.-J., Nanobiotechnology and nanomedicine: small change brings big difference. Springer: 2018.
281. Ramos, A. P.; Cruz, M. A.; Tovani, C. B.; Ciancaglini, P., Biomedical applications of nanotechnology. *Biophysical reviews* **2017**, *9* (2), 79-89.
282. Muthu, M. S.; Leong, D. T.; Mei, L.; Feng, S.-S., Nanotheranostics- application and further development of nanomedicine strategies for advanced theranostics. *Theranostics* **2014**, *4* (6), 660.
283. Ma, X.; Gong, N.; Zhong, L.; Sun, J.; Liang, X.-J., Future of nanotherapeutics: Targeting the cellular sub-organelles. *Biomaterials* **2016**, *97*, 10-21.
284. Zhang, C.; Wu, W.; Li, R. Q.; Qiu, W. X.; Zhuang, Z. N.; Cheng, S. X.; Zhang, X. Z., Peptide - Based Multifunctional Nanomaterials for Tumor Imaging and Therapy. *Advanced Functional Materials* **2018**, *28* (50), 1804492.
285. Thiruppathi, R.; Mishra, S.; Ganapathy, M.; Padmanabhan, P.; Gulyás, B., Nanoparticle functionalization and its potentials for molecular imaging. *Advanced Science* **2017**, *4* (3), 1600279.

286. Ren, W.; Zhou, Y.; Wen, S.; He, H.; Lin, G.; Liu, D.; Jin, D., DNA-mediated anisotropic silica coating of upconversion nanoparticles. *Chemical Communications* **2018**, *54* (52), 7183-7186.
287. Zhang, J.; Cheng, F.; Li, J.; Zhu, J.-J.; Lu, Y., Fluorescent nanoprobe for sensing and imaging of metal ions: Recent advances and future perspectives. *Nano today* **2016**, *11* (3), 309-329.
288. Kim, B. Y.; Rutka, J. T.; Chan, W. C., Nanomedicine. *New England Journal of Medicine* **2010**, *363* (25), 2434-2443.
289. Chan, W. C. W., Nanomedicine 2.0. *Acc Chem Res* **2017**, *50* (3), 627-632.
290. Kuchur, O.; Tsymbal, S.; Shestovskaya, M.; Serov, N.; Dukhinova, M.; Shtil, A., Metal-derived nanoparticles in tumor theranostics: Potential and limitations. *Journal of Inorganic Biochemistry* **2020**, 111117.
291. Rong, L.; Qin, S.-Y.; Zhang, C.; Cheng, Y.-J.; Feng, J.; Wang, S.-B.; Zhang, X.-Z., Biomedical applications of functional peptides in nano-systems. *Materials today chemistry* **2018**, *9*, 91-102.
292. Kurrikoff, K.; Vunk, B.; Langel, Ü., Status Update in the Use of Cell Penetrating Peptides for the Delivery of Macromolecular Therapeutics. *Expert Opinion on Biological Therapy* **2020**.
293. Chou, L. Y.; Ming, K.; Chan, W. C., Strategies for the intracellular delivery of nanoparticles. *Chemical Society Reviews* **2011**, *40* (1), 233-245.
294. Silva, S.; Almeida, A. J.; Vale, N. J. B., Combination of cell-penetrating peptides with nanoparticles for therapeutic application: A review. **2019**, *9* (1), 22.
295. Woythe, L.; Tito, N. B.; Albertazzi, L., A quantitative view on multivalent nanomedicine targeting. *Adv Drug Deliv Rev* **2021**, *169*, 1-21.
296. Selec, M.; Selec, D. A.; Jonczyk, R.; Stahl, F.; Blume, C.; Scheper, T., Smart multifunctional nanoparticles in nanomedicine. *BioNanoMaterials* **2016**, *17* (1-2), 33-41.
297. Valcourt, D. M.; Harris, J.; Riley, R. S.; Dang, M.; Wang, J.; Day, E. S., Advances in targeted nanotherapeutics: From bioconjugation to biomimicry. *Nano Res* **2018**, *11* (10), 4999-5016.
298. Fonseca, S. B.; Pereira, M. P.; Kelley, S. O., Recent advances in the use of cell-penetrating peptides for medical and biological applications. *Advanced drug delivery reviews* **2009**, *61* (11), 953-964.
299. Augustine, R.; Hasan, A.; Primavera, R.; Wilson, R. J.; Thakor, A. S.; Kevadiya, B. D., Cellular uptake and retention of nanoparticles: Insights on particle properties and interaction with cellular components. *Materials Today Communications* **2020**, 101692.
300. Copolovici, D. M.; Langel, K.; Eriste, E.; Langel, U., Cell-penetrating peptides: design, synthesis, and applications. *ACS nano* **2014**, *8* (3), 1972-1994.
301. Pramanik, S. K.; Das, A., Fluorescent probes for imaging bioactive species in subcellular organelles. *Chemical Communications* **2021**, *57* (91), 12058-12073.

302. Habault, J.; Poyet, J.-L., Recent advances in cell penetrating peptide-based anticancer therapies. *Molecules* **2019**, *24* (5), 927.
303. Bohara, R. A.; Thorat, N. D.; Pawar, S. H., Role of functionalization: strategies to explore potential nano-bio applications of magnetic nanoparticles. *RSC advances* **2016**, *6* (50), 43989-44012.
304. Stewart, K. M.; Horton, K. L.; Kelley, S. O., Cell-penetrating peptides as delivery vehicles for biology and medicine. *Organic & biomolecular chemistry* **2008**, *6* (13), 2242-2255.
305. Ruoslahti, E., Tumor penetrating peptides for improved drug delivery. *Advanced drug delivery reviews* **2017**, *110*, 3-12.
306. Cui, H.; Chen, X., Peptides and peptide conjugates in medicine. *Advanced drug delivery reviews* **2017**, *110*, 1-2.
307. Chen, C.; Ng, D. Y. W.; Weil, T., Polymer bioconjugates: Modern design concepts toward precision hybrid materials. *Progress in Polymer Science* **2020**, 101241.
308. Feiner, I. V. J.; Longo, B.; Gomez-Vallejo, V.; Calvo, J.; Chomet, M.; Vugts, D. J.; Windhorst, A. D.; Padro, D.; Zanda, M.; Rejc, L.; Llop, J., Comparison of analytical methods for antibody conjugates with application in nuclear imaging - Report from the trenches. *Nucl Med Biol* **2021**, *102-103*, 24-33.
309. Gorris, H. H.; Resch-Genger, U., Perspectives and challenges of photon-upconversion nanoparticles - Part II: bioanalytical applications. *Anal Bioanal Chem* **2017**, *409* (25), 5875-5890.
310. Borrelli, A.; Tornesello, A. L.; Tornesello, M. L.; Buonaguro, F. M., Cell Penetrating Peptides as Molecular Carriers for Anti-Cancer Agents. *Molecules* **2018**, *23* (2).
311. Ghosh, G.; Panicker, L., Protein–nanoparticle interactions and a new insight. *Soft Matter* **2021**, *17* (14), 3855-3875.
312. Vozlic, M.; Cernic, T.; Gyergyek, S.; Majaron, B.; Ponikvar-Svet, M.; Kostiv, U.; Horak, D.; Lisjak, D., Formation of phosphonate coatings for improved chemical stability of upconverting nanoparticles under physiological conditions. *Dalton Trans* **2021**, *50* (19), 6588-6597.
313. Kang, Z.; Meng, Q.; Liu, K., Peptide-based gene delivery vectors. *Journal of materials chemistry B* **2019**, *7* (11), 1824-1841.
314. Bashyal, S.; Noh, G.; Keum, T.; Choi, Y. W.; Lee, S., Cell penetrating peptides as an innovative approach for drug delivery; then, present and the future. *Journal of Pharmaceutical Investigation* **2016**, *46* (3), 205-220.
315. David, A., Peptide ligand-modified nanomedicines for targeting cells at the tumor microenvironment. *Advanced drug delivery reviews* **2017**, *119*, 120-142.
316. Hu, X. L.; Kwon, N.; Yan, K. C.; Sedgwick, A. C.; Chen, G. R.; He, X. P.; James, T. D.; Yoon, J., Bio - Conjugated Advanced Materials for Targeted Disease Theranostics. *Advanced Functional Materials* **2020**, *30* (13), 1907906.

317. Kang, Z.; Ding, G.; Meng, Z.; Meng, Q., The rational design of cell-penetrating peptides for application in delivery systems. *Peptides* **2019**, 170149.
318. Ramsey, J. D.; Flynn, N. H., Cell-penetrating peptides transport therapeutics into cells. *Pharmacology & therapeutics* **2015**, *154*, 78-86.
319. Futaki, S.; Nakase, I., Cell-surface interactions on arginine-rich cell-penetrating peptides allow for multiplex modes of internalization. *Accounts of chemical research* **2017**, *50* (10), 2449-2456.
320. Mousavizadeh, A.; Jabbari, A.; Akrami, M.; Bardania, H., Cell targeting peptides as smart ligands for targeting of therapeutic or diagnostic agents: a systematic review. *Colloids and Surfaces B: Biointerfaces* **2017**, *158*, 507-517.
321. Chen, C.; Richter, F.; Guerrero-Sanchez, C.; Traeger, A.; Schubert, U. S.; Feng, A.; Thang, S. H., Cell-Penetrating, Peptide-Based RAFT Agent for Constructing Penetration Enhancers. *ACS Macro Letters* **2020**, *9* (2), 260-265.
322. Lestrell, E.; Patolsky, F.; Voelcker, N. H.; Elnathan, R., Engineered nano-bio interfaces for intracellular delivery and sampling: Applications, agency and artefacts. *Materials Today* **2020**, *33*, 87-104.
323. Klimpel, A.; Lützenburg, T.; Neundorf, I., Recent advances of anti-cancer therapies including the use of cell-penetrating peptides. *Current opinion in pharmacology* **2019**, *47*, 8-13.
324. Huang, J. G.; Leshuk, T.; Gu, F. X., Emerging nanomaterials for targeting subcellular organelles. *Nano Today* **2011**, *6* (5), 478-492.
325. , J.; Hejt , A.; Ka ě , M. H.; Špa , H., The utilization of cell-penetrating peptides in the intracellular delivery of viral nanoparticles. *Materials* **2019**, *12* (17), 2671.
326. Guidotti, G.; Brambilla, L.; Rossi, D., Cell-Penetrating Peptides: From Basic Research to Clinics. *Trends Pharmacol Sci* **2017**, *38* (4), 406-424.
327. Yao, C.; Wang, P.; Wang, R.; Zhou, L.; El-Toni, A. M.; Lu, Y.; Li, X.; Zhang, F., Facile peptides functionalization of lanthanide-based nanocrystals through phosphorylation tethering for efficient in vivo NIR-to-NIR bioimaging. *Analytical chemistry* **2016**, *88* (3), 1930-1936.
328. Xu, R.; Cao, H.; Lin, D.; Yu, B.; Qu, J., Lanthanide-doped upconversion nanoparticles for biological super-resolution fluorescence imaging. *Cell Reports Physical Science* **2022**, 100922.
329. Oliveira, J. P.; Prado, A. R.; Keijok, W. J.; Antunes, P. W. P.; Yapuchura, E. R.; Guimaraes, M. C. C., Impact of conjugation strategies for targeting of antibodies in gold nanoparticles for ultrasensitive detection of 17beta-estradiol. *Sci Rep* **2019**, *9* (1), 13859.
330. Richards, D. A.; Maruani, A.; Chudasama, V., Antibody fragments as nanoparticle targeting ligands: a step in the right direction. *Chemical science* **2017**, *8* (1), 63-77.
331. Schumacher, D.; Helma, J.; Schneider, A. F. L.; Leonhardt, H.; Hackenberger, C. P. R., Nanobodies: Chemical Functionalization Strategies and Intracellular Applications. *Angew Chem Int Ed Engl* **2018**, *57* (9), 2314-2333.

332. Bathula, N. V.; Bommadevara, H.; Hayes, J. M., Nanobodies: The Future of Antibody-Based Immune Therapeutics. *Cancer Biother Radiopharm* **2021**, *36* (2), 109-122.
333. Zhang, H.; Li, F.; Dever, B.; Li, X.-F.; Le, X. C., DNA-mediated homogeneous binding assays for nucleic acids and proteins. *Chemical reviews* **2013**, *113* (4), 2812-2841.
334. Yoo, J.; Park, C.; Yi, G.; Lee, D.; Koo, H., Active targeting strategies using biological ligands for nanoparticle drug delivery systems. *Cancers* **2019**, *11* (5), 640.
335. Bannas, P.; Hambach, J.; Koch-Nolte, F., Nanobodies and Nanobody-Based Human Heavy Chain Antibodies As Antitumor Therapeutics. *Front Immunol* **2017**, *8*, 1603.
336. Bertrand, N.; Wu, J.; Xu, X.; Kamaly, N.; Farokhzad, O. C., Cancer nanotechnology: the impact of passive and active targeting in the era of modern cancer biology. *Adv Drug Deliv Rev* **2014**, *66*, 2-25.
337. Sivaram, A. J.; Wardiana, A.; Howard, C. B.; Mahler, S. M.; Thurecht, K. J. J. A. h. m., Recent advances in the generation of antibody–nanomaterial conjugates. **2018**, *7* (1), 1700607.
338. Früh, S. M.; Matti, U.; Spycher, P. R.; Rubini, M.; Lickert, S.; Schlichthaerle, T.; Jungmann, R.; Vogel, V.; Ries, J.; Schoen, I., Site-specifically-labeled antibodies for super-resolution microscopy reveal in situ linkage errors. *ACS nano* **2021**, *15* (7), 12161-12170.
339. Barakat, S.; Berksoz, M.; Zahedimaram, P.; Piepoli, S.; Erman, B., Nanobodies as molecular imaging probes. *Free Radical Biology and Medicine* **2022**.
340. Welch, N. G.; Scoble, J. A.; Muir, B. W.; Pigram, P. J., Orientation and characterization of immobilized antibodies for improved immunoassays. *Biointerphases* **2017**, *12* (2), 02D301.
341. Lou, D.; Ji, L.; Fan, L.; Ji, Y.; Gu, N.; Zhang, Y., Antibody-Oriented Strategy and Mechanism for the Preparation of Fluorescent Nanoprobes for Fast and Sensitive Immunodetection. *Langmuir* **2019**, *35* (14), 4860-4867.
342. Reddy, N. C.; Kumar, M.; Molla, R.; Rai, V., Chemical methods for modification of proteins. *Organic & Biomolecular Chemistry* **2020**, *18* (25), 4669-4691.
343. Marques, A.; Costa, P.; Velho, S.; Amaral, M., Functionalizing nanoparticles with cancer-targeting antibodies: A comparison of strategies. *Journal of Controlled Release* **2020**.
344. Sivaram, A.; Wardiana, A.; Howard, C.; Mahler, S.; Thurecht, K., Recent Advances in the Generation of Antibody-Nanomaterial Conjugates. *Advanced healthcare materials* **2018**, *7* (1).
345. Hermanson, G. T., *Bioconjugate techniques*. Academic press: 2013.
346. Spicer, C. D.; Pashuck, E. T.; Stevens, M. M., Achieving Controlled Biomolecule-Biomaterial Conjugation. *Chem Rev* **2018**, *118* (16), 7702-7743.
347. Han, S.; Qin, X.; An, Z.; Zhu, Y.; Liang, L.; Han, Y.; Huang, W.; Liu, X., Multicolour synthesis in lanthanide-doped nanocrystals through cation exchange in water. *Nature communications* **2016**, *7* (1), 1-7.
348. Samah, S.; Vasilevich, Z. A., Photoluminescent nanomaterials for medical biotechnology. *Acta Naturae (англоязычная версия)* **2021**, *13* (2), 16-31.

349. Wong, X. Y.; Sena-Torralba, A.; Álvarez-Diduk, R.; Muthoosamy, K.; Merkoçi, A., Nanomaterials for nanotheranostics: tuning their properties according to disease needs. *ACS nano* **2020**, *14* (3), 2585-2627.
350. Borse, S.; Rafique, R.; Murthy, Z.; Park, T. J.; Kailasa, S. K., Applications of upconversion nanoparticles in analytical and biomedical sciences: A review. *Analyst* **2022**.
351. Giner-Casares, J. J.; Henriksen-Lacey, M.; Coronado-Puchau, M.; Liz-Marzán, L. M., Inorganic nanoparticles for biomedicine: where materials scientists meet medical research. *Materials Today* **2016**, *19* (1), 19-28.
352. Zheng, Y.; Gao, Y., Molecular targeted nanotheranostics for future individualized cancer treatment. Taylor & Francis: 2020.
353. Jia, T.; Chen, G., Lanthanide nanoparticles for near-infrared II theranostics. *Coordination Chemistry Reviews* **2022**, *471*, 214724.
354. Liu, H.; Xu, C. T.; Dumlupinar, G.; Jensen, O. B.; Andersen, P. E.; Andersson-Engels, S., Deep tissue optical imaging of upconverting nanoparticles enabled by exploiting higher intrinsic quantum yield through use of millisecond single pulse excitation with high peak power. *Nanoscale* **2013**, *5* (20), 10034-10040.
355. Gao, P.; Pan, W.; Li, N.; Tang, B., Fluorescent probes for organelle-targeted bioactive species imaging. *Chemical science* **2019**, *10* (24), 6035-6071.
356. Varberg, J. M.; Unruh, J. R.; Bestul, A. J.; Khan, A. A.; Jaspersen, S. L., Quantitative analysis of nuclear pore complex organization in *Schizosaccharomyces pombe*. *Life science alliance* **2022**, *5* (7).
357. Hezwani, M.; Fahrenkrog, B. In *The functional versatility of the nuclear pore complex proteins*, Seminars in cell & developmental biology, Elsevier: 2017; pp 2-9.
358. Valli, J.; Sanderson, J., Super - Resolution Fluorescence Microscopy Methods for Assessing Mouse Biology. *Current Protocols* **2021**, *1* (8), e224.
359. Jonkman, J.; Brown, C. M.; Wright, G. D.; Anderson, K. I.; North, A. J., Tutorial: guidance for quantitative confocal microscopy. *Nature protocols* **2020**, *15* (5), 1585-1611.
360. Thompson, M. A.; Lew, M. D.; Moerner, W., Extending microscopic resolution with single-molecule imaging and active control. *Annual review of biophysics* **2012**, *41*, 321-342.
361. Hansel, C. S.; Holme, M. N.; Gopal, S.; Stevens, M. M., Advances in high-resolution microscopy for the study of intracellular interactions with biomaterials. *Biomaterials* **2020**, *226*, 119406.
362. Fish, K. N., Total internal reflection fluorescence (TIRF) microscopy. *Current protocols in cytometry* **2009**, *50* (1), 12.18. 1-12.18. 13.
363. Yan, R.; Wang, B.; Xu, K., Functional super-resolution microscopy of the cell. *Curr Opin Chem Biol* **2019**, *51*, 92-97.
364. So, S.; Kim, M.; Lee, D.; Nguyen, D. M.; Rho, J., Overcoming diffraction limit: From microscopy to nanoscopy. *Applied Spectroscopy Reviews* **2018**, *53* (2-4), 290-312.

365. Yang, X.; Yang, Z.; Wu, Z.; He, Y.; Shan, C.; Chai, P.; Ma, C.; Tian, M.; Teng, J.; Jin, D., Mitochondrial dynamics quantitatively revealed by STED nanoscopy with an enhanced squaraine variant probe. *Nature communications* **2020**, *11* (1), 1-9.
366. Stender, A. S.; Marchuk, K.; Liu, C.; Sander, S.; Meyer, M. W.; Smith, E. A.; Neupane, B.; Wang, G.; Li, J.; Cheng, J.-X., Single cell optical imaging and spectroscopy. *Chemical reviews* **2013**, *113* (4), 2469-2527.
367. Lee, C.; Xu, E. Z.; Liu, Y.; Teitelboim, A.; Yao, K.; Fernandez-Bravo, A.; Kotulska, A. M.; Nam, S. H.; Suh, Y. D.; Bednarkiewicz, A.; Cohen, B. E.; Chan, E. M.; Schuck, P. J., Giant nonlinear optical responses from photon-avalanching nanoparticles. *Nature* **2021**, *589* (7841), 230-235.
368. Fang, H.; Li, M.; Liu, Q.; Gai, Y.; Yuan, L.; Wang, S.; Zhang, X.; Ye, M.; Zhang, Y.; Gao, M., Ultra-sensitive Nanoprobe Modified with Tumor Cell Membrane for UCL/MRI/PET Multimodality Precise Imaging of Triple-Negative Breast Cancer. *Nano-Micro Letters* **2020**, *12* (1), 1-14.
369. Mikhaylova, M.; Cloin, B.; Finan, K.; Van Den Berg, R.; Teeuw, J.; Kijanka, M. M.; Sokolowski, M.; Katrukha, E. A.; Maidorn, M.; Opazo, F., Resolving bundled microtubules using anti-tubulin nanobodies. *Nature communications* **2015**, *6* (1), 1-7.
370. Hao, R.; Peng, Z.; Zhang, B., Single-molecule fluorescence microscopy for probing the electrochemical interface. *ACS omega* **2019**, *5* (1), 89-97.
371. Zhou, J.; Chizhik, A. I.; Chu, S.; Jin, D., Single-particle spectroscopy for functional nanomaterials. *Nature* **2020**, *579* (7797), 41-50.
372. Liao, J.; Jin, D.; Chen, C.; Li, Y.; Zhou, J., Helix Shape Power-Dependent Properties of Single Upconversion Nanoparticles. *The Journal of Physical Chemistry Letters* **2020**.
373. Zhou, J.; Chen, G.; Wu, E.; Bi, G.; Wu, B.; Teng, Y.; Zhou, S.; Qiu, J., Ultrasensitive polarized up-conversion of Tm<sup>3+</sup>-Yb<sup>3+</sup> doped  $\beta$ -NaYF<sub>4</sub> single nanorod. *Nano letters* **2013**, *13* (5), 2241-2246.
374. Hesse, J.; Klier, D. T.; Sgarzi, M.; Nsubuga, A.; Bauer, C.; Grenzer, J.; Hübner, R.; Wislicenus, M.; Joshi, T.; Kumke, M. U., Rapid Synthesis of Sub - 10 nm Hexagonal NaYF<sub>4</sub> - Based Upconverting Nanoparticles using Therminol® 66. *ChemistryOpen* **2018**, *7* (2), 159-168.
375. Wu, X.; Chen, G.; Shen, J.; Li, Z.; Zhang, Y.; Han, G., Upconversion nanoparticles: a versatile solution to multiscale biological imaging. *Bioconjugate chemistry* **2015**, *26* (2), 166-175.
376. van de Linde, S.; Aufmkolk, S.; Franke, C.; Holm, T.; Klein, T.; Löschberger, A.; Proppert, S.; Wolter, S.; Sauer, M., Investigating cellular structures at the nanoscale with organic fluorophores. *Chemistry & biology* **2013**, *20* (1), 8-18.
377. Wiesholler, L. M.; Hirsch, T., Strategies for the design of bright upconversion nanoparticles for bioanalytical applications. *Optical Materials* **2018**, *80*, 253-264.
378. Li, D.; Wen, S.; Kong, M.; Liu, Y.; Hu, W.; Shi, B.; Shi, X.; Jin, D., Highly Doped Upconversion Nanoparticles for In Vivo Applications Under Mild Excitation Power. *Analytical Chemistry* **2020**, *92* (16), 10913-10919.

379. Zheng, K.; Loh, K. Y.; Wang, Y.; Chen, Q.; Fan, J.; Jung, T.; Nam, S. H.; Suh, Y. D.; Liu, X., Recent advances in upconversion nanocrystals: Expanding the kaleidoscopic toolbox for emerging applications. *Nano Today* **2019**, *29*, 100797.
380. Wu, S.; Han, G.; Milliron, D. J.; Aloni, S.; Altoe, V.; Talapin, D. V.; Cohen, B. E.; Schuck, P. J., Non-blinking and photostable upconverted luminescence from single lanthanide-doped nanocrystals. *Proceedings of the National Academy of Sciences* **2009**, *106* (27), 10917-10921.
381. Zhan, Q.; Liu, H.; Wang, B.; Wu, Q.; Pu, R.; Zhou, C.; Huang, B.; Peng, X.; Agren, H.; He, S., Achieving high-efficiency emission depletion nanoscopy by employing cross relaxation in upconversion nanoparticles. *Nat Commun* **2017**, *8* (1), 1058.
382. Shin, K.; Jung, T.; Lee, E.; Lee, G.; Goh, Y.; Heo, J.; Jung, M.; Jo, E.-J.; Lee, H.; Kim, M.-G., Distinct mechanisms for the upconversion of NaYF<sub>4</sub>: Yb<sup>3+</sup>, Er<sup>3+</sup> nanoparticles revealed by stimulated emission depletion. *Physical Chemistry Chemical Physics* **2017**, *19* (15), 9739-9744.
383. Liu, Y.; Wang, F.; Lu, H.; Fang, G.; Wen, S.; Chen, C.; Shan, X.; Xu, X.; Zhang, L.; Stenzel, M., Super - Resolution Mapping of Single Nanoparticles inside Tumor Spheroids. *Small* **2020**, *16* (6), 1905572.
384. Liu, B.; Chen, C.; Di, X.; Liao, J.; Wen, S.; Su, Q. P.; Shan, X.; Xu, Z.-Q.; Ju, L. A.; Mi, C., Upconversion nonlinear structured illumination microscopy. *Nano Letters* **2020**.
385. Choi, N.-E.; Lee, J.-Y.; Park, E.-C.; Lee, J.-H.; Lee, J., Recent advances in organelle-targeted fluorescent probes. *Molecules* **2021**, *26* (1), 217.
386. Pelaz, B.; Alexiou, C.; Alvarez-Puebla, R. A.; Alves, F.; Andrews, A. M.; Ashraf, S.; Balogh, L. P.; Ballerini, L.; Bestetti, A.; Brendel, C., Diverse applications of nanomedicine. ACS Publications: 2017.
387. Kavand, A.; Serra, C. A.; Blanck, C.; Lenertz, M.; Anton, N.; Vandamme, T. F.; Mély, Y.; Przybilla, F.; Chan-Seng, D., Controlled synthesis of NaYF<sub>4</sub>: Yb, Er upconversion nanocrystals as potential probe for bioimaging: a focus on heat treatment. *ACS Applied Nano Materials* **2021**, *4* (5), 5319-5329.
388. Torresan, M. F.; Wolosiuk, A., Critical aspects on the chemical stability of NaYF<sub>4</sub>-based upconverting nanoparticles for biomedical applications. *ACS Applied Bio Materials* **2021**, *4* (2), 1191-1210.
389. Na, H.; Woo, K.; Lim, K.; Jang, H. S., Rational morphology control of beta-NaYF<sub>4</sub>:Yb,Er/Tm upconversion nanophosphors using a ligand, an additive, and lanthanide doping. *Nanoscale* **2013**, *5* (10), 4242-51.
390. Gupta, S. K.; Sudarshan, K.; Kadam, R. M., Optical nanomaterials with focus on rare earth doped oxide: A Review. *Materials Today Communications* **2021**, *27*.
391. Zhang, Y.; Wei, W.; Das, G. K.; Tan, T. T. Y., Engineering lanthanide-based materials for nanomedicine. *Journal of Photochemistry and Photobiology C: Photochemistry Reviews* **2014**, *20*, 71-96.



392. Mackenzie, L. E.; Goode, J. A.; Vakurov, A.; Nampi, P. P.; Saha, S.; Jose, G.; Millner, P. A., The theoretical molecular weight of NaYF<sub>4</sub>:RE upconversion nanoparticles. *Sci Rep* **2018**, *8* (1), 1106.
393. Ansari, A. A.; Parchur, A. K.; Thorat, N. D.; Chen, G., New advances in pre-clinical diagnostic imaging perspectives of functionalized upconversion nanoparticle-based nanomedicine. *Coordination Chemistry Reviews* **2021**, *440*, 213971.
394. Rafique, R.; Baek, S. H.; Park, C. Y.; Chang, S.-J.; Gul, A. R.; Ha, S.; Nguyen, T. P.; Oh, H.; Ham, S.; Arshad, M., Morphological evolution of upconversion nanoparticles and their biomedical signal generation. *Scientific reports* **2018**, *8* (1), 1-11.
395. Maurizio, S. L.; Tessitore, G.; Mandl, G. A.; Capobianco, J. A., Luminescence dynamics and enhancement of the UV and visible emissions of Tm<sup>3+</sup> in LiYF<sub>4</sub>: Yb<sup>3+</sup>, Tm<sup>3+</sup> upconverting nanoparticles. *Nanoscale Advances* **2019**, *1* (11), 4492-4500.
396. Nampi, P. P.; Vakurov, A.; Saha, S.; Jose, G.; Millner, P. A., Surface modified hexagonal upconversion nanoparticles for the development of competitive assay for biodetection. *Biomaterials Advances* **2022**, *136*, 212763.
397. Zhao, L.; Choi, J.; Lu, Y.; Kim, S. Y., NIR photoregulated theranostic system based on hexagonal-phase upconverting nanoparticles for tumor-targeted photodynamic therapy and fluorescence imaging. *Nanomaterials* **2020**, *10* (12), 2332.
398. Wilhelm, S.; Kaiser, M.; Wurth, C.; Heiland, J.; Carrillo-Carrion, C.; Muhr, V.; Wolfbeis, O. S.; Parak, W. J.; Resch-Genger, U.; Hirsch, T., Water dispersible upconverting nanoparticles: effects of surface modification on their luminescence and colloidal stability. *Nanoscale* **2015**, *7* (4), 1403-10.
399. Agrahari, V.; Agrahari, V., Advances and applications of block-copolymer-based nanoformulations. *Drug Discovery Today* **2018**, *23* (5), 1139-1151.
400. Daniels, G. C.; Hinnant, K. M.; Brown, L. C.; Weise, N. K.; Aukerman, M. C.; Giordano, B. C., Copolymer Reversible Addition-Fragmentation Chain Transfer Synthesis of Polyethylene Glycol (PEG) Functionalized with Hydrophobic Acrylates: A Study of Surface and Foam Properties. *Langmuir* **2022**.
401. Fu, C.; Huang, Z.; Hawker, C. J.; Moad, G.; Xu, J.; Boyer, C., RAFT-mediated, visible light-initiated single unit monomer insertion and its application in the synthesis of sequence-defined polymers. *Polymer Chemistry* **2017**, *8* (32), 4637-4643.
402. Duncan, R.; Vicent, M. J., Polymer therapeutics-prospects for 21st century: the end of the beginning. *Advanced drug delivery reviews* **2013**, *65* (1), 60-70.
403. Kaupbayeva, B.; Russell, A. J., Polymer-enhanced biomacromolecules. *Progress in Polymer Science* **2020**, *101*, 101194.
404. Dietrich, M.; Glassner, M.; Gruending, T.; Schmid, C.; Falkenhagen, J.; Barner-Kowollik, C., Facile conversion of RAFT polymers into hydroxyl functional polymers: a detailed investigation of variable monomer and RAFT agent combinations. *Polymer chemistry* **2010**, *1* (5), 634-644.

405. Whitfield, R.; Parkatzidis, K.; Truong, N. P.; Junkers, T.; Anastasaki, A., Tailoring polymer dispersity by RAFT polymerization: a versatile approach. *Chem* **2020**, *6* (6), 1340-1352.
406. Wang, K.; Amin, K.; An, Z.; Cai, Z.; Chen, H.; Chen, H.; Dong, Y.; Feng, X.; Fu, W.; Gu, J., Advanced functional polymer materials. *Materials Chemistry Frontiers* **2020**.
407. Yilmaz, G.; Yagci, Y., Light-induced step-growth polymerization. *Progress in Polymer Science* **2020**, *100*, 101178.
408. Demina, P. A.; Sholina, N. V.; Akasov, R. A.; Khochenkov, D. A.; Arkharova, N. A.; Nechaev, A. V.; Khaydukov, E. V.; Generalova, A. N., A versatile platform for bioimaging based on colominic acid-decorated upconversion nanoparticles. *Biomaterials Science* **2020**, *8* (16), 4570-4580.
409. Giaouzi, D.; Pispas, S., PNIPAM-b-PDMAEA double stimuli responsive copolymers: Effects of composition, end groups and chemical modification on solution self-assembly. *European Polymer Journal* **2020**, *135*, 109867.
410. Huang, H.-J.; Tsai, Y.-L.; Lin, S.-H.; Hsu, S.-h., Smart polymers for cell therapy and precision medicine. *Journal of Biomedical Science* **2019**, *26* (1), 73.
411. Zhang, K.; Gao, H.; Deng, R.; Li, J., Emerging Applications of Nanotechnology for Controlling Cell - Surface Receptor Clustering. *Angewandte Chemie International Edition* **2019**, *58* (15), 4790-4799.
412. Nazeer, N.; Ahmed, M., Hydrophilic and salt responsive polymers promote depletion aggregation of bacteria. *European Polymer Journal* **2019**, *119*, 148-154.
413. Erathodiyil, N.; Chan, H.-M.; Wu, H.; Ying, J. Y., Zwitterionic polymers and hydrogels for antibiofouling applications in implantable devices. *Materials Today* **2020**.
414. Lin, J.; Miao, L.; Zhong, G.; Lin, C.-H.; Dargazangy, R.; Alexander-Katz, A., Understanding the synergistic effect of physicochemical properties of nanoparticles and their cellular entry pathways. *Communications Biology* **2020**, *3* (1), 1-10.
415. Shende, P.; Wakade, V. S., Biointerface: a nano-modulated way for biological transportation. *Journal of Drug Targeting* **2020**, *28* (5), 456-467.
416. Mukherjee, S.; Gowen, A., A review of recent trends in polymer characterization using non-destructive vibrational spectroscopic modalities and chemical imaging. *Analytica chimica acta* **2015**, *895*, 12-34.
417. Duong, H. T.; Chen, Y.; Tawfik, S. A.; Wen, S.; Parviz, M.; Shimoni, O.; Jin, D. J. R. a., Systematic investigation of functional ligands for colloidal stable upconversion nanoparticles. **2018**, *8* (9), 4842-4849.
418. Xu, J.; He, J.; Fan, D.; Tang, W.; Yang, Y., Thermal decomposition of dithioesters and its effect on RAFT polymerization. *Macromolecules* **2006**, *39* (11), 3753-3759.
419. Postma, A.; Davis, T. P.; Li, G.; Moad, G.; O'Shea, M. S., RAFT polymerization with phthalimidomethyl trithiocarbonates or xanthates. On the origin of bimodal molecular weight distributions in living radical polymerization. *Macromolecules* **2006**, *39* (16), 5307-5318.

420. Maddahfar, M.; Wen, S.; Hosseinpour Mashkani, S. M.; Zhang, L.; Shimoni, O.; Stenzel, M.; Zhou, J.; Fazekas de St Groth, B.; Jin, D., Stable and Highly Efficient Antibody-Nanoparticles Conjugation. *Bioconjug Chem* **2021**, *32* (6), 1146-1155.
421. Thérien-Aubin, H.; Chen, L.; Ober, C. K., Fouling-resistant polymer brush coatings. *Polymer* **2011**, *52* (24), 5419-5425.
422. Badv, M.; Bayat, F.; Weitz, J. I.; Didar, T. F., Single and multi-functional coating strategies for enhancing the biocompatibility and tissue integration of blood-contacting medical implants. *Biomaterials* **2020**, 120291.
423. Tan, X.; Zhan, J.; Zhu, Y.; Cao, J.; Wang, L.; Liu, S.; Wang, Y.; Liu, Z.; Qin, Y.; Wu, M., Improvement of uveal and capsular biocompatibility of hydrophobic acrylic intraocular lens by surface grafting with 2-methacryloyloxyethyl phosphorylcholine-methacrylic acid copolymer. *Scientific reports* **2017**, *7* (1), 1-13.
424. Jiang, L.; Zhu, W.; Qian, H.; Wang, C.; Chen, Y.; Liu, P., Fabrication of PMPC/PTM/PEGDA micropatterns onto polypropylene films behaving with dual functions of antifouling and antimicrobial activities. *Journal of Materials Chemistry B* **2019**, *7* (33), 5078-5088.
425. Gaborieau, M.; Castignolles, P., Size-exclusion chromatography (SEC) of branched polymers and polysaccharides. *Analytical and bioanalytical chemistry* **2011**, *399* (4), 1413-1423.
426. Moad, G.; Rizzardo, E.; Thang, S. H. J. P. I., End - functional polymers, thiocarbonylthio group removal/transformation and reversible addition–fragmentation–chain transfer (RAFT) polymerization. **2011**, *60* (1), 9-25.
427. Seetasang, S.; Xu, Y., Recent progress and perspectives in applications of 2-methacryloyloxyethyl phosphorylcholine polymers in biodevices at small scales. *Journal of Materials Chemistry B* **2022**.
428. Iwata, R.; Suk-In, P.; Hoven, V. P.; Takahara, A.; Akiyoshi, K.; Iwasaki, Y., Control of nanobiointerfaces generated from well-defined biomimetic polymer brushes for protein and cell manipulations. *Biomacromolecules* **2004**, *5* (6), 2308-2314.
429. Azzaroni, O., Polymer brushes here, there, and everywhere: Recent advances in their practical applications and emerging opportunities in multiple research fields. *Journal of Polymer Science Part A: Polymer Chemistry* **2012**, *50* (16), 3225-3258.
430. Jayaraman, A., Polymer grafted nanoparticles: Effect of chemical and physical heterogeneity in polymer grafts on particle assembly and dispersion. *Journal of Polymer Science Part B: Polymer Physics* **2013**, *51* (7), 524-534.
431. DaCosta, M. V.; Doughan, S.; Han, Y.; Krull, U. J. J. A. c. a., Lanthanide upconversion nanoparticles and applications in bioassays and bioimaging: A review. **2014**, *832*, 1-33.
432. Sangermano, M.; Razza, N., Light induced grafting-from strategies as powerful tool for surface modification. *eXPRESS Polymer Letters* **2019**, *13* (2), 135.
433. Wolfbeis, O. S., An overview of nanoparticles commonly used in fluorescent bioimaging. *Chemical Society Reviews* **2015**, *44* (14), 4743-4768.

434. Boyer, J.-C.; Manseau, M.-P.; Murray, J. I.; Van Veggel, F. C. J. L., Surface modification of upconverting NaYF<sub>4</sub> nanoparticles with PEG–phosphate ligands for NIR (8 nm) biolabeling within the biological window. *2009*, *26* (2), 1157-1164.
435. Chen, Y.; D'Amario, C.; Gee, A.; Duong, H. T. T.; Shimoni, O.; Valenzuela, S. M., Dispersion stability and biocompatibility of four ligand-exchanged NaYF<sub>4</sub>: Yb, Er upconversion nanoparticles. *Acta Biomater* **2020**, *102*, 384-393.
436. Kureha, T.; Ohira, M.; Takahashi, Y.; Li, X.; Gilbert, E. P.; Shibayama, M., Nanoscale Structures of Poly (oligo ethylene glycol methyl ether methacrylate) Hydrogels Revealed by Small-Angle Neutron Scattering. *Macromolecules* **2022**, *55* (5), 1844-1854.
437. Pham, L. N.; Walsh, T. R., Design Traits for Diblock Copolymer Coating Properties on NaGdF<sub>4</sub> Upconversion Nanoparticles. *ACS Applied Polymer Materials* **2022**, *4* (7), 5224-5233.
438. Youn, Y. S.; Bae, Y. H., Perspectives on the past, present, and future of cancer nanomedicine. *Advanced drug delivery reviews* **2018**, *130*, 3-11.
439. Fu, L.; Morsch, M.; Shi, B.; Wang, G.; Lee, A.; Radford, R.; Lu, Y.; Jin, D.; Chung, R., A versatile upconversion surface evaluation platform for bio–nano surface selection for the nervous system. *Nanoscale* **2017**, *9* (36), 13683-13692.
440. Andresen, E.; Würth, C.; Prinz, C.; Michaelis, M.; Resch-Genger, U., Time-resolved luminescence spectroscopy for monitoring the stability and dissolution behaviour of upconverting nanocrystals with different surface coatings. *Nanoscale* **2020**, *12* (23), 12589-12601.
441. Bixner, O.; Lassenberger, A.; Baurecht, D.; Reimhult, E., Complete exchange of the hydrophobic dispersant shell on monodisperse superparamagnetic iron oxide nanoparticles. *Langmuir* **2015**, *31* (33), 9198-9204.
442. Byzova, N. A.; Safenkova, I. V.; Slutskaia, E. S.; Zherdev, A. V.; Dzantiev, B. B., Less is more: A comparison of antibody–gold nanoparticle conjugates of different ratios. *Bioconjugate chemistry* **2017**, *28* (11), 2737-2746.
443. Loo, J. F.-C.; Chien, Y.-H.; Yin, F.; Kong, S.-K.; Ho, H.-P.; Yong, K.-T., Upconversion and downconversion nanoparticles for biophotonics and nanomedicine. *Coordination Chemistry Reviews* **2019**, *400*, 213042.
444. Cordell, P.; Carrington, G.; Curd, A.; Parker, F.; Tomlinson, D.; Peckham, M., Affimers and nanobodies as molecular probes and their applications in imaging. *Journal of Cell Science* **2022**, *135* (14), jcs259168.
445. Cho, T. J.; Hackley, V. A., Assessing the chemical and colloidal stability of functionalized gold nanoparticles. *NIST Special Publication* **2018**, *1200*, 26.
446. Hoshyar, N.; Gray, S.; Han, H.; Bao, G., The effect of nanoparticle size on in vivo pharmacokinetics and cellular interaction. *Nanomedicine* **2016**, *11* (6), 673-692.
447. Jia, X.; Yin, J.; He, D.; He, X.; Wang, K.; Chen, M.; Li, Y., Polyacrylic acid modified upconversion nanoparticles for simultaneous pH-triggered drug delivery and release imaging. *J Biomed Nanotechnol* **2013**, *9* (12), 2063-72.

448. Drelich, J.; Wang, Y. U., Charge heterogeneity of surfaces: Mapping and effects on surface forces. *Advances in colloid and interface science* **2011**, *165* (2), 91-101.
449. Chantasirichot, S.; Inoue, Y.; Ishihara, K., Introduction of functional groups to reactive ABA block-copolymers composed of poly (2-methacryloyloxyethyl phosphorylcholine) and poly (glycidyl methacrylate) for spontaneous hydrogel formation. *Polymer* **2017**, *123*, 100-106.
450. Wang, F.; Zhang, H.; Yu, B.; Wang, S.; Shen, Y.; Cong, H., Review of the research on anti-protein fouling coatings materials. *Progress in Organic Coatings* **2020**, *147*, 105860.
451. Tong, L.; Lu, E.; Pichaandi, J.; Cao, P.; Nitz, M.; Winnik, M. A., Quantification of surface ligands on NaYF<sub>4</sub> nanoparticles by three independent analytical techniques. *Chemistry of Materials* **2015**, *27* (13), 4899-4910.
452. Shin, I.; Nam, J.; Lee, K.; Kim, E.; Kim, T.-H., Poly (ethylene glycol)(PEG)-crosslinked poly (vinyl pyridine)-PEG-poly (vinyl pyridine)-based triblock copolymers prepared by RAFT polymerization as novel gel polymer electrolytes. *Polymer Chemistry* **2018**, *9* (42), 5190-5199.
453. Soliman, F. M.; Yang, W.; Guo, H.; Shinger, M. I.; Idris, A. M.; Hassan, E. S., Preparation of carboxymethyl cellulose-g-poly (acrylic acid-2-acrylamido-2-methylpropane sulfonic acid)/attapulgite superabsorbent composite. *Am. J. Oil Chem. Technol* **2016**, *2*, 11-19.
454. Benavides, R.; Oenning, L.; Paula, M.; Da Silva, L., Properties of polystyrene/acrylic acid membranes after sulphonation reactions. *Journal of New Materials for Electrochemical Systems* **2014**, *17* (2), 085-090.
455. Gosecka, M.; Basinska, T., Hydrophilic polymers grafted surfaces: preparation, characterization, and biomedical applications. Achievements and challenges. *Polymers for Advanced Technologies* **2015**, *26* (7), 696-706.
456. Kumar, B.; Malhotra, K.; Fuku, R.; Van Houten, J.; Qu, G. Y.; Piunno, P. A.; Krull, U. J., Recent trends in the developments of analytical probes based on lanthanide-doped upconversion nanoparticles. *TrAC Trends in Analytical Chemistry* **2021**, *139*, 116256.
457. Arai, M. S.; de Camargo, A. S. S., Exploring the use of upconversion nanoparticles in chemical and biological sensors: from surface modifications to point-of-care devices. *Nanoscale Advances* **2021**, *3* (18), 5135-5165.
458. Guedes, S.; Neves, B.; Vitorino, R.; Domingues, R.; Cruz, M. T.; Domingues, P., Contact dermatitis: in pursuit of sensitizer's molecular targets through proteomics. *Archives of toxicology* **2017**, *91* (2), 811-825.
459. Ji, Y.; Yang, X.; Ji, Z.; Zhu, L.; Ma, N.; Chen, D.; Jia, X.; Tang, J.; Cao, Y., DFT-calculated IR spectrum amide I, II, and III band contributions of N-methylacetamide fine components. *ACS omega* **2020**, *5* (15), 8572-8578.
460. Braun, A. C.; Gutmann, M.; Luhmann, T.; Meinel, L., Bioorthogonal strategies for site-directed decoration of biomaterials with therapeutic proteins. *J Control Release* **2018**, *273*, 68-85.
461. Occhipinti, E.; Verderio, P.; Natalello, A.; Galbiati, E.; Colombo, M.; Mazzucchelli, S.; Salvadè, A.; Tortora, P.; Doglia, S. M.; Prosperi, D., Investigating the structural

biofunctionality of antibodies conjugated to magnetic nanoparticles. *Nanoscale* **2011**, 3 (2), 387-390.

462. Barth, A., Infrared spectroscopy of proteins. *Biochimica et Biophysica Acta (BBA)-Bioenergetics* **2007**, 1767 (9), 1073-1101.

463. Wang, L.; Frei, M. S.; Salim, A.; Johnsson, K., Small-Molecule Fluorescent Probes for Live-Cell Super-Resolution Microscopy. *J Am Chem Soc* **2019**, 141 (7), 2770-2781.

464. Wang, C.; Li, X.; Zhang, F., Bioapplications and biotechnologies of upconversion nanoparticle-based nanosensors. *Analyst* **2016**, 141 (12), 3601-3620.

465. Chen, H.; Ding, B.; Lin, J., Recent Progress in Upconversion Nanomaterials for Emerging Optical Biological Applications. *Advanced Drug Delivery Reviews* **2022**, 114414.

466. Dong, H.; Sun, L.-D.; Yan, C.-H., Lanthanide-doped upconversion nanoparticles for super-resolution microscopy. *Frontiers in Chemistry* **2021**, 8, 619377.

467. Zijlmans, H.; Bonnet, J.; Burton, J.; Kardos, K.; Vail, T.; Niedbala, R.; Tanke, H., Detection of cell and tissue surface antigens using up-converting phosphors: a new reporter technology. *Analytical biochemistry* **1999**, 267 (1), 30-36.

468. Li, S.; Wei, X.; Li, S.; Zhu, C.; Wu, C., Up-Conversion Luminescent Nanoparticles for Molecular Imaging, Cancer Diagnosis and Treatment. *Int J Nanomedicine* **2020**, 15, 9431-9445.

469. Zhang, Y.; Li, S.; Zeng, C.; Huang, G.; Zhu, X.; Wang, Q.; Wang, K.; Zhou, Q.; Yan, C.; Zhang, W., Molecular architecture of the luminal ring of the *Xenopus laevis* nuclear pore complex. *Cell research* **2020**, 30 (6), 532-540.

470. Stawicki, S. P.; Steffen, J. M., Republication: The nuclear pore complex-A comprehensive review of structure and function. *International Journal of Academic Medicine* **2017**, 3, 51-59.

471. Boisvert, F.-M.; van Koningsbruggen, S.; Navascués, J.; Lamond, A. I., The multifunctional nucleolus. *Nature reviews Molecular cell biology* **2007**, 8 (7), 574-585.

472. Martin, R. M.; Ter-Avetisyan, G.; Herce, H. D.; Ludwig, A. K.; Lattig-Tunnemann, G.; Cardoso, M. C., Principles of protein targeting to the nucleolus. *Nucleus* **2015**, 6 (4), 314-25.

473. Deng, K.; Wang, L.; Xia, Q.; Liu, R.; Qu, J., A nucleic acid-specific fluorescent probe for nucleolus imaging in living cells. *Talanta* **2019**, 192, 212-219.

474. Chen, X.; Zhu, Y.; Zhou, D.; Xu, W.; Zhu, J.; Pan, G.; Yin, Z.; Wang, H.; Cui, S.; Song, H., Size-dependent downconversion near-infrared emission of NaYF<sub>4</sub>: Yb<sup>3+</sup>, Er<sup>3+</sup> nanoparticles. *Journal of Materials Chemistry C* **2017**, 5 (9), 2451-2458.

475. Etienne - Manneville, S., Actin and microtubules in cell motility: which one is in control? *Traffic* **2004**, 5 (7), 470-477.

476. Garcin, C.; Straube, A., Microtubules in cell migration. *Essays Biochem* **2019**, 63 (5), 509-520.

477. Etienne-Manneville, S., Microtubules in cell migration. *Annu Rev Cell Dev Biol* **2013**, 29 (1), 471-499.

478. McKayed, K. K.; Simpson, J. C., Actin in action: imaging approaches to study cytoskeleton structure and function. *Cells* **2013**, *2* (4), 715-731.
479. Li, W.; Kaminski Schierle, G. S.; Lei, B.; Liu, Y.; Kaminski, C. F., Fluorescent Nanoparticles for Super-Resolution Imaging. *Chemical Reviews* **2022**.
480. Savulescu, A. F.; Shorer, H.; Kleifeld, O.; Cohen, I.; Gruber, R.; Glickman, M. H.; Harel, A., Nuclear import of an intact preassembled proteasome particle. *Molecular biology of the cell* **2011**, *22* (6), 880-891.
481. Najbauer, E. E.; Ng, S. C.; Griesinger, C.; Görlich, D.; Andreas, L. B., Atomic resolution dynamics of cohesive interactions in phase-separated Nup98 FG domains. *Nature communications* **2022**, *13* (1), 1-16.
482. Strambio-De-Castillia, C.; Niepel, M.; Rout, M. P., The nuclear pore complex: bridging nuclear transport and gene regulation. *Nature reviews Molecular cell biology* **2010**, *11* (7), 490-501.
483. Schlichthaerle, T.; Strauss, M. T.; Schueder, F.; Auer, A.; Nijmeijer, B.; Kueblbeck, M.; Jimenez Sabinina, V.; Thevathasan, J. V.; Ries, J.; Ellenberg, J., Direct visualization of single nuclear pore complex proteins using genetically - encoded probes for DNA - PAINT. *Angewandte Chemie* **2019**, *131* (37), 13138-13142.
484. Damasco, J. A.; Chen, G.; Shao, W.; Ågren, H.; Huang, H.; Song, W.; Lovell, J. F.; Prasad, P. N., Size-tunable and monodisperse Tm<sup>3+</sup>/Gd<sup>3+</sup>-doped hexagonal NaYbF<sub>4</sub> nanoparticles with engineered efficient near infrared-to-near infrared upconversion for in vivo imaging. *ACS applied materials & interfaces* **2014**, *6* (16), 13884-13893.
485. Lou, D.; Fan, L.; Jiang, T.; Zhang, Y., Advances in nanoparticle - based lateral flow immunoassay for point - of - care testing. *View* **2022**, *3* (1), 20200125.
486. Banerjee, R.; Jaiswal, A., Recent advances in nanoparticle-based lateral flow immunoassay as a point-of-care diagnostic tool for infectious agents and diseases. *Analyst* **2018**, *143* (9), 1970-1996.
487. He, M.; Li, Z.; Ge, Y.; Liu, Z., Portable upconversion nanoparticles-based paper device for field testing of drug abuse. *Analytical chemistry* **2016**, *88* (3), 1530-1534.
488. Gowri, A.; Ashwin Kumar, N.; Suresh Anand, B. S., Recent advances in nanomaterials based biosensors for point of care (PoC) diagnosis of Covid-19 - A minireview. *Trends Analyt Chem* **2021**, *137*, 116205.
489. Zhuang, L.; Ji, Y.; Tian, P.; Wang, K.; Kou, C.; Gu, N.; Zhang, Y., Polymerase chain reaction combined with fluorescent lateral flow immunoassay based on magnetic purification for rapid detection of canine parvovirus 2. *BMC veterinary research* **2019**, *15* (1), 1-13.
490. Shirshahi, V.; Liu, G., Enhancing the analytical performance of paper lateral flow assays: From chemistry to engineering. *TrAC Trends in Analytical Chemistry* **2021**, *136.0*